



Calhoun: The NPS Institutional Archive
DSpace Repository

Reports and Technical Reports

Faculty and Researchers' Publications

2011-12

Integrated masts for ship radiofrequency
electromagnetic interference mitigation a
preliminary electromagnetic characterization
study (u)

DallArmi-Stoks, Giuseppina

Monterey, California. Naval Postgraduate School

<https://hdl.handle.net/10945/6908>

This publication is a work of the U.S. Government as defined in Title 17, United States Code, Section 101. Copyright protection is not available for this work in the United States.

Downloaded from NPS Archive: Calhoun



Calhoun is the Naval Postgraduate School's public access digital repository for research materials and institutional publications created by the NPS community. Calhoun is named for Professor of Mathematics Guy K. Calhoun, NPS's first appointed -- and published -- scholarly author.

Dudley Knox Library / Naval Postgraduate School
411 Dyer Road / 1 University Circle
Monterey, California USA 93943

<http://www.nps.edu/library>



NAVAL POSTGRADUATE SCHOOL

MONTEREY, CALIFORNIA

**INTEGRATED MASTS FOR SHIP RADIOFREQUENCY
ELECTROMAGNETIC INTERFERENCE MITIGATION –
A PRELIMINARY ELECTROMAGNETIC
CHARACTERIZATION STUDY (U)**

by

Giuseppina Dall'Armi-Stoks

December 2011

Approved for public release; distribution is unlimited

Prepared for: Defense Science and Technology Organization Australia
Edinburgh SA 5111, Australia

Naval Postgraduate School
Monterey, CA 93943

THIS PAGE INTENTIONALLY LEFT BLANK

**NAVAL POSTGRADUATE SCHOOL
Monterey, California 93943-5000**

Daniel T. Oliver
President

Leonard A. Ferrari
Executive Vice President and
Provost

The report entitled “*Integrated Masts for Ship Radiofrequency Electromagnetic Interference Mitigation – A Preliminary Electromagnetic Characterization Study*” was prepared for Defence Science and Technology Organization and the Naval Postgraduate School. The work was done under the auspice of the Australian and United States of America Engineers and Scientists Exchange Program (ESEP) agreement.

Further distribution of all or part of this report is authorized.

This report was prepared by:

Giuseppina Dall’Armi-Stoks
Visiting Research Associate

Reviewed by:

R. Clark Robertson, Chair
Department of Electrical and
Computer Engineering

David C. Jenn, Professor
Department of Electrical and
Computer Engineering

Released by:

Douglas Fouts
Interim Vice President and
Dean of Research

THIS PAGE INTENTIONALLY LEFT BLANK

REPORT DOCUMENTATION PAGE				<i>Form Approved</i> OMB No. 0704-0188	
Public reporting burden for this collection of information is estimated to average 1 hour per response, including the time for reviewing instructions, searching existing data sources, gathering and maintaining the data needed, and completing and reviewing this collection of information. Send comments regarding this burden estimate or any other aspect of this collection of information, including suggestions for reducing this burden to Department of Defense, Washington Headquarters Services, Directorate for Information Operations and Reports (0704-0188), 1215 Jefferson Davis Highway, Suite 1204, Arlington, VA 22202-4302. Respondents should be aware that notwithstanding any other provision of law, no person shall be subject to any penalty for failing to comply with a collection of information if it does not display a currently valid OMB control number. PLEASE DO NOT RETURN YOUR FORM TO THE ABOVE ADDRESS.					
1. REPORT DATE (DD-MM-YYYY) 01-02-2012		2. REPORT TYPE Technical Report		3. DATES COVERED (From-To) Jan 2011 – Dec 2011	
4. TITLE AND SUBTITLE Integrated Masts for Ship Radiofrequency Electromagnetic Interference Mitigation – A Preliminary Electromagnetic Characterization Study (U)				5a. CONTRACT NUMBER	
				5b. GRANT NUMBER	
				5c. PROGRAM ELEMENT NUMBER	
6. AUTHOR(S) Giuseppina Dall’Armi-Stoks				5d. PROJECT NUMBER	
				5e. TASK NUMBER	
				5f. WORK UNIT NUMBER	
7. PERFORMING ORGANIZATION NAME(S) AND ADDRESS(ES) AND ADDRESS(ES) Naval Postgraduate School Monterey, CA 93943				8. PERFORMING ORGANIZATION REPORT NUMBER NPS-EC-12-002	
9. SPONSORING / MONITORING AGENCY NAME(S) AND ADDRESS(ES) Defense Science and Technology Organization Australia PO Box 1500 Edinburgh SA 5111 Australia Under the Auspice of the AUS-USA ESEP agreement				10. SPONSOR/MONITOR’S ACRONYM(S)	
				11. SPONSOR/MONITOR’S REPORT NUMBER(S)	
12. DISTRIBUTION / AVAILABILITY STATEMENT Approved for public release; distribution is unlimited					
13. SUPPLEMENTARY NOTES					
14. ABSTRACT This report provides an electromagnetic characterization analysis in order to ascertain if integrated masts are an effective ship radiofrequency electromagnetic interference mitigation strategy. Free space and fitted antenna radiation patterns, and fitted relative near field power flux densities of a linear array transmitting antenna, and the mutual antenna-to-antenna coupling between a linear array transmit and receive antennas, both fitted on the same mast structure, was determined. Overall, the mast structure can reduce the mutual antenna-to-antenna coupling (up to ~20dB) and can affect the fitted antenna radiation pattern. There is both significantly high (i.e., up to 0 dB) and low (~-30dB) fitted relative near field power flux density within the vicinity of the transmitting antenna and regions around the mast structure. All this depends on the location and position of the transmit antenna relative to the mast structure, and the location of the receiver antenna relative to the transmit antenna. Both desensitization and third order sub-harmonic distortions non-linear effects on the receiver antenna system were also assessed due to the fitted relative near field power densities. Depending on the specifications of the receiver system, desensitization (or gain compression) was found to be significant, whereas, third order sub-harmonic distortion was not..					
15. SUBJECT TERMS Electronic Warfare, Antennas, Electromagnetic Characterization Analysis, Integrated Masts, Radiofrequency Electromagnetic Interference Mitigation, Antenna Radiation, Antenna-to-Antenna Coupling, Radiation Pattern					
16. SECURITY CLASSIFICATION OF:			17. LIMITATION OF ABSTRACT	18. NUMBER OF PAGES	19a. NAME OF RESPONSIBLE PERSON David Jenn
a. REPORT	b. ABSTRACT	c. THIS PAGE			
Unclassified	Unclassified	Unclassified	UU	223	

Standard Form 298 (Rev. 8-98)
Prescribed by ANSI Std. Z39.18

THIS PAGE INTENTIONALLY LEFT BLANK

Acknowledgments

I would like to thank **Defence Science Technology Organization** for providing me with the opportunity to undertake the 12 months **Defence Science Fellowship** at the **Naval Postgraduate School** under the **Engineer and Scientist Exchange Program ESEP**.

I would also like to thank **Professor Dave Jenn** for his interest, support, advice and willingness to host me at the **Naval Postgraduate School** in the **Electrical and Computer Engineering Department** for my 12months **Defence Science Fellowship**.

THIS PAGE INTENTIONALLY LEFT BLANK

ABSTRACT

This report provides an electromagnetic characterization analysis in order to ascertain if integrated masts are an effective ship radiofrequency electromagnetic interference mitigation strategy. Free space and fitted antenna radiation patterns, and fitted relative near field power flux densities of a linear array transmitting antenna, and the mutual antenna-to-antenna coupling between a linear array transmit and receive antennas, both fitted on the same mast structure, was determined. Overall, the mast structure can reduce the mutual antenna-to-antenna coupling (up to ~ 20 dB) and can affect the fitted antenna radiation pattern. There is both significantly high (i.e., up to 0 dB) and low (~ -30 dB) fitted relative near field power flux density within the vicinity of the transmitting antenna and regions around the mast structure. All this depends on the location and position of the transmit antenna relative to the mast structure, and the location of the receiver antenna relative to the transmit antenna. Both desensitization and third order sub-harmonic distortions non-linear effects on the receiver antenna system were also assessed due to the fitted relative near field power densities. Depending on the specifications of the receiver system, desensitization (or gain compression) was found to be significant, whereas, third order sub-harmonic distortion was not.

THIS PAGE INTENTIONALLY LEFT BLANK

TABLE OF CONTENTS

1.	INTRODUCTION.....	1
2.	INTEGRATED MASTS.....	5
2.1	MAST STRUCTURE	5
2.2	ANTENNA.....	9
2.2.1	Planar Arrays	10
2.2.2	Conformal Antenna (or Array)	10
2.3	INTEGRATED MASTS AND PHASED ARRAY ANTENNAS	11
2.3.1	Rectangle Panel Faceted Mast Structures and Planar Array Antennas	11
2.3.2	Conformal Mast Structures and Conformal Array Antennas	13
3.	THEORY, MODELS, ASSUMPTIONS, AND METHODOLOGY	15
3.1	ANTENNA THEORY	15
3.1.1	Microstrip Antennas.....	15
3.1.2	Circular Patch Microstrip Antenna.....	16
3.1.2.1	<i>Radiation Pattern</i>	16
3.1.2.2	<i>Directivity</i>	20
3.1.3	Linear Array Antenna.....	21
3.1.3.1	<i>Radiation Pattern</i>	21
3.1.3.2	<i>Directivity</i>	22
3.1.4	Power Flux Density	22
3.1.5	Near Field Regions of an Antenna.....	23
3.1.6	Free Space Average Near Field Power Density.....	24
3.1.7	Mutual Antenna-to-Antenna Coupling.....	26
3.1.7.1	<i>Friis Transmission Equation</i>	26
3.1.7.2	<i>Scattering Matrix and Reciprocity Theorem</i>	28
3.2	RADIO FREQUENCY RECEIVER SYSTEMS	31
2.1	Non-Linear Effects on RF Receiver Systems.....	33
3.2.1.1	<i>Sub-harmonic Distortion</i>	34
3.2.1.2	<i>Desensitization (or Gain Compression)</i>	35
3.3	MODELS AND ASSUMPTIONS.....	36
3.3.1	Linear Polarized Circular Patch Microstrip Antenna	36
3.3.2	Linear Polarized Circular Patch Microstrip 4x1 Linear Array Antenna.....	39
3.3.3	Near Field Power Flux Density	42
3.3.4	Mutual Antenna-to-Antenna Coupling.....	42
3.3.5	Mast Structure	43
3.4	SOFTWARE TOOLS.....	45
3.4.1	Computation Electromagnetic Software Tools	45
3.4.1.1	<i>FEKO - Full Wave Solver – Frequency Domain</i>	45
3.4.1.2	<i>Microwave Studio - Full Wave Solver – Time Domain</i>	45
3.4.1.3	<i>Savant - Asymptotic (High Frequency) Solver</i>	46
3.4.2	Radio Frequency Circuit Performance – ADS Systems.....	48

	3.4.2.1 Radio Frequency (RF) Systems Budget Analysis Component Models.....	49
	3.4.3 Mast Structure	52
	3.3.3.1 Rhinoceros v4.....	52
3.5	ERRORS AND CONSTRAINTS	52
	3.5.1 Limitations of Computation Electromagnetics (CEM) Software tools	52
	3.5.2 Numerical Errors	53
	3.5.2.1 Finite Discretization.....	53
	3.5.2.2 Round-off errors	56
	3.5.3 Model Errors	56
	3.5.3.1 Free space (without mast structure).....	56
	3.5.3.2 Fitted (with mast structure)	57
	3.5.4 Combined Estimated Errors.....	58
4	RESULTS AND DISCUSSION	59
4.1	CIRCULAR PATCH MICROSTRIP ANTENNA	59
	4.1.1 Radiation Pattern.....	59
	4.1.2 Directivity	61
4.2	LINEAR ARRAY ANTENNA.....	62
	4.2.1 Radiation Pattern.....	62
	4.2.1.1 Free space and Fitted Radiation Pattern in elevation θ , cut at azimuth= 0° - Antenna Fitted Front Panel of Mast structure.....	62
	4.2.1.2 Free space and Fitted Radiation Pattern in azimuth ϕ , cut at elevation $\theta=90^\circ$ - Antenna Fitted Front Panel of Mast structure.....	66
	4.2.1.3 Free space and Fitted Radiation Pattern in elevation θ , cut at azimuth $\phi=0$ degrees-Antenna fitted Side-Panel of Mast Structure	69
	4.2.1.4 Free space and Fitted Radiation Pattern in azimuth ϕ , cut at elevation $\theta=90$ degrees - Antenna fitted Side Panel of Mast Structure	72
	4.2.2 Linear Array Antenna Beamwidths.....	75
	4.2.3 Linear Array Antenna Directivity.....	76
	4.2.4 Near Field Power Density.....	78
	4.2.4.1 Free Space Near Field Power Density	78
	4.2.4.2 Fitted Near Field Power Flux Density - Antenna fitted Front Panel of Mast Structure.....	79
	4.2.3.3 Fitted Near Field Power Flux Density - Antenna fitted Side panel of Mast Structure	97
4.3	MUTUAL ANTENNA-TO-ANTENNA COUPLING	106
	4.3.1 Antenna 2 located Above Antenna 1	106
	4.3.1.1. Free space (Without Mast Structure)	106
	4.3.1.1 Fitted (With Mast Structure)	112
	4.3.2 Antenna 2 located on Side Panel.....	117
	4.3.2.1 Free space (Without mast structure).....	117

4.3.2.1	<i>Fitted (With Mast Structure)</i>	122
4.4	DIFFERENT ANTENNA MOUNTING OPTIONS	126
4.4.1	Antenna Radiation Pattern	127
4.4.2	Fitted Near Field Power Flux Density in Vicinity of Antenna and Around Mast Structure	131
4.4.2.1	<i>Antenna Fully Integrated (Flush Mounted) – Option A</i>	132
4.4.2.2	<i>Integrated Antenna Partially boxed- front ends – Option B</i>	136
4.4.2.3	<i>Integrated Antenna partially boxed –side ends – Option C</i>	140
4.4.2.4	<i>Integrated Antenna – Fully boxed – Option D</i>	144
4.5	NON-LINEAR EFFECTS OF A RF RECEIVER SYSTEM	151
4.5.1	Receiver System	151
4.6.3	Receiver Desensitization (or Gain Compression)	154
4.6.2	Sub-Harmonic Distortion	162
5	CONCLUSIONS AND FUTURE WORK	165
APPENDIX A	167
A.1	FREE SPACE 4X1 LINEAR ARRAY RADIATION PATTERN AND BEAMWIDTHS	167
A.2	FREE SPACE AVERAGE NEAR FIELD POWER DENSITY CALCULATIONS FIGURES	175
A.3	ESTIMATED VERTICAL HEIGHT AS AFUNCTION OF AZIMUTH ANGLE WITH DIFFERENT RADIUS OF A CIRCLE	179
A.4	FITTED RELATIVE NEAR FIELD POWER FLUX DENSITY IN REGION 2 AT RADIAL DISTANCE $R \approx 0.75M$ FOR DIFFERENT ANTENNA MOUNTING OPTIONS	180
A.5	MUTUAL ANTENNA-TO-ANTENNA COUPLING	183
A.5.1	Mutual antenna-to-antenna coupling S–parameters notation in computational electromagnetic software	183
A.5.2	Antenna locations in Savant for Mutual antenna-to-antenna coupling	184
A.5.3	Analytical and Savant simulated Mutual antenna-to-antenna coupling	185
A.6	NON-LINEAR EFFECTS OF A RF RECEIVER SYSTEM	187
6.	BIBLIOGRAPHY	191
INITIAL DISTRIBUTION LIST	195

LIST OF FIGURES

Figure 1. Thales I-MAST integrated mast with sensor systems accommodated on and within the mast structure. Image from [3] shown for illustrative purposes.	6
Figure 2. Schematic diagram of the Advanced Enclosed Mast/Sensor system (AEM/S) for the US LPD-17 amphibious platform [11]. The image shown is only for illustrative purposes.	7
Figure 3. Integrated mast structure for the US LPD-17 amphibious land platform. Image extracted from [12]. The image shown is only for illustrative purposes.	7
Figure 4. Integrated mast and some systems on the US DDG1000 Zumwalt class destroyer platform. Integrated mast structure highlighted by red circles in image. Image extracted from [13]. The image is shown here only for illustrative purposes. ...	8
Figure 5. Swedish Corvette platform, (a) Platform highlighting the conical shape mast structure (depicted by the red circle) and (b) Platform schematics highlighting onboard systems. Images extracted from [14]. The images are shown here only for illustrative purposes.....	9
Figure 6. A 4x4 planar array antenna. Image extracted from [15]. The image shown is only for illustrative purposes.	10
Figure 7. An example of a conformal antenna (or array). Image extracted from [16]. The image shown is only for illustrative purposes.....	10
Figure 8. An example of a conformal array radar antenna. Image extracted from [17]. The image shown is only for illustrative purposes.....	11
Figure 9. A few examples, not meant to be an exhaustive list, of different masts structures which are basically made of either square, rectangular or both shaped panels fitted for planar array type antennas. Image (a) extracted from [3], Image (b) extracted from [20] and image (c) extracted from [21]. Image (d) is the APAR (active phased array) multi-function radar, planar array as shown on ship mast on the German Saschen class platforms. Image extracted from [22], and (e) is an image of the IM-400 integrated mast, which will accommodate all major radars, sensors and antennas of a naval vessel for the Holland class Ocean Patrol Vessel (OPV) for the Royal Netherlands Navy. Image extracted from [23]. All images shown are only for illustrative purposes.	12
Figure 10. A few examples of conformal arrays. (a) Conformal array on sonar seekers. Image from [26], and (b) Image of the EL/M-2075 Phalcon solid-state L-band conformal mounted array radar system on an aircraft. Image extracted from [27]. The images shown are for illustrative purposes.	14
Figure 11. Different types of microstrip antenna, (From <i>Left to Right</i>) Travelling wave (TW), microstrip slot and patch. TW microstrip images from [28], microstrip slot images from [29] and microstrip patch images from [28].	15
Figure 12. Schematic diagram of a typical circular patch microstrip antenna. Here a denotes the radius of the circular patch, ϵ_r denotes the relative permittivity of the dielectric substrate, h denotes the thickness of the substrate, ρ denotes the position of the antenna feed port and ϕ denotes the angular direction.	16

Figure 13. Cylindrical cavity bounded at the top and bottom by electric walls and on its sides by a magnetic wall, then the fields within the dielectric region of the microstrip corresponds to a TM_{mn}	17
Figure 14. Schematic of a linear array highlighting antenna element separation, d_x and array length L	21
Figure 15. Schematic of calculating the average near field power density of a collinear array antenna. Image here interpolated from Faraone <i>et al.</i> 2000 [35].....	24
Figure 16. Near field correction factor $(CF)_E$ as a function of distance normalized to 1.5λ for a full-wave dipole in free space. Image extracted from [36].	26
Figure 17. Schematic diagram to illustrate Friis transmission equation.....	27
Figure 18. Schematic of a typical Electronic Support Measure (ESM) system. Image extracted from [41]. Highlighted by the red square are the components associated with, including the radio frequency (RF) receiver subsystem, of an ESM System. The image is shown here only for illustrative purposes.	31
Figure 19 Schematic diagrams of typical RF receiver systems. (a) RF receiver system without automatic gain control (AGC) loop. Image extracted from [42]. Figure 19 (b) RF receiver system schematic with AGC feedback loop. Image extracted from [43] and [42], with some slight modifications. Here IF amplifier denotes intermediate frequency amplifier. All images shown are only for illustrative purposes.	32
Figure 20. Typical linear and nonlinear component transfer functions. Images extracted from [44] are for illustrative purposes.	33
Figure 21. Schematic diagrams of linear, polarized, circular patch, microstrip element antenna. Figures 21 (a) 3D schematic of element antenna, (b) Plan view of circular patch antenna highlighting circular patch diameter, D and location of antenna feed offset from center of circular patch, S_F and (c) Perspective view of element antenna highlighting substrate height h , substrate permittivity ϵ_r , feed diameter ($2F_R$, where F_R denotes the feed radius) and feed offset S_F	37
Figure 22. 3D Schematic of linear, polarized, circular patch, microstrip antenna model used in the CEM software tools (FEKO and MWS). Green denotes the substrate material and orange denotes perfect electric conductor circular patch.	38
Figure 23. 3D schematic of 4x1 linear polarized circular patch microstrip linear array antenna. The separation d_x between each of the antenna elements is $\lambda_o/2$ m, and the length $L (=Nd_x$, where N denotes the number of elements) of the linear array is $2\lambda_o$ m. Linear array antenna elements are numbered (from L to R) as 4, 2, 1, 3. Here z -axis, is assumed, to be pointing out of the page.....	39
Figure 24. 4x1 linear array antenna and radiation pattern (frequency $f=2.96\text{GHz}$) in Savant using current sources. Red dipole depicts the perfect electrical conductor antenna element and the pair of green dipoles depicts the infinite substrate and infinite ground plane.	41
Figure 25. 1x1 single element antenna and radiation pattern (frequency $f=2.96\text{GHz}$) in Savant using current sources. Red dipole depicts the perfect electrical conductor antenna element and the pair of green dipoles depicts the infinite substrate and infinite ground plane.	41

Figure 26. 3D perspective view of the generic octagon shape, rectangle panel faceted mast structure.....	43
Figure 27. Schematic diagram, including dimensions of the generic octagon shaped rectangle panel faceted mast structure.....	44
Figure 28 Two-port, two-pin component schematic with signal wave directions. Image extracted from ADS Systems' RF system Budget Analysis [52]. a_1 denotes the signal wave into port 1, b_1 denotes the wave out of port 1, a_2 denotes the signal wave into port 2 and b_2 denotes the signal wave out of port 2.	49
Figure 29. Numerical error as a function of number of nodes per wavelength for finite discretization based numerical techniques. Graph extracted from [48].....	53
Figure 30. Reflection coefficient, S_{11} as a function of frequency (in GHz) for the antenna model using MWS.	57
Figure 31. E_θ (or E plane) field as a function of elevation θ at azimuth $\varphi=0^\circ$ mode $n=1$ for linear polarized circular patch microstrip antenna.....	59
Figure 32 E_φ (or H plane) field as a function of elevation θ , cut at azimuth $\varphi=90^\circ$, mode $n=1$ for linear polarized circular patch microstrip antenna.	60
Figure 33. Normalized free space and fitted radiation pattern as a function elevation θ , cut at azimuth $\varphi=0^\circ$ for 4x1 linear array antenna with uniform illumination, for an antenna scan angle $\theta=0^\circ$. Fitted antenna radiation pattern assumed antenna was located at a vertical height $h \sim 0.740\text{m}$ from the base of the mast structure, front panel, and positioned at different distances from the mast structure's front panel (i.e., 0.113m and $\lambda/4\text{m}$)	63
Figure 34 Normalized free space and fitted far field radiation pattern for linear polarized 4x1 circular patch linear array antenna as a function of elevation θ , cut at azimuth $\varphi=0^\circ$, with uniform illumination for different 4x1 linear array antenna electronic scan angles, (a) $\theta \sim 5^\circ$, (b) $\theta \sim 11^\circ$ and (c) $\theta \sim 18^\circ$ degrees. For the fitted antenna radiation pattern the antenna was assumed to be located at a vertical height $h \sim 0.740\text{m}$ from the base of the mast structure, and positioned at different distances from the mast structure's front panel (i.e., 0.113m and $\lambda/4\text{m}$)	65
Figure 35. Normalized free space and fitted far field radiation pattern for 4x1 linear array antenna as a function of azimuth φ , cut at elevation $\theta=90^\circ$, for different 4x1 linear array antenna scan angles. (a) scan angle $\theta=0^\circ$, (b) scan angle $\theta \sim 5^\circ$, (c) scan angle $\theta \sim 11^\circ$ and (d) scan angle $\theta \sim 18^\circ$. For the fitted radiation pattern the 4x1 linear array antenna is located at a vertical height $h \sim 0.740\text{m}$ from the base of the mast structure and positioned at different distances from the mast structure's front panel (i.e., 0.113m and $\lambda/4\text{m}$).....	68
Figure 36. Normalized free space and fitted antenna radiation pattern for linear polarized 4x1 circular patch linear array as a function of elevation θ , cut at azimuth $\varphi=0^\circ$ for different antenna scan angles θ , (a) $\theta=0^\circ$, (b) $\theta \sim 5^\circ$, (c) $\theta \sim 11^\circ$ and (d) $\theta \sim 18^\circ$. For the fitted antenna radiation pattern the antenna is located at a vertical height $h \sim 0.782\text{m}$ from the base of the mast structure sidepanel and positioned at different distances (i.e., 0.113m or $\lambda/4\text{m}$) from the surface of the mast structure's sidepanel.....	71

Figure 37. Normalized free space and fitted antenna radiation pattern for 4x1 linear array as a function of azimuth φ , cut at elevation $\theta=90^\circ$, for different 4x1 linear array antenna scan angles. (a) $\theta=0^\circ$, (b) $\theta\sim 5^\circ$, (c) $\theta\sim 11^\circ$ and (d) $\theta\sim 18^\circ$. For the fitted antenna radiation pattern the antenna was located at a vertical height $h\sim 0.782\text{m}$ from the base of the mast structure sidepanel and positioned at different distances (i.e., 0.113m and $\lambda/4\text{m}$) from the mast structure's sidepanel.	74
Figure 38. Near field regions calculated for different locations around the mast structure and in the vicinity of the 4x1 linear array antenna in FEKO. Linear array antenna located at a vertical height $h\sim 0.740\text{m}$ from base of mast structure and positioned at different distances, i.e., 0.113m and $\lambda/4\text{m}$, from mast structure front panel.	80
Figure 39. Schematic illustrating the transmit antenna scan angles orientations. The transmit antenna scan angles $\theta=0^\circ$, $\theta\sim 5^\circ$, $\theta\sim 11^\circ$ and $\theta\sim 18^\circ$ were measured from the z-axis, which here is assumed to be directed out of page, antenna scan angle $\theta=0^\circ$ is along antenna bore sight (i.e., along the z-axis).	81
Figure 40 Fitted relative near field power flux density (dB) in region 1 at different antenna-to-mast separation (from <i>L</i> to <i>R</i>) $\lambda/4\text{m}$ and 0.113m and different antenna scan angles (from <i>Top to Bottom</i>) $\theta=0^\circ$, $\theta\sim 5^\circ$, $\theta\sim 11^\circ$ and $\theta\sim 18^\circ$. All results from FEKO simulation.	84
Figure 41 Fitted relative near field power flux density (dB) in region 1 at antenna-to-mast separation $\sim \lambda/4\text{m}$ and different antenna scan angles (<i>L</i> to <i>R</i>) $\theta=0^\circ$ and $\theta\sim 11^\circ$. Near field distribution simulation results from Savant.	85
Figure 42. Fitted relative near field power flux density (dB) in region 2 at different antenna to mast separation (from <i>L</i> to <i>R</i>) $\lambda/4\text{m}$ and 0.113m and different antenna scan angles (from <i>Top to Bottom</i>) $\theta=0^\circ$, $\theta\sim 5^\circ$, $\theta\sim 11^\circ$ and $\theta\sim 18^\circ$	88
Figure 43. Fitted relative near field power flux density (dB) in right hand sector of region 2 for an antenna-to-mast separation $\sim \lambda/4\text{m}$ for different antenna scan angles, (<i>L</i> to <i>R</i>) $\theta=0^\circ$ and $\theta\sim 11^\circ$. The near field distribution was simulated using Savant.	90
Figure 44. Comparison of fitted relative near field power flux density as a function azimuth φ , cut at elevation $\theta=90^\circ$ at a radial distance $R=0.75\text{m}$, from center of the 4x1 linear array antenna, for different antenna-to-mast separation (i.e., $\lambda/4\text{m}$ and 0.113m) and different antenna scan angles θ (From <i>Top to Bottom</i>) $\theta=0^\circ$, $\theta\sim 5^\circ$, $\theta\sim 11^\circ$, and $\theta\sim 18^\circ$. Here the transmit antenna is located at a vertical height $h\sim 0.74\text{m}$ from the base of the mast structure frontpanel.	92
Figure 45. Fitted relative near field power flux density (dB) in a cross sectional area of region 3, in particular radial ρ , $0.35\text{ m} \leq \rho \leq 0.55\text{ m}$ as a function of angle φ , $180^\circ \leq \varphi \leq 300^\circ$, cut at height $y\sim 0.8\text{m}$, at different antenna-to-mast separation (<i>L</i> to <i>R</i>) $\lambda/4\text{m}$ and 0.113m and different antenna scan angles (from <i>top to bottom</i>) $\theta=0^\circ$, $\sim 5^\circ$, $\sim 11^\circ$ and $\sim 18^\circ$. All near field computed using FEKO.	95
Figure 46. Schematic of the near field regions nearby the transmitting antenna when antenna mounted side panel at different separation distances from mast structure for FEKO simulations. Here only near fields were calculated for regions A (i.e.,	

	above antenna) and B (i.e., around antenna). Near field regions were calculated in FEKO.	97
Figure 47.	Fitted relative near field power flux density in region A, i.e., above transmit antenna. Here it is assumed different distances from the mast structure sidepanel (<i>From L to R</i>) $\lambda/4$ m and 0.113m, and different antenna scan angles (<i>From Top to Bottom</i>) $\theta=0^\circ, \theta\sim 5^\circ, \theta\sim 11^\circ$ and $\theta\sim 18^\circ$. All near fields calculated using FEKO.	99
Figure 48.	Relative fitted near field power flux density in region B i.e., around antenna and mast structure side panel. Here it is assumed different antenna distances from mast structure side panel (<i>From L to R</i>) $\lambda/4$ m and 0.113m, for different antenna scan transmit antenna angles (<i>From Top to Bottom</i>) $\theta=0^\circ, \theta\sim 5^\circ, \theta\sim 11^\circ$, and $\theta\sim 18^\circ$. All near fields computed using FEKO.....	102
Figure 49.	Fitted relative near field power flux density (dB) as a function of azimuth ϕ , cut at elevation $\theta=90^\circ$ at a radial distance $R\sim 0.75$ m, for 4x1 linear array antenna located at different distances (i.e., $\lambda/4$ m and 0.113m) from the mast structure side panel for different antenna scan angles (<i>From Top to bottom</i>) $\theta=0^\circ, \theta\sim 5^\circ, \theta\sim 11^\circ$, and $\theta\sim 18^\circ$	105
Figure 50.	Schematic of the locations of antenna 1 and antenna 2. Here the z -axis, or boresight of antenna 1 is directed out of page, and the angle of orientation Φ of antenna 2 is measured relative from the boresight of antenna 1. Therefore, the antenna 2 angle of orientation curve is highlighted here as a dotted line to indicate that the direction is going from out of page into the page.	107
Figure 51.	Free space mutual antenna-to-antenna coupling between a 4x1 linear array transmitter and a 1x1 linear array receiver, for transmit antenna scan angle $\theta=0^\circ$. Receiver antenna is located at a distance $d=0.9039$ m and orientated at an angle $\Phi=92.2^\circ$, relative from the center of the 4x1 linear array transmitter antenna to feed port of receive antenna. Antenna aperture efficiency η for both transmitter and receiver antenna in the Friis transmission calculation is assumed to be unity (i.e., 100% efficiency). * Friis transmission with mismatch polarization and free space path losses * Friis transmission with free space path loss without mismatch polarization loss, □ Scattering Matrix & Reciprocity Theorem (Roubine and Bolomey (1987) [39], ◇ S_{12} parameter –Savant (SBR) Tx and Rx current sources, ◇ S_{12} parameter–Savant (SBR) Tx current source and Rx radiation pattern, ○ S_{15} parameter–FEKO (MoM), ○ S_{14} parameter – FEKO (MoM), ○ S_{13} parameter–FEKO (MoM), ○ S_{12} parameter –FEKO (MoM), and ○ S parameters average–FEKO.....	108
Figure 52.	Freespace mutual antenna-to-antenna coupling between a 4x1 linear array transmitter and a 1x1 linear array receiver, for different transmitter antenna scan angles (<i>from Top to Bottom</i>) $\theta\sim 5^\circ, \theta\sim 11^\circ$ and $\theta\sim 18^\circ$. Receiver is assumed to be at an angle $\Phi=92.2^\circ$ and distance $d=0.9039$ m relative from the center of the 4x1 linear array transmitter antenna to feed port of receive antenna. ◇ S_{12} parameter –Savant (SBR) Tx and Rx current sources, ◇ S_{12} parameter–Savant (SBR) Tx current source and Rx radiation pattern, ○ S_{15} parameter–FEKO (MoM), ○ S_{14} parameter–FEKO (MoM), ○ S_{13} parameter–	

FEKO (MoM), \circ S_{12} parameter –FEKO (MoM), and \circ S parameters average–FEKO.111

Figure 53. Schematic of the locations of antenna 1 and antenna 2 for the fitted mutual antenna-to-antenna coupling FEKO simulations. Antenna 1, not shown here, is located at distance $\sim\lambda/4$ m away from the mast structure, front panel. Antenna 2 is located at a vertical height $h_2 \approx 1.643$ m from the base of the mast structure, and slightly displaced from the top edge of the mast structure, front panel by a distance $d' \approx 0.03$ m. Relative to antenna 1, antenna 2 is orientated at an angle $\Phi \approx 92.2^\circ$, from the boresight of antenna 1, and a distance $d=0.9039$ m away from the center of antenna 1 to the feedport of antenna 2. Similar, antenna locations and positions were used for the Savant simulations.113

Figure 54. Fitted mutual antenna-to-antenna coupling between a 4x1 linear array transmitter and a 1x1 linear array receiver, for different transmitter antenna scan angles (from *Top to Bottom*) $\theta=0^\circ$, $\sim 5^\circ$, $\sim 11^\circ$ and $\sim 18^\circ$. Receiver is assumed to be at an angle $\Phi=92.2395^\circ$ and distance $d=0.9039$ m relative from the center of the 4x1 linear array transmitter antenna to feed port of the receive antenna. \diamond S_{12} parameter–Savant (SBR) Tx and Rx current sources, \diamond S_{12} parameter–Savant (SBR) Tx current source and Rx radiation pattern, \circ S_{15} parameter–FEKO (MLFMM), \circ S_{14} parameter–FEKO (MLFMM), \circ S_{13} parameter–FEKO (MLFMM), \circ S_{12} parameter –FEKO (MLFMM), and \circ S parameters average–FEKO. Savant results included internally defined diffraction model.115

Figure 55. Schematic of the locations of antenna 1 and antenna 2 for the mutual antenna-to-antenna coupling, where antenna 2 is orientated at an angle $\Phi \approx 89.5^\circ$ and at a distance $d=0.9101$ m, relative from the center of antenna 1 to the feed port of antenna 2. The angle of orientation Φ for antenna 2 is depicted as a dashed curve to represent that the angle is measured relative from the boresight (i.e., z-axis) of antenna 1, which is directed out of page here.117

Figure 56. Free space mutual antenna-to-antenna coupling between a 4x1 linear array transmitter and a 1x1 linear array receiver for transmit antenna scan angle $\theta=0^\circ$. Receiver is assumed to be at an angle $\Phi \approx 89.5^\circ$ and distance $d=0.9101$ m relative from the center of the 4x1 linear array transmitter antenna to the receiver antenna port. Antenna aperture efficiency η for transmit and receive antennas in Friis equation is assumed to be unity (i.e., 100% efficiency). *Friis transmission with mismatch polarization and free space path losses * Friis transmission without mismatch polarization loss with free space path loss, \square Scattering Matrix & Reciprocity Theorem (Roubine and Bolomey 1987) [(39)], \diamond S_{12} parameter –Savant (SBR) Tx and Rx current sources w/o line of sight (LOS), \diamond S_{12} parameter–Savant (SBR) Tx and Rx current sources with LOS, \diamond S_{12} parameter –Savant (SBR) Tx current sources and Rx radiation pattern w/o LOS, \diamond S_{12} parameter –Savant (SBR) Tx current sources and Rx radiation pattern with LOS, \circ S_{15} parameter–FEKO (MoM), \circ S_{14} parameter –FEKO (MoM), \circ S_{13} parameter–FEKO (MoM), \circ S_{12} parameter –FEKO (MoM), and \circ S parameters average–FEKO.118

Figure 57. Free space mutual antenna-to-antenna coupling between a 4x1 linear array transmitter and a 1x1 linear array receiver antenna, for difference scan angles

(from *Top to Bottom*) $\theta \sim 5^\circ$, $\theta \sim 11^\circ$ and $\theta \sim 18^\circ$. Receiver is assumed to be located at an angle $\Phi \approx 89.5^\circ$ and distance $d=0.9101\text{m}$ relative from the center of the 4×1 linear array transmitter antenna to the receiver antenna feed port. \diamond S_{12} parameter –Savant (SBR) Tx and Rx current sources w/o line of sight (LOS), \diamond S_{12} parameter–Savant (SBR) Tx and Rx current sources with LOS, \diamond S_{12} parameter –Savant (SBR) Tx current sources and Rx radiation pattern w/o LOS, \diamond S_{12} parameter –Savant (SBR) Tx current sources and Rx radiation pattern with LOS, \circ S_{15} parameter–FEKO (MoM), \circ S_{14} parameter –FEKO (MoM), \circ S_{13} parameter–FEKO (MoM), \circ S_{12} parameter –FEKO (MoM), and \circ S parameters average–FEKO.121

Figure 58. Schematic of locations of antenna 1 and antenna 2 for fitted mutual antenna-to-antenna coupling simulations in FEKO. Antenna 1 is located at a vertical height $h_1 \approx 0.740\text{m}$ along the mast structure front panel, and positioned at a distance $\sim \lambda/4\text{m}$ away from the mast structure front panel surface. Antenna 2 is also positioned at a distance $\sim \lambda/4\text{m}$ away from the mast structure side panel surface, however, located at a vertical height $h_2 \approx 0.840\text{m}$ from the base of the mast structure. Similar locations for antenna 1 and antenna 2 were used also for the mutual antenna-to-antenna coupling simulations in Savant.123

Figure 59. Fitted mutual antenna-to-antenna coupling between a 4×1 linear array transmitter antenna and a 1×1 linear array receiver, for different transmit antenna scan angles (from *Top to Bottom*) $\theta=0^\circ$, $\theta \sim 5^\circ$, $\theta \sim 11^\circ$ and $\theta \sim 18^\circ$. Receiver antenna is assumed to be located at an angle $\Phi \approx 89.5^\circ$ and distance $d=0.9101\text{m}$ relative from the center of the 4×1 linear array transmitter antenna to the receiver antenna feed port. \diamond S_{12} parameter –Savant (SBR) Tx and Rx current sources w/o line of sight (LOS), \diamond S_{12} parameter–Savant (SBR) Tx and Rx current sources with LOS, \diamond S_{12} parameter –Savant (SBR) Tx current sources and Rx radiation pattern w/o LOS, \diamond S_{12} parameter –Savant (SBR) Tx current sources and Rx radiation pattern with LOS, \circ S_{15} parameter–FEKO (MoM), \circ S_{14} parameter –FEKO (MoM), \circ S_{13} parameter–FEKO (MoM), \circ S_{12} parameter –FEKO (MoM), and \circ S parameters average–FEKO. Savant results included internally defined diffraction model.....125

Figure 60. Free space and fitted radiation patterns as a function elevation θ , cut at $\varphi=0^\circ$, for different antenna mounting options of the 4×1 linear array antenna on mast structure front panel. All results from FEKO simulations. — 4×1 linear array antenna free space, — 4×1 linear array antenna separated 0.113m from complete mast structure, — 4×1 linear array antenna separated $\lambda/4\text{m}$ from complete mast structure, — 4×1 linear array antenna fully integrated with mast (mounting option A), — 4×1 linear array antenna partial boxed-front ends (mounting option B), — 4×1 linear array antenna partial boxed-side ends (mounting option C) and — 4×1 linear array antenna fully boxed (mounting option D).128

Figure 61. Free space and fitted antenna radiation patterns as a function of azimuth φ , cut at elevation $\theta \approx 90^\circ$, for each of the different mounting options of the 4×1 linear array antenna on mast structure front panel, at an antenna scan angle $\theta = 0^\circ$. All results from FEKO simulations. — 4×1 linear array antenna free space, —

4x1 linear array antenna separated 0.113m from complete mast structure, —
 4x1 linear array antenna separated $\lambda/4$ m from complete mast structure, --- 4x1
 linear array antenna fully integrated with mast structure (mounting option A),
 --- 4x1 linear array antenna partial boxed-front ends (mounting option B), ---
 4x1 linear array antenna partial boxed-side ends (mounting option C) and ---
 4x1 linear array antenna fully boxed (mounting option D).130

Figure 62. Near field regions in the vicinity of the integrated 4x1 linear array antenna and around mast structure.132

Figure 63. Fitted relative near field power flux density (dB) at different regions around the antenna and mast structure for a 4x1 linear array antenna fully integrated (or flush mounted) with mast structure, i.e., antenna mounting option A for different antenna scan angles. (a) Fitted relative near field power flux density in region 1 for each antenna scan angle (*L to R*) $\theta=0^\circ, \sim 5^\circ, \sim 11^\circ$ and $\sim 18^\circ$, (b) Fitted relative near field power flux density in region 2 for each antenna scan angle (*L to R*) $\theta=0^\circ, \theta \sim 5^\circ, \theta \sim 11^\circ$ and $\theta \sim 18^\circ$, and (c) Fitted relative near field power flux density in region 3, at radii $0.35 \text{ m} \leq \rho \leq 0.55 \text{ m}$ as a function of angle $180^\circ \leq \phi \leq 300^\circ$, cut at height $y \sim 0.8\text{m}$, for each antenna scan angle (*L to R*) $\theta=0^\circ, \theta \sim 5^\circ, \theta \sim 11^\circ$ and $\theta \sim 18^\circ$135

Figure 64. Fitted relative near field power flux density (dB) at different locations around antenna and mast structure for a 4x1 linear array antenna partially boxed-front ends, i.e., mounting option B at different antenna scan angles. (a) Fitted relative near field power flux density in region 1, for different antenna scan angles (*L to R*) $\theta=0^\circ, \theta \sim 5^\circ, \theta \sim 11^\circ$ and $\theta \sim 18^\circ$, (b) Fitted relative near field power flux density in region 2, for different antenna scan angles (*L to R*) $\theta=0^\circ, \theta \sim 5^\circ, \theta \sim 11^\circ$ and $\theta \sim 18^\circ$, and (c) Fitted relative near field power flux density in region 3, at radii $0.35 \text{ m} \leq \rho \leq 0.55 \text{ m}$ as a function of angle $180^\circ \leq \phi \leq 300^\circ$, cut at a height $y \sim 0.8\text{m}$ for different antenna scan angles (*L to R*) $\theta=0^\circ, \theta \sim 5^\circ, \theta \sim 11^\circ$ and $\theta \sim 18^\circ$139

Figure 65. Fitted relative near field power flux density (dB) at different locations around the antenna and mast structure for a 4x1 linear array antenna mounted partially boxed-side ends on mast structure, i.e., mounting option C for different antenna scan angles, $\theta=0^\circ, \theta \sim 5^\circ, \theta \sim 11^\circ$ and $\theta \sim 18^\circ$. Figure 65 (a) Fitted relative near field power flux density in region 1 at each antenna scan angle, Figure 65 (b) Fitted relative near field power flux density (dB) in region 2 at each antenna scan angle, and Figure 65 (c) Fitted relative near field power flux density (dB) in region 3, for radii $0.35 \text{ m} \leq \rho \leq 0.55 \text{ m}$ as a function of angles $180^\circ \leq \phi \leq 300^\circ$, cut at a height $y \sim 0.8\text{m}$ at each antenna scan angle. .143

Figure 66. Fitted relative near field power flux density (dB) at different locations on around antenna and mast structure for a 4x1 linear array antenna mounted fully boxed on mast structure, i.e., mounting option D, for different antenna scan angles (a) Fitted relative near field power flux density in region 1 for each antenna scan angle (*L to R*) $\theta=0^\circ, \theta \sim 5^\circ, \theta \sim 11^\circ$ and $\theta \sim 18^\circ$, (b) Fitted relative near field power flux density in region 2 for each antenna scan angle (*L to R*) $\theta=0^\circ, \theta \sim 5^\circ, \theta \sim 11^\circ$ and $\theta \sim 18^\circ$, and (c) Fitted relative near field power flux density in

region 3, for radii $0.35 \text{ m} \leq \rho \leq 0.55 \text{ m}$ as a function of angle $180^\circ \leq \phi \leq 300^\circ$, cut at height $y \sim 0.8 \text{ m}$ for each antenna scan angle (*L to R*) $\theta=0^\circ$, $\theta \sim 5^\circ$, $\theta \sim 11^\circ$ and $\theta \sim 18^\circ$147

- Figure 67. Schematic of RF receiver system with an AGC loop. RF system circuit template extracted from ADS Systems *Budget Analysis_AGC* examples [54], with several modifications in the electronic component parameters.152
- Figure 68. Noise figure/factor for each component in RF system depicted in RF system depicted in Figure 67. Here, *Cmp_index*=0 denotes bandpass filter (BPF2), *Cmp_index*=1 denotes the automatic control gain amplifier (AGC_Amp), *Cmp_index*=2 denotes the RF amplifier (AMP2), and *Cmp_index*=3 denotes the automatic gain control power control (AGC_Pwr_control).153
- Figure 69 Power delivered into system at component output (left image, (a)) and signal-to-noise (S/N) for power delivered into system load at component output (right image, (b)) for each component of RF system depicted in Figure 67. Here $- P_{in} = -104 \text{ dBm}$, $- P_{in} = -92 \text{ dBm}$, $- P_{in} = -80 \text{ dBm}$, $- P_{in} = -68 \text{ dBm}$, $- P_{in} = -56 \text{ dBm}$, and $- P_{in} = -54 \text{ dBm}$. Here *Cmp_Index*=0 refers to the electronic component denoted as *BPF_Butterworth*, *Cmp_Index*=1 refers the electronic component denoted as *AGC_Amp*, *Cmp_Index*=2 refers to electronic component denoted as *Amplifier2* and *Cmp_Index*=3 refers to the electronic component denoted as *AGC_PwrControl*, as depicted in the RF receiver system in Figure 67.154
- Figure 70. Minimum signal to noise ratio $(S/N)_{min}$ as a function of input signal power level P_{in} for a RF receiver system with a noise factor $NF=3 \text{ dB}$, operating temperature $T=290 \text{ K}$ and $BW=1.25 \text{ kHz}$, and a minimum signal level threshold $\sim -65 \text{ dBm}$. Here — Theory, and — Budget analysis simulation (i.e., from above figure, Figure 69 (b)) with a least square fit curve denoted by red line.156
- Figure 71. Schematic of RF system to evaluate gain compression of a non-linear component due to large input signal power levels. Schematic template adopted from ADS Systems examples [54].157
- Figure 72. Simulated output signal power level P_{out} as a function of input signal power level P_{in}157
- Figure 73. Simulated gain compression of the nonlinear component (i.e., amplifier) as a function of input signal, power level. In this simulation an interpolation was used to give better resolution.158
- Figure 74. RF receiver system schematic with mixer and local oscillator. RF system circuit template adopted from ADS Systems' Budget Analysis Examples [54].159
- Figure 75. RF system parameters for RF receiver system depicted in Figure 74. Here nonlinear effects are not enabled in the simulation. For graphs *OutSNR_Total_dB* vs. *Cmp_Index* and *OutPwr_dBm* vs. *Cmp_Index* $- P_{in} = -104 \text{ dBm}$, $- P_{in} = -93.2 \text{ dBm}$, $- P_{in} = -82 \text{ dBm}$, $- P_{in} = -71.6 \text{ dBm}$, $- P_{in} = -60.8 \text{ dBm}$, and $- P_{in} = -50 \text{ dBm}$160
- Figure 76. RF system parameters for RF receiver system depicted in Figure 74. Here nonlinear analysis (3rd order) is enabled. For graphs *OutSNR_Total_dB* vs. *Cmp_Index*, *OutPwr_dBm* vs. *Cmp_Index*, and *OutPGain_dB* vs. *Cmp_Index*

$P_{in} = -104\text{dBm}$, $P_{in} = -93.2\text{dBm}$, $P_{in} = -82\text{dBm}$, $P_{in} = -71.6\text{dBm}$,
 $P_{in} = -60.8\text{dBm}$, and $P_{in} = -50\text{dBm}$161

Figure 77. 3-D radiation pattern along boresight for the 4x1 linear array antenna in the computation electromagnetic software tools (From *top to bottom*) FEKO (MoM), Microwave Studio (or CST) (FDTD) and Savant (SBR–current source, 2x models).....168

Figure 78. Normalized free space radiation pattern $f(\theta)$ as a function of $u (= \sin(\theta) \cos(\phi=0))$, (Mailloux 2005 [32]) along boresight for a 4x1 linear array antenna with uniform illumination. Beamwidth (=3dB from maximum or FWHM) $\approx 36.87^\circ (=0.644 \text{ radians})$171

Figure 79. Normalized free space radiation pattern as a function of elevation (along boresight for a 4x1 linear array antenna using current sources in Savant. Beamwidth (= -3dB (or 0.5) from maximum or FWHM) $\approx 32^\circ$. — 4x1 linear array antenna current source model, assuming 4x electric dipoles to replicate each of the PEC single element antenna and 42x electric & magnetic dipole pairs to replicate an infinite substrate and ground plane, and \circ 4x1 linear array antenna current source model assuming 4x electric and magnetic dipole pairs replicating each PEC single element antenna, as depicted below in.....172

Figure 80. Image of antenna current source model in Savant assuming 4x electric and magnetic dipole pairs to replicate the PEC single element antenna.172

Figure 81. Free space radiation pattern as a function of elevation θ , cut at azimuth $\phi=0^\circ$ for 4x1 linear array antenna model in FEKO. Beamwidth (=3dB (or 0.5) from maximum or FWHM) $\approx 35^\circ (=2x \approx 17.5^\circ)$173

Figure 82. Free space radiation pattern as a function of elevation θ , cut at azimuth $\phi=0^\circ$ for 4x1 linear array antenna model in Microwave Studio (or CST). Beamwidth (= -3dB (or 0.5) from maximum or FWHM) $\approx 34^\circ (=2x \approx 17^\circ)$174

Figure 83. Calculated extrapolated normalized correction factor and normalized correction factor electric field from the APD_Program [36] distance all normalized to 1.5λ . Extrapolated curve fit function is $y = -4.728x^{0.259} + 5.902$, using MATLAB curve fitting tools.175

Figure 84. Relative near field power density (dB) along the linear array (assumed along x -axis), excluding sidelobes, at a distance $R= 0.75\text{m}$ away from and in front of antenna. (a) FEKO results; and (b) Savant Results, $-4x$ electric and magnetic dipole pair linear array antenna model; and $*$ 4x electric dipole and 46x electric and magnetic dipole pair linear array antenna model.176

Figure 85. 3D schematic in FEKO of locations where near field power density was calculated at different locations in the vicinity of the 4x1 linear array antenna.177

Figure 86. Estimated vertical height (in m) as a function of angle ($^\circ$) for different radial distances r (i.e., $r=0.2\text{m}$, 0.5m and 0.7m) from center of the transmit antenna.179

Figure 87. Fitted relative near field power flux density (dB) in region 2 at a radial distance $R \approx 0.75\text{m}$ from the center of the array antenna for different mounting positions and different antenna scan angles (from *Top to Bottom*) $\theta=0^\circ$, $\sim 5^\circ$, $\sim 11^\circ$, and $\sim 18^\circ$. \bullet Numerical-FEKO 4x1 linear array antenna separated $\lambda/4\text{m}$ from

complete mast structure, xNumerical-Microwave Studio (or CST) 4x1 linear array antenna separated 0.113m from complete mast structure, ●Numerical-FEKO 4x1 linear array antenna separated 0.113m from complete mast structure, +Numerical-FEKO 4x1 linear array antenna fully integrated with mast structure (mounting option A), +Numerical-FEKO 4x1 linear array antenna partial boxed-front ends (mounting option B) , +Numerical-FEKO 4x1 linear array antenna partial boxed-side ends (mounting option C), and +Numerical-FEKO 4x1 linear array antenna fully boxed (mounting option D).

.....	182
Figure 88. The antenna-to-antenna mutual coupling S-parameter notation for the 4x1 linear array antenna in FEKO.	183
Figure 89. Typical Savant free space mutual antenna-to-antenna coupling as a function of frequency f	185
Figure 90. Typical Friis transmission equation mutual antenna-to-antenna coupling as a function of frequency f	186
Figure 91. Budget Analysis RF circuit performance parameters as a function of component index for RF receiver system depicted in Figure 67. Here 3 rd order nonlinearities included in analysis. Similar results are obtained when nonlinearities are not considered in simulation. For completion NF (NF_RefIn_dB) and output power (OutPwr_dBm), and S/N (OutSNR_Total_dB) figures, as depicted in Figure 68 and Figure 69, respectively, have been included here. Here $P_{in} = -104\text{dBm}$, $P_{in} = -92\text{dBm}$, $P_{in} = -80\text{dBm}$, $P_{in} = -68\text{dBm}$, $P_{in} = -56\text{dBm}$, and $P_{in} = -54\text{dBm}$	188

LIST OF TABLES

Table 1 Bessel function roots of $J'(ka)=0$. Table extracted from [31].	19
Table 2 Linear polarized circular patch microstrip antenna dimensions.	38
Table 3 Phase shift ($^{\circ}$) for each 4x1 linear array antenna element to obtain different linear array antenna scan angles.	40
Table 4 A summary of the computational electromagnetic softwares (i.e., FEKO, Microwave Studio and Savant) that were used for the present study. E in the column titled “Version” denotes Educational (or University) version. The educational /University versions for FEKO and Microwave Studio had limited computer memory (\sim 2GByte), which restricted the size of the models that could be used for simulation.	48
Table 5 Summary of the models, numerical methods and mesh sizes (where applicable) used for each CEM software tool in the present study. Here FEM=Finite Element Method, MoM=Method of Moments, FDTD=Finite Difference Time Domain, MLFMM=MultiLevel Fast Method of Moments and SBR=Shooting and Bouncing Rays method.	55
Table 6 Directivity D for a linear polarized circular patch microstrip antenna	61
Table 7 Beamwidth of the 4x1 linear array antenna using different techniques for the freespace antenna radiation pattern. Free space antenna radiation patterns used to determine the beamwidths are provided in Appendix A, Section A.1.75	75
Table 8 Directivity for a 4x1 Linear array assuming omnidirectional elements at array scan angle from endfire, $\theta=0$.	76
Table 9 Averaged free space near field power density simulated and analytical for 4x1 linear array antenna at distance from antenna $R=0.75$ m in free space at antenna along boresight. Here antenna wavelength $\lambda =0.10135$ m and antenna Gain (G) \sim 14.45.	78
Table 10 Summary of Different antenna Mounting Options and description	127
Table 11 Calculated average near field power density in locations in the vicinity of the 4x1 linear array in free space. For completeness previously calculated boresight average near field power density has been included.	177
Table 12 Co-ordinates for transmitter and receiver antenna for mutual antenna-antenna coupling simulations in Savant. Antenna scan angles were done mechanically.	184
Table 13 Electronic component parameters and specifications for RF receiver system, as depicted in Figure 67.	187
Table 14 Electronic component parameters and specifications for RF receiver system depicted in Figure 74 .	189
Table 15 Description each output parameter defined in ADS Systems’ Budget Analysis. Each description provided here was taken directly from ADS Systems RF System Budget Analysis documentation [52].	190

THIS PAGE INTENTIONALLY LEFT BLANK

GLOSSARY OF TERMS

APD	Antenna Power Density
AEM/S	Advanced Enclosed Mast/Sensor System
AGC	Automatic Gain Control
CEM	Computational Electromagnetic
C4ISREW	Command, Control, Communication, Computing, Intelligence, Surveillance Reconnaissance & Electronic Warfare
CF	Correction Factors
ESM	Electronic Support Measure
EMC	Electromagnetic Compatibility
EMI	Electromagnetic Interference
EW	Electronic Warfare
FDTD	Finite Difference Time Domain
FEM	Finite Element Method
GTD	Geometrical Theory of Diffraction
HF	High Frequency
IF	Intermediate Frequency
I	Integral
MLFMM	Multiple Level Fast Multipole Method
MS	Microstrip Slot
MWS	Microwave Studio
NF	Noise Figure/Factor
PO	Physical Optics
RAM	Radar Absorbing Material
RF	Radio Frequency
SBR	Shooting and Bouncing Rays
TOI	Third Order Intercept
TW	Traveling Wave
PTD	Physical Theory of Diffraction
REW&C	Radar, Electronic Warfare and Communication
S/N	Signal-to-Noise Ratio
UTD	Uniform Theory of Diffraction

THIS PAGE INTENTIONALLY LEFT BLANK

1. INTRODUCTION

Command, Control, Communication, Computing, Intelligence, Surveillance Reconnaissance and Electronic Warfare (C4ISREW) systems have to meet their operational capability in a maritime environment. However, with the increasing number of C4ISREW systems, in particular **Radar, Electronic Warfare and Communication (REW&C)** systems, being fitted onboard maritime platforms there has been a concomitant increase in unacceptable design compromises. In particular, systems which intentionally radiate energy, viz. **Radar, Electronic Warfare and Communication (EWR&C)** systems create major design challenges including: [1] managing radar cross section; antenna placement; weight, space and moment issues, maintenance and repair costs; and electromagnetic interference.

Electromagnetic interference and electromagnetic compatibility (EMI/EMC) is a major issue affecting the capability of EWR&C systems, since mutual interference can adversely affect operational performance. Traditionally, blanking and filtering techniques have been used to achieve **Electromagnetic compatibility (EMC)** between **radio frequency (RF)** systems (e.g. with REW&C systems). However, such interference mitigation solutions are becoming inefficient and ineffective in dealing with the increasing number of REW&C systems and thus the increasing complexity of EMI problems.

In addition, there are also EMI issues for REW&C systems created by the ship structure causing blockages to the antenna, leading to elevated antenna radiation, pattern sidelobes and reduced main beam gain. This, in turn will affect the overall performance of the sensor system. Whilst there are mitigation strategies for such interference, such as re-shaping the ship structure to minimize blockages and/or having artificially cylindrical hard (e.g. longitudinally corrugated) surfaces mounted in front of an antenna [2]. These mitigation strategies can be expensive when taking into consideration: **a)** The cost in modifying a ship structure; **b)** the maintenance cost of replacing surfaces on the ship due to wearing and damage; and **c)** the long service life of the ship, typically 30 years for most military ships.

Therefore it is has become essential to find more cost effective and efficient alternative solutions in order to mitigate EMI, without impacting on the overall performance of the radio frequency systems. Some alternative solutions include integrated masts [3]; integrated, multifunction, and multi-beam topside (InTop) aperture ([4] and [5]), and low power distributed networked antennas ([6] and [7]).

Integrated masts are essentially a central mast structure where transmitter and receiver systems are accommodated in, and mounted on. Integrated masts, that currently exist, are prominent on modern military ships and it is claimed that they “...*eliminate*...”electromagnetic interference [3].

Integrated, multifunction, multi-beam topside aperture (InTop) is essentially where transmitter and receiver systems share the same antenna aperture, rather than having numerous and different antennas for transmitters and receivers on a ship. InTop is in its experimental and research phase, and typically has a phased array radar antenna aperture, which acts as both a transmitter and receiver system antenna for e.g. radar, and also a receiver antenna system, for e.g. electronic support system ([4] and [5]).

Low power distributed antennas is essentially a concept where low-power distributed and networked antennas are distributed around a ship [6]. By networking the distributed antennas, the radiation pattern of the antenna can be created in the direction required for system operation and at the same time creating a null in the direction of the RF system where adverse EMI may occur [7].

Each of the above suggested, alternative solutions, are either currently being considered or researched to determine their feasibility as EMI mitigation strategies. However, what they do establish is that a more effective and efficient way is needed of addressing EMI, without impacting the overall performance and capability of the RF system.

For the present report an investigation in the use of integrated masts as an EMI mitigation strategy will be given.

There are many issues to consider regarding integrated masts, some include:

- i) Interference between antennas and the mast structure,
- ii) Mast structure shape, height, weight and material,
- iii) Mast structure radar cross section,
- iv) Stability of ship, with a large central structure with sensor systems mounted,
- v) Mutual antenna-to-antenna coupling between the antennas fitted and in close proximity to each other on a central structure, and
- vi) The high intensity near fields due to transmitting antennas on other antennas in close proximity. Such near fields can be high enough to impact the performance of the other antenna systems.

There is a dearth of information, at least in the open literature, on the electromagnetic assessment of integrated masts on ships, despite there been numerous papers published in the open literature on integrated masts (e.g. [3] and [8]), where they claim that integrated masts eliminate ship radiofrequency electromagnetic interference.

However, Burkholder *et al.* 2006 [8] provided a hybrid framework to electromagnetically assess (e.g. mutual antenna coupling) antenna/platform interference for maritime platforms. In particular their electromagnetic assessment was done using asymptotic numerical techniques, which enabled all of the ship structure to be simulated, including an integrated mast type structure.

Asymptotic (or high frequency) techniques in general provide quicker simulation times and use less computer memory, but in general provide less accurate results compared to full wave numerical techniques, for example, Finite Element Method, Method of Moments or Finite Difference Time Domain.

For the present report not all of the issues regarding integrated masts stated above (i.e. i - vi) will be covered, mainly due to time constraints. However, what will be considered in this report is an electromagnetic characterization of antennas mounted on a central mast structure. The electromagnetic characterization will include antenna radiation patterns (free and fitted), near field power flux density and mutual antenna-to-antenna coupling (free space and fitted). In addition, it will also include some assessment of the non-linear effects to receiver systems, which are in close vicinity of transmitter power signal levels.

For the present analysis the transmitting antenna was a 4x1 linear array, the receive antenna was a 1x1 linear array and the mast structure was a generic octagon faceted structure, with inclined rectangle panels made from perfect electrical conducting material. The mast structure dimensions ($\sim 10\lambda$ m) relative to the linear array antenna dimensions ($\leq 2\lambda$ m) was large enough that it could be considered as a large electrical structure. The transmitter antenna operating frequency was 2.96GHz.

The electromagnetic characterization for the present analysis was done using commercial-off-the-shelf **computational electromagnetic (CEM)** software tools. The CEM software tools used for this study included FEKO, **Microwave Studio (or CST)** and Savant. FEKO is principally a full wave solver in the frequency domain, which includes **Method of Moments (MoM)** and **Finite Element Method (FEM)** numerical techniques. It does also offer asymptotic (or high frequency) techniques (e.g. UTD, GO and PO). Microwave Studio (or CST) is a full wave solver, principally in the time domain, which includes **Finite Difference Time Domain (FDTD)** numerical technique. Microwave Studio also has available frequency domain solvers (MoM) and asymptotic techniques. Savant is an asymptotic (or high frequency) solver, based on Shooting and Bouncing Rays techniques. Throughout this study, comparisons in simulated results were made, where possible, using both full wave and asymptotic numerical techniques. In addition, simulated numerical results, obtained from the CEM software tools, were also verified, where possible, with analytical results.

This report is structured in the following way:

Chapter 2 provides an overview of integrated masts and antennas that are typically associated with integrated masts. The present discussion will be limited to phased array antennas on mast structures. However, this is not to neglect the fact other type of radar systems, such as parabolic scanning radar systems, dipole, and satellite communications systems may also be accommodated on a central mast structure. **Chapter 3** provides theory, assumptions, models and methodology of the antenna and mast structure that was considered for the present analysis. **Chapter 4** provides the results and discussion, and **Chapter 5** provides some conclusions and future work.

THIS PAGE INTENTIONALLY LEFT BLANK

2. INTEGRATED MASTS

2.1 MAST STRUCTURE

It is becoming more prevalent in modern ship designs to have a central mast structure integrated with most, if not all, ship sensor systems (both active and passive). The concept of integrated masts on modern ships, at least from the perspective where a central mast structure is fitted with an array antenna, has, in some instances, transpired not as a means to mitigate ship electromagnetic interference, but rather as a requirement to accommodate new radar systems, as part of a ship's life upgrade programs.

There have recently been numerous published papers in the open literature on integrated masts for ships, which highlight their advantages and how they can mitigate ship radio frequency electromagnetic interference (EMI). However, from these published papers there is a dearth of information providing any evidence to support certain claims, e.g. "...integrated masts eliminate EMI..." ([3] and [9]) made in such papers.

As previously highlighted in Chapter 1, Introduction, there are many issues that need to be considered, regarding the concept of integrated masts, which can include;

- There is no clear definition of what defines an integrated mast. From the different integrated masts that are evident in the open literature it would give the impression that an integrated mast can be characterized definitely as a central large structure where the ship sensor systems are either:
 - i) Accommodated (or mounted) both on and within the mast structure,
 - ii) Embedded (or flush mounted) where the antenna (most cases a phased array antenna) is integrated into the mast structure, i.e., the mast structure becomes a part of the antenna, or
 - iii) A combination of both i) and ii) from above.
- Mutual coupling between antennas. The mutual coupling between antennas in close proximity to each other on a mast structure may be significant due to the large near fields, which can in turn impact the performance of the sensor systems.
- Mutual coupling, between antenna and mast structure, and mast structure blockages. The mutual interference between an antenna and mast structure can affect the antenna's radiation pattern by increasing its sidelobes and reducing its mainbeam thus affecting the performance of the sensor. A mast structure could also cause structural blockages impacting a sensor system from operating effectively. Conversely, structural blockages could be advantageous, as the mast structure may prevent transmitted electromagnetic energy from one antenna reaching another collocated antenna. Therefore, in turn reducing the amount of power reaching and entering the collocated sensor, and reducing the mutual coupling between both antennas, and Ship radar cross-section. Having a large central mast structure on a ship, such as an integrated mast (or deckhouse) can impact a ship's overall radar cross-section. Therefore, the shape and material type of the mast structure is important. Ship hulls and masts were typically made of

steel and in order to mitigate many EMI interferences associated with the ship structure **Radar Absorbing Material (RAM)** was used. However, now it is becoming more common for ships and even possibly mast structures (or deckhouses) to be made of lightweight type material, such as carbon fiber or composite carbon fiber material [10]. It is interesting to note, that with the cases of accommodated or flush-mounted antenna arrays on ship mast structures, there would need to be some consideration regarding the type of material used for the mast structure in order to electromagnetically screen sensor systems from the mast structure. The analysis of different shapes and material type for mast structure is out of the scope of this report, mainly due to time constraints. However, it would be of interest to consider different mast structural shapes and materials in any future work. For the present analysis the mast structure material was assumed to be a perfect electrical conductor, to replicate a worst case scenario.

Figure 1 to Figure 5 illustrates some of the currently available integrated masts, which are not meant to be an exhaustive list. As illustrated by **Figure 1 to Figure 5**, the integrated masts are of different shapes, ranging from rectangle faceted to conformal faceted structures. It would appear that each mast structure has a number of different types of sensor systems (e.g. phased array radar, parabolic radar and communication type systems) accommodated on and within the mast structure.

Figure 1 illustrates the Thales *I-MAST* mast structure and shows how sensor systems are accommodated on and within the mast structure.

As illustrated in Figure 1 the integrated mast structure appears to be constructed of sloped rectangle faceted panels built into a rectangular shape frame and appears to have sensor systems accommodated on and within the mast structure.



Figure 1. Thales I-MAST integrated mast with sensor systems accommodated on and within the mast structure. Image from [3] shown for illustrative purposes.

Figure 2 illustrates a schematic diagram of the **Advanced Enclosed Mast/Sensor system (AEM/S)** for the US LPD-17 amphibious platform integrated mast structure.

Highlighted in **Figure 2** are the mast dimensions, and some of the systems accommodated on and within the mast structure.

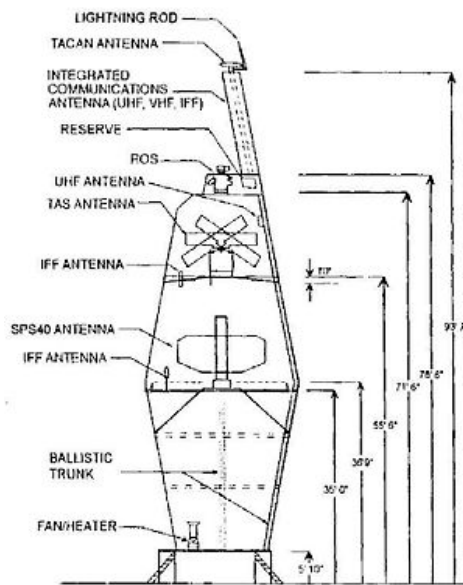


Figure 2. Schematic diagram of the Advanced Enclosed Mast/Sensor system (AEM/S) for the US LPD-17 amphibious platform [11]. The image shown is only for illustrative purposes.

Figure 3 illustrates the integrated mast structure for the US LPD-17 amphibious land platform.



Figure 3. Integrated mast structure for the US LPD-17 amphibious land platform. Image extracted from [12]. The image shown is only for illustrative purposes.

As illustrated by **Figure 3** the mast structure is made up of slanted rectangle faceted panels.

Figure 4 illustrates the integrated mast and some of the systems on the US DDG1000 Zumwalt class destroyer platform. As illustrated in **Figure 4**, the mast (highlighted by the red circles in **Figure 4**) structure is made up of slanted rectangle faceted panels joined to form a conformal type shape mast structure.

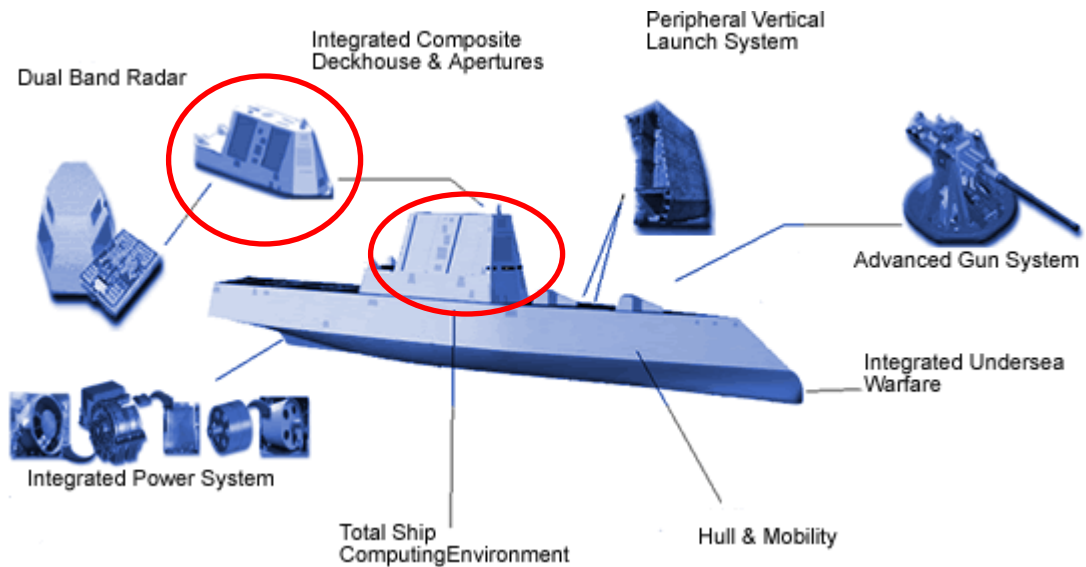
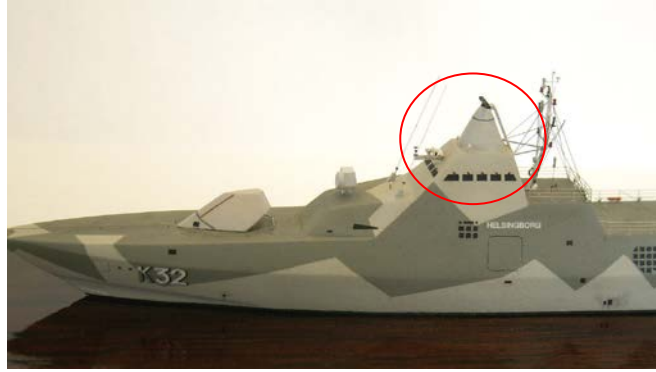


Figure 4. Integrated mast and some systems on the US DDG1000 Zumwalt class destroyer platform. Integrated mast structure highlighted by red circles in image. Image extracted from [13]. The image is shown here only for illustrative purposes.

Figure 5 (a) illustrates the Swedish corvette platform, highlighting (denoted by red circle) its integrated mast, which appears to be a conical shape structure. **Figure 5 (b)** illustrates the Swedish corvette platform schematics highlighting onboard systems.



(a)



(b)

Figure 5. Swedish Corvette platform, (a) Platform highlighting the conical shape mast structure (depicted by the red circle) and (b) Platform schematics highlighting onboard systems. Images extracted from [14]. The images are shown here only for illustrative purposes.

2.2 ANTENNA

Phased arrays are emerging as the standard type of antenna for electronic warfare, radar and communications systems fitted on modern ships. Conventional antennas, e.g. parabolic and rotational scanned antenna, for sensor systems will still exist on modern ships, as they are required for certain sensor systems, but the number of them on future modern ships will be very minimal. Therefore, the ensuing discussion will focus mainly on phased array antennas. A phased array antenna, in general, is an array of antennas both active and passive, with varying antenna element phases, electronically steer EM energy in different directions, simultaneously.

2.2.1 Planar Arrays

Figure 6 illustrates an example of a 4x4 planar array antenna. A planar phased array antenna, in general, is an array of antennas, both active and passive, that lies in a plane. Planar arrays are, in general, the most common type of phased array antennas fitted on modern ships. The linear array is the fundamental building block for planar phased array antennas.

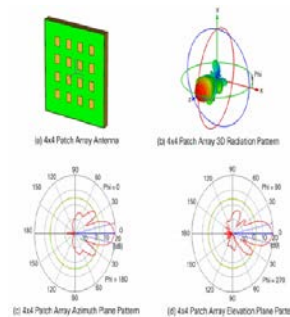


Figure 6. A 4x4 planar array antenna. Image extracted from [15]. The image shown is only for illustrative purposes.

2.2.2 Conformal Antenna (or Array)

Figure 7 and **Figure 8** illustrate another type of phased array antenna, namely conformal array antennas.

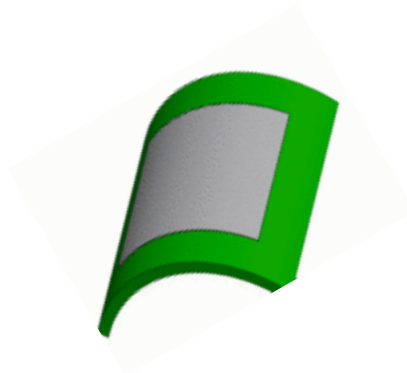


Figure 7. An example of a conformal antenna (or array). Image extracted from [16]. The image shown is only for illustrative purposes.

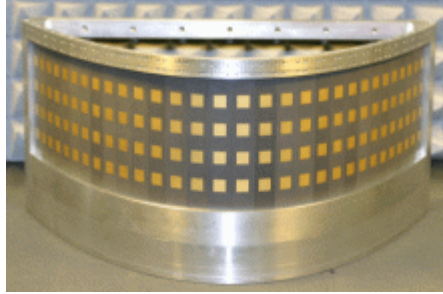


Figure 8. An example of a conformal array radar antenna. Image extracted from [17]. The image shown is only for illustrative purposes.

As illustrated by **Figure 7** and **Figure 8**, and defined by [18] a conformal array antenna “...is a cylindrical, spherical, or some other shape, with the radiating elements mounted on or integrated into the smoothly curved surface...”.

Circular arrays (i.e., antenna elements placed in a circular formation), which can also be considered a conformal antennas, as stated by [19] are “...able to scan a beam azimuthally through 360 degrees with little change in either the beamwidth or the sidelobe level...”, and “...steer over 360 degrees with different types of antenna main beams, e.g., an omnidirectional, multiple or a narrow beam...”. In addition, circular arrays can be designed in different ways to achieve the 360 degree coverage, which can include “...three separate antennas, each covering a 120° sector or in as one cylindrical array, resulting in a much more compact installation and less cost...”.

2.3 INTEGRATED MASTS AND PHASED ARRAY ANTENNAS

2.3.1 Rectangle Panel Faceted Mast Structures and Planar Array Antennas

For different faceted, mast structures there will most likely be appropriately shaped antennas fitted on or within the mast structure. For example, planar array antennas would most likely be fitted with rectangle faceted mast structures, whereas for conformal array antennas would most likely be fitted on curved faceted mast structure.

Figure 9 illustrates a few examples of planar arrays antennas integrated with rectangle/square faceted mast structures. A planar array antenna will be described here as an antenna which has its elements all lying on a plane and either fitted on or embedded (or flush mounted) in a mast structure. For the case of a linear /planar array, given the flat plane geometry and shape of the antenna, it is reasonable to assert that the integrated mast (or deckhouse) would typically have to be of a shape basically made up of flat rectangle or square faceted surfaces. It needs to be noted that structures created with rectangular or square faceted surfaces can create right angles in the structure which can cause large reflections and thus large radar signatures. Therefore, it would be imperative for rectangular faceted mast structure that the edges do not form any right angle.



(a)



(b)



(c)



(d)



(e)

Figure 9. A few examples, not meant to be an exhaustive list, of different masts structures which are basically made of either square, rectangular or both shaped panels fitted for planar array type antennas. Image (a) extracted from [3], Image (b)

extracted from [20] and image (c) extracted from [21]. Image (d) is the APAR (active phased array) multi-function radar, planar array as shown on ship mast on the German Saschen class platforms. Image extracted from [22], and (e) is an image of the IM-400 integrated mast, which will accommodate all major radars, sensors and antennas of a naval vessel for the Holland class Ocean Patrol Vessel (OPV) for the Royal Netherlands Navy. Image extracted from [23]. All images shown are only for illustrative purposes.

2.3.2 Conformal Mast Structures and Conformal Array Antennas

A brief discussion, for completeness, will be provided here on conformal masts and conformal arrays, although conformal integrated masts and conformal arrays were not considered in this study. However, should be in any future work.

The concept of conformal arrays in integrated masts is not a new. Bird *et al* 1995 [24] performed some analysis assessing the use of conformal arrays embedded in deckhouse/mast structures. Bird *et al.* 1995 [24] found that such arrays can indeed reduce the antenna interference and reduce radar cross section, depending on the deckhouse/mast structure design.

For the purposes of the present discussion, a conformal array will be defined as a circular shape array either placed on a mast structure or embedded into the mast structure. It is interesting to note, that compared to rectangular or square faceted mast structures primarily used for planar array antennas, a conformal array antenna either on a circular, spherical or cylindrical faceted structure, there would be no issue regarding right angle edges. Therefore, large reflections due to corner reflectors type structure and thus minimal effect on the radar cross section of the mast structure. Furthermore, conformal arrays can be either narrowband or wideband arrays. For the case of wideband conformal array antenna, where it is wideband, phased array where adaptive nulling and beam forming is possible and having 360° azimuth coverage would be useful as a receiver system, such as a microwave electronic support measure system. This concept is not new. Karavassilis *et al.* 1986 [25] proposed an experimental high frequency (HF) circular array with direction finding and null steering capabilities.

There are currently available conformal arrays which are embedded (or flush mounted) in platform structure, e.g. aircrafts, weapons and sonar seekers. Embedded (or flush mounted) conformal arrays are fully integrated with the platform structure, i.e., the antenna and platform structure are a single structure.

Figure 10 illustrates some examples of embedded (or flush mounted) conformal arrays. **Figure 10 (a)** illustrates a conformal array on sonar seekers. **Figure 10 (b)** illustrates the

EL/M-2075 Phalcon solid-state L-band conformally mounted array radar system on an aircraft.

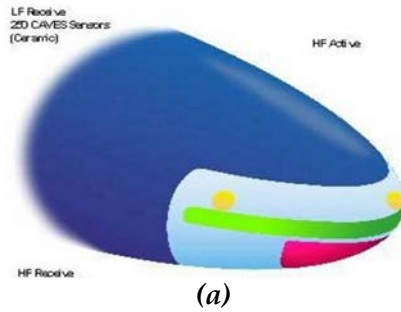


Figure 10. A few examples of conformal arrays. (a) Conformal array on sonar seekers. Image from [26], and (b) Image of the EL/M-2075 Phalcon solid-state L-band conformal mounted array radar system on an aircraft. Image extracted from [27]. The images shown are for illustrative purposes.

3. THEORY, MODELS, ASSUMPTIONS, AND METHODOLOGY

3.1 ANTENNA THEORY

Antennas are basically electrical devices which convert electric currents into radio waves, and vice-a-versa. The antenna is one of the essential components of any radar, EW and communication system. Depending on the function and operating frequency of the system will govern, to a large extent, the type and design of the antenna for that system. There are many different types of antennas; some include, not meant to be an exhaustive list, wire antennas, reflector, travelling wave, aperture, and microstrip.

3.1.1 Microstrip Antennas

Figure 11 illustrates several different types and shapes of microstrip antennas. Some of the different types of microstrip antennas, as illustrated in **Figure 11**, include **Travelling Wave (TW)**, **Microstrip Slot (MS)**, and patch antennas. In general, microstrip antennas are broadband, i.e., $\sim 100\text{MHz}$ to $\sim 50\text{GHz}$, which includes the microwave region. Microstrip antennas, are utilized, extensively in different Electronic Warfare, Radar and Communication sensor systems. For example, satellite communication, Doppler and other radars (e.g. phased array) and remote sensing.

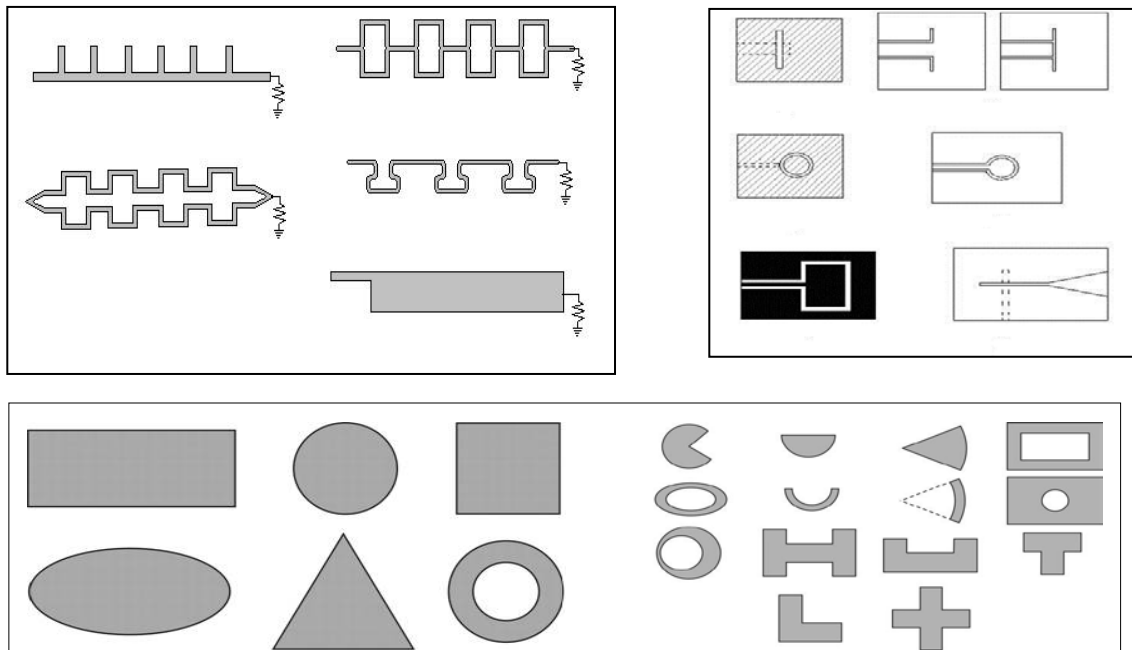


Figure 11. Different types of microstrip antenna, (From Left to Right) Travelling wave (TW), microstrip slot and patch. TW microstrip images from [28], microstrip slot images from [29] and microstrip patch images from [28].

3.1.2 Circular Patch Microstrip Antenna

For the present study a linear polarized circular patch microstrip antenna was chosen. To the author's knowledge, the antenna design and operating frequency $f = 2.96\text{GHz}$ did not replicate any sensor system currently available or in operation. If indeed so, it is only by coincident.

A circular patch microstrip antenna, is basically, a disk antenna comprising of a thin, conducting circular patch on a dielectric substrate backed by a ground plane. **Figure 12** illustrates a schematic diagram of a typical circular patch antenna.

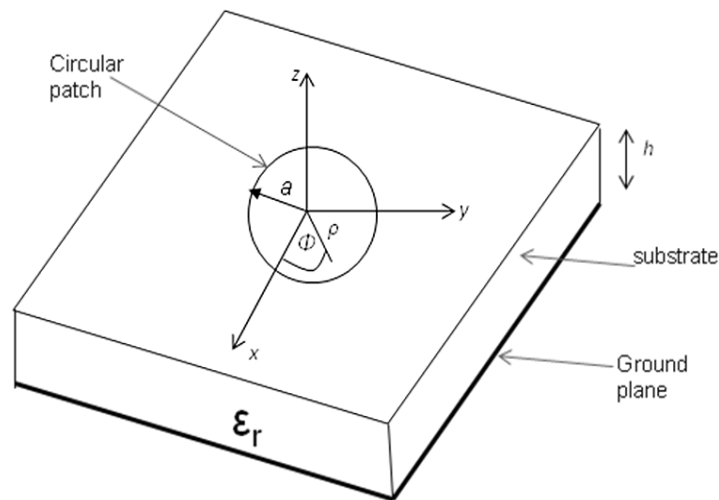


Figure 12. Schematic diagram of a typical circular patch microstrip antenna. Here a denotes the radius of the circular patch, ϵ_r denotes the relative permittivity of the dielectric substrate, h denotes the thickness of the substrate, ρ denotes the position of the antenna feed port and ϕ denotes the angular direction.

3.1.2.1 Radiation Pattern

There are many theoretical models available to determine the radiation pattern of a circular patch microstrip antenna. Some of the theories include (Bahl and Bhartia 1980 [30]):

- The simple cavity model,
- The cavity model with source,
- The modal expansion model,
- The wire grid model, and
- The Green's function method model.

As a first order approximation, the simple cavity model, will be described here. If a circular patch microstrip antenna is assumed to have the same dimensions, as given by

Figure 12, and has its antenna fed by a coaxial waveguide underneath the circular antenna, along the z -axis, and that the substrate thickness h is less than the operating wavelength λ_0 , then following the theory from Garg *et al.* 2001 [31]. The microstrip patch can be modeled as a cylindrical cavity bounded at the top and bottom by electric walls and on its sides by a magnetic wall. **Figure 13** illustrates schematically the microstrip patch modeled as a cylindrical cavity bounded at the top and bottom by electric walls and on its sides by a magnetic wall.

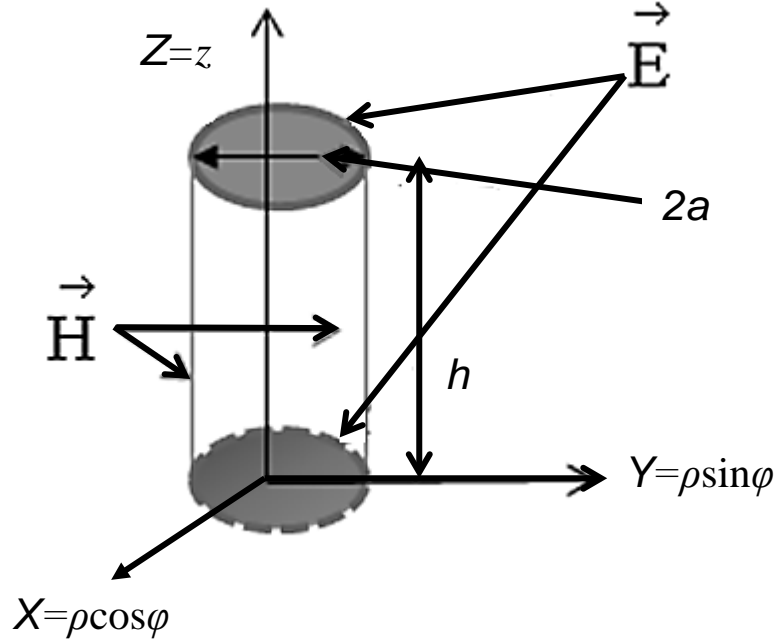


Figure 13. Cylindrical cavity bounded at the top and bottom by electric walls and on its sides by a magnetic wall, then the fields within the dielectric region of the microstrip corresponds to a TM_{mn} .

To calculate the radiation pattern in the electric field E plane and magnetic field H plane, using the simple cavity model for a circular patch microstrip, and following in detail Garg *et al.* 2001 [31], the wave equation is used.

From electromagnetic theory the wave equation, assuming no current, is as follows

$$(\nabla^2 + k^2)\vec{E} = 0 \quad (1)$$

where

$k = \omega\sqrt{\mu\varepsilon}$. Here ω denotes the angular frequency ($=2\pi f$), μ denotes the free space permeability, and ε denotes the free space permittivity.

To ensure that the solution fields satisfy the wave equation, i.e., Equation (1) and the magnetic wall boundary conditions, which are as follows

$$\vec{E} = \hat{z}E_z, \text{ and} \quad (2)$$

$$\left. \frac{\partial \vec{E}}{\partial \rho} \right|_{\rho=a} = 0 \quad (3)$$

The solution to the wave equation, assuming cylindrical co-ordinates, is as follows [31]

$$E_z = E_o J_n(k\rho) \cos n\phi \quad (4)$$

where

$$J_n(k\rho) = \text{Bessel functions of order } n.$$

Since the electric field \vec{E} is in the z-component, the magnetic field components become [31]

$$H_\rho = \frac{j}{\omega\mu\rho} \frac{\partial E_z}{\partial \phi} = \frac{-jnE_o J_n(k\rho) \sin(n\phi)}{\omega\mu\rho} \quad (5)$$

$$H_\phi = \frac{-j}{\omega\mu} \frac{\partial E_z}{\partial \rho} = \frac{-jkE_o J'_n(k\rho) \cos(n\phi)}{\omega\mu} \quad (6)$$

where

J' denotes the first derivative of the Bessel function w.r.t. to the argument.

We note that there are no radial and angular components of the electric field and no z-component of the magnetic field, since $\vec{E}_\rho = \vec{E}_\phi = \vec{H}_z = 0$.

The magnetic field \vec{H} inside the cavity creates an induced electric current, and the surface currents on the circular patch, can be calculated from

$$\vec{K} = \hat{n} \times \vec{H} = \hat{\rho} H_\phi - \hat{\phi} H_\rho \quad (7)$$

where

$\hat{\rho}$ and $\hat{\phi}$ are unit vectors in the radial ρ and angular ϕ directions.

At the edge of the circular patch the components of the surface current $K_\rho(\rho = a) = H_\phi(\rho = a) = 0$. Therefore, $J'_n(ka) = 0$.

This indicates that for each mode of configuration a radius may be found that results in a resonance corresponding to zeros of the derivative of the Bessel functions, J' .

The components of field and surface currents for the modes $m=n=1$ are as follows

$$\vec{E}_z = E_0 J_1(k\rho) \cos \varphi, \quad (8)$$

$$\vec{H}_\rho = -K_\phi = \frac{-jE_0 J_1(k\rho) \sin \varphi}{\omega\mu\rho}, \text{ and} \quad (9)$$

$$\vec{H}_\varphi = -K_g = \frac{-jkE_0 J_1(k\rho) \cos \varphi}{\omega\mu}. \quad (10)$$

Table 1 provides a few root terms of the Bessel function for different modes.

Table 1 Bessel function roots of $J'(ka) = 0$. Table extracted from [31].

Mode (n,m)	Root (ka)
(0,1)	0
(1,1) (fundamental mode)	1.84118
(2,1)	3.05424
(0,2)	3.83171

The far field radiation of a disk antenna can be calculated from either the electric or magnetic vector potential functions. The radiation from the circular patch can be derived either from the electric field in the z -component across the aperture between the disk and the ground plane at $z=0$, using vector electric potential, Or from currents in the circular patch conductor, employing magnetic potentials. The radiation in the upper half space can be derived by image theory, where the ground plane can be replaced by an equivalent magnetic current source, i.e.,

$$\vec{M} = 2\vec{E} \times \hat{n}, \text{ or } \vec{M} = 2E_z \hat{\phi}. \quad (11)$$

Using the equivalent magnetic current source and integrating over the aperture, the vector electric potential, can be calculated. The far field in spherical co-ordinates, can then be derived from this potential, and are as follows

$$E_{\theta} = \frac{j^n V a k_o}{2} \frac{e^{-jk_o r}}{r} \cos n\phi [J_{n+1}(k_o a \sin \theta) - J_{n-1}(k_o a \sin \theta)] \quad (12)$$

$$E_{\phi} = \frac{j^n V a k_o}{2} \frac{e^{-jk_o r}}{r} \cos \theta \sin n\phi [J_{n+1}(k_o a \sin \theta) - J_{n-1}(k_o a \sin \theta)] \quad (13)$$

where

$$V = h E_o J_n(ka), \text{ denotes the edge voltage at } \phi = 0.$$

For the lowest order mode, i.e., n=1 the electric far field components are [31]

$$E_{\theta} = \frac{j V a k_o}{2} \frac{e^{-jk_o r}}{r} \cos \phi [J_2(k_o a \sin \theta) - J_0(k_o a \sin \theta)], \text{ and} \quad (14)$$

$$E_{\phi} = \frac{j V a k_o}{2} \frac{e^{-jk_o r}}{r} \cos \theta \sin \phi [J_2(k_o a \sin \theta) - J_0(k_o a \sin \theta)]. \quad (15)$$

3.1.2.2 Directivity

The Directivity D for a circular disk excited in the dominant mode (n=1), can be described as follows (Bahl and Bhartia 1980 [30])

$$D = \frac{\frac{1}{2} \text{Re}(E_{\theta} H_{\phi}^* - E_{\phi} H_{\theta}^*)|_{\theta=0}}{P_r / 4\pi r^2} \text{ or } \frac{8}{I} \quad (16)$$

where

$$P_r \text{ denotes the total radiated power upper half of the space only} \\ = \frac{1}{4} \left\{ \text{Re} \iint_S (\vec{E} \times \vec{H}) \cdot d\vec{S} \right\}, \text{ here } S \text{ is the total spherical surface area,}$$

$H_\theta = \frac{E_\phi}{\eta_o}$, and $H_\phi = \frac{E_\theta}{\eta_o}$, here η_o denotes free space impedance= $120\pi \Omega$, and

$$I = \int_0^\pi \left[\left\{ J_{n+1}(k_o a \sin \theta) - J_{n-1}(k_o a \sin \theta) \right\}^2 + \cos^2 \theta \left\{ J_{n+1}(k_o a \sin \theta) + J_{n-1}(k_o a \sin \theta) \right\}^2 \right] \sin \theta d\theta.$$

3.1.3 Linear Array Antenna

3.1.3.1 Radiation Pattern

Figure 14 illustrates a schematic of a typical linear array antenna. If it is assumed that the linear array antenna is an N -element linear array antenna, operating with a wavelength λ_o , with antenna element spacing $d_x = \frac{\lambda_o}{2}$ m, and each antenna element having uniform illumination, then the normalized broadside antenna radiation pattern $f(\theta)$ can be approximated, as follows (Mailloux 2005 [32])

$$f(\theta) = \frac{\sin(L\pi u / \lambda_o)}{N \sin(\pi d_x u / \lambda_o)} \quad (17)$$

where

$u = \sin \theta \cos \phi$ (here θ denotes elevation angle and ϕ denotes azimuth angle), and L is the linear array antenna length ($= Nd_x$).

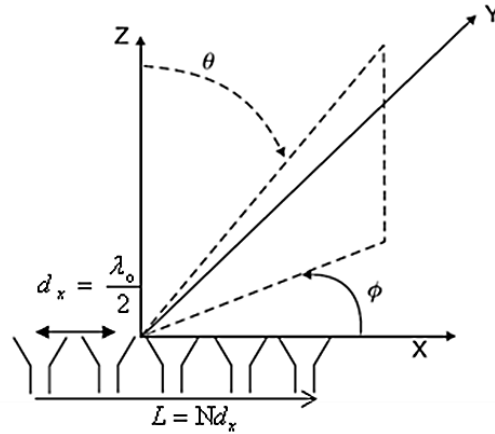


Figure 14. Schematic of a linear array highlighting antenna element separation, d_x and array length L .

3.2.2.2 Directivity

The directivity D of an $N \times M$ array assuming omnidirectional elements, can be approximated, as follows (Mailloux 2005 [32])

$$D = \frac{\left\{ \sum_n |a_n| \right\}^2}{\sum_n \sum_m |a_n| |a_m| \exp[-jkd_x(n-m)\cos\theta_o] \text{sinc}[kd_x(n-m)]} \quad (18)$$

where

a_n denotes the amplitude of linear array elements $n=1 \dots N$,

a_m denotes the amplitude of linear array elements $m=1 \dots M$,

θ_o denotes the array scan angle measured from end fire (when array scan

angle, $(\theta, \phi) = \left(\frac{\pi}{2}, 0\right)$), and

$$\text{sinc}(x) = \frac{\sin x}{x}.$$

3.1.4 Power Flux Density

The direction in which energy travels in an electromagnetic wave can be described by the Poynting Vector \vec{S} [33]

$$\vec{S} = \vec{E} \times \vec{H}. \quad (19)$$

The magnitude of the power flux density S (Wm^{-2}) can be determined as follows [33]

$$S = E_o H_o = \frac{E_o^2}{\eta_o} \quad (20)$$

where

E_o denotes the magnitude of the E-field,

$H_o \left(= \frac{E_o}{\eta_o} \right)$ denotes the magnitude of the H-field, and

η_o denotes the free space impedance ($=120\pi \Omega$).

3.1.5 Near Field Regions of an Antenna

There are three main field regions for the radiation pattern of an antenna. At distances very close to the antenna, the dominant energy is non-radiating, and is called the reactive near field. Farther away, but still near the antenna, is the radiating near field (or Fresnel) region [34]. It is within the Fresnel, or near field region where the energy radiated produces the conventional antenna pattern when viewed from the far field and where the angular field distribution is dependent upon the distance from the antenna. Then further away from the antenna is the Fraunhofer, or far field region, where the energy radiated produces the antenna radiation pattern and where the angular field distribution is essentially independent of the distance from the antenna. The transitions between each of the field regions are not exact and the changes between them are gradual. In the present analysis the near field power (or flux) density calculations will be in the Fresnel region, and in the transition regions between the Fresnel and Fraunhofer field regions.

Kizer 2010 [34] provided an estimation of the near field power for a microwave antenna, in free space, and notes that “...*the near field power density has not been extensively studied...*”. Further to this, it is reasonable to assert that, at least in the open literature, there has not been any extensive studies determining near field power density (or flux density) of antennas, in the vicinity, of large electrical objects. This present study will provide some initial results on assessing near field power density close to large electrical objects.

Free space near field power density analysis has generally been done mainly to assess human exposure and protection to electromagnetic radiation (e.g. Faraone *et al.* 2000 [35] and APD Program [36]) by determining the average near field power density.

3.1.6 Free Space Average Near Field Power Density

Faraone *et al.* 2000 [35] provided an estimation of average near field power density of a collinear array antenna, with length L , assuming the near field is cylindrical, with each collinear array element spacing $d_x \leq \lambda$, with radius ρ , at boresight of the antenna, as depicted schematically in **Figure 15** [35].

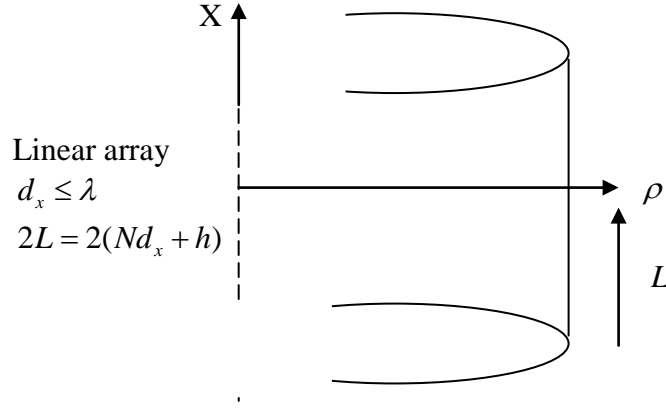


Figure 15. Schematic of calculating the average near field power density of a collinear array antenna. Image here interpolated from Faraone *et al.* 2000 [35].

The average, near field power density \bar{P}_d , at a distance ρ from the collinear array along the linear array length L can be estimated to be as follows [35]

$$\bar{P}_d(\rho, L) = \frac{P_{\text{rad}}}{4L\pi\rho\sqrt{1 + \left(\frac{\rho}{\rho_0}\right)^2}} \quad (21)$$

where

P_{rad} denotes the radiated power from collinear array,

ρ denotes the distance from the collinear array, and

ρ_o denotes the distance when the $P_{\text{cycl}}(\rho, L) \leq P_{\text{sph}}(\rho, L)$ condition is valid, which is when $\rho \leq G_A L$ (here G_A is the collinear array broadside gain), this considerations will occur at a distance $\rho_o = G_A L$.

An alternative theory to estimate average near field power density is the **Antenna Power Density (APD)** program [36]. The APD provides a simplified procedure for estimating the near field power density of a number of common types of antennas and graphically checking the compliance of systems with different emission exposure standards or user defined limits. In the APD program, it is assumed that the near field E_N and far field E_F intensities in Vm^{-1} are related by the following equation [36]

$$E_N = E_F (CF)_E \quad (22)$$

where

$(CF)_E$ denotes, the E-field correction factor at a normalized distance d from the antenna.

Near field power density P_N (in mW/cm^2), can be estimated by the following equation [36]

$$P_N = \frac{(E_N)^2}{120\pi}. \quad (23)$$

The APD program states that to estimate the near fields for collinear antennas the **correction factors** $(CF)_E$, of a full wave dipole can be used. **Figure 16** image extracted from [36] illustrates the free space near field electric field correction factor $(CF)_E$, as a function of distance normalized to 1.5λ away from a full wave dipole.

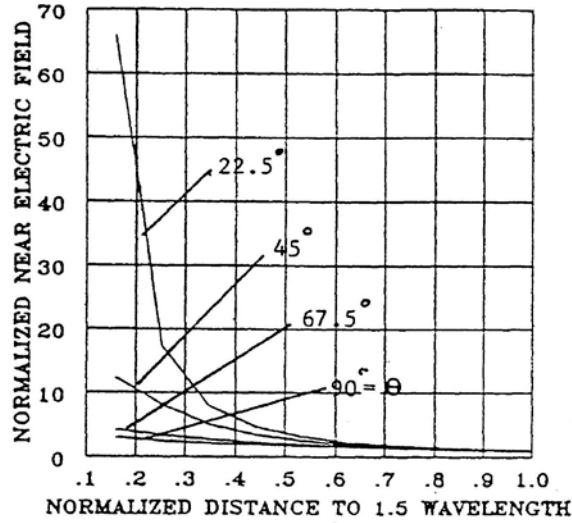


Figure 16. Near field correction factor $(CF)_E$ as a function of distance normalized to 1.5λ for a full-wave dipole in free space. Image extracted from [36].

3.1.7 Mutual Antenna-to-Antenna Coupling

Chen *et al.* 2010 [37] provided a theory on predicting the mutual antenna-to-antenna coupling in the near field regions at very small distances d between a transmitter and receiver antenna, i.e., $0.5\lambda < d < \lambda$, assuming transmit and receive antennas are along boresight, and $0.43\lambda < d < 0.73\lambda$, assuming transmit and receive antennas are 20° off axis. The accuracy of Chen's theory degrades outside these separation ranges [37].

For the present study the separation distances d between the transmitter and receiver antennas are much larger than λ m, in fact the separation distances $d > 7.7\lambda$ m (i.e., $d > 0.8$ m), which are larger than the estimated far field (or Fraunhofer) region range R_{ff} for the 4x1 linear array transmit antenna (i.e., $R_{ff} \sim 0.8$ m). Therefore, the mutual antenna-to-antenna coupling for the present study was determined by using the Friis transmission equation [38] or Scattering Matrix and Reciprocity theorem [39].

3.1.7.1 Friis Transmission Equation

Figure 17 illustrates the schematic of a receive antenna along boresight (i.e., $\Phi = 0^\circ$) of a transmit antenna, separated by a distance d . Assuming that the receive antenna lies within the far field region of the transmit antenna is polarized matched with the transmitter antenna, and both the transmit and receive antennas are isotropic, then from the Friis transmission equation, an antenna-antenna coupling constant, C , can be determined as follows [38]

$$\frac{P_r}{P_t} = G_r G_t \left(\frac{\lambda}{4\pi d} \right)^2 = C \quad (24)$$

where

P_r denotes the power received by the receive antenna,

P_t denotes the power transmitted by the transmit antenna,

G_r denotes the gain of the receive antenna,

G_t denotes the gain of the transmit antenna,

d denotes the distance between the transmit and receive antenna, and

λ denotes the operating wavelength of the transmit antenna.

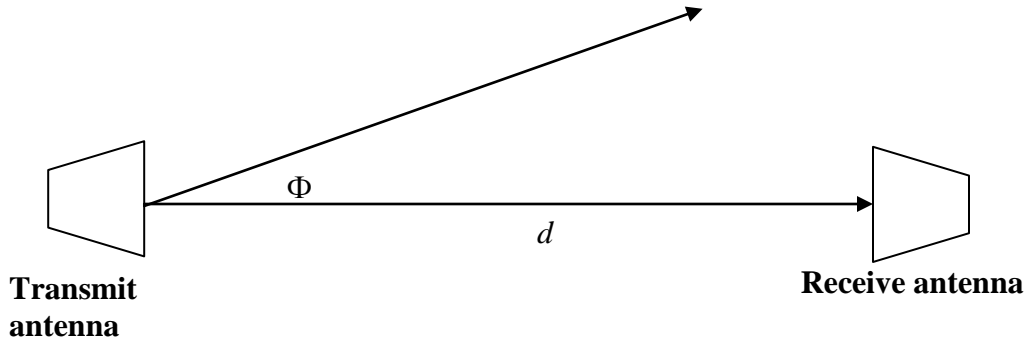


Figure 17. Schematic diagram to illustrate Friis transmission equation.

The $G_r G_t \left(\frac{\lambda}{4\pi d} \right)^2$ expression in Equation (24) is known as the transmission or attenuation loss factor.

If the receive antenna is not located along the boresight (i.e., $\Phi \neq 0^\circ$) of the transmit antenna then a power loss can occur due to mismatch polarization. This mismatch polarization power loss, C_{PL} can be estimated as follows [40]

$$C_{PL} = \cos^2(\Phi) \quad (25)$$

The mismatch polarization power loss C_{PL} can be included in the Friis transmission equation, Equation (24), so that Equation (24) can be re-written as follows

$$\frac{P_r}{P_t} = C = G_r G_t \left(\frac{\lambda}{4\pi d} \right)^2 C_{PL} \quad (26)$$

3.1.7.2 Scattering Matrix and Reciprocity Theorem

An alternative theory that can be used to determine the mutual antenna-to-antenna coupling is using the scattering matrix and reciprocity theorem. Following Roubine and Bolomey 1987 [39] derivation, and extending it for a more general case, the coupling between N transmitting antennas with amplitudes of the incident and reflected waves α_i and β_i , respectively, in a chosen reference plane P_i ($i=1,2,\dots,N$, here 1 denotes antenna 1, 2 denotes antenna 2 and N denotes antenna N) can be written as follows

$$\begin{bmatrix} \beta_1 \\ \beta_2 \\ \cdot \\ \cdot \\ \cdot \\ \beta_N \end{bmatrix} = \begin{bmatrix} S_{11} & S_{12} & \dots & S_{1N} \\ S_{21} & S_{22} & \dots & S_{2N} \\ \cdot & \cdot & \cdot & \cdot \\ \cdot & \cdot & \cdot & \cdot \\ \cdot & \cdot & \cdot & \cdot \\ S_{N1} & S_{N2} & \dots & S_{NN} \end{bmatrix} \begin{bmatrix} \alpha_1 \\ \alpha_2 \\ \cdot \\ \cdot \\ \cdot \\ \alpha_N \end{bmatrix} \quad (28)$$

where

S_{ii} (for $i=1, 2, 3,\dots$) in the Scattering S matrix denotes reflection coefficients, and S_{ij} ($i=1,2,3,\dots, j=1,2,3,\dots$ and $i \neq j$) in the Scattering S matrix denotes transmission coefficients.

Assuming only two antennas, i.e., antenna 1 and antenna 2, the theorem of reciprocity presupposes that the amount of transmitted power by antenna 1 towards antenna 2 equals the amount of transmitted power by antenna 2 towards antenna 1. This can be described mathematically as follows (Roubine and Bolomey (1987) [39], with some modifications to subscripts)

$$\int_{S_1 \cup S_2} \left(\vec{E}_1 \times \vec{H}_2 \right) \cdot \vec{n} \, dS = \int_{S_1 \cup S_2} \left(\vec{E}_2 \times \vec{H}_1 \right) \cdot \vec{n} \, dS \quad (29)$$

where

S_1 and S_2 denote two separate surfaces surrounding the transmit antenna (antenna 1) and receive antenna (antenna 2), respectively,

\vec{n} denotes the unit vector normal to $S_1 \cup S_2$ directed out of a domain denoted by Ω ,

\vec{E}_1 and \vec{H}_1 denotes the electric and magnetic fields, respectively, at each point of the domain Ω , for the case when antenna 1 is in transmission mode and antenna 2 in reception mode, and

\vec{E}_2 and \vec{H}_2 denotes the electric and magnetic fields, respectively, at each point of the domain Ω , for the case when antenna 1 is in reception and antenna 2 in transmission mode.

Assuming further, that the antennas are supplied by ideal voltage generators, which implies that in passive mode, the antennas are short circuited, then the power P

$$P = I_2 V_1 = I_1 V_2. \quad (30)$$

The coupling impedance between both antennas (antenna 1 and antenna 2) can be described, as follows [39]

$$Z_{12} = \frac{V_1}{I_2} = \frac{V_2}{I_1} = Z_{21} \quad (31)$$

Therefore relating Equation (29) with Equation (31) we obtain the following

$$I_1 V_2 = - \int_{S_1 \cup S_2} \left(\vec{E}_1 \times \vec{H}_2 - \vec{E}_2 \times \vec{H}_1 \right) \cdot \vec{n} \, dS = -I(\Pi) \quad (32)$$

since

$$Z_{12} = \frac{V_1 I_1}{I_2 I_1} = -\frac{I(\Pi)}{I_2 I_1} . \quad (33)$$

Given that the antenna impedance coupling Z_{ij} is equivalent to the transmission (or coupling) factor S_{ij} then the transmission factor can be determined using Equation (33) as follows [39]

$$S_{12} = S_{21} = \frac{\alpha_1 \beta_1}{\alpha_1 \alpha_2} = -\frac{1}{\alpha_1 \alpha_2} I(\Pi) . \quad (34)$$

The parameter $I(\Pi)$ in Equation (33), is related to the E and H field distribution of the antennas on a surface surrounding each of the antennas, in particular, on a plane that separates them both. This field determination involves calculating the transmitting antenna radiation field. If it is pre-supposed, that the antennas are separated at a large distance d from each other, taking into consideration attenuation of the radiated fields, it can be assumed as a first order approximation that in the plane Π the fields E and H for both antennas are the same as if they were radiating along in free space. Therefore, the antenna far field expression could be used. However, errors will occur as a function of $1/d^2$ [39].

Therefore, assuming a transmitting antenna, denoted as antenna 1, with a normalized broadside radiation far field $f(\theta)$, and a passive antenna, denoted as antenna 2, where both antennas lie in the same plane, $\phi = 0^\circ$ plane, the transmission (or antenna-to-antenna coupling) factor S_{12} can be estimated, using Equation (34) as follows

$$S_{12} = S_{21} = \frac{\alpha_1 \beta_1}{\alpha_1 \alpha_2} \approx -\frac{1}{\alpha_1 \alpha_2 \eta_o} \int_{\Pi(\phi=0 \text{ plane})} f(\theta) dS \quad (35)$$

where η_o denotes the free space impedance ($=120\pi$ ohms).

The free space impedance η_o has been included in Equation (35) to take into consideration the effect of free space impedance loss, as the EM wave travels from the transmission antenna to the receiver antenna. It needs to be noted that if there are a multiple N transmitting antennas, then there would far field antenna expressions in the integral term in Equation (35) for each transmitting antenna [39].

3.2 RADIO FREQUENCY RECEIVER SYSTEMS

Figure 18 illustrates a typical **Electronic Warfare (EW)** receiver system, i.e., an **Electronic Support Measure (ESM)** system. ESM system's function, is basically to detect and identify **radiofrequency (RF)** energy/signals.

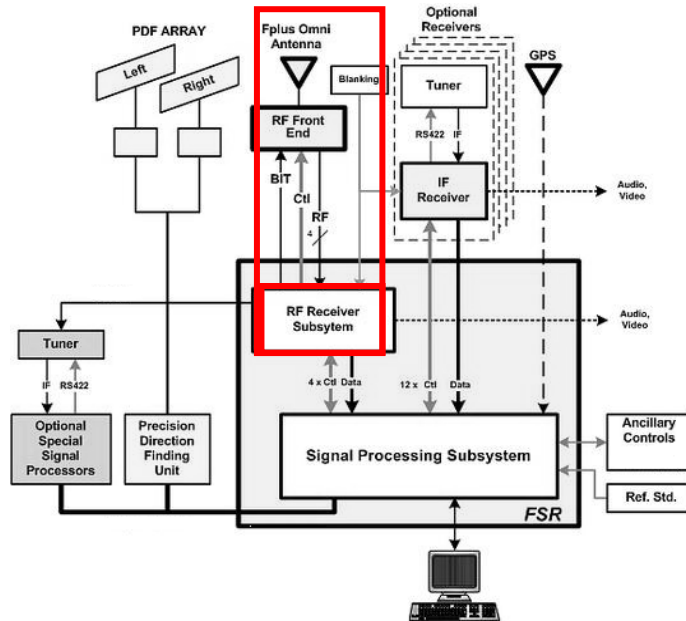
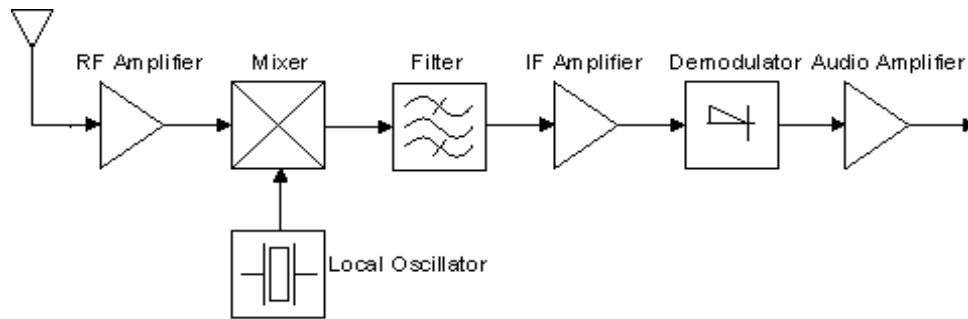


Figure 18. Schematic of a typical Electronic Support Measure (ESM) system. Image extracted from [41]. Highlighted by the red square are the components associated with, including the radio frequency (RF) receiver subsystem, of an ESM System. The image is shown here only for illustrative purposes.

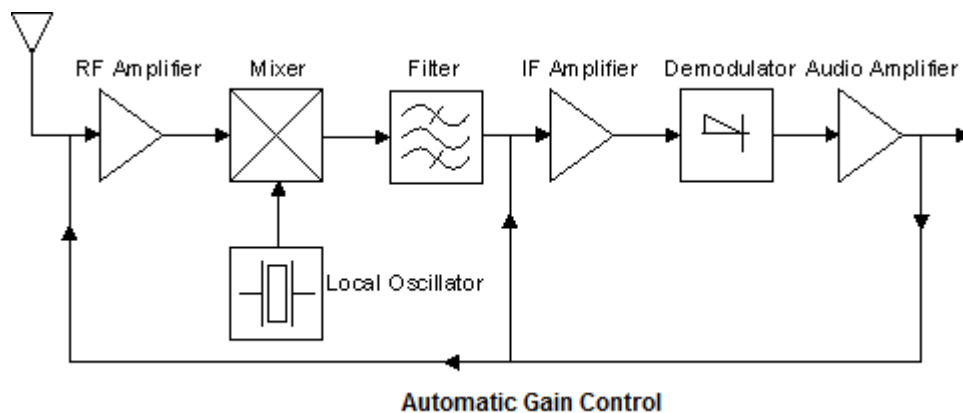
As illustrated in Figure 18, there are many subsystems that make up an ESM system. Two of the primary subsystems of an ESM system is the **radio frequency (RF)** receiver subsystem (i.e., detect) and signal processing subsystem (i.e., identify).

For the ensuing discussion, only the RF receiver subsystem of the ESM system, as depicted in Figure 18 and highlighted in red, will be considered.

Figure 19 (a) and Figure 19 (b) illustrate the schematics of two typical, but different, RF receiver systems.



(a)



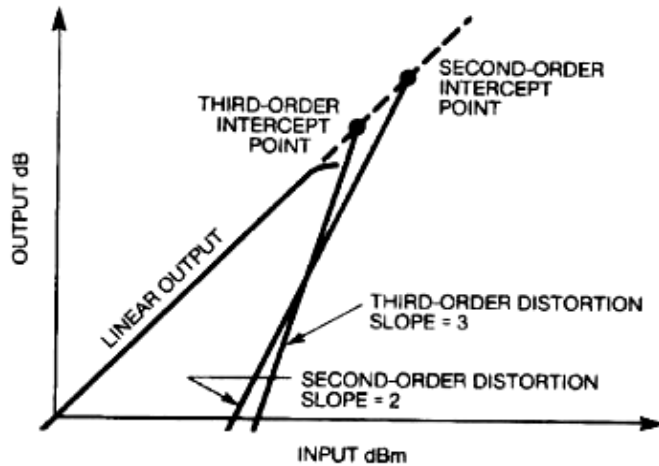
(b)

Figure 19 Schematic diagrams of typical RF receiver systems. (a) RF receiver system without automatic gain control (AGC) loop. Image extracted from [42]. **Figure 19 (b)** RF receiver system schematic with AGC feedback loop. Image extracted from [43] and [42], with some slight modifications. Here IF amplifier denotes intermediate frequency amplifier. All images shown are only for illustrative purposes.

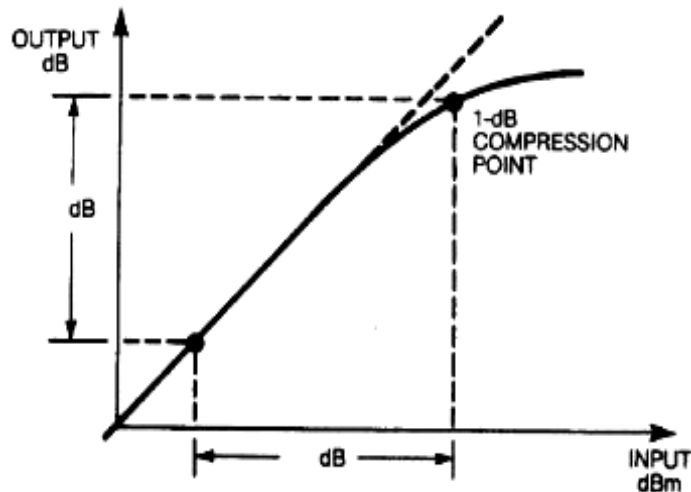
As illustrated in **Figure 19** both schematics (i.e., (a) and (b)) are similar in terms of the components that make up the receiver system, such as antenna, RF and **intermediate frequency (IF)** amplifiers, mixers and local oscillators, and filters. However, the main difference is that **Figure 19 (b)** receiver system has an automatic gain control feedback loop, whereas **Figure 19 (a)** does not.

2.1 Non-Linear Effects on RF Receiver Systems

Figure 20 illustrates typical linear and nonlinear electronic component transfer functions.



(a)



(b)

Figure 20. Typical linear and nonlinear component transfer functions. Images extracted from [44] are for illustrative purposes.

As illustrated in **Figure 20 (a)** and assuming an input fundamental signal frequency, f entering a linear electronic component, as expected, the transfer function would be linear with a gradient of unity. However, for an input fundamental signal frequency f entering a non-linear electronic component high order harmonics of the fundamental frequency f (e.g. 2nd and 3rd harmonics) can occur, which produces a change in the gradient of the transfer function (i.e., gradient=3 for 3rd order distortion and gradient=2 for 2nd order distortion). The point where the 2nd and 3rd harmonics distortion transfer functions

intercepts the linear output transfer function is called 2nd and 3rd order intercept point, respectively.

As illustrated in **Figure 20 (b)** as input power increases the output power from a non-linear electronic component will initially follow a linear response transfer function. However, as the input power continues to increase there will come a point where the output power levels off (or saturates). The difference between the points where saturation occurs in the non-linear transfer function from the linear transfer function is called the 1dB compression point. In particular, for a 2nd harmonic distortion the output power drops 2 dB for every 1dB drop in input power. Similarly, for a 3rd harmonic distortion the output power drops 3dB for every 1dB in input power.

Some of the non-linear effects on RF receiver systems due to transmitting signals can include [45]:

- Front end damage to receivers
- Sub-harmonic distortion,
- Desensitization (or Gain compression)
- Intermodulation, and
- Cross modulation

For the present study only one transmitter and one receiver system will be considered and so only non-linear effects due to a minimum of one transmitter and receiver antenna is considered (i.e., sub-harmonic distortion and desensitization). Non-linear effects, such as intermodulation and cross-modulation, which typically occurs with multiple, transmit antennas, were not assessed. However, for any future work where more sensor systems are fitted on a mast structure, then such non-linear effects (intermodulation and cross modulation) will need to be considered.

3.2.1.1 Sub-harmonic Distortion

Sub-harmonic distortion in a RF receiver system occurs when spectral components or harmonics (typically 2nd and 3rd harmonics) of the fundamental input signal frequency are generated due to the non-linearity of the receiver systems components.

The maximum allowable input power P_{in} at the fundamental, given a harmonic intercept point, nOI (in dBm) and a maximum harmonic level L (in dBm) can be estimated as follows [45]

$$P_{in} < \frac{(n-1)nOI + L}{n} \quad (36)$$

where

n denotes the high order harmonic distortion (i.e., $n=2, 3, 4\dots$).

If there are input power signals entering a RF receiver system that are greater than or equal to the maximum allowable input power P_{in} then high order harmonics of the transmitted fundamental frequency can be generated.

3.2.1.2 Desensitization (or Gain Compression)

The sensitivity S_{min} in a RF receiver system is defined as the minimum input signal required to produce a specified output signal having a specified signal-to-noise $(S/N)_{min}$ ratio and is determined as follows [46]

$$S_{min} = \left(\frac{S}{N} \right)_{min} kTB(NF) \quad (37)$$

or

$$MOS = \frac{\left(\frac{S}{N} \right)_{min} kTB(NF)}{G} \quad (38)$$

where

$\left(\frac{S}{N} \right)_{min}$ denotes minimum signal-to-noise ratio needed to process a signal,

NF denotes the noise figure/factor,

k denotes Boltzmann's constant $=1.38 \times 10^{-23} \text{ J/}^\circ\text{K}$,

B denotes the receiver bandwidth (Hz),

T denotes absolute temperature of the receiver input ($^\circ\text{K}$)

G denotes the antenna/system gain, and

MOS = minimum operational sensitivity.

In general, if there are input power signals entering a RF receiver system greater than the minimum input signal required to produce a specified output signal S_{\min} then the RF receiver can be desensitized (or gain compression), so that it is not able to effectively detect RF signals.

3.3 MODELS AND ASSUMPTIONS

3.3.1 Linear Polarized Circular Patch Microstrip Antenna

Figure 21 illustrates different schematics of the design of the linear polarized circular patch microstrip element antenna utilized in the present study and used in the numerical simulations in the present study. **Figure 21 (a)** illustrates a 3D schematic of the element antenna highlighting major parameters of the antenna, including circular patch antenna radius, a , substrate and ground plane. **Figure 21 (b)** illustrates a top plan view of the circular patch antenna, highlighting circular patch diameter, D and the location of the antenna feed offset S_F . From the center of circular patch and **Figure 21 (c)** illustrates a perspective view of the element antenna highlighting substrate height h , substrate permittivity ϵ_r , feed diameter ($2F_R$, where F_R denotes the feed radius) and the feed offset S_F . Dimensions of the circular patch antenna illustrated in **Figure 21** is provided in **Table 2**.

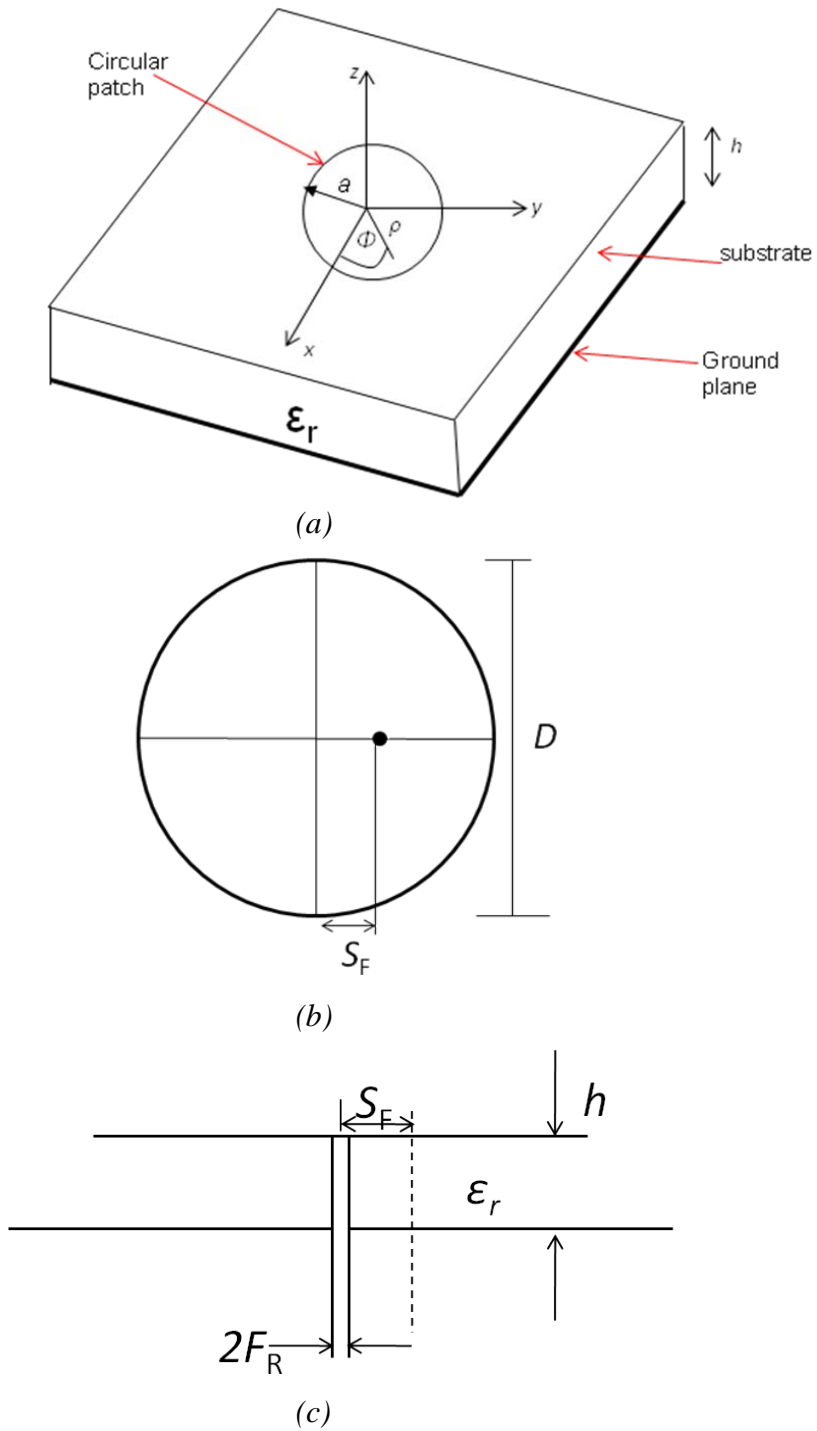


Figure 21. Schematic diagrams of linear, polarized, circular patch, microstrip element antenna. Figures 21 (a) 3D schematic of element antenna, (b) Plan view of circular patch antenna highlighting circular patch diameter, D and location of antenna feed offset from center of circular patch, S_F and (c) Perspective view of element antenna highlighting substrate height h , substrate permittivity ϵ_r , feed diameter ($2F_R$, where F_R denotes the feed radius) and feed offset S_F .

Table 2 Linear polarized circular patch microstrip antenna dimensions.

Parameter	Value
Patch antenna diameter, D (mm)	35.49
patch antenna radius, a (mm)	17.745
Substrate thickness, h (mm)	2.00
Substrate relative permittivity, ϵ_r	2.5
Input impedance, Z_o (Ω)	50
Feed offset, S_F (mm)	4.15
Feed pin radius, F_R (mm)	166.7
Substrate (mm)	106x106
Ground plane (mm)	106 x106

Figure 22 illustrates the 3D schematic of the linear, polarized, circular patch, microstrip antenna model used in CEM software tools (FEKO and **Microwave Studio (MWS or CST)**).

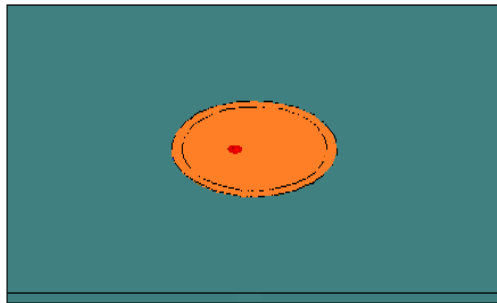


Figure 22. 3D Schematic of linear, polarized, circular patch, microstrip antenna model used in the CEM software tools (FEKO and MWS). Green denotes the substrate material and orange denotes perfect electric conductor circular patch.

3.3.2 Linear Polarized Circular Patch Microstrip 4x1 Linear Array Antenna

Figure 23 illustrates the schematic of the 4x1 linear polarized circular patch microstrip linear array antenna (or 4x1 linear array antenna) model.

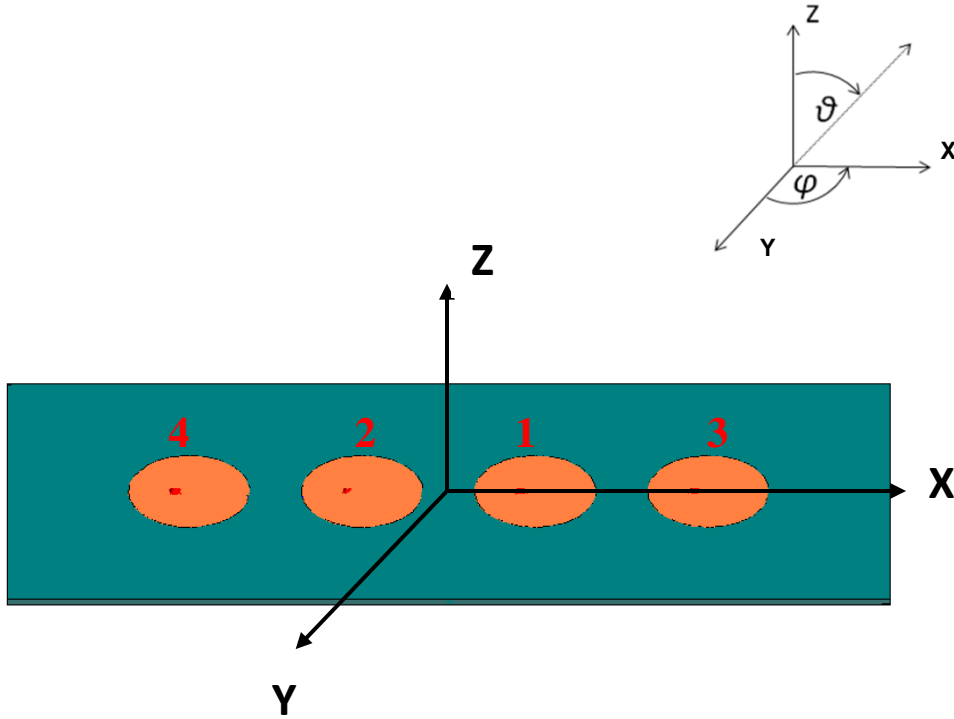


Figure 23. 3D schematic of 4x1 linear polarized circular patch microstrip linear array antenna. The separation d_x between each of the antenna elements is $\lambda_0/2$ m, and the length $L (=Nd_x$, where N denotes the number of elements) of the linear array is $2\lambda_0$ m. Linear array antenna elements are numbered (from L to R) as 4, 2, 1, 3. Here z -axis, is assumed, to be pointing out of the page.

As illustrated by **Figure 23** the four antenna elements were placed along the x -axis plane, with a separation d_x of $\frac{\lambda_0}{2}$ m and the length, L of the linear array was $2\lambda_0$ m. The antenna elements were all assumed to be transmitting simultaneously and that the coupling between each antenna element was also considered in all simulations. For orientation purposes a co-ordinate system is also presented in **Figure 23** to illustrate the elevation θ and azimuth ϕ angles orientation with respect to the linear array antenna model.

The excitation of the antenna elements were via a voltage source and the amplitude for each antenna element was set to 1V. To obtain different electronic scan angles for the linear array antenna the phase shift for each of the antenna elements' voltage sources

were varied in FEKO and MWS. **Table 3** presents the phase shift in degrees for each of the antenna element feed ports to achieve different antenna scan angles. Illumination was assumed to be uniform and was set at 1V for each antenna feed port.

Table 3 Phase shift (°) for each 4x1 linear array antenna element to obtain different linear, array, antenna scan angles.

Antenna electronic scan angle θ (°)	Antenna element	Phase shift angle on each linear array antenna element (°)
0	1	0.00
	2	0.00
	3	0.00
	4	0.00
~ 5	1	-10.00
	2	10.00
	3	-30.00
	4	30.00
~11	1	-21.25
	2	21.25
	3	-63.75
	4	63.75
~18	1	-32.50
	2	32.50
	3	-97.50
	4	97.50

In Savant the antenna could be modeled by importing a 3-D antenna radiation pattern or creating a current source file. The difference between the 3-D radiation pattern and current source file was that any simulations using a 3-D antenna radiation pattern would not consider any near field effects, whereas the current source, would consider near field effects. Since Savant was to be used for antenna-to-antenna coupling simulations current source files had to be created to model the linear array antenna so that near field effects could be taken into consideration in the simulations in order to obtain better simulation results.

Figure 24 illustrates the 4x1 linear array antenna model using current sources in Savant.

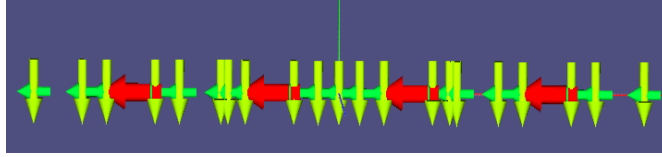


Figure 24. 4x1 linear array antenna and radiation pattern (frequency $f=2.96\text{GHz}$) in Savant using current sources. Red dipole depicts the perfect electrical conductor antenna element and the pair of green dipoles depicts the infinite substrate and infinite ground plane.

As illustrated in **Figure 24** the 4x1 linear array antenna model assumed four perfect electrical conducting elements (depicted as red electric hertzian dipoles), along the x -axis, with a spacing of $\lambda / 2$ m between each element, and mounted on an infinite substrate and ground plane (depicted as pairs of green electric and magnetic hertzian dipoles) [47]. The current moments for each antenna element (i.e., Hertzian dipoles), were assumed to be 1 A-m.

The receive antenna radiation pattern and current source was considered in the Savant simulations. **Figure 25** illustrates the 1x1 receiver antenna model using current sources (i.e., electric hertzian dipoles to depict the perfect electrical conductor element and pairs of electric and magnetic dipoles to depict an infinite substrate and ground plane [47]).

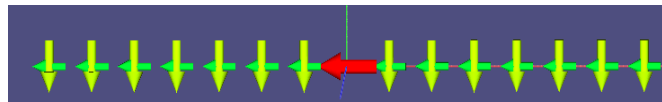


Figure 25. 1x1 single element antenna and radiation pattern (frequency $f=2.96\text{GHz}$) in Savant using current sources. Red dipole depicts the perfect electrical conductor antenna element and the pair of green dipoles depicts the infinite substrate and infinite ground plane.

For Savant, the different antenna scan angles in the present study were achieved by mechanically scanning the antenna.

3.3.3 Near Field Power Flux Density

The near field power flux density was determined by computing the near electric field (in Vm^{-1}) using the CEM software tools and then using the expression $S(\text{Wm}^{-2}) = \frac{1}{\eta_o} E_o^2$ to calculate and plot S , which was done using MATLAB. In particular, to verify simulated free space near field power density, the average near field power density for a collinear array antenna in free space, was compared with analytical results. The fitted near field power flux density was determined by calculating the near electric fields at different locations around the transmit antenna and mast structure. Then the magnitude of the Poynting vector S was determined, normalized (in dB) and then plotted using MATLAB. The Poynting vector, was normalized, to represent the fitted relative near field power flux density independent of the units of power.

More detail on the different locations around the antenna and mast structure where near fields were calculated for each CEM tool will be provided in the proceeding chapter, Chapter 4, Results and Discussion.

3.3.4 Mutual Antenna-to-Antenna Coupling

The mutual antenna-to-antenna coupling simulation assumed only two antennas. One antenna was a transmitting antenna and the other a passive receive antenna. The transmit antenna was assumed to be a 4x1 linear array antenna and the receiver antenna a 1x1 linear array.

The transmit antenna was assumed to be located at the front panel of the mast structure and the receiver antenna was positioned at two different locations on the mast structure. The first position of the receive antenna was above the transmit antenna, and the second position of the receive antenna was on the side panel mast structure, relative to the panel where the transmit antenna was located.

In FEKO the transmission scattering S matrix parameters, i.e., S_{ij} were determined for each antenna feed port (i.e., S parameter subscript $j=2, 3, 4, 5$) of the 4x1 linear array with the receive antenna feed port (S_{ij} , i subscript =1). Further detail on the notation associated with the linear array antenna element numbering and S parameter subscripts are given in **Appendix A.3**.

The free space (i.e., without mast structure) mutual antenna-to-antenna coupling calculations in FEKO was done using the MoM technique, with discretization (or mesh) sizes $\sim\lambda/20$ m. Whereas, for the fitted (i.e., with mast structure) mutual antenna-to-antenna coupling the **Multiple Level Fast Multipole Method (MLFMM)** was used however, with discretization (or mesh) sizes $\sim\lambda/7$ m.

For the mutual antenna-to-antenna coupling, simulations in Savant, were performed, using a **Shooting and Bouncing Rays (SBR)** technique. A maximum of 5 bounces and a

ray intensity of 4 rays per wavelength were used for the simulations. Further details regarding exact location of transmitter and receiver antenna for the mutual coupling in Savant is given in **Appendix A.4**. The co-ordinates associated to the position for both the transmit antenna and receive antenna for the Savant simulations were taken from the FEKO model. This was to replicate, as close as possible, the positions of each antenna, so direct comparisons of the results could be made between both CEM software simulations.

3.3.5 Mast Structure

A generic mast structure was designed using the 3D design software tool, called Rhinoceros version 4.0. Once the design of the mast structure was completed, it was exported into specific formats, so it could be imported into each of the CEM software tools.

The mast structure design for the present analysis, was not meant to replicate any integrated mast structure currently available or fitted on ships. However, the only features that were adopted from currently available integrated masts in designing the mast structure for the present study were the basic panel faceted shapes (e.g. rectangle) and how the panels are positioned in order to form the mast structure framework (i.e., panels angled inwards or outwards).

Figure 26 illustrates a 3D view of the generic mast structure designed for the present study. As illustrated, in **Figure 26** the mast structure was designed as an octagon shape structure made up of up of angled rectangle faceted panels. The eight rectangle panels were made up of 4x two different sized rectangle panels. **Figure 27** illustrates different schematic diagrams, including dimensions, of the generic, octagon-shape mast structure used for the present analysis.

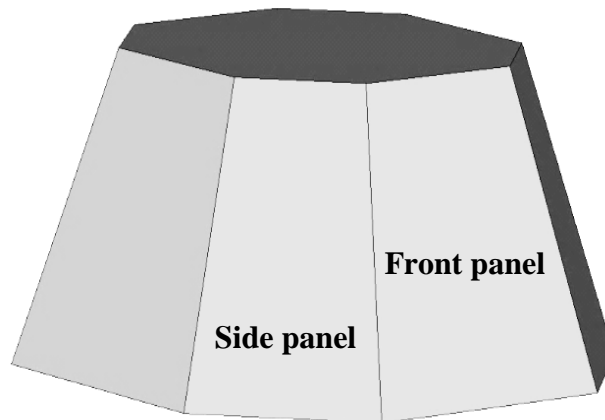


Figure 26. 3D perspective view of the generic octagon shape, rectangle panel faceted mast structure.

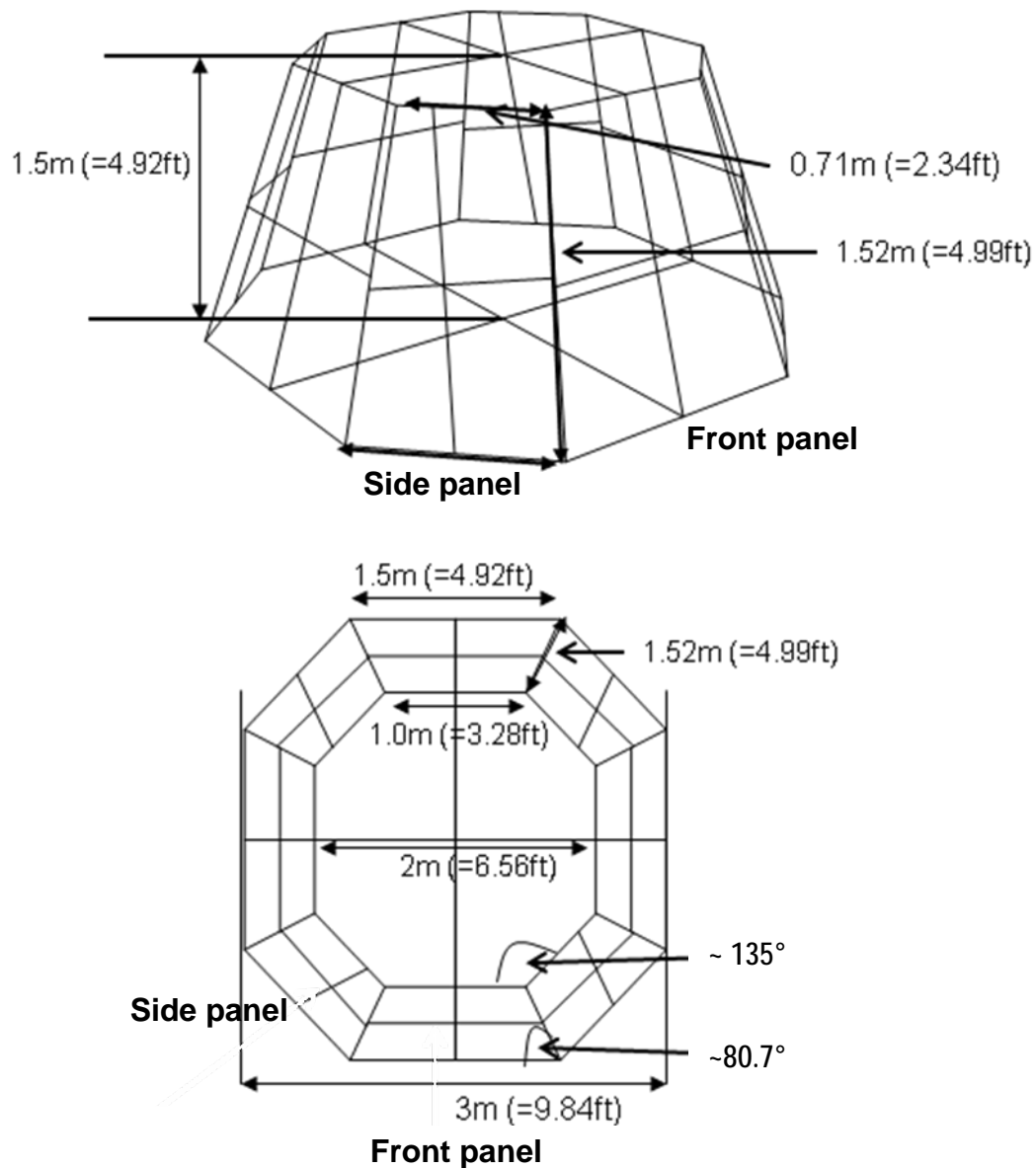


Figure 27. Schematic diagram, including dimensions of the generic octagon shaped rectangle panel faceted mast structure.

As illustrated in **Figure 27** the rectangle panel denoted as “Front panel” has dimensions 1m (top edge) x 1.5m (bottom edge) x 1.52m (slanted edge). The second rectangle panel denoted as “side panel” has dimensions 0.71m (top edge) x 1.06m (bottom each) x 1.52m (slanted edge). The mast structure panels has an incline angle of $\sim 80.7^\circ$ from the base of the mast structure and the angle between the side panel and front panels is $\sim 135^\circ$.

The mast structure for the present analysis was assumed to be made of perfect electrical conducting material.

3.4 SOFTWARE TOOLS

3.4.1 Computation Electromagnetic Software Tools

The present analysis was done using three commercial-off-the-shelf **computational electromagnetic (CEM)** software, including FEKO, Microwave Studio (or CST) and Savant. Each of the three different CEM softwares is based on different numerical techniques to determine the electromagnetic fields.

3.4.1.1 FEKO - Full Wave Solver – Frequency Domain

FEKO is a full wave solver principally in the frequency domain (e.g. FEM and Method of Moments techniques). Typically, the Helmholtz equations, are used as the starting the point [48]

$$\nabla \times \vec{H} = j\omega\epsilon \vec{E} + \vec{J} \quad (39)$$

$$\nabla \times \vec{E} = -j\omega\mu \vec{H} + \vec{M} \quad (40)$$

The local currents, can be caused by a source (e.g. an antenna feed) or from an impressed field (e.g. equivalent sources of an incident wave). The solutions of the above two equations (i.e., Equation (39) and Equation (40)), for different conditions, for both \vec{E} and \vec{H} are integral equations, which includes the Green function (i.e., $G\left(\vec{r}, \vec{r}'\right) = \frac{e^{-jk|\vec{r}-\vec{r}'|}}{4\pi|\vec{r}-\vec{r}'|}$)

which the exact solution of the integral equation are generally not possible to solve. Therefore, a numerical solution of the integral equations is required. The Method of Moments is a numerical technique that converts the integral equations into a linear system that can be solved, on a computer using matrix inversion. FEKO also offers a **Multi-level Fast Multipole Method (MLFMM)**, which is based on MoM, but uses a technique to make the simulation go faster and use less computer memory. FEKO also offers other solvers including asymptotic (or high frequency) solvers (e.g. **Uniform Theory of Diffraction (UTD)** and **Physical Optics (PO)**).

3.4.1.2. Microwave Studio - Full Wave Solver – Time Domain

Microwave Studio (MWS) is full wave **solver** principally in the time domain, typically called **Finite Difference Time Domain (FDTD)** technique. The FDTD technique uses the differential form of Maxwell Equations as its starting point [48]

$$\nabla \times \vec{E} = -\mu \frac{\partial \vec{H}}{\partial t} \quad (41)$$

$$\nabla \times \vec{H} = \epsilon \frac{\partial \vec{E}}{\partial t} + \sigma \vec{E} + \vec{J}. \quad (42)$$

The Yee Scheme, typically used for FDTD, uses Cartesian orthogonal cells to build the grid discretization (i.e., in Δx , Δy , and Δz). The process uses staggered \vec{E} and \vec{H} cells and where the field components are located on the edges of those cells. For the FDTD to be stable it is required that the following condition (called the Courant–Friedrich-Levy) be met

$$\Delta t \leq \frac{1}{c \sqrt{\frac{1}{(\Delta x)^2} + \frac{1}{(\Delta y)^2} + \frac{1}{(\Delta z)^2}}} . \quad (43)$$

Microwave Studio also offers a frequency domain solver, i.e., MoM, called *F* solver, and a fast MoM solver, i.e., similar to the MLFMM in FEKO, called the **Integral (I)** solver. In addition, Microwave Studio also offers asymptotic solvers. However, the version of Microwave studio (i.e., Education version) that was available for the present study did not include the asymptotic (or high frequency) solvers.

3.4.1.3 Savant - Asymptotic (High Frequency) Solver

Savant is an asymptotic (or high frequency) technique, based on a Shooting and Bouncing Ray technique. Other asymptotic (or high frequency) solvers include Geometrical optics, Physical Optics, **Geometrical Theory of Diffraction (GTD)**, **Uniform Theory of Diffraction (UTD)** and **Physical Theory of Diffraction (PTD)**.

In general, asymptotic (or high frequency) solvers, are based on the concepts of ray tracing to describe EM wave propagation mechanisms. For example, in free space or in homogeneous regions, the rays are observed to behave as straight lines along which the light propagates, and for close to structures the rays behave under the laws of reflection diffraction and refraction.

A description for all techniques will not be given here, only for the Shoot and Bouncing Ray technique, as this was used for the present analysis.

Shooting and Bouncing Rays (SBR) is a technique similar to the geometrical ray tracing technique. However, the ray tracing procedure is simplified by representing the source radiation in terms of discrete ray tubes and then traces of each ray tube is done independently. As described by [49] each ray tube represents a pulse function that has uniform amplification and quadratic phase variation over its cross section. In Savant, the ray bundles are launched separately and processed from each short dipole source of a transmit antenna characterized by current sources. The ray field generated by the SBR algorithm, in Savant, includes the higher-order $1/R^2$ and $1/R^3$ terms, as this is necessary to accurately compute the scattering from surfaces near the antenna. The results due to each current source are then coherently united [50].

In Savant the radiated equivalent currents to observation angles/points is calculated using the following equation [50]

$$\bar{E}_s(\bar{r}) = \frac{1}{4\pi} \int_{S'} dS' \left[(\hat{n}' \cdot \bar{E}) \nabla \cdot \frac{e^{-jkR}}{R} + (\hat{n}' \times \bar{E}) \times \nabla \cdot \frac{e^{-jkR}}{R} - j\omega\mu(\hat{n}' \times \bar{H}) \frac{e^{-jkR}}{R} \right]. \quad (44)$$

For antenna-to-antenna coupling simulations with a receiver antenna the following factor is included in Equation (44) [50]

$$b = \frac{-j\lambda}{\sqrt{4\pi\eta_0}} \bar{E} \cdot \bar{d}_{Rx}. \quad (45)$$

The incident electric field \bar{E}_i generated by implementing an antenna radiation pattern is determined by the following [50]

$$\bar{E}_i = \sqrt{\frac{P\eta_0}{4\pi}} \left[d_\theta \hat{\theta} + d_\phi \hat{\phi} \right] \frac{e^{-jkR}}{R}. \quad (46)$$

As described in [50], for antennas placed in close vicinity to significant scattering geometry, i.e., the geometry is at distance $R < R_{ff}$ (where R_{ff} is the Fraunhofer field region of the transmit antenna) Savant requires an accurate representation of the transmitter antenna (and receiver antenna for coupling scenarios) in both its near and far-field regions. This purpose, in Savant, is served by depicting the free-standing antenna in terms of current sources, where each current source is a short electric or magnetic dipole with a position, orientation, and weight (moment). The moments (or weights) can be frequency-dependent. The units for these moments are amp-meters and volt-meters for electric and magnetic sources, respectively. There are exact formulas for the fields generated by an electrically short (so-called Hertzian) dipole that are valid at all distances. These include terms proportional to $1/R^2$ and $1/R^3$ that dominate in the Fresnel (or near field) field region but decay rapidly to become negligible in the far-field region. Hence, the current source representation of an antenna is always more accurate and more broadly usable than its antenna radiation pattern [50].

Table 4 provides a summary of the different computational electromagnetic software used in the present study, along with the discretization sizes for the full wave solvers used in the present study.

Table 4 A summary of the computational electromagnetic softwares (i.e., FEKO, Microwave Studio and Savant) that were used for the present study. E in the column titled “Version” denotes Educational (or University) version. The educational /University versions for FEKO and Microwave Studio had limited computer memory (~ 2GByte), which restricted the size of the models that could be used for simulation.

CEM Tool	Technique	Method	Domain (Frequency(F)/ Time(T))	Maxwell Equation Type	Discretization (or mesh) size and type	Version
FEKO	FEM	Full Wave	F	Differential	$< \lambda/10$ & volume	E
	MoM	Full Wave	F	Integral	$\sim \lambda/5$ & surface	
	MLFMM	Full Wave	F	Integral	$\sim \lambda/5$ & surface	
	UTD/GO	Asymptotic high-frequency		Field-based (ray tracing)	N/A	
Microwave Studio (MWS)	T* solver (=FDTD)	Full wave	T	Differential	$< \lambda/10$ & volume	E
	F*Solver (=MoM)	Full wave	F	Integral	$\sim \lambda/5$ & surface	
	Integral Solver (I*)=(MLFMM)	Full Wave	F	Integral	$\sim \lambda/5$ & surface	
Savant	Shooting and Bouncing Rays (SBR)	Asymptotic high-frequency		Field based (ray tracing)		V2.1

3.4.2 Radio Frequency Circuit Performance – ADS Systems

It was of interest to assess the performance of a RF receiver system when subjected to near field power signal levels from a transmit antenna, which is in close proximity to it on the same mast structure.

A methodology generally used to evaluate the performance of RF circuit is a Budget Analysis. A budget analysis, in general, determines the performance, behavior of linear and nonlinear characteristics of an RF system.

For this study, it was of interest to evaluate the performance of a RF receiver system when subjected to the fitted relative near field power flux densities, from a 4x1 linear array-transmitting antenna in close proximity on a mast structure. The fitted relative near field power flux densities (in dB) of the 4x1 linear array antenna were determined for different locations around the antenna and mast structure, using the computational electromagnetic software simulations and MATLAB. The computed relative near field

power flux densities (in dB), entering the RF receiver system was then converted to a near field power signal level in dBm, assuming an effective receiver antenna area A_e . This near field power signal level (in dBm) was assumed to be the input signal power level into the RF receiver system for the budget analysis simulations.

The budget analysis simulations were done using Agilent ADS Systems software. The performance of the RF receiver system components and system were evaluated for varying input signal power levels. The output parameters from the budget analysis simulations included **third order intercept (TOI)**, **signal-to-noise ratio (S/N)**, **noise figure/factor (NF)**, output power, output power gain, just to name a few.

The performance of two different RF receiver system circuits was assessed. One of the RF receiver systems included an **automatic gain control (AGC)** loop and the other did not.

The RF receiver system modeled in ADS Systems had to be limited to only two-pin two-port linear and non-linear components in order for the budget analysis simulations. Therefore, antenna and demodulator components of an RF receiver system, had to be excluded from the RF receiver model in ADS Systems, as such components were not permitted in the budget analysis simulations.

3.4.2.1 Radio Frequency (RF) Systems Budget Analysis Component Models

ADS Systems software was used for the present study, since it was available and is widely used among RF Engineers for RF circuit analysis [51].

The RF budget analysis component model in ADS Systems, basically, use scattering matrix theory between two-port, two-pin circuit components, as depicted in **Figure 28** [52].



Figure 28 Two-port, two-pin component schematic with signal wave directions. Image extracted from ADS Systems’ RF system Budget Analysis [52]. a_1 denotes the signal wave into port 1, b_1 denotes the wave out of port 1, a_2 denotes the signal wave into port 2 and b_2 denotes the signal wave out of port 2.

The parameters for the standard scattering matrix S for a two-port, two-pin electronic component are as follows [52]

$$\begin{bmatrix} \mathbf{b}_1 \\ \mathbf{b}_2 \end{bmatrix} = \begin{bmatrix} s_{11} & s_{12} \\ s_{21} & s_{22} \end{bmatrix} \begin{bmatrix} \mathbf{a}_1 \\ \mathbf{a}_2 \end{bmatrix} \quad (47)$$

where

s_{ij} , for $i=j$ are the reflection coefficients,

s_{ij} , for $i \neq j$, are the transmission coefficients.

a_1 denotes the signal wave into port 1,

b_1 denotes the signal wave out of port 1,

a_2 denotes the signal wave into port 2 and

b_2 denotes the signal wave out of port 2.

In ADS Systems' budget analysis the S parameters are defined with respect to a reference impedance at both ports 1 and 2 of 50Ω . This in turn simplifies the calculations so that the transmission S parameter S_{21} , for example, is just the voltage gain of the component from port 1 to port 2.

By solving the matrix in Equation (47) for the signal waves coming in and out of each port, i.e., b_1 and a_1 in terms of a_2 and b_2 , yields the transmission matrix T parameters [52]

$$\begin{bmatrix} \mathbf{b}_1 \\ \mathbf{a}_1 \end{bmatrix} = \begin{bmatrix} t_{11} & t_{12} \\ t_{21} & t_{22} \end{bmatrix} \begin{bmatrix} \mathbf{a}_2 \\ \mathbf{b}_2 \end{bmatrix},$$

where

$$[\mathbf{T}] = \begin{bmatrix} t_{11} & t_{12} \\ t_{21} & t_{22} \end{bmatrix} = \begin{bmatrix} (s_{12} - s_{11} \frac{s_{22}}{s_{21}}) & \frac{s_{11}}{s_{21}} \\ -\frac{s_{22}}{s_{21}} & \frac{1}{s_{21}} \end{bmatrix} \quad (48)$$

A detailed description and derivation for each of the different RF budget analysis linear and non-linear component models are given in [52], so therefore a detailed description will not be given here. Instead, what will be provided is a brief description of each component model with some mathematical model.

For a linear passive two-port, two-pin component the noise model, is described, by the noise correlation matrix $[\mathbf{N}]$, as follows [52]

$$[\mathbf{N}] = kT \{[\mathbf{I}] - [\mathbf{S}][\mathbf{S}^*]\} \quad (49)$$

where

$$[N]=\begin{bmatrix} n_{11} & n_{12} \\ n_{21} & n_{22} \end{bmatrix},$$

k =Boltzmann's constant,

T =physical temperature in K

$$[I]=\text{the identity matrix}=\begin{bmatrix} 1 & 0 \\ 0 & 1 \end{bmatrix}$$

$[S]$ =scattering matrix, and

$[S^*]$ =the transpose of the conjugate of the $[S]$ matrix.

In addition, for passive linear component the S-parameters satisfy the energy conservation requirement for port index $i=1$ to N [52]

$$\sum_{i=1}^N |S_{ij}|^2 \leq 1. \quad (50)$$

For active two-pin, two-port linear components with noise wave parameters are related to the more common noise parameters of NF_{\min} , G , and R_n , i.e., minimum noise in dB, optimum source reflection coefficient for NF_{\min} , and equivalent input normalized noise resistance, respectively. There is a physical requirement for the noise parameters of the two-port, two-pin active components regarding the equivalent input normalized noise

resistance R_n that has to be met. It requires that $R_n \geq \frac{(10^{NF_{\min}/10})|1+G_{\text{opt}}|^2(1-|s_{11}|^2)}{(4|1-s_{11}G_{\text{opt}}|^2)}$.

This constraint is based on the requirement that component's combined noise wave power at port1 ≥ 0 . Any active component has its noise parameters checked against this physics requirement. Therefore, if the user supplied noise parameter $NP < R_n$ then either an error will occur and the simulation will stop or the simulation will proceed by setting R_n to this limit value.

For all non-linear two-pin, two port circuit components the scattering matrix parameters varying with input power is based on a dataset that has been measured in a hardware measurement laboratory for a non-linear RF two-pin, two-port component. This dataset "...has been accepted as a convenient means of characterizing non-linear devices by their large signal S-parameter and have been successfully used for designing power amplifiers and oscillators, etc...", [52]. The noise wave parameters for nonlinear components are determined in the same away as those defined for an active linear component. The nonlinear model with defined **third order intercept (TOI)** is used for the already defined circuit components Amplifier, Amplifier2 and AGC_Amp, of the Budget analysis, and only when these components are at the top of the RF system design being analyzed. Some of the output parameters from the budget analysis if this model is used are Cmp_OutTOI and $InTOI_dBm$.

3.4.3 Mast Structure

3.3.3.1 *Rhinoceros v4*

Rhinoceros is a 3D free form geometric modeling software tool, developed by Robert McNeel & Associates [53]. Rhinoceros v4, was used for the present study, because of its availability, to design the mast structure. Once the mast structure was designed the 3-D model was then exported in different formats (i.e., *.obj format for Microwave Studio (or CST) and Savant, and parasolid (i.e., *.x_t, *.x_b) format for FEKO) to be then imported into each of the CEM software tools.

3.5 ERRORS AND CONSTRAINTS

3.5.1 Limitations of Computation Electromagnetics (CEM) Software tools

Computation electromagnetic (CEM) software are tools that attempt to solve the Maxwell's equation in discrete form (i.e., full wave solvers) or with ray tracing technique (asymptotic techniques) to obtain approximate solutions with accuracy consistent with desired requirements. One of the main limitations of the CEM software tools for the present study was the limited computer memory availability (i.e., ~2GByte) associated with the version (i.e., Education or University version) of each of the different CEM software tools (i.e., FEKO and **Microwave Studio (MWS)**). The limited computer memory availability governed the finite discretization (or mesh) size, model size and computation time associated with full wave solver techniques (i.e., FDTD and MoM). Conversely, asymptotic (or high frequency) techniques (e.g., UTD, PO or SBR) could have been used for the present study, instead of full wave solver techniques, which would have supported large scale models, less computer memory and less computation time. However, accuracy would have been forgone.

Accuracy was the primary focus for the present study, so full wave solver techniques were used for both free space and fitted simulations. However, asymptotic (or high frequency) techniques, namely **Shooting and Bouncing rays (SBR)** via Savant software was also used in the present study mainly to compare simulated results from different simulation techniques (i.e., full wave solver versus asymptotic techniques).

3.5.2 Numerical Errors

3.5.2.1 Finite Discretization

Figure 29 illustrates the numerical error as a function of number of nodes per wavelength for finite discretization based numerical techniques.

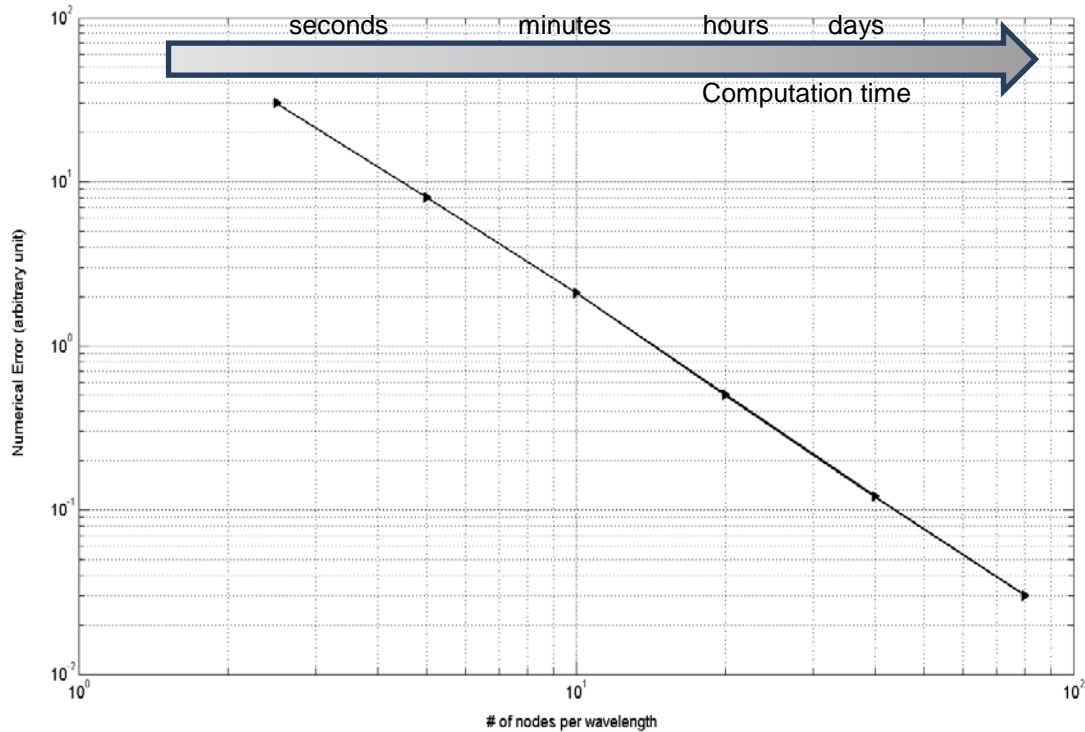


Figure 29. Numerical error as a function of number of nodes per wavelength for finite discretization based numerical techniques. Graph extracted from [48].

As illustrated in **Figure 29**, as the number of nodes per wavelength increases or the discretization size decreases the numerical error decreases, but with an increase in computation time close to days. Conversely, as the number of nodes per wavelength decreases (i.e., discretization size increases) the numerical error increases. However, the computation time is reduced from days to only a few seconds. Therefore, for the present study a compromise had to be made between discretization size and numerical error given the limited computer memory available.

Table 5 presents a summary of the models; numerical method; discretization sizes (where applicable); and associated estimated numerical error, taken from **Figure 29**, that was used for each CEM software tool in the present study.

As presented in Table 5 for the fitted simulations (i.e. fitted antenna radiated patterns, fitted near field and fitted mutual antenna-to-antenna coupling) a larger discretization size, i.e. $\lambda/10 \text{ m} < \Delta < \lambda/5 \text{ m}$ was used for the full wave solver techniques.

The discretization sizes for the full wave solver techniques (i.e., FEM, MoM, FDTD and MLFMM) had to be adjusted for different simulation models (i.e., without and with mast structure) mainly due to the computer memory restrictions. In general, for all the free space simulations (i.e., free space antenna radiation patterns, free space near field power density and free space mutual antenna-to antenna coupling) a smaller discretization (or mesh) size, i.e., $\lambda/20 \text{ m} < \Delta < \lambda/10 \text{ m}$ was used for the full wave solver techniques. The time step Δt used for the FDTD was $\sim 4 \text{ ns}$.

The discretization (or mesh size) was automatically determined by MWS when the transient solver was activated. In addition, an accuracy of -80dB was used for the absorbing boundary condition in the MWS transient solver simulations. An accuracy of -80dB is typically a good accuracy to use for a perfect matched layer in order to absorb electromagnetic waves [48].

Table 5 Summary of the models, numerical methods and mesh sizes (where applicable) used for each CEM software tool in the present study. Here FEM=Finite Element Method, MoM=Method of Moments, FDTD=Finite Difference Time Domain, MLFMM=MultiLevel Fast Multipole Method and SBR=Shooting and Bouncing Rays method.

Model	CEM S/W	Discretization (or Mesh) size Δ (m) or time size Δt (sec); and Mesh type	Method	Estimated Numerical error (NE) (from Figure 29) for finite discretization
Circular patch antenna; <i>includes free space radiation pattern and Directivity</i>	FEKO	$\lambda/20 < \Delta < \lambda/10$ Surface	MoM	$0.8 < NE < 2.5$
		$\lambda/20 < \Delta < \lambda/10$ Volume	FEM	
	MWS	$\Delta t = 3.686 \times 10^{-9}$ Volume	FDTD (Transient Solver) Accuracy at -80dB	
		$\Delta \sim \lambda/20$ Surface	Frequency Solver (MoM)	$NE \sim 0.8$
	Savant	N/A	N/A	N/A
Linear Array antenna; <i>includes, free space radiation patterns, Directivity, free space near field and free space mutual antenna-to-antenna coupling</i>	FEKO	$\lambda/20 < \Delta < \lambda/10$ Surface	MoM	$0.8 < NE < 2.5$
	MWS	N/A	Internal Array wizard	N/A
	Savant	N/A		N/A
Fitted (with mast structure) Linear array antenna ; <i>Includes fitted antenna radiation pattern, fitted near field, and fitted mutual antenna-to-antenna coupling</i>	FEKO	$\lambda/10 < \Delta < \lambda/5$ Surface	MLFMM (convergence $\sim 1 \times 10^{-3}$)	$2 < NE \leq 10$
	MWS	$\lambda/10 < \Delta < \lambda/5$ Surface	MLFMM (i.e. Integral Solver) (convergence $\sim 1 \times 10^{-3}$)	$2 < NE \leq 10$
	Savant	N/A	SBR	N/A

3.5.2.2 Round-off errors

For CEM software tools round-off errors could sidle into the simulated results. The real, (or complex) numbers in a computer are represented by certain number of bits, (i.e., single precision 32-bit, and double precision 64-bit). This can limit the smallest difference between two numbers that the computer recognizes. In general, for FDTD technique this is typically not a problem and single precision numbers can be used without reducing accuracy. However, for MoM technique, where matrices need to be inverted, the finite machine precision can become a problem for not well defined problems [48]. To minimise any round-off numerical errors for the FEKO simulations, which used the inversion of matrices, all simulations, were done using double precision accuracy. In addition, all simulations using the MLFMM (i.e., FEKO and MWS) converged steadily to its convergence of $\sim 1 \times 10^{-3}$ accuracy.

Another type of round-off numerical errors that can arise is due to the different simulation step sizes used in different simulations. This round-off type error became evident when comparing the free space linear array antenna radiation pattern between MWS and FEKO. There was a one degree difference in the antenna radiation pattern mainbeam look direction for the different antenna scan angle. This difference was most likely attributed to the different angle increment that was used in each CEM tool simulation, i.e., $\Delta\theta = \Delta\varphi = 5^\circ$ in FEKO compared to $\Delta\theta = \Delta\varphi = 1^\circ$ in MWS. The difference in angle step size affected how the CEM tool plotted the simulated results.

3.5.3 Model Errors

All antenna designs, mast structure, and antenna operational parameters for the present study, as mentioned previously, to the author's knowledge, are generic and do not duplicate any currently available or ship fitted system. In addition to the computer memory limitation, which governed the size of the model simulated, it was also intentional to initially assess the electromagnetic characterization of the sensors and mast structure on a small scale in order to understand the physics and science and to verify numerical simulations with theory. These small scale antenna and mast structure models can be built upon to increase the size and include more complexity in the antenna and mast structure models in any future work to replicate realistic ship systems.

3.5.3.1 Free space (without mast structure)

Errors can occur due to the models used in the CEM software tools. The main error due to the models, for the present study, is most likely, attributed to the circular patch and linear array antenna models. One way of determining the accuracy of the antenna model was to determine the resonance frequency of the antenna.

Figure 30 illustrates a typical simulated reflection coefficient S_{11} as a function of frequency (in GHz) for the antenna model using MWS.

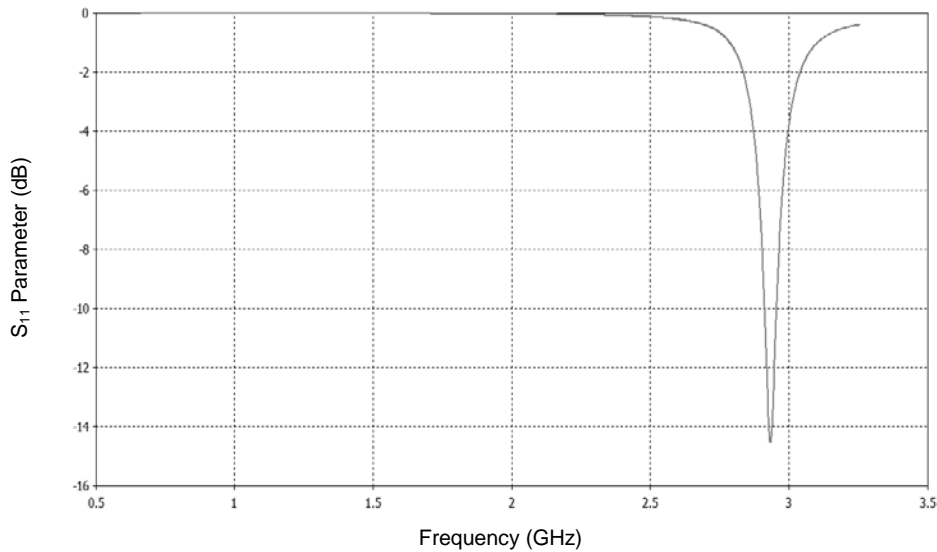


Figure 30. Reflection coefficient, S_{11} as a function of frequency (in GHz) for the antenna model using MWS.

As illustrated in Figure 30 the circular patch antenna model used for the present study has a resonant frequency $f \sim 2.96$ GHz, as should be expected. If there were any inaccuracies in the design of the antenna model then errors would be evident in the antenna's resonant frequency result. Furthermore, to mitigate any additional errors in the antenna model (i.e., single element antenna and linear array antenna models) used in the present analysis, comparisons were made of the simulated freespace antenna results (i.e., antenna radiation patterns, antenna beamwidths, antenna Directivity, linear array antenna average near field power density and mutual antenna-to-antenna coupling) with analytical results (or theory). This in turn provided an indication of the accuracy of the antenna model and the simulated numerical results.

3.5.3.2 Fitted (with mast structure)

For the fitted (i.e., with mast structure) simulations using numerical full wave solver techniques (i.e., FDTD, MLFMM and MoM) the mast structure size had to be reduced to include only the necessary parts of the mast structure. This reduction in mast structure was attributed mainly because of the limitations in the available computer memory. However, for the fitted simulations using Savant (i.e., SBR), which is an asymptotic (or high frequency) technique, modifications to mast structure model size due to computer memory availability was not an issue.

Furthermore, the limitations in the Savant simulations included; the approximation of the field amplitude and phases associated with using geometrical, physical theory of

diffraction ray tracing methods, errors associated with modeling the array antennas (linear array and single element array) assuming unity moments for each electric and magnetic dipoles and each frequency, and infinite substrate instead of a finite substrate. Errors in combining coherently the radiation pattern of transmit and receive antenna models, in particular in case where one antenna is orientated away from the other antenna.

3.5.4 Combined Estimated Errors

As a result of considering the above mentioned errors, (i.e., antenna model, finite discretization, and round-off errors) the mitigation strategies that were used, in the present study to minimize these errors, i.e, antenna model and round-off errors. It is reasonable to assert, that the error contributing significantly to the overall error in the simulated free space results using full wave solver techniques is the numerical error associated with the finite discretization size. Therefore, it is reasonable to assert that the overall error for the simulated freespace simulation results using full wave solver techniques can be estimated to $< \sim \pm 3\text{dB}$. The overall error for the asymptotic (or high frequency) technique (i.e., SBR) can be estimated to be $> \pm 3\text{dB}$, since full wave solvers are in general more accurate than asymptotic (or high frequency) techniques [48].

Similarly, for the fitted (i.e., fitted antenna radiation patterns, fitted near field and mutual antenna-to-antenna coupling) simulation results using full wave solver techniques the overall combined estimated error is $> \pm 3\text{dB}$, since the discretization (or mesh) size had to be made larger due to the computer constraints. The upper bound for the estimated error for the fitted simulation results using full wave solver techniques is $\sim \pm 10\text{dB}$. For the fitted simulated results using the asymptotic (or high frequency) SBR technique, the estimated error is $\geq \sim \pm 10\text{dB}$, given that full wave solvers are more accurate than asymptotic (or high frequency) techniques [48].

4 RESULTS AND DISCUSSION

4.1 CIRCULAR PATCH MICROSTRIP ANTENNA

4.1.1 Radiation Pattern

Figure 31 illustrates the free space antenna radiation pattern as a function of elevation θ , cut at azimuth $\varphi=0^\circ$ (or E plane field) for the linear polarized circular patch microstrip antenna, at an operating frequency of 2.96GHz. Similarly, **Figure 32** illustrates the free space antenna radiation pattern as a function of azimuth φ , cut at elevation $\theta=90^\circ$ (or H field plane) for the linear polarized circular patch microstrip antenna at an operating frequency of 2.96GHz. In both, **Figure 31** and **Figure 32**, comparisons are made, between the numerical and analytical results.

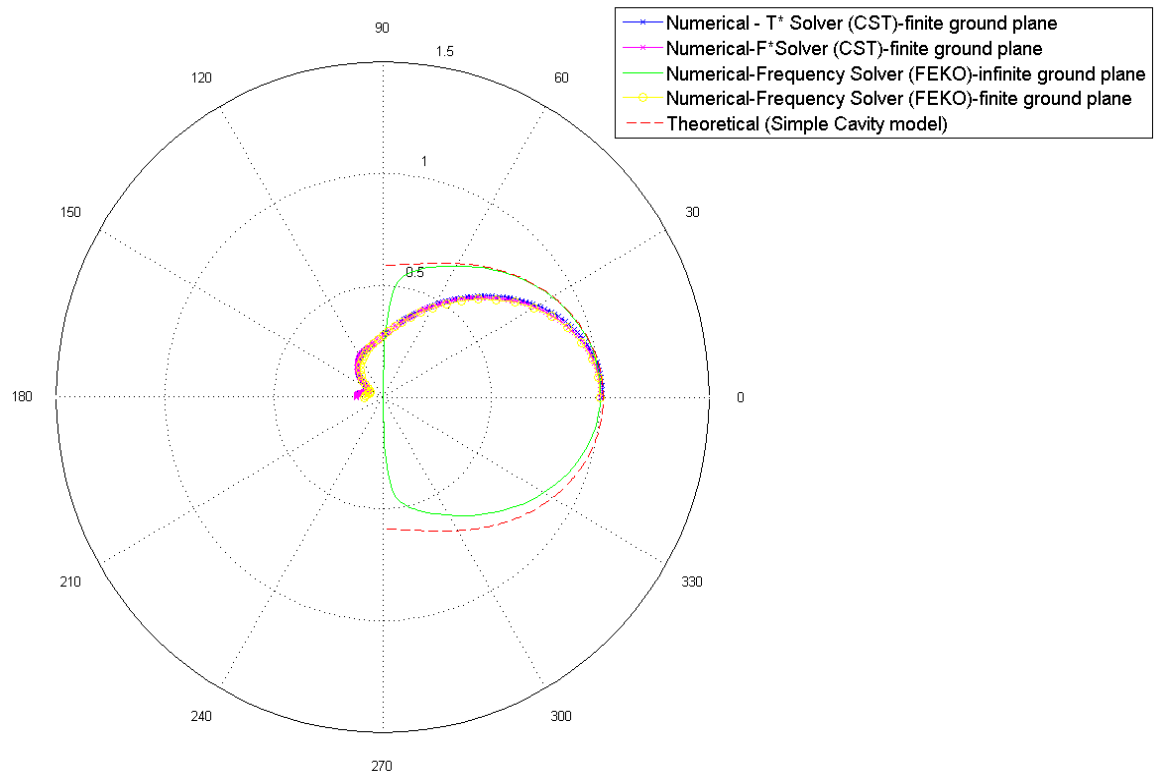


Figure 31. E_θ (or E plane) field as a function of elevation θ at azimuth $\varphi=0^\circ$ mode $n=1$ for linear polarized circular patch microstrip antenna.

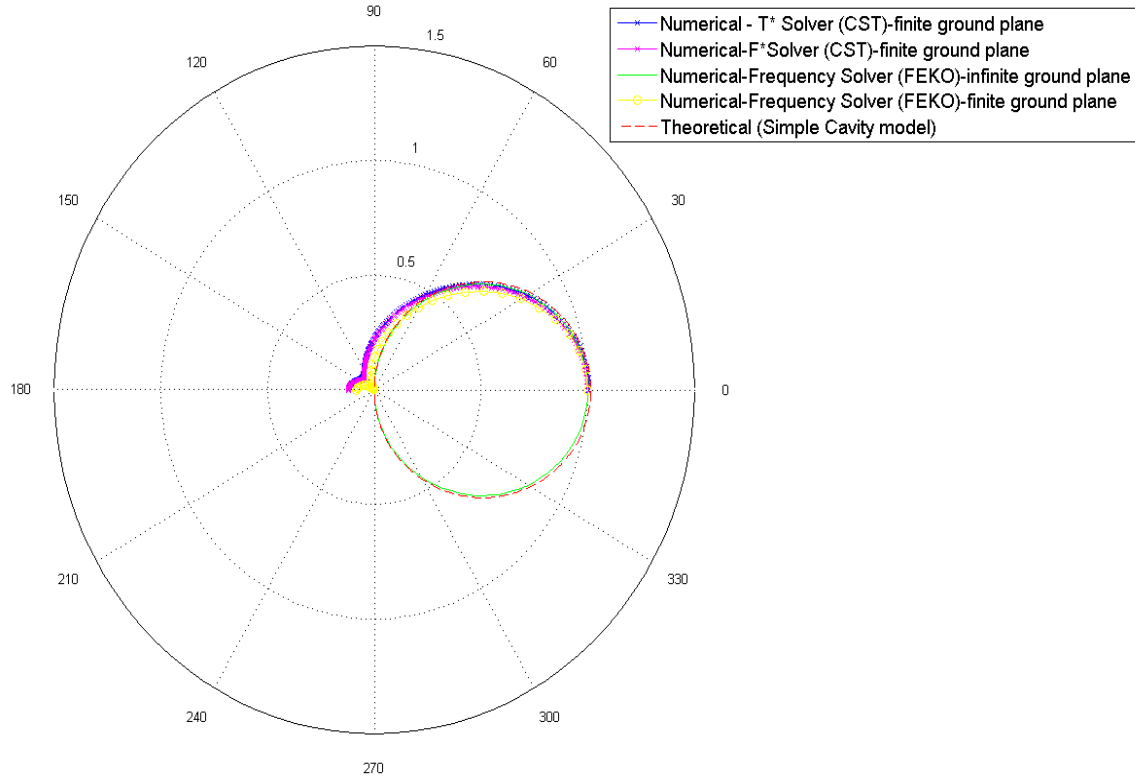


Figure 32 E_ϕ (or H plane) field as a function of elevation θ , cut at azimuth $\phi=90^\circ$, mode $n=1$ for linear polarized circular patch microstrip antenna.

As illustrated in **Figure 31**, as a first order approximation, the analytical (i.e., simple cavity model) E plane (or E_θ) field result is comparable with the numerical simulated E-plane field for a circular microstrip patch antenna. However, there is a difference between the analytical and numerical simulated E-plane field at the endfire, i.e., $\theta=90^\circ$, where the numerical simulated E-field results either goes to zero (i.e., FEKO -assuming infinite substrate and ground plane) or goes to zero with a backlobe (i.e., FEKO and MWS (or CST) assuming a finite substrate and ground plane), whereas the analytical E-plane field is non-zero. This non-zero E-plane field, at the endfire i.e., $\theta=90^\circ$, is as expected for a circular patch antenna using the simple cavity model, is most likely attributed to the limitations and assumptions of the simple cavity model associated with the truncation of the substrate and ground plane to the edge of the circular patch antenna. Since the substrate and ground plane influences the antenna radiation near the endfire direction [31].

As illustrated in **Figure 32** both the analytical and numerical simulated H plane (i.e., E_ϕ) field results show good agreement, except for the case for different substrate and ground planes. In the case of an infinite substrate and ground plane (i.e., numerical FEKO) the H plane field goes to zero at $\theta=90^\circ$, whereas, for a finite substrate and ground plane (i.e.,

numerical FEKO and MWS) radiation tends to zero but has a backlobe at $\theta \geq 90^\circ$. This result is as expected and the difference is attributed to the different assumptions made associated with the antenna model's substrate and ground plane. The analytical H-plane field result using the simple cavity model is comparable with the FEKO numerical simulated result assuming an antenna with an infinite substrate and ground plane. This would tend to suggest that, at least in the H-plane, the substrate and ground plane is assumed to be infinite in the simple cavity model.

Further assumptions can be made to the analytical simple cavity model or other models can be used (e.g. cavity model with source, modal expansion model, wire grid model and Green's function) to improve the analytical antenna model to characterize it more like the antenna model used in the CEM softwares. However, as a first approximation the comparison between numerical and analytical for the single element antenna provides a level of confidence in the results obtained by the computational electromagnetic software tools given the assumptions and approximations made within the software tools techniques (i.e., FEKO and Microwave Studio).

4.1.2 Directivity

To verify further, the single, element array, antenna model, the simulated Directivity D of the single element array antenna, was compared to, analytical calculation of directivity for a circular patch antenna.

Table 6 provides the numerical and analytical calculated directivity for a circular patch microstrip antenna. The simulated results (i.e., FEKO and CST) for the directivity was obtained for different assumptions of the antenna model, mainly regarding the ground plane (i.e., either infinite or finite), and for different numerical techniques (i.e., **Finite Element Method (FEM)**, **Method of Moments (MoM)** & **Finite Difference Time Domain (FDTD)**).

Table 6 Directivity D for a linear polarized circular patch microstrip antenna

Tool	Technique	Model Description	Directivity (D) (dB) $\theta=0^\circ$ (approx.)
FEKO	Numerical – Frequency Domain Solver	Infinite ground plane model of the antenna using MoM	6.4
	Numerical – Frequency Domain Solver	Finite ground plane model of the antenna using FEM	7.9

MWS (or CST)	Numerical – Frequency Domain Solver	Finite ground plane model of antenna using F* Solver (MoM)	8.1
	Numerical- Time Domain Solver	Finite ground plane model of antenna using T*Solver (FDTD)	8.0
MATLAB	Analytical	Bharl and Bhartia 1980 [30]	7.7

As presented in **Table 6** the simulated directivity D (i.e. 6.4dB (FEKO-MoM)), 7.9dB FEKO-FEM), 8.1dB (MWS-MoM) and 8.0dB (MWS-FDTD)) are within good agreement with analytical calculations (7.7dB). The slight difference in magnitude between simulated and analytical is due to assumptions made in the antenna models both CEM S/W model and analytical equation. It is interesting to note that in the case where an infinite ground plane was assumed the directivity was much lower (i.e., 6.4dB) compared to the analytical result (7.7dB). This implies that there is some loss in the amount of energy directed into the main beam of the antenna, which suggests that a finite ground plane compared to an infinite ground plane improves the directivity of energy for an antenna.

4.2 LINEAR ARRAY ANTENNA

4.2.1 Radiation Pattern

4.2.1.1 Free space and Fitted Radiation Pattern in elevation θ , cut at azimuth= 0° - Antenna Fitted Front Panel of Mast structure

Figure 33 illustrates the normalized free space and fitted antenna radiation patterns as a function of elevation θ , cut at azimuth $\varphi=90^\circ$ for the 4x1 linear array antenna with scan angle $\theta=0^\circ$, for different antenna to mast structure front panel separations (i.e., $\lambda/4$ m and 0.113m). For the fitted antenna radiation patterns the linear array is located at a vertical height $h \sim 0.740$ m, from the base of the mast structure. Free space 3-D antenna radiation patterns for the 4x1 linear array were also obtained in each of the different computational electromagnetic software tools, (i.e., FEKO and MWS and Savant) and are illustrated in **Figure 77** in **Appendix A.1**.

It needs to be noted here that all antenna radiation patterns, both in elevation and azimuth, figures presented in the proceeding sections in this chapter, Chapter 4, have all been normalized to each of their own respective maximum electric field magnitude.

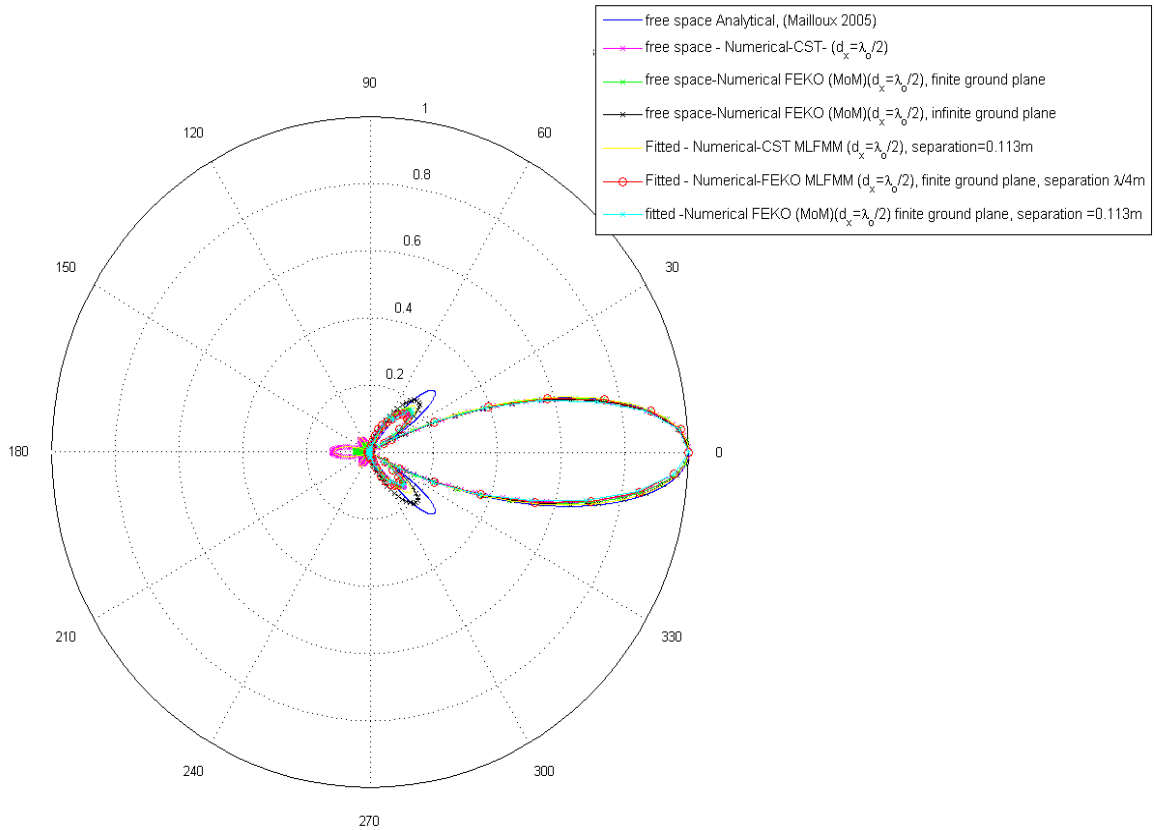
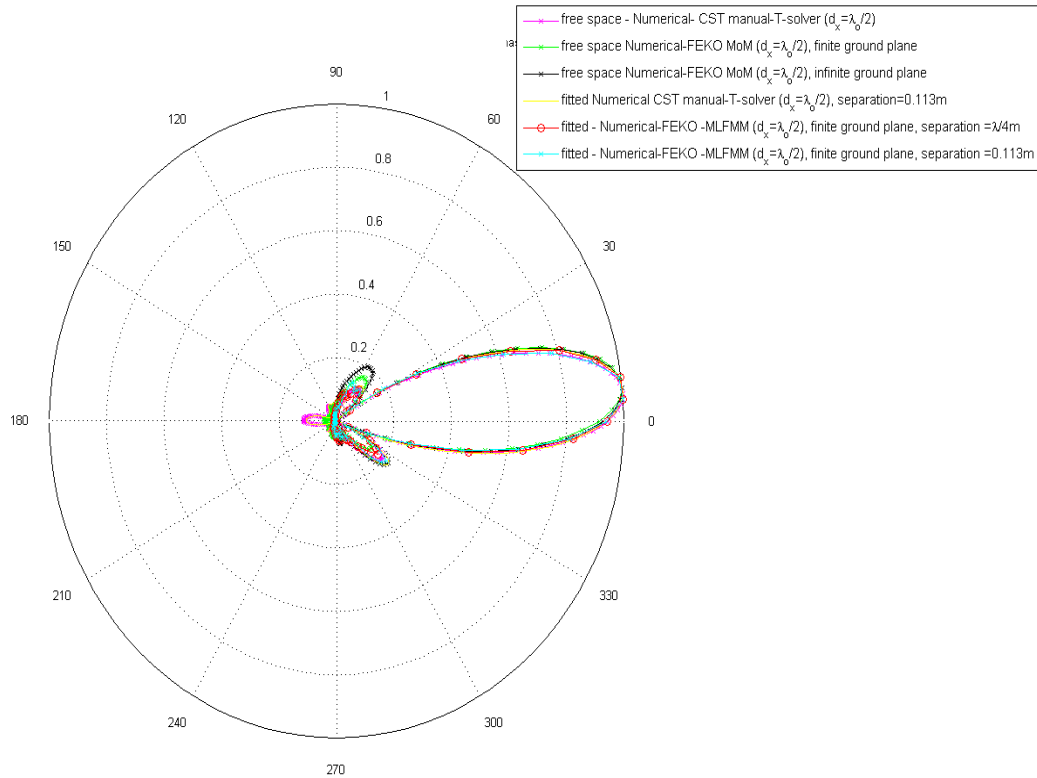


Figure 33. Normalized free space and fitted radiation pattern as a function elevation θ , cut at azimuth $\varphi=0^\circ$ for 4x1 linear array antenna with uniform illumination, for an antenna scan angle $\theta=0^\circ$. Fitted antenna radiation pattern assumed antenna was located at a vertical height $h \sim 0.740\text{m}$ from the base of the mast structure, front panel, and positioned at different distances from the mast structure's front panel (i.e., 0.113m and $\lambda/4\text{m}$)

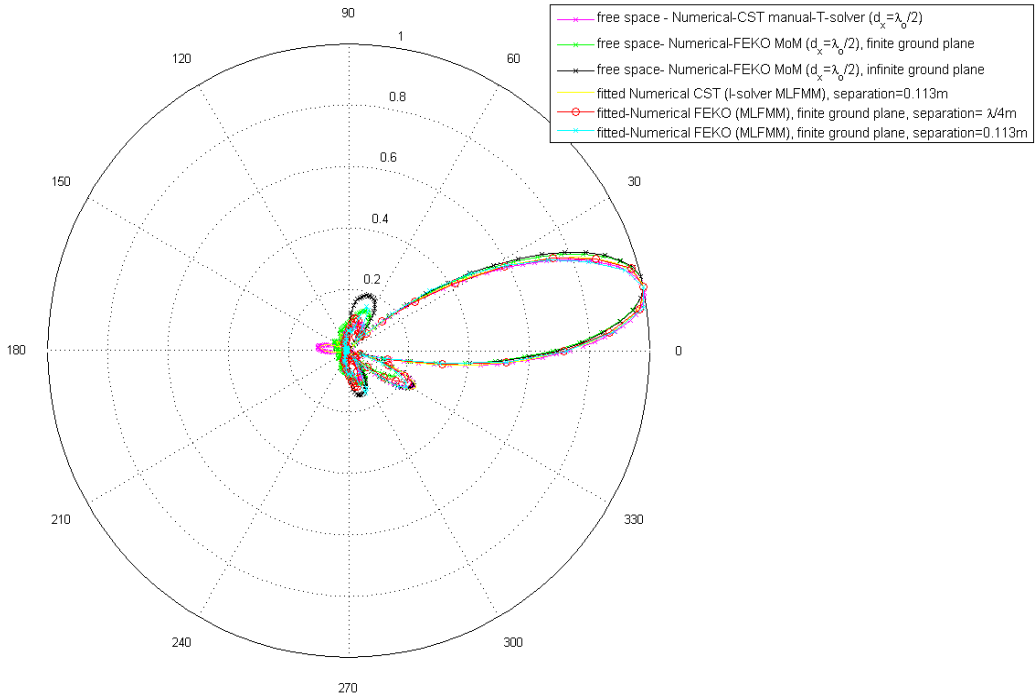
As illustrated in **Figure 33** there is overall good agreement in the normalized free space antenna radiation pattern between numerical (or simulated) and analytical results. However, there is some difference in the radiation pattern in the sidelobes, where the sidelobes of the analytical result (i.e., Mailloux 2005 [31]) of the antenna radiation pattern is higher than the simulated results (i.e., FEKO and MWS (or CST)). In addition, the antenna radiation for the numerical simulation results shows a non-zero backlobe whereas the analytical result shows a zero backlobe. These differences, are most likely attributed to the assumptions made in the linear array model in the analytical and in the numerical techniques. The numerical simulations assumed a circular patch microstrip linear array with a finite ground plane, whereas the theory used for the analytical results assumed just a generic linear array antenna and with no ground plane. Furthermore, as illustrated in **Figure 33**, overall the fitted linear, array antenna, radiation pattern is comparable with the free space antenna, radiation pattern, for both antenna to mast separations of $\lambda/4\text{m}$ and 0.113m . This would indicate that at least in elevation θ , and cut

at an azimuth $\varphi=0^\circ$, and at different separation between antenna from mast structure, there is no significant interference between the antenna and mast structure to cause any significant increase in antenna radiation pattern sidelobes to affect the antenna's radiation pattern main beam.

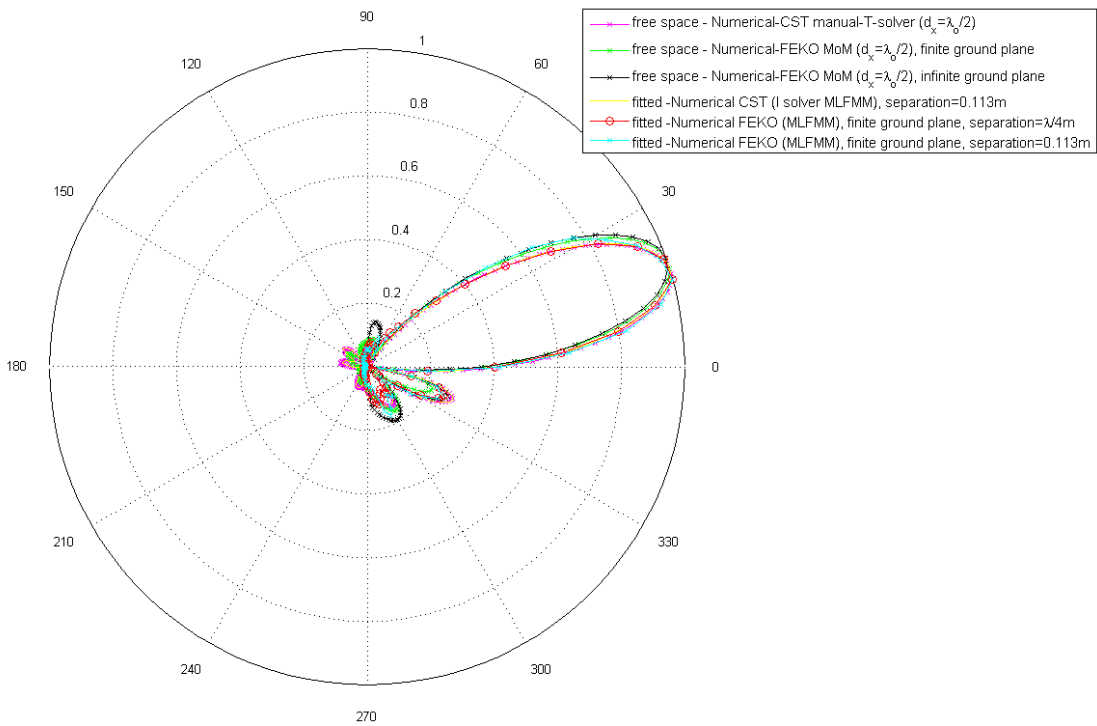
Figure 34 illustrates the normalized free space and fitted antenna radiation pattern as a function of elevation θ , cut at azimuth $\varphi=0^\circ$ for different antenna scan angles (i.e., $\theta \sim 5^\circ, \sim 11^\circ$ and $\sim 18^\circ$) for the linear array and different antenna-to-mast separations (i.e., $\lambda/4\text{m}$ and 0.113m). In particular, **Figure 34 (a)** illustrates the antenna radiation pattern as a function of elevation θ , cut at azimuth $\varphi=0^\circ$ for an antenna scan angle $\theta \sim 5^\circ$. **Figure 34 (b)** illustrates the antenna radiation pattern as a function of elevation θ , cut at azimuth $\varphi=0^\circ$ for an antenna scan angle $\theta \sim 11^\circ$ and **Figure 34 (c)** illustrates an antenna radiation pattern as a function of elevation θ , cut at azimuth $\varphi=0^\circ$ for an antenna scan angle $\theta \sim 18^\circ$.



(a)



(b)



(c)

Figure 34 Normalized free space and fitted far field radiation pattern for linear polarized 4x1 circular patch linear array antenna as a function of elevation θ , cut at

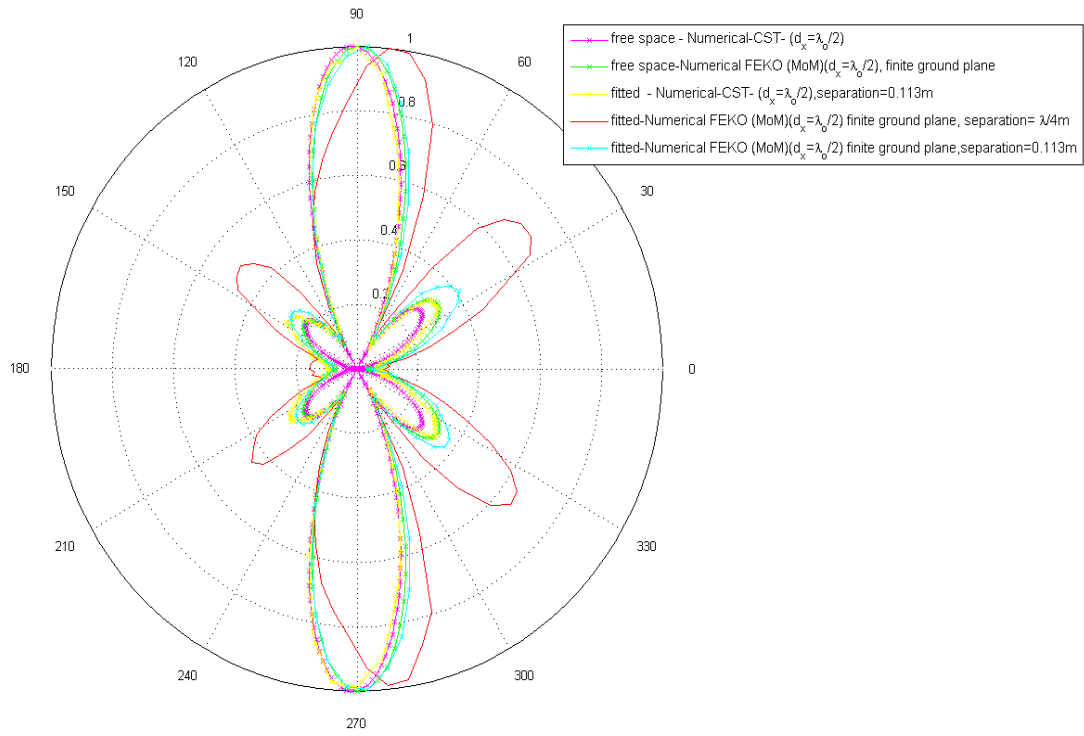
azimuth $\varphi=0^\circ$, with uniform illumination for different 4x1 linear array antenna electronic scan angles, (a) $\theta\sim 5^\circ$, (b) $\theta\sim 11^\circ$ and (c) $\theta\sim 18^\circ$. For the fitted antenna radiation pattern the antenna was assumed to be located at a vertical height $h\sim 0.740\text{m}$ from the base of the mast structure, and positioned at different distances from the mast structure's front panel (i.e., 0.113m and $\lambda/4\text{m}$).

As illustrated in **Figure 34** there is overall good agreement in the free space and fitted antenna radiation patterns for different antenna to mast separations using different CEM techniques, at each different antenna scan angle. However, there are some differences in the sidelobes of the antenna radiation pattern at each of the antenna scan angle, whereby, as the antenna scan, angle increases there is an elevation in one of the sidelobes and a decrease in the other sidelobe. This is most likely due to interference between the antenna radiation and mast structure. However, this interference does not appear to be so significant to cause any major impact on the antenna radiation mainbeam.

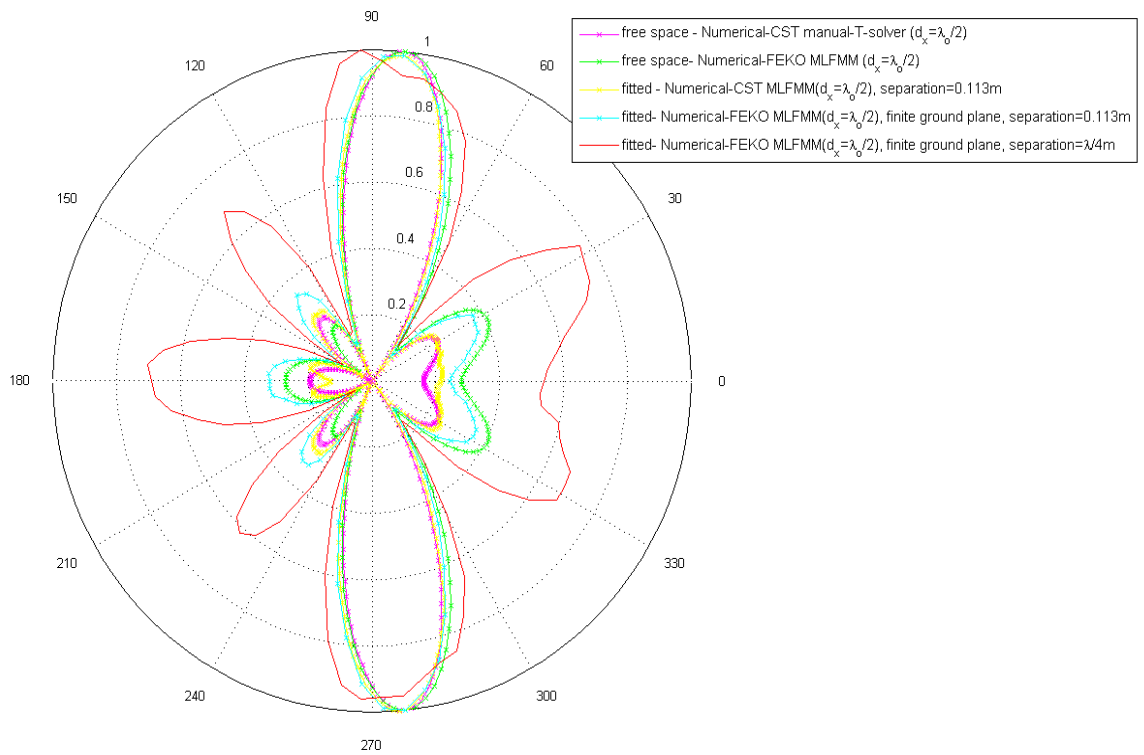
It is interesting to note that there are some slight differences in the look direction of the antenna mainbeam between the FEKO and MWS results at different antenna scan angles. That is for an antenna scan angle of 5° in FEKO in MWS (or CST) it measured 6° , for an antenna scan angle of 11° in FEKO, it was measured 12° and an antenna scan angle of 18° in FEKO it was measured to be 19° . This discrepancy, is most likely attributed to, the angle increments used for the simulations in each of the CEM software tool. For example in MWS the angle increment was 1° in each simulation, whereas the angle increment used for the FEKO simulation was 5° . From here on each antenna scan angle will be described as follows; for antenna scan angle $5/6^\circ$ will be $\sim 5^\circ$, for $11/12^\circ$ as $\sim 11^\circ$ and $18/19^\circ$ as $\sim 18^\circ$.

4.2.1.2 Free space and Fitted Radiation Pattern in azimuth φ , cut at elevation $\theta=90^\circ$ - Antenna Fitted Front Panel of Mast structure

Figure 35 illustrates the normalized free space and fitted radiation patterns for 4x1 linear array antenna as a function of azimuth φ , cut at elevation $\theta=90^\circ$, for different antenna scan angles (i.e., $\theta=0^\circ, \sim 5^\circ, \sim 11^\circ$ and $\sim 18^\circ$). **Figure 35 (a)** illustrates the antenna radiation patterns for an antenna scan angle $\theta=0^\circ$, **Figure 35 (b)** illustrates the antenna radiation patterns for an antenna scan angle $\theta\sim 5^\circ$, **Figure 35 (c)** illustrates the antenna radiation patterns for an antenna scan angle $\theta\sim 11^\circ$ and **Figure 35 (d)** illustrates the antenna radiation patterns for an antenna scan angle $\theta\sim 18^\circ$. The linear array antenna is assumed to be located at a vertical height $h\sim 0.740\text{m}$ from the base of the mast structure and positioned at different distances (i.e., 0.113m and $\lambda/4\text{m}$) from the mast structure's front panel.



(a)



(b)

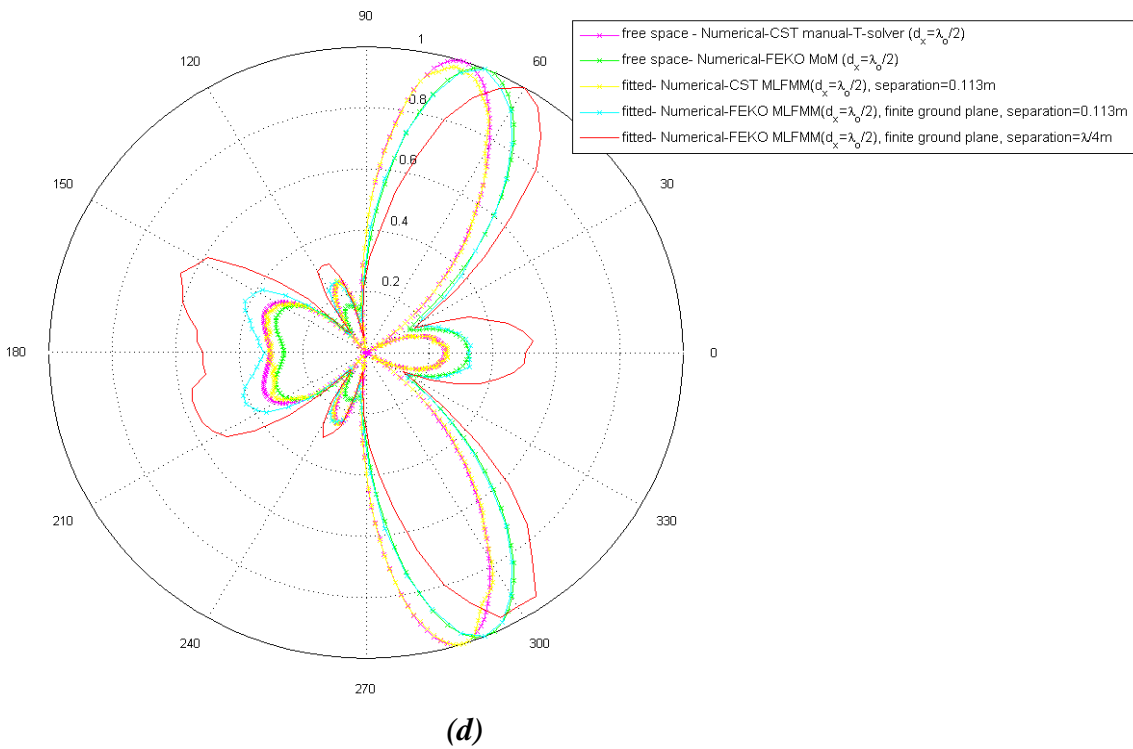
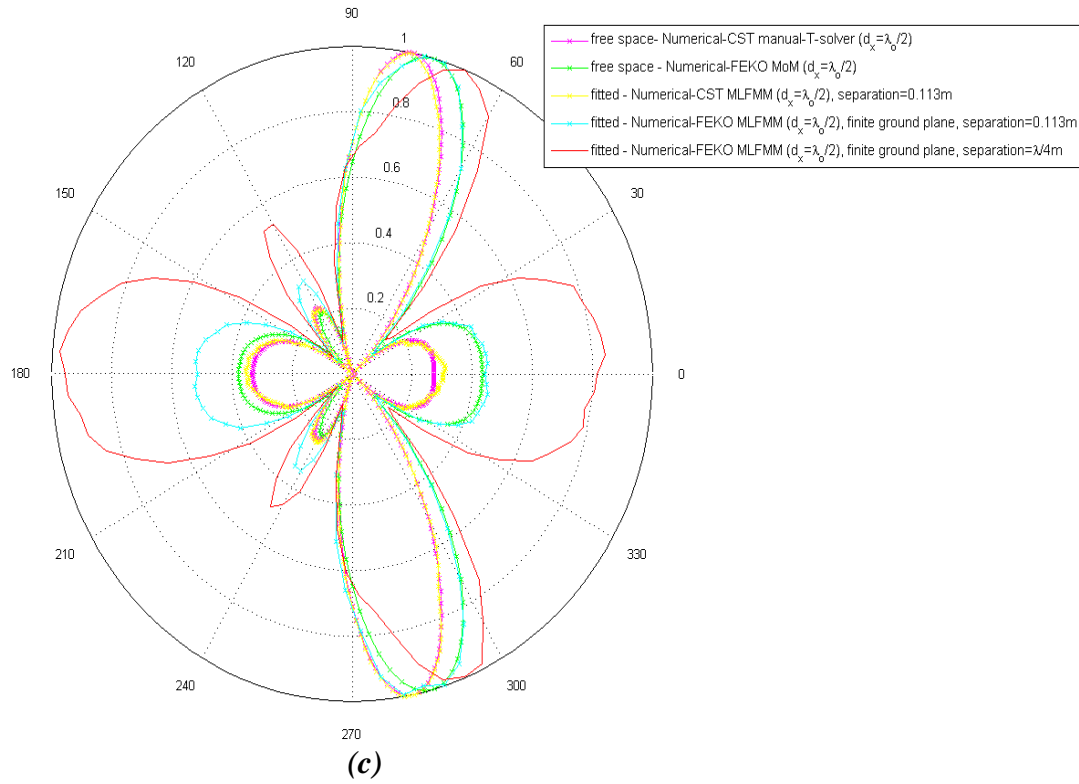


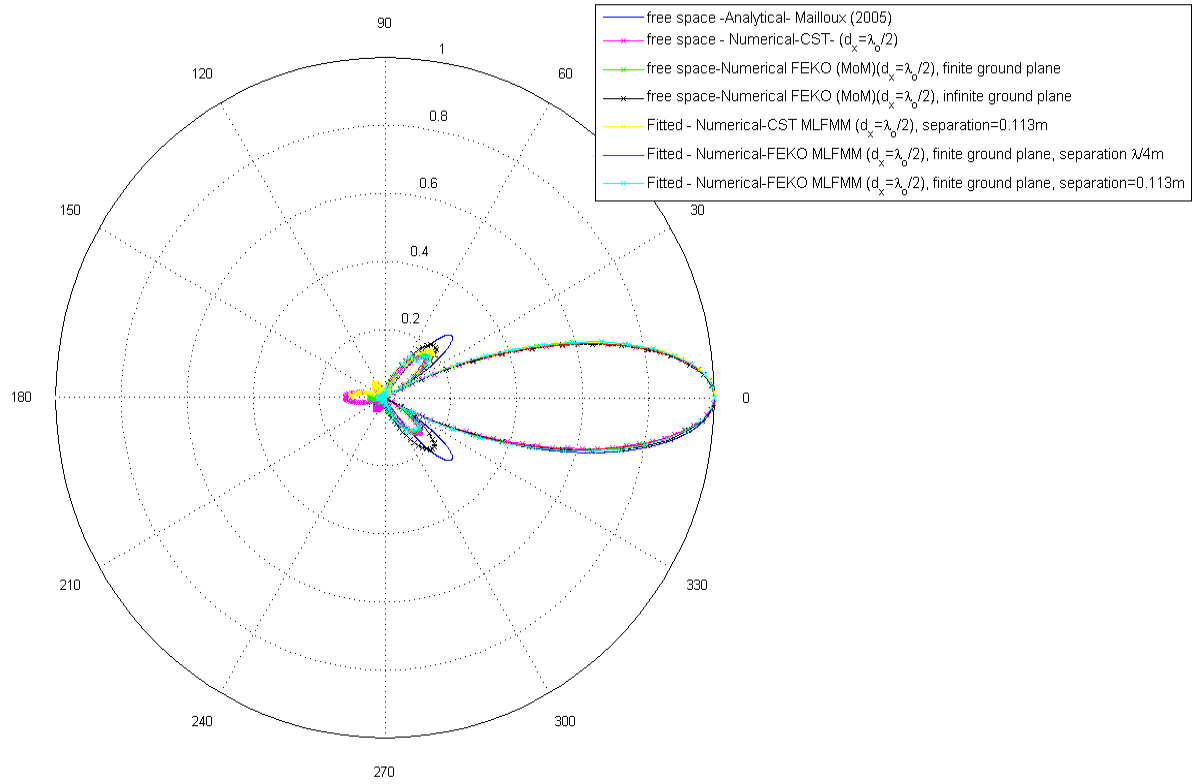
Figure 35. Normalized free space and fitted far field radiation pattern for 4x1 linear array antenna as a function of azimuth φ , cut at elevation $\theta=90^\circ$, for different 4x1

linear array antenna scan angles. (a) scan angle $\theta=0^\circ$, (b) scan angle $\theta\sim 5^\circ$, (c) scan angle $\theta\sim 11^\circ$ and (d) scan angle $\theta\sim 18^\circ$. For the fitted radiation pattern the 4x1 linear array antenna is located at a vertical height $h\sim 0.740\text{m}$ from the base of the mast structure and positioned at different distances from the mast structure's front panel (i.e., 0.113m and $\lambda/4\text{m}$)

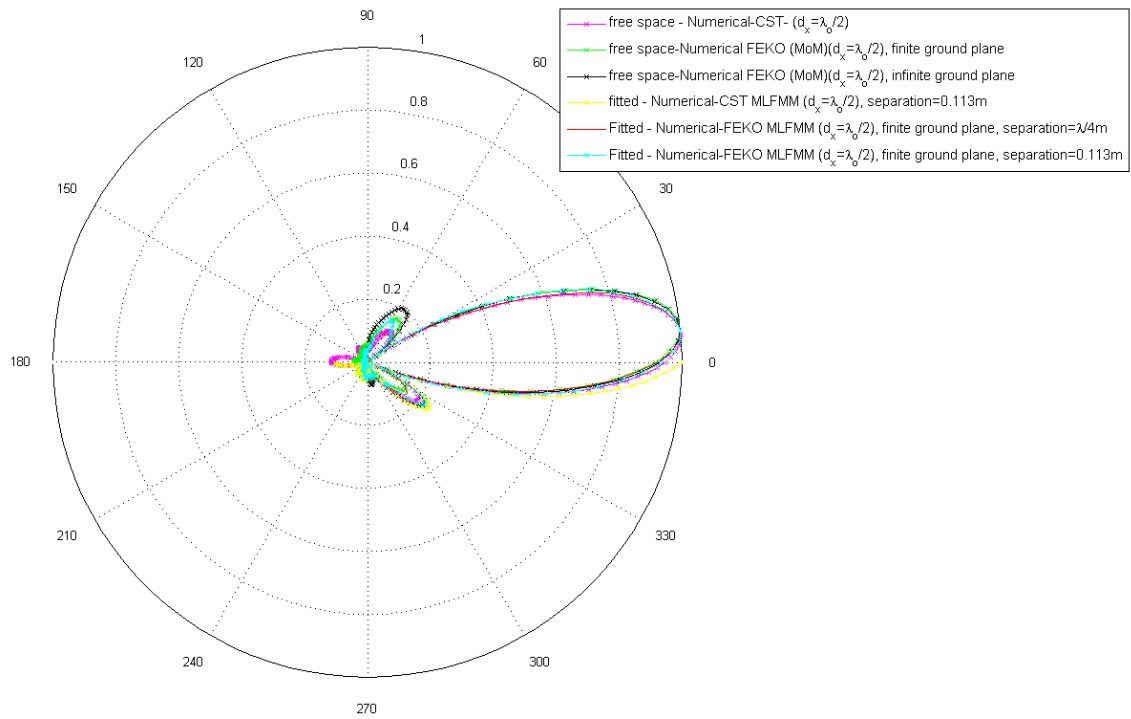
As illustrated in **Figure 35 (a)** to **Figure 35 (d)**, there is a significant elevation in the fitted antenna radiation pattern in azimuth φ , cut at elevation $\theta=90^\circ$, sidelobes, for each of the different antenna scan angles (i.e., $\theta=0^\circ$, $\theta\sim 5^\circ$, $\theta\sim 11^\circ$ and $\theta\sim 18^\circ$) compared to the free space antenna radiation pattern in azimuth φ , cut at elevation $\theta=90^\circ$. This elevation in the sidelobes is significant enough that it has elevated and altered the antenna radiation, pattern mainbeam. For example, the fitted antenna radiation pattern main beam is affected in that the direction of the antenna mainbeam is altered. For example, for antenna scan angle $\theta=18^\circ$ the antenna radiation pattern mainbeam is directed along azimuth angle $\varphi\sim 45^\circ$, in free space, compared to $\varphi\sim 50^\circ$ for the fitted antenna. Furthermore, there also appears to be significant impact in the fitted antenna, radiation pattern in azimuth φ for different antenna separation from the mast structure's front panel. When the antenna is placed closer to the mast structure (i.e., from 0.113m to $\lambda/4\text{m}$) there is a significant elevation in the antenna's radiation pattern sidelobes, thus impacts the antenna radiation mainbeam. This suggests that there is significant interference between the antenna and mast structure in azimuth φ . This interference, is most likely attributed to the mutual coupling between the perfect electrical conducting material surfaces of the antenna's ground plane and the mast structure.

4.2.1.3 Free space and Fitted Radiation Pattern in elevation θ , cut at azimuth $\varphi=0$ degrees-Antenna fitted Side-Panel of Mast Structure

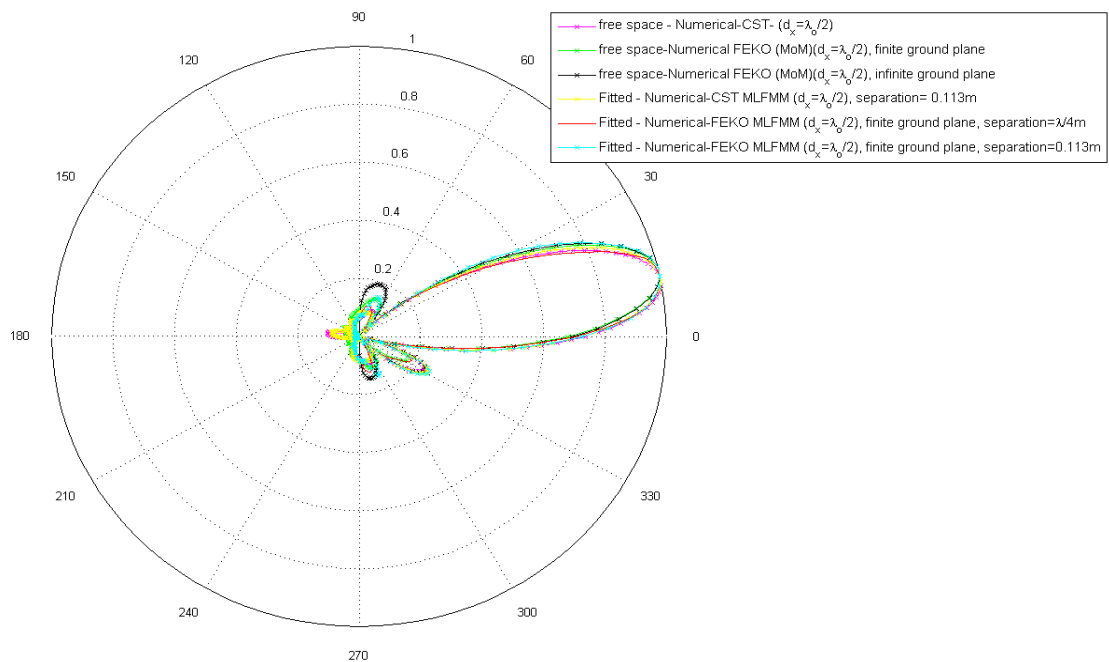
Figure 36 illustrates the normalized free space and fitted antenna radiation patterns for the 4x1 linear array as a function of elevation θ , cut at azimuth $\varphi=0^\circ$ for different antenna scan angles (i.e., $\theta=0^\circ$, $\theta\sim 5^\circ$, $\theta\sim 11^\circ$ and $\theta\sim 18^\circ$) and different antenna separations (i.e., 0.113m and $\lambda/4\text{m}$) from the mast structure's sidepanel. **Figure 36 (a)** illustrates the antenna radiation patterns for antenna scan angle $\theta=0^\circ$, **Figure 36 (b)** illustrates the antenna radiation patterns for antenna scan angle $\theta\sim 5^\circ$, **Figure 36 (c)** illustrates the antenna radiation patterns for antenna scan angle $\theta\sim 11^\circ$ and **Figure 36 (d)** illustrates the antenna radiation patterns for antenna scan angle $\theta\sim 18^\circ$.



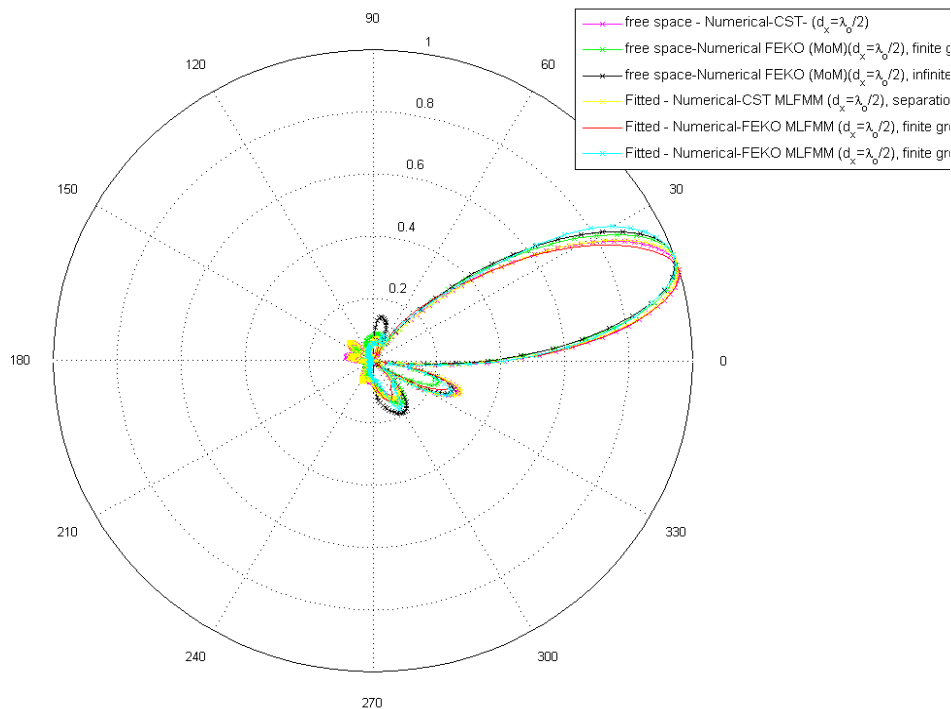
(a)



(b)



(c)



(d)

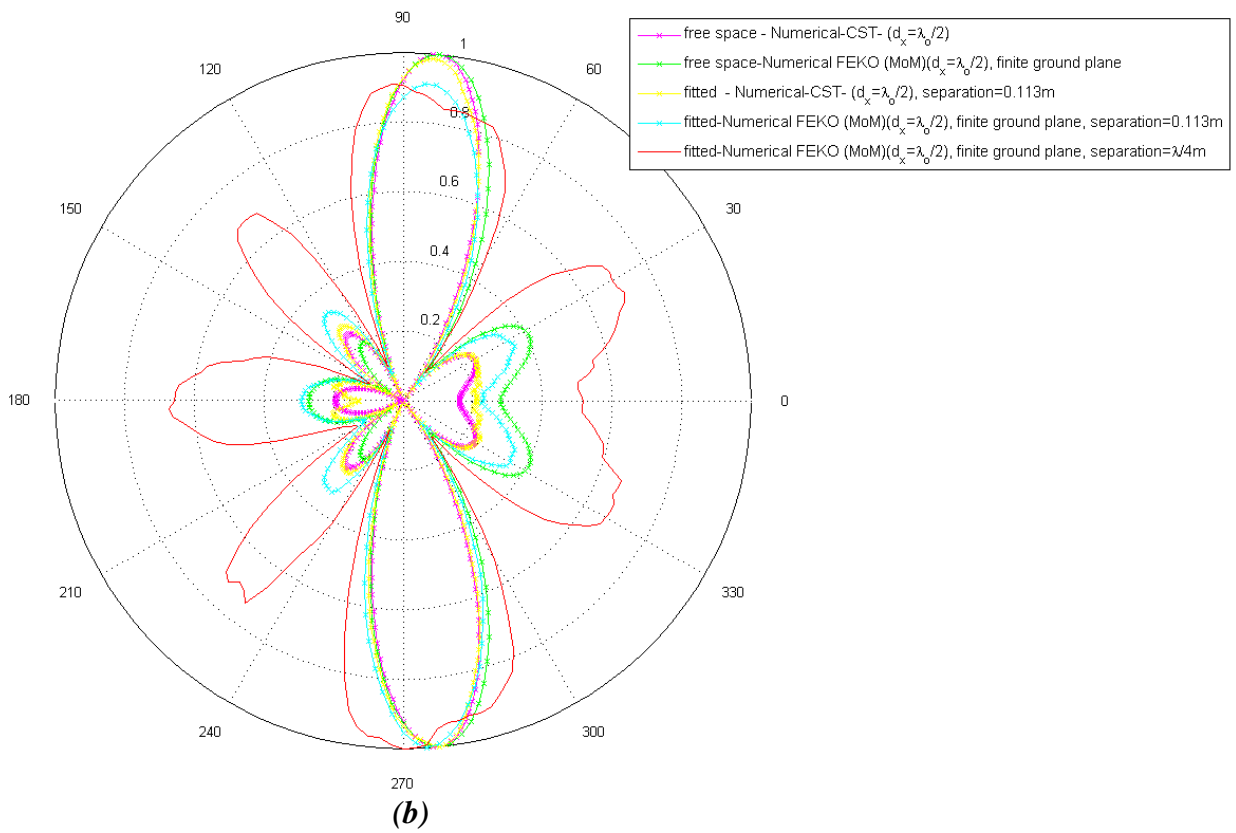
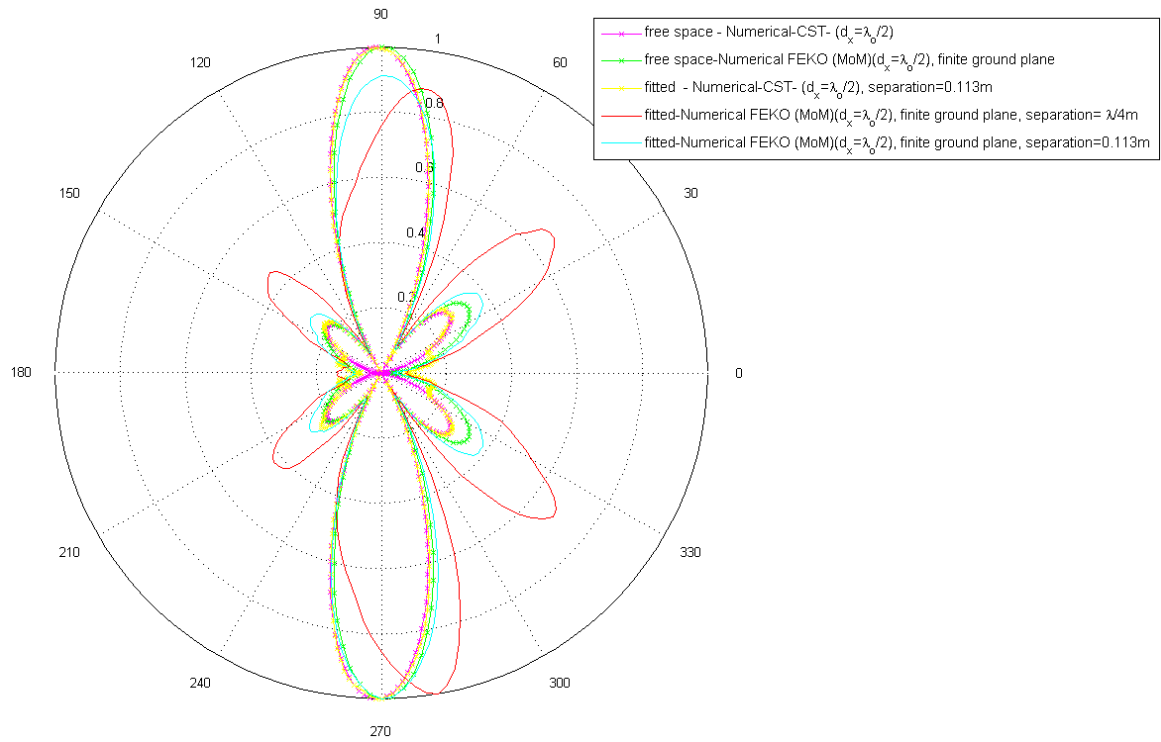
Figure 36. Normalized free space and fitted antenna radiation pattern for linear polarized 4x1 circular patch linear array as a function of elevation θ , cut at azimuth

$\varphi=0^\circ$ for different antenna scan angles θ , (a) $\theta=0^\circ$, (b) $\theta\sim 5^\circ$, (c) $\theta\sim 11^\circ$ and (d) $\theta\sim 18^\circ$. For the fitted antenna radiation pattern the antenna is located at a vertical height $h\sim 0.782\text{m}$ from the base of the mast structure sidepanel and positioned at different distances (i.e., 0.113m or $\lambda/4\text{m}$) from the surface of the mast structure's sidepanel.

As illustrated in **Figure 36 (a)** to **Figure 36 (d)** there is good agreement between the different numerical (i.e., FEKO and MWS) simulated results in the free space and fitted antenna radiation patterns in elevation θ , cut at an azimuth $\varphi=0^\circ$. However, there are differences in the levels of the antenna fitted radiation pattern sidelobes compared to free space antenna radiation, pattern sidelobes. The fitted antenna radiation, pattern sidelobes are either elevated on one side or decreased on the other, compared to the free space antenna radiation, pattern sidelobes. This is, as mentioned previously, is most likely attributed to the mutual interference between antenna radiation and the mast structure. However, there are some differences in the fitted antenna radiation, pattern mainbeam appearance at different antenna separations from the mast structure sidepanel. For example, an antenna separation of $\lambda/4\text{m}$ from the mast structure sidepanel, the fitted antenna radiation, pattern mainbeam has a reduced beamwidth compared to the fitted antenna radiation pattern mainbeam beamwidth when the antenna, is positioned further away (0.113m) from the mast structure sidepanel. This difference, could be attributed to the increment size used in each of the CEM simulations. For example in MWS (or CST) a 1° increment was used in the simulation, whereas in FEKO a 5° increment in angle was used in the simulations.

4.2.1.4 Free space and Fitted Radiation Pattern in azimuth φ , cut at elevation $\theta=90$ degrees - Antenna fitted Side Panel of Mast Structure

Figure 37 illustrates the normalized free space and fitted radiation patterns of a 4×1 linear array as a function of azimuth φ , cut at elevation $\theta=90^\circ$, for different antenna scan angles (i.e., $\theta=0^\circ$, $\sim 5^\circ$, $\sim 11^\circ$, $\sim 18^\circ$) and positioned at different distances (i.e., 0.113m and $\lambda/4\text{m}$) from the mast structure sidepanel. **Figure 37 (a)** illustrates the antenna radiation patterns for antenna scan angle $\theta=0^\circ$, **Figure 37 (b)** illustrates the antenna radiation patterns for antenna scan angle $\theta\sim 5^\circ$, **Figure 37 (c)** illustrates the antenna radiation patterns for antenna scan angle $\theta\sim 11^\circ$ and **Figure 37 (d)** illustrates the antenna radiation patterns for antenna scan angle $\theta\sim 18^\circ$.



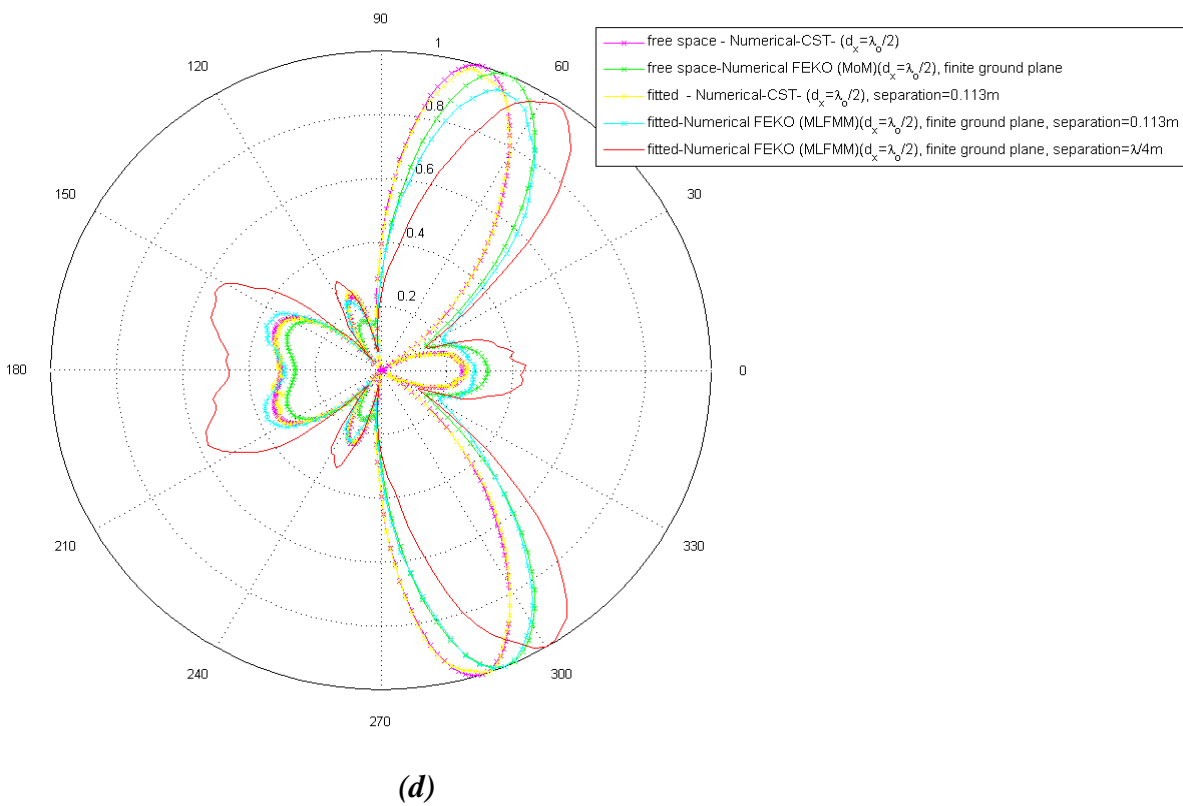
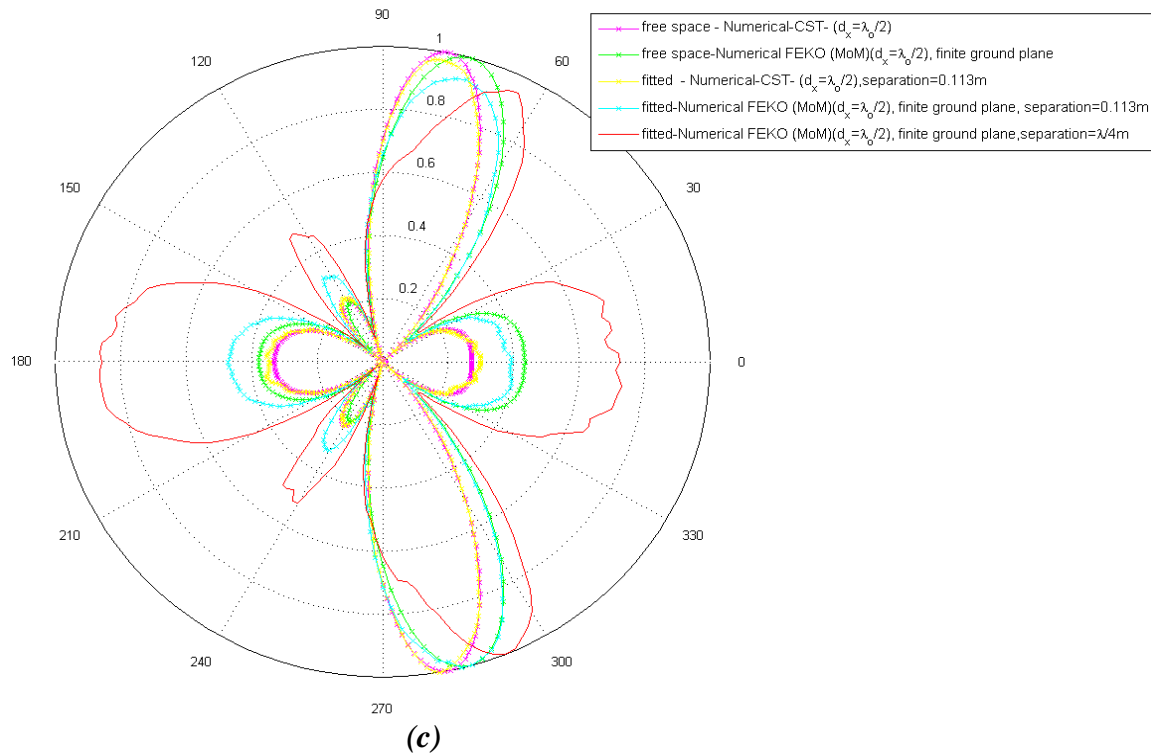


Figure 37. Normalized free space and fitted antenna radiation pattern for 4x1 linear array as a function of azimuth ϕ , cut at elevation $\theta=90^\circ$, for different 4x1 linear

array antenna scan angles. (a) $\theta=0^\circ$, (b) $\theta\sim 5^\circ$, (c) $\theta\sim 11^\circ$ and (d) $\theta\sim 18^\circ$. For the fitted antenna radiation pattern the antenna was located at a vertical height $h\sim 0.782\text{m}$ from the base of the mast structure sidepanel and positioned at different distances (i.e., 0.113m and $\lambda/4\text{m}$) from the mast structure's sidepanel.

Similarly, for the case where the antenna, is located at the front panel facet of the mast structure, as illustrated in **Figure 37 (a)** to **Figure 37 (d)**, when the antenna is located on the sidepanel of the mast structure, as the linear array antenna scan angle, θ increases from 0° to $\sim 18^\circ$ the fitted radiation pattern of the 4×1 linear array antenna in azimuth is affected by the mast structure, where the side lobes are elevated significantly to have an impact on the antenna's main beam, whereby the mainbeam profile and look direction in azimuth are altered. For example, for antenna scan angle $\theta\sim 18^\circ$ the antenna mainbeam is directed at angle $\varphi\sim 45^\circ$, in free space compared to $\varphi\sim 50^\circ$, fitted on the mast. Furthermore, there also appears to be significant impact in the fitted antenna radiation pattern in azimuth for different antenna separation from the front panel of the mast. As the antenna is mounted closer to the mast structure (from 0.113m to $\lambda/4\text{m}$) there is a significant elevation in the antenna's radiation pattern sidelobes, impacting the fitted antenna's mainbeam. For example, the antenna's mainbeam look direction in freespace is $\varphi\sim 45^\circ$ compared to $\varphi\sim 60^\circ$ for a fitted antenna located at a distance $\lambda/4\text{m}$ from the mast structure sidepanel. This suggests that there is significant interference between the antenna and mast structure in azimuth that the antenna's radiation energy is reflected off the mast structure and re-directed, most likely due to the interference between the two perfect electrical conducting surfaces of the antenna ground plane and the mast structure.

4.2.2 Linear Array Antenna Beamwidths

Table 7 provides the beamwidth of the 4×1 linear array antenna using different antenna models and computational techniques. The freespace, antenna radiation patterns used to determine the antenna beamwidths, presented in **Table 7**, are illustrated in **Appendix A**, Section A.1 by **Figure 78**, **Figure 79**, **Figure 81** and **Figure 82**.

Table 7 Beamwidth of the 4×1 linear array antenna using different techniques for the freespace, antenna radiation pattern. Free space antenna radiation patterns used to determine the beamwidths are provided in Appendix A, Section A.1.

Model & Technique	Antenna beamwidth ($^\circ$)
Analytical (Mailloux 2005 [32])	~ 37
FEKO (MoM)	~ 35

MWS (or CST) (internal array wizard using single element array radiation pattern using FDTD)	~34
Savant (current source SBR)	~32

As shown in **Table 7** there is very good agreement between the numerical and analytical antenna beamwidths for the 4x1 linear array. The antenna beamwidths from the simulated antenna radiation pattern using MWS and FEKO (i.e., $\sim 35^\circ$) are in better agreement with the analytical (i.e., beamwidth $= 37^\circ$) antenna beamwidth than the antenna beamwidth from the simulated antenna radiation pattern using Savant (i.e., 32°). This would be, as expected, since full wave solver techniques, such as MoM and FDTD, tend to be more accurate compared to asymptotic (or high frequency) techniques. However, as a first order approximation, there is good agreement in antenna beamwidths between the numerical techniques and analytical results. Any difference in the antenna beamwidths would be attributed to the different approximations in each of the simulation tools and the antenna model. Overall, this good agreement in the antenna beamwidths provide some level of confidence in the 4x1 linear array antenna model used in each of the CEM software tools.

4.2.3 Linear Array Antenna Directivity

Table 8 provides the Directivity D for a 4x1 linear array antenna, assuming omnidirectional elements, each array element amplitude having the same weighting (i.e., $a_n = 1$), in phase, and an array scan angle from endfire, $\theta = 0$.

Table 8 Directivity for a 4x1 Linear array assuming omnidirectional elements at array scan angle from endfire, $\theta = 0$.

Technique	Linear array Directivity D (dB)
Numerical -FEKO (4x1 linear array model)	~13
Numerical MWS (or CST, using the internal array functionality)	~14
Analytical	~12

(Mailloux 2005) [32]	
----------------------	--

As presented in **Table 8** the numerical simulated directivity D using FEKO and MWS (i.e., ~13dB and ~14dB) for the 4x1 linear array antenna is comparable with the analytical (i.e., Mailloux 2005 [32]) directivity D (i.e., ~12dB) result. However, the directivity D using MWS (i.e., ~14dB) is larger in comparison to the simulated numerical directivity using FEKO (i.e., ~13dB) and the analytical (~12dB). This difference could be that the 4x1 linear array antenna in MWS was modeled by using MWS's internal functionality, which determined the linear array antenna radiation pattern by using the antenna radiation pattern of a single element of the linear array, whereas for FEKO the directivity was calculated using an actual 4x1 linear array antenna model. Overall, as a first order approximation, the good agreement between simulated numerical and analytical determination of the directivity D provides some level of confidence in the 4x1 linear array antenna model and the simulated results from each of the CEM software tool.

4.2.4 Near Field Power Density

4.2.4.1 Free Space Near Field Power Density

To verify numerical simulated near field power density for the 4x1 linear array antenna model used in the present study, the normalized free space near field power density was calculated in FEKO, at a distance $R=0.75\text{m}$ away from the antenna, and then to compared to the estimated average near field power density using theory from Faraone *et al.* 2000 [35] and the APD Program [36]. **Table 9** presents the simulated and analytical average near field power density results.

Table 9 Averaged free space near field power density simulated and analytical for 4x1 linear array antenna at distance from antenna $R=0.75\text{m}$ in free space at antenna along boresight. Here antenna wavelength $\lambda=0.10135\text{m}$ and antenna Gain (G) ~ 14.45 .

Technique	Average near field Power density (dBW/m ²)	Description
Analytical	≈ -2.95	Faraone <i>et al.</i> 2000 [35] (assume antenna efficiency=1.0)
Analytical	≈ -2.41	APD Program [36] (assume a CF ≈ -1.25 (from estimated extrapolation of normalized correction factor of full dipole (refer to Figure 83 in Appendix A.1) and using analytical free space antenna radiation pattern calculated from Mailloux 2005 [32])
Numerical	≈ -2.90	FEKO (MoM) Circular patch 4x1 linear array antenna. Element illumination=1, antenna scan angle=0°. Averaged the simulated near field power density as a function of distance parallel to linear array, excluding endfire regions and sidelobes, assuming only mainbeam (refer to Figure 84 (Page 181) in Appendix A.1)
Numerical	≈ -3.31	Savant (SBR) (4x electric dipoles and 46x electric/magnetic dipoles pair) antenna model
	≈ -3.17	Savant (SBR) (4x electric and magnetic dipoles pair) antenna model

As presented in **Table 9** there is relatively agreement between the simulated (i.e., FEKO and Savant) and the analytical estimation (Faraone and APD Program) “average” near field power density for the 4x1 linear array linear array antenna in free space. There is particularly good agreement between the simulated average near field power flux density using FEKO and the analytical estimation of the near field power flux density from the estimation theory of Faraone *et al.* 2000 [35]. The analytical estimation of the average near field power flux density using the APD program [36] was lower in magnitude (i.e., $\sim -2.41\text{dBW/m}^2$) compared to the analytical result of Faraone *et al.* 2000 ($\sim -2.91\text{dBW/m}^2$) and the simulated result from FEKO ($\sim -2.90\text{dBW/m}^2$) and Savant ($\sim -3.17\text{dBW/m}^2$ and $\sim -3.31\text{dBW/m}^2$). The discrepancies between simulated and analytical results, are mainly attributed to the assumptions and approximations made in determining the average near field power density.

Overall, there is a reasonably good agreement between the analytical estimation and simulated average near field power density for the 4x1 linear array antenna model in free space. This good agreement in the free space average near field power density provides, as mentioned previously, a high level of confidence in the results produced by the CEM software tools.

It was also of interest to determine how the average near field power density at different locations around the vicinity of the 4x1 linear array antenna in free space. The results and discussion, will not be presented here, but are presented in **Appendix A, Section A.2**. Suffice to say, that the free space average near field power flux density in regions above and below the antenna is high (i.e., $\sim -4.21\text{dBW/m}^2$) compared to the average near field power density along the axis of the array and perpendicular to the array antenna (i.e., $\sim -6.64\text{dBW/m}^2$). However, lower than the average near field power density along the antenna boresight (i.e., $\sim -2.90\text{dBW/m}^2$).

4.2.4.2 Fitted Near Field Power Flux Density - Antenna fitted Front Panel of Mast Structure

The fitted near field power density here refers to the near field power density when the transmit antenna is installed or placed in close vicinity to the mast structure.

Figure 38 illustrates the regions around the 4x1 linear array transmit antenna and mast structure, where the near fields were calculated in FEKO. Here the antenna was placed at distances $d = \lambda/4$ m and 0.113 m away from the surface of the mast structure.

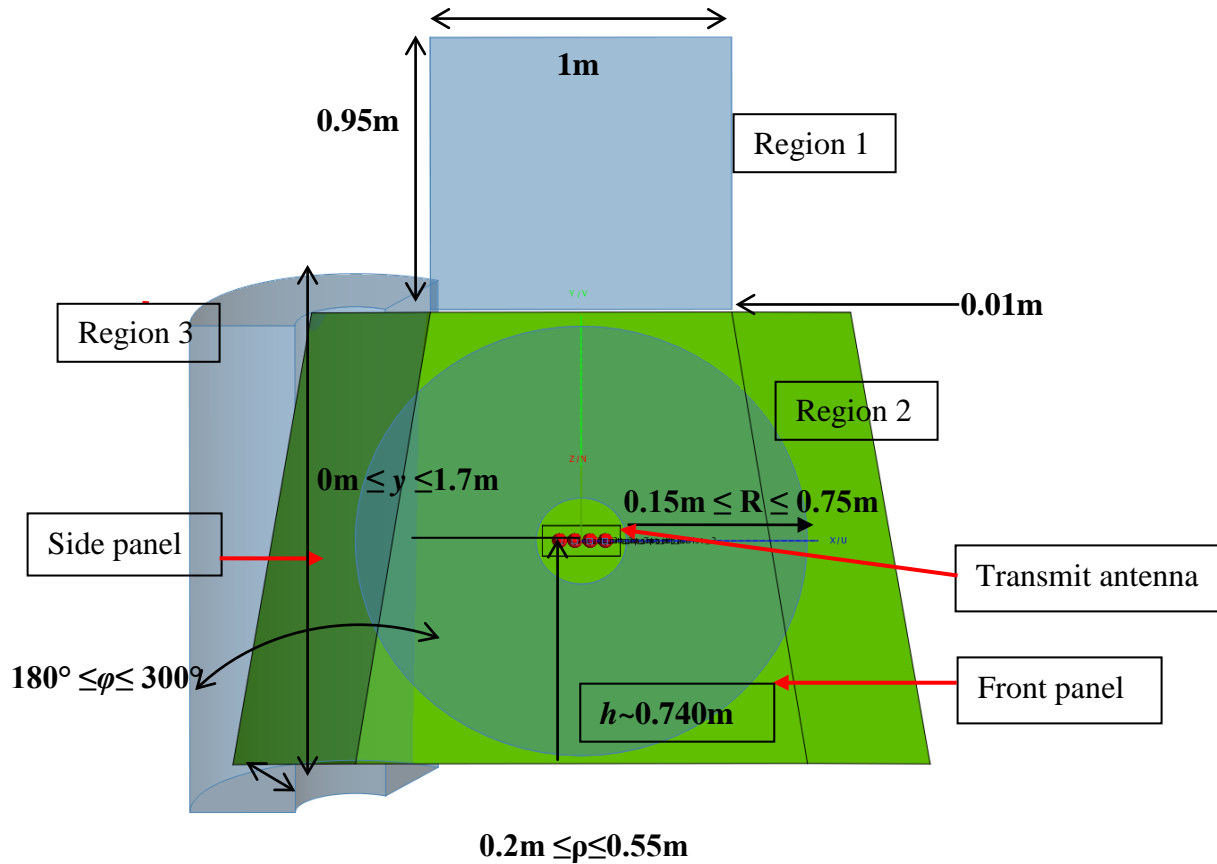


Figure 38. Near field regions calculated for different locations around the mast structure and in the vicinity of the 4x1 linear array antenna in FEKO. Linear array antenna located at a vertical height $h \sim 0.740\text{m}$ from base of mast structure and positioned at different distances, i.e., 0.113m and $\lambda/4\text{m}$, from mast structure front panel.

As illustrated in **Figure 38** the near field was calculated in three regions around the mast structure.

- **Region 1** was a region with an area of 0.95m^2 (i.e., $1\text{m} \times 0.95\text{m}$) above the transmitting antenna, at distance 0.01m above the top edge of the mast structure's front panel,
- **Region 2** was a circular plane region around the transmit antenna, with radial distances R , $0.15\text{m} \leq R \leq 0.75\text{m}$, from the center of the antenna, in azimuth ϕ , $0^\circ \leq \phi \leq 360^\circ$, cut at an elevation angle $\theta = 90^\circ$, and
- **Region 3** was a cylindrical region, using cylindrical co-ordinates (i.e., (ρ, y, ϕ)) along the y -axis, to include the mast structure sidepanel. The radial distance ρ dimension was $0.2\text{m} \leq \rho \leq 0.55\text{m}$; the angle ϕ dimension was $180^\circ \leq \phi \leq 300^\circ$ and the y -axis dimension was $0\text{m} \leq y \leq 1.7\text{m}$.

The transmit antenna was positioned at different distances, i.e., 0.113m and $\lambda/4$ m, from the mast structure front panel and different antenna scan angles (i.e., $\theta=0^\circ$, $\theta\sim 5^\circ$, $\theta\sim 11^\circ$ and $\theta\sim 18^\circ$) were also considered. **Figure 39** illustrates the transmit antenna scan angle θ orientation when antenna is fitted on the mast structure.

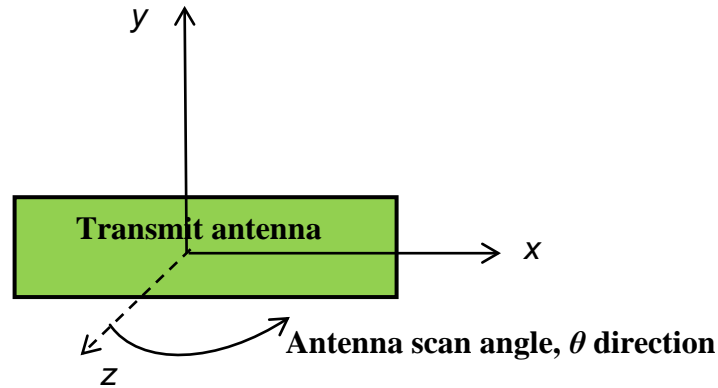


Figure 39. Schematic illustrating the transmit antenna scan angles orientations. The transmit antenna scan angles $\theta=0^\circ$, $\theta\sim 5^\circ$, $\theta\sim 11^\circ$ and $\theta\sim 18^\circ$ were measured from the z-axis, which here is assumed to be directed out of page, antenna scan angle $\theta=0^\circ$ is along antenna bore sight (i.e., along the z-axis).

The simulated fitted relative near field power flux density for each of the three near field regions, as depicted in Figure 38 for each of the CEM software tools (FEKO, MWS and Savant) were compared where possible. The circumstances where comparisons between the fitted relative near field power flux density between the different CEM software tools were not possible was because not all of the near field regions, as depicted in Figure 38 could be defined in the CEM software tools (i.e., Savant and MWS).

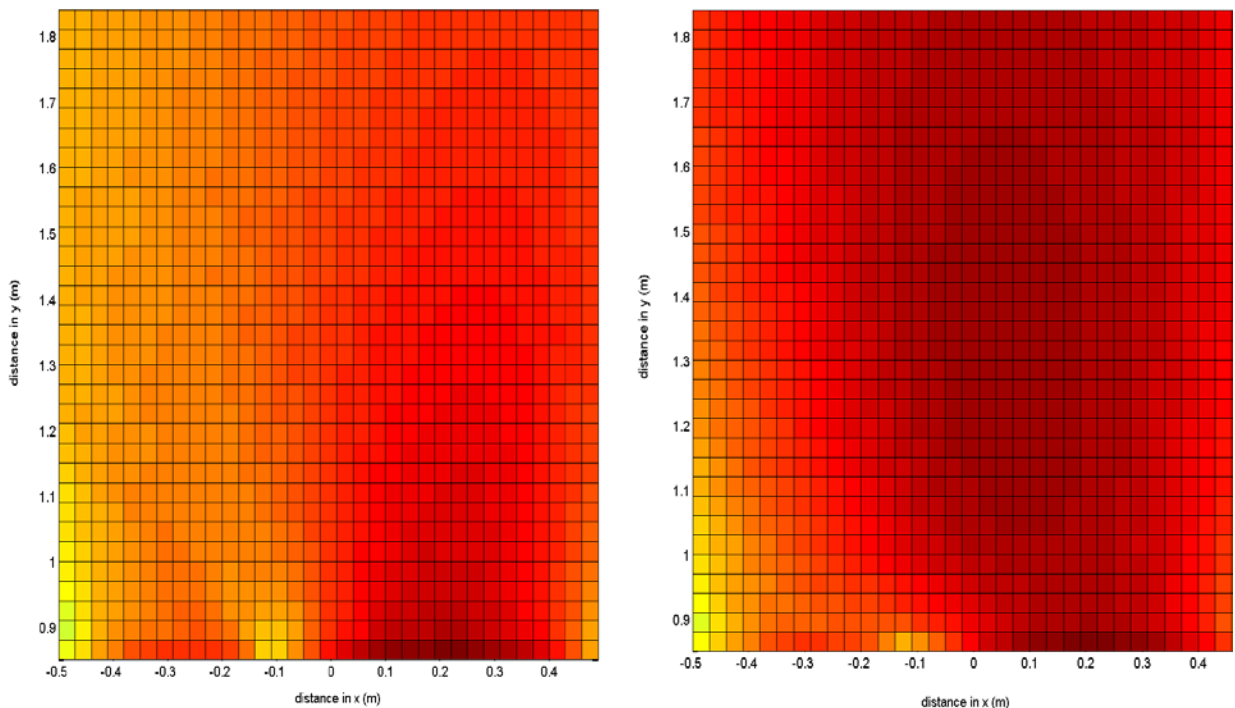
Therefore, for region1, as depicted in Figure 38 comparisons in the fitted relative near field power flux density results were possible between FEKO and Savant, but not for MWS (or CST). No comparison could be made between FEKO and MWS, despite MWS having 2-D plane near field monitors, because in MWS the 2-D plane monitors could only be defined in either the x, y or z plane, with predefined dimensions. Consequently, no 2-D plane monitor, could be defined, in MWS in order to replicate region 1.

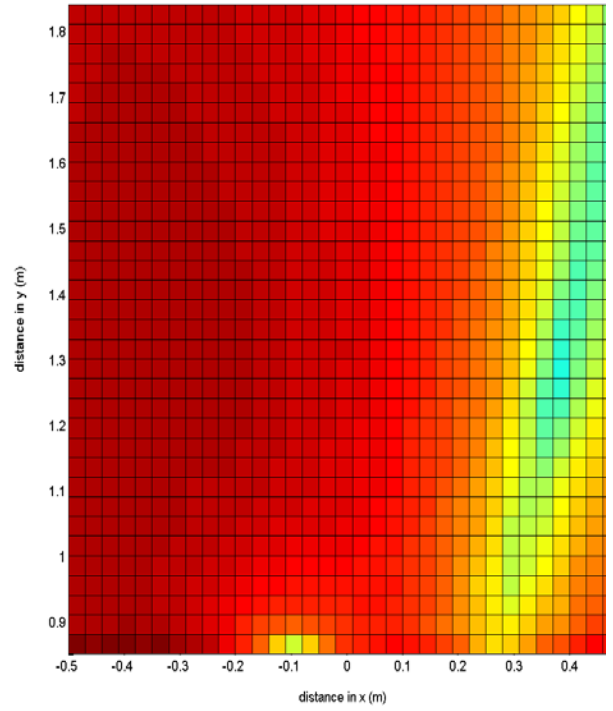
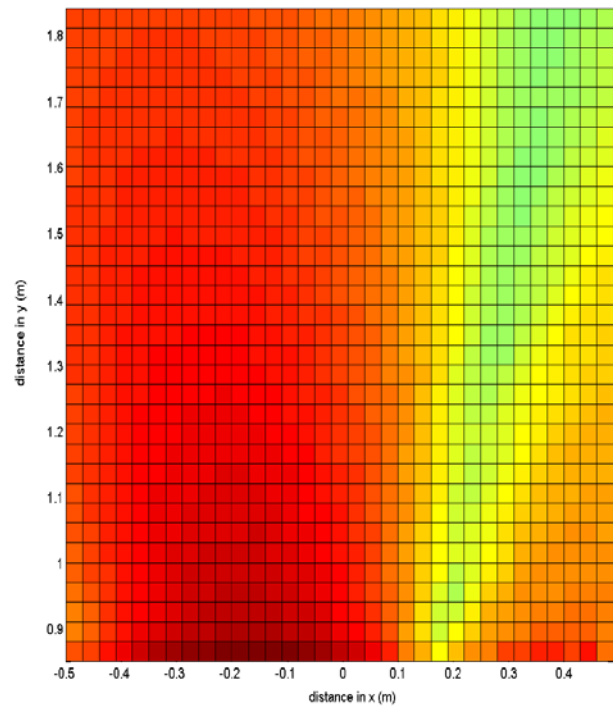
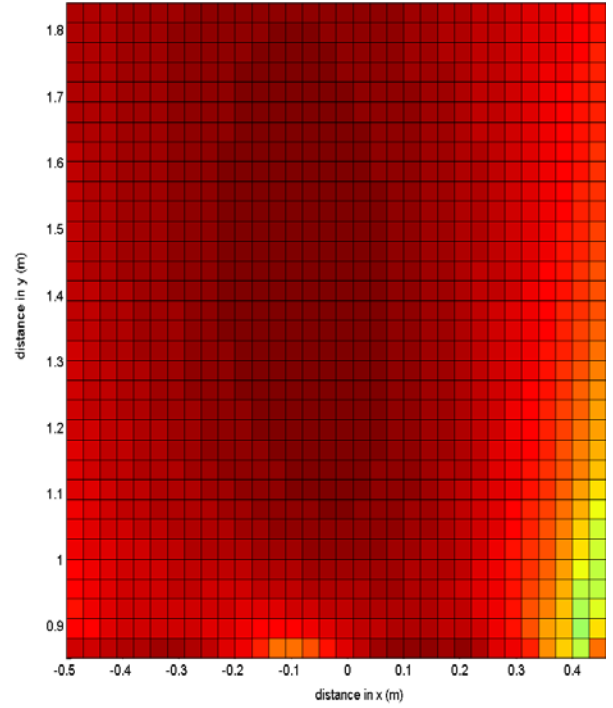
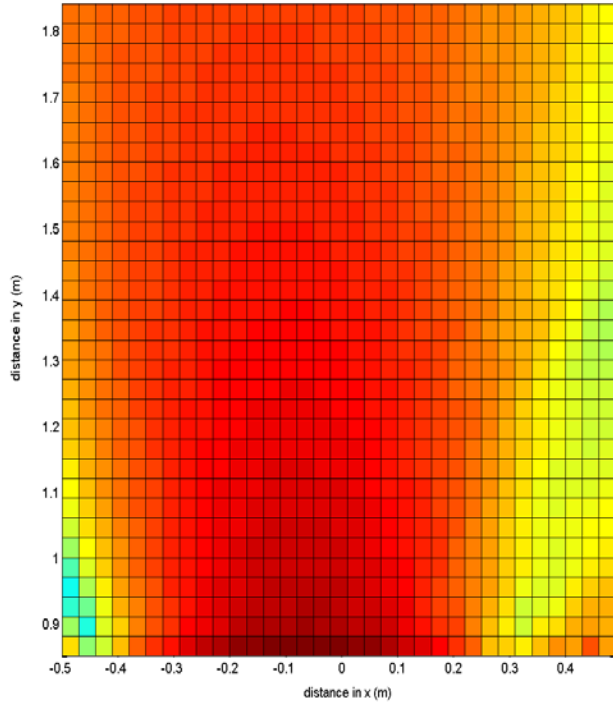
The fitted relative near field power flux density results for region 2, as depicted in Figure 38, could be compared, between FEKO and MWS (or CST). However, comparison could only be made at specified radial distances R from the center of the transmit antenna. For the same region, i.e., region 2 comparisons in the fitted relative near field power flux density results were possible between FEKO and Savant. However, the near field distribution regions in Savant could only be defined as 2-D planes. Therefore, in order to replicate, as close as possible the near field distribution region 2, as depicted in Figure 38, in Savant, 2-D planes had to be defined around the transmit antenna. In

order to provide some comparison for this report only one near field distribution 2-D plane was simulated in Savant. In particular, the region was a 2-D plane in the xz -plane (i.e., radial distance and height from center of transmit antenna) with dimensions in the x -plane, $0.15 \text{ m} \leq x \leq 0.75 \text{ m}$ and z -plane, $0 \text{ m} \leq z \leq 0.75 \text{ m}$ all measured from the center of the transmit antenna. This in turn meant that some post processing needed to be done in order to make direct comparisons between the fitted relative near field power flux density results from FEKO and Savant. This is because the fitted relative near field power flux density results from FEKO for region 2 are a function of radial distance R and azimuth angle φ , whereas the relative fitted near field power flux density results from Savant are a function of radial distance (R or x) and height z . Therefore, the azimuth angle φ in the FEKO result had to be converted to a height z value.

No comparisons could be made, between the fitted relative near field power flux density for region 3, as depicted in Figure 38, between FEKO and MWS, or FEKO and Savant, since the exact or similar region could not be defined in either Savant or MWS CEM software tools.

Figure 40 illustrates the fitted relative power flux density (dB) in region 1 (i.e., above panel where transmitter antenna is located) for different antenna-to-mast structure separations (i.e., $\lambda/4\text{m}$ and 0.113m) and antenna scan angles (i.e., $\theta=0^\circ$, $\theta \sim 5^\circ$, $\theta \sim 11^\circ$ and $\theta \sim 18^\circ$) using FEKO.





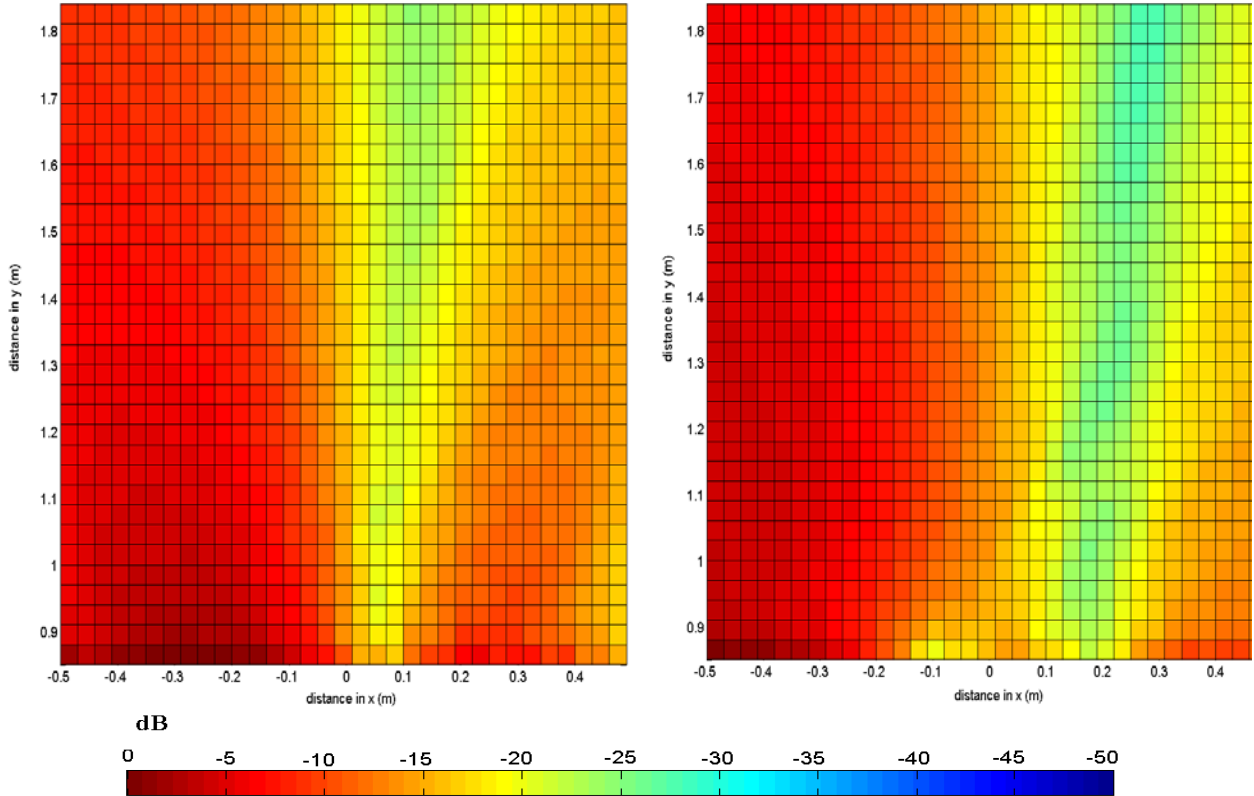


Figure 40 Fitted relative near field power flux density (dB) in region 1 at different antenna-to-mast separation (from *L* to *R*) $\lambda/4\text{m}$ and 0.113m and different antenna scan angles (from *Top* to *Bottom*) $\theta=0^\circ$, $\theta\sim 5^\circ$, $\theta\sim 11^\circ$ and $\theta\sim 18^\circ$. All results from FEKO simulation.

As illustrated in **Figure 40** there is significantly high relative near field power flux density, i.e., reaching up to 0 dB, in the region above the antenna (i.e., region 1), for each of the antenna scan angles, in particular smaller scan angles, i.e., $\theta=0^\circ$ and $\sim 5^\circ$. However, there tends to an increase in intensity within this region when the antenna is placed further away (i.e., 0.113m), from the mast structure, compared to when it is placed angle of zero degrees. There is more antenna radiation to mast structure interference occurring for the case where the antenna is placed closer to the mast structure than further away. The interference here for when the antenna is closer to the structure is advantageous as the mast structure tends to block/scatter the antenna radiation. Thus, reducing the overall intensity of the power density reaching the region above the antenna, compared to when the antenna is placed further away from the mast structure, where the mast structure does not obstruct as much of the antenna radiation reaching the region above the antenna.

This overall high relative power flux density in this region above the antenna would tend to suggest that if there is any other antenna located within this region top of the mast it would encounter significantly high power density, thus experiencing interference due to

the transmit antenna located at the front panel. It is worth noting that this power density region is calculated at distances greater than the far field region of the 4x1 linear array transmit antenna ($\sim 0.8\text{m}$) utilized in the present analysis. This in turn further suggests that there can be significantly large power density regions around the mast structure, not only within the near field region of the transmitter.

Figure 41 illustrates the simulated fitted relative near field power flux density from Savant in region 1 (region dimension $0.95\text{m} \times 1\text{m}$), i.e., above the transmitting antenna, at antenna scan angles 0° and $\sim 11^\circ$ and at an antenna to mast separation of $\sim \lambda/4\text{m}$ using an asymptotic (or high frequency) technique (i.e., shooting and bouncing rays).

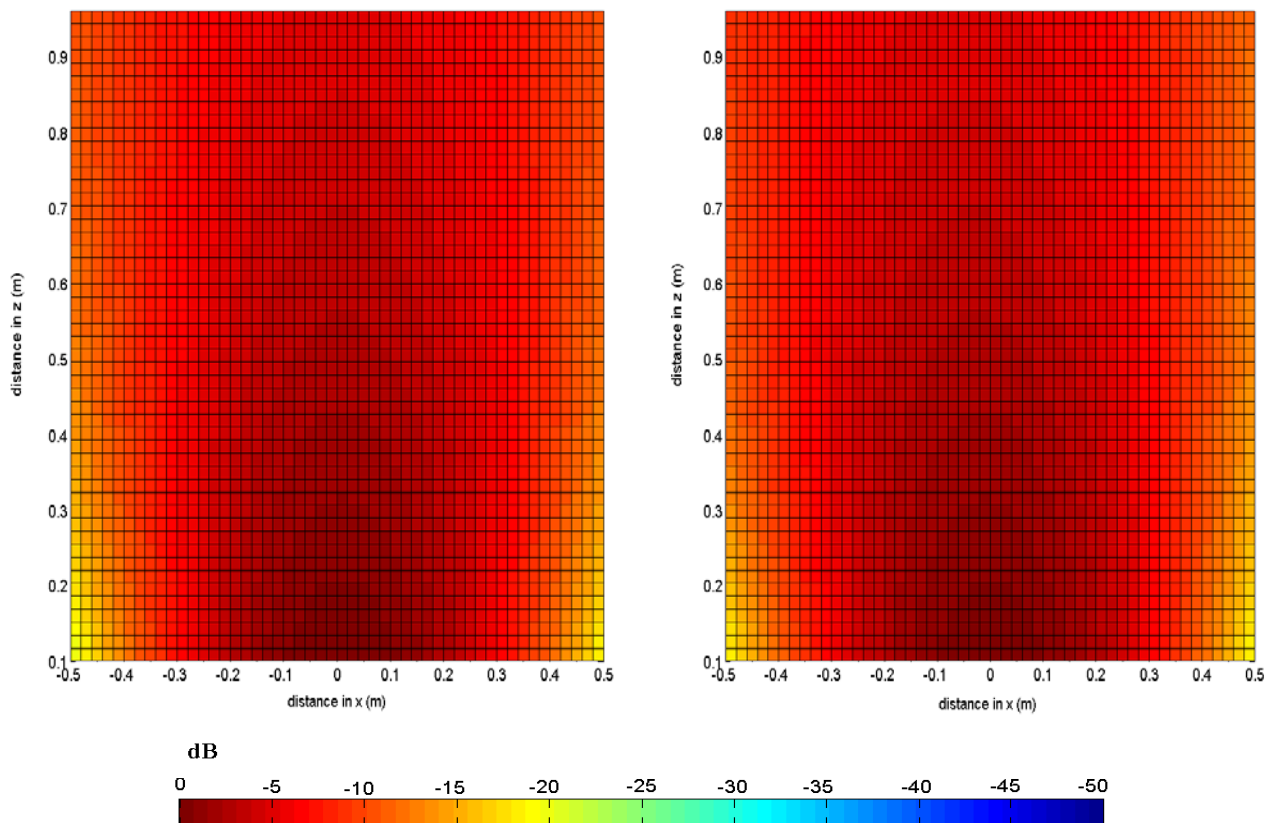
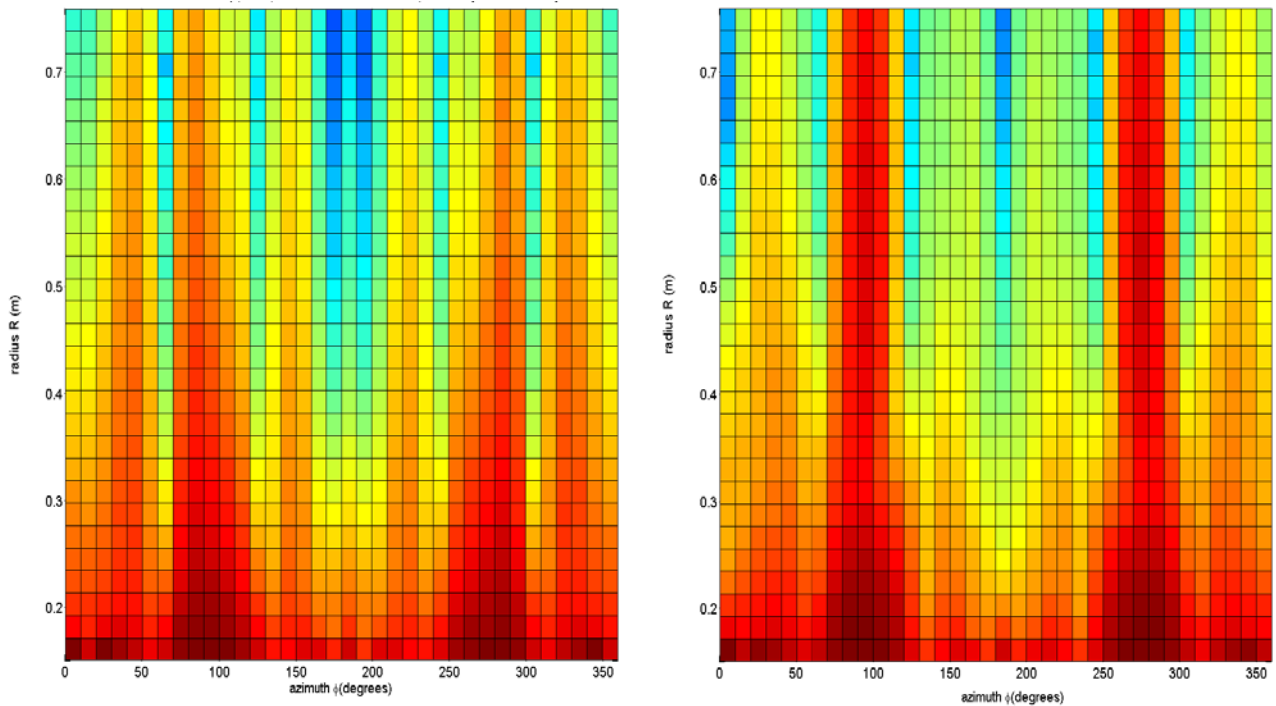


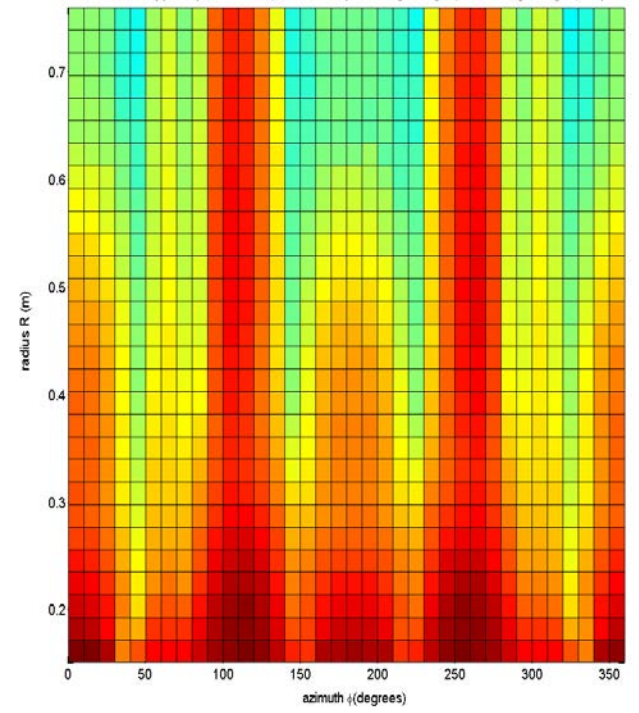
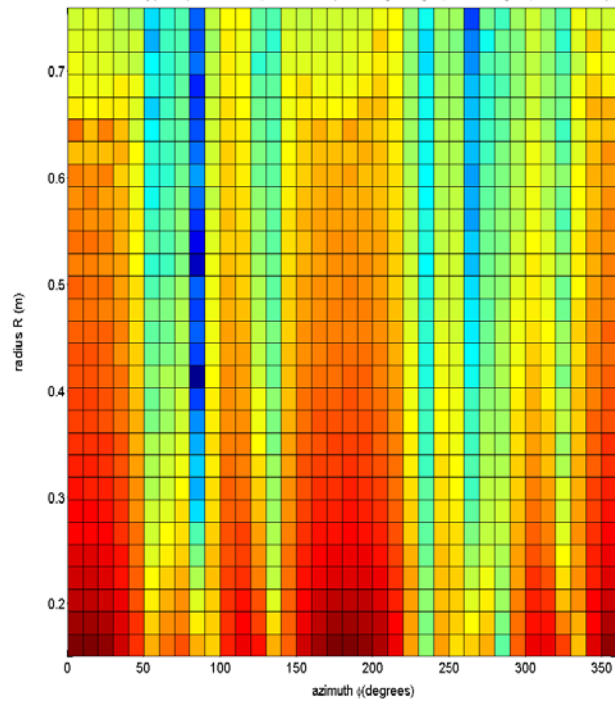
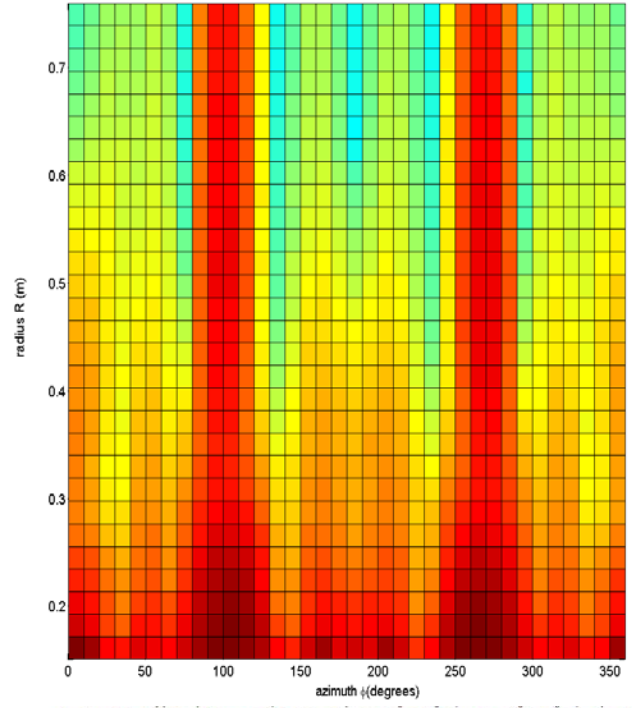
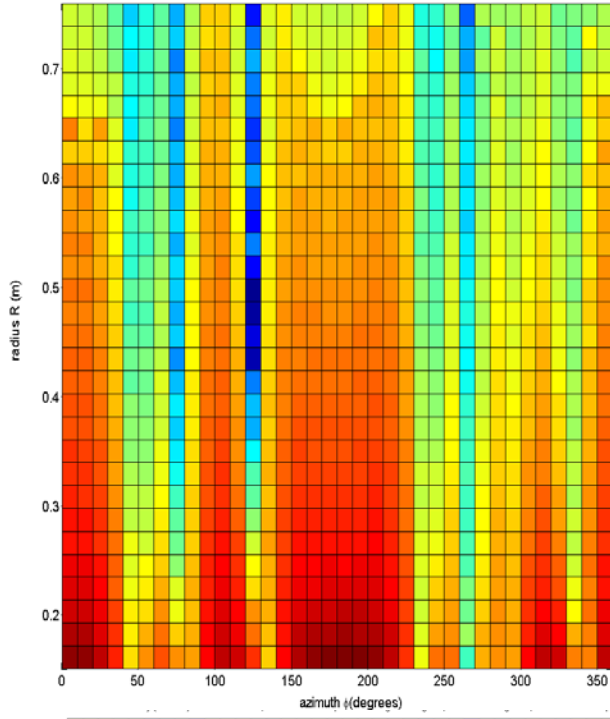
Figure 41 Fitted relative near field power flux density (dB) in region 1 at antenna-to-mast separation $\sim \lambda/4\text{m}$ and different antenna scan angles (L to R) $\theta=0^\circ$ and $0\sim 11^\circ$. Near field distribution simulation results from Savant.

As illustrated in **Figure 41** the relative near field power flux density is significantly high (up to 0dB) in region 1, i.e., above the transmitter antenna at each different antenna scan angles (i.e., 0° and 11°).

By comparing the fitted relative near field power flux density results from, FEKO and Savant, i.e., **Figure 40** and **Figure 41**, shows overall the results are in good agreement. Both (i.e., FEKO and Savant) simulated results show that at an antenna scan angles of 0° and 11° and at an antenna-to-mast separation of $\lambda/4\text{m}$ there is a significantly high (up to 0dB) fitted relative near field power flux density in region 1, i.e., above the transmitter antenna. However, in the Savant results this significantly high relative power flux density is evident across all of the region 1, with a very little section in region1, i.e., on the lower edges of the defined region of region 1, where there is low fitted relative near field power flux density (i.e., $\sim -20\text{dB}$). Compared to the FEKO results there is a small narrow but diffused area in region 1, in particular in the center of region 1, where the relative power flux density is low (i.e., down to $\sim -25\text{dB}$).

Figure 42 illustrates, the fitted relative near field power flux density (dB) in region 2 (i.e., nearby the transmitter antenna) plotted in a 2-D plane (i.e., the circular region extended out as a rectangular plane, with azimuth ϕ as a function of radial distance R). For different antenna to mast separations (i.e., $\lambda/4\text{m}$ and 0.113m) and different transmitter antenna scan angles (i.e., $\theta=0^\circ$, $\theta\sim 5^\circ$, $\theta\sim 11^\circ$ and $\theta\sim 18^\circ$).





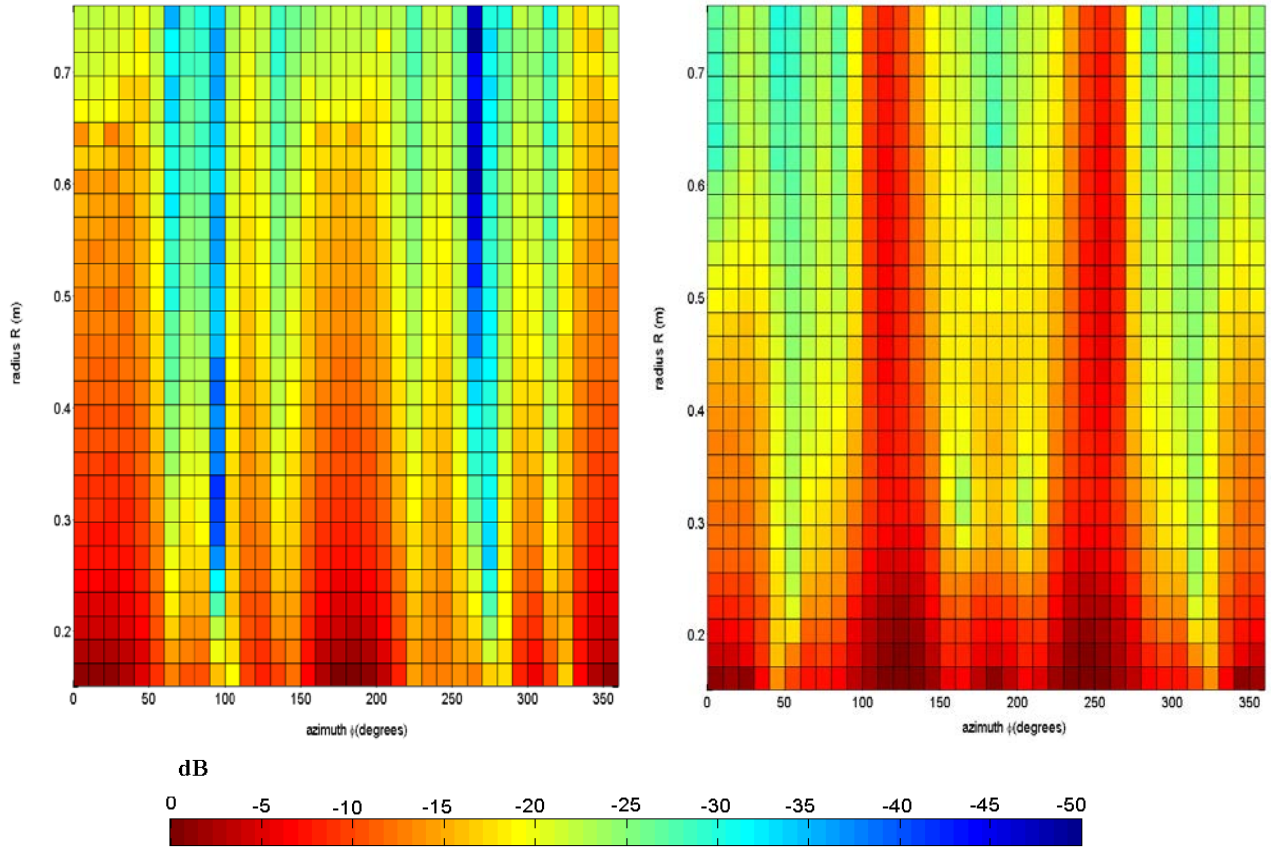


Figure 42. Fitted relative near field power flux density (dB) in region 2 at different antenna to mast separation (from *L* to *R*) $\lambda/4m$ and $0.113m$ and different antenna scan angles (from *Top* to *Bottom*) $\theta=0^\circ$, $\theta\sim 5^\circ$, $\theta\sim 11^\circ$ and $\theta\sim 18^\circ$.

As illustrated in **Figure 42** there are regions nearby the antenna and around the mast panel where the transmitter is located where the fitted near field power flux density is significantly high (up to 0 dB). These high relative power densities nearby the transmitting antenna would be as expected as within these close regions the high intensity near fields of the antenna are evident. Furthermore, the results suggest that when the antenna is closer to the mast structure (i.e., $\lambda/4m$) there are regions where the power density is lower ($< -30dB$) compared to when the antenna is placed further away from the mast structure (i.e., $0.113m$).

Figure 43 illustrates the simulated fitted relative near field power density results from Savant, which is for a small section (i.e., 2-D plane, dimension $0.6m \times 0.75m$) of region 2. As mentioned previously, the near field, power flux density, results for region 2, as depicted in **Figure 38**, is a function of azimuth angle ϕ and radial distance R from the center of the transmit antenna. Whereas, the near field power flux density results from Savant are plotted as a function of radial distance and vertical height from the center of the transmit antenna. Therefore, before any direct comparisons can be made between the simulated relative near field power flux density results from Savant can be compared with

the fitted relative near field power flux density results from FEKO the azimuth angle φ needs to be converted to a vertical height z . From basic trigonometry and geometry theory, the vertical height z , at a subtended angle φ of a circle, with a radius R , can be estimated as follows, $z \sim R \sin \varphi$.

Therefore, for a radial distance $R=0.5\text{m}$ and at subtended angle $\varphi=50^\circ$, the vertical height can be estimated to be $z \sim 0.4\text{m}$. If we refer to the FEKO fitted relative near field power flux density results, from **Figure 42**, for the case where the antenna to mast separation is $\lambda/4\text{m}$ and antenna scan angle $\theta=0^\circ$, at a radial distance R of 0.5m and azimuth angle $\varphi=50^\circ$, the fitted relative near field power flux density is $\sim -18\text{dB}$. If we now refer to the relative near field power flux density calculated in Savant, from **Figure 43**, for a radial distance $R=0.5\text{m}$ (along the x -axis) and a vertical height $z \sim 0.4\text{m}$ the calculated power density is $\sim -20\text{dB}$. By considering the errors due to approximations made in each CEM software tool (i.e., FEKO and Savant) and height to angle estimation, overall the results are in good agreement.

Similarly, for a transmit antenna scan angle $\theta \sim 11^\circ$, and considering the same radial distance $R=0.5\text{m}$, azimuth angle $\varphi=50^\circ$ and antenna-to-mast separation $=\lambda/4\text{m}$, from the FEKO results in **Figure 42**, the fitted relative near field power flux density is between $\sim -15\text{dB}$ and $\sim -25\text{dB}$. Whereas, from the Savant results, from **Figure 43**, for the same radial distance $R=0.5\text{m}$ and corresponding vertical height $z \sim 0.4\text{m}$, the fitted relative near field power flux density is between $\sim -15\text{dB}$ and $\sim -20\text{dB}$. By taking into consideration errors due to numerical approximations in each of the CEM software tool (i.e., FEKO and Savant) and the vertical height-to-angle estimation, overall the fitted relative near field power flux density within region 2 between the FEKO and Savant are in good agreement.

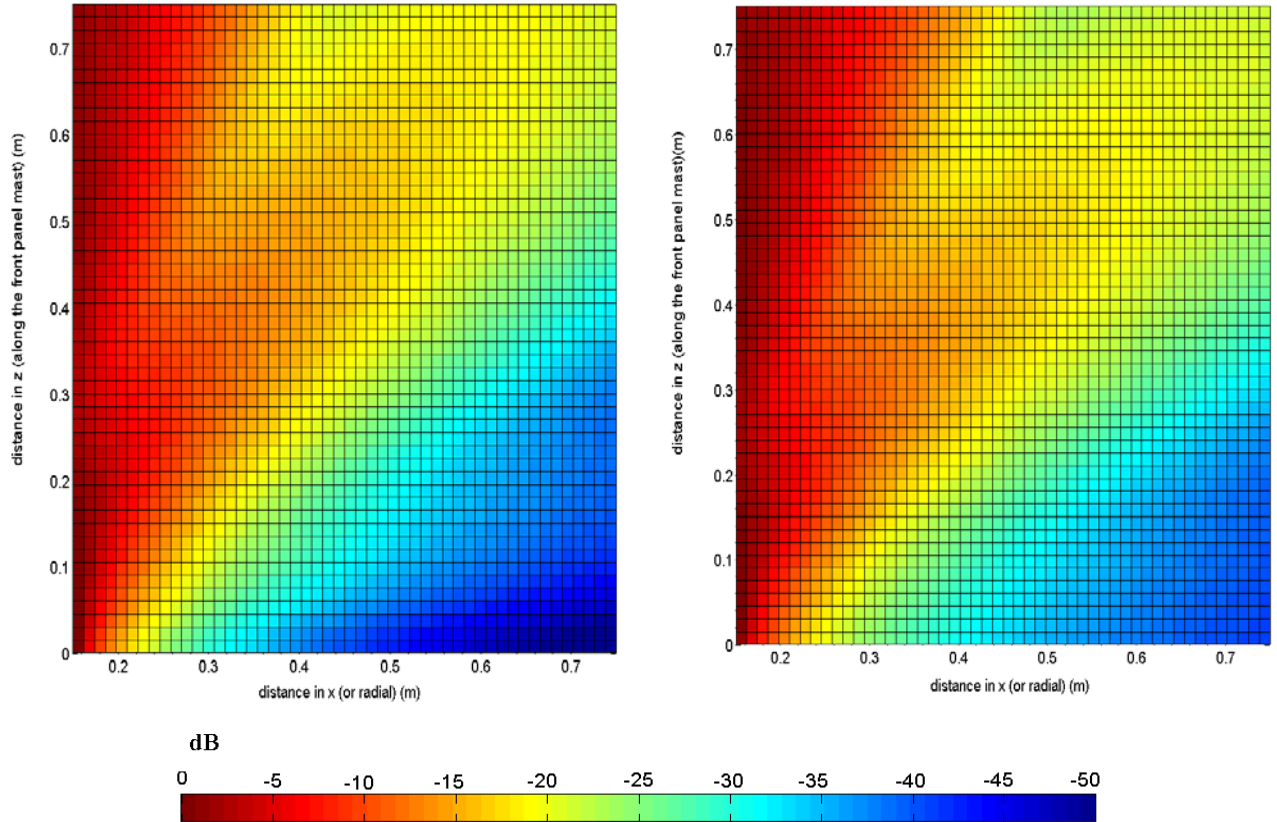
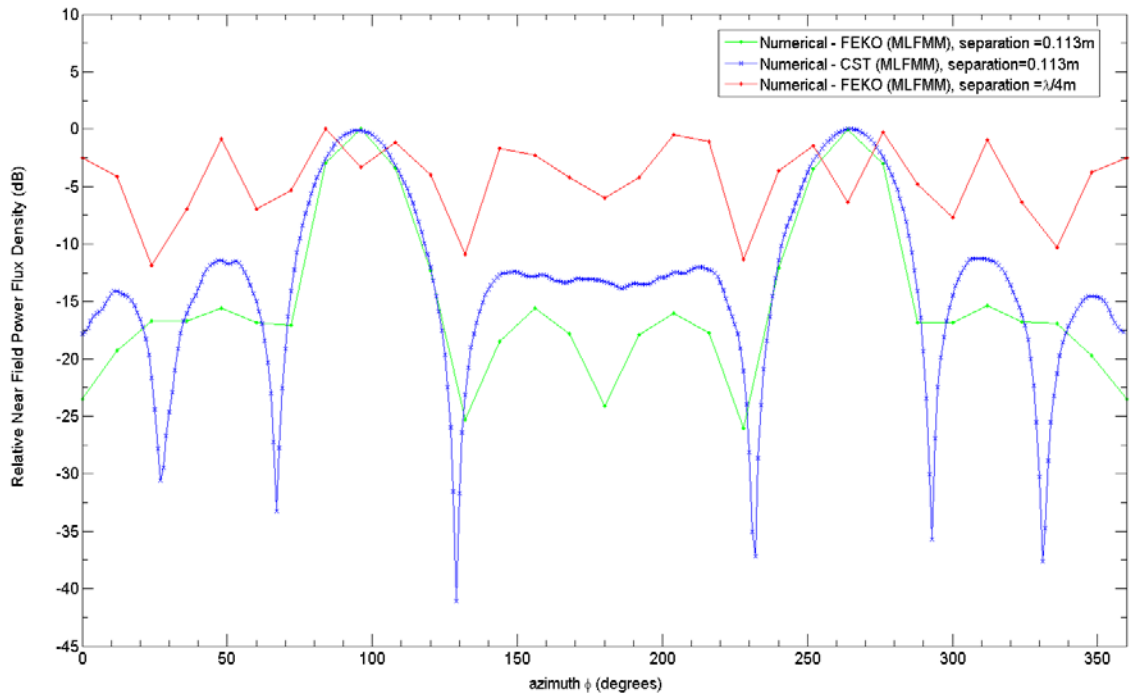
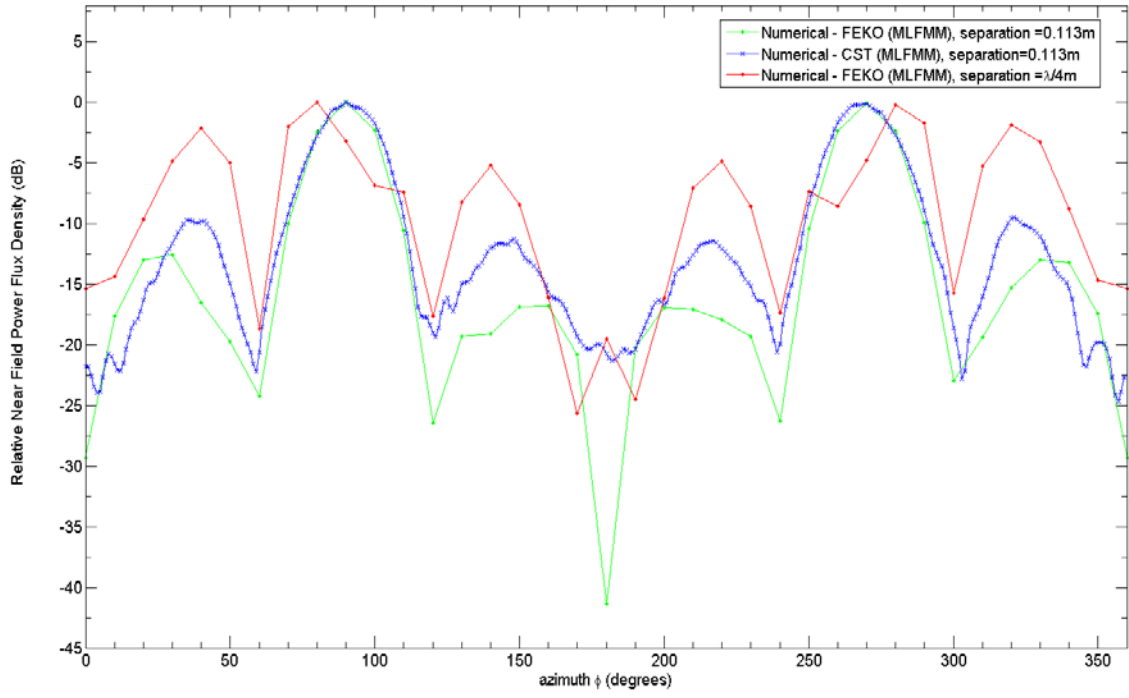


Figure 43. Fitted relative near field power flux density (dB) in right hand sector of region 2 for an antenna-to-mast separation $\sim\lambda/4$ m for different antenna scan angles, (L to R) $\theta=0^\circ$ and $\theta \sim 11^\circ$. The near field distribution was simulated using Savant.

Figure 44 illustrates the comparison of the simulated fitted relative near field power flux density in region 2 (i.e., near field as a function of azimuth φ , cut at elevation $\theta=90^\circ$), at a radial distance $R=0.75$ m (from the centroid of the linear array antenna) using FEKO and MWS (or CST). The transmit antenna is positioned at different distances (i.e., 0.113m and $\lambda/4$ m) from the mast structure's front panel and different transmit antenna scan angles (i.e., $\theta=0^\circ$, $\theta\sim 5^\circ$, $\theta\sim 11^\circ$ and $\theta\sim 18^\circ$) were considered.



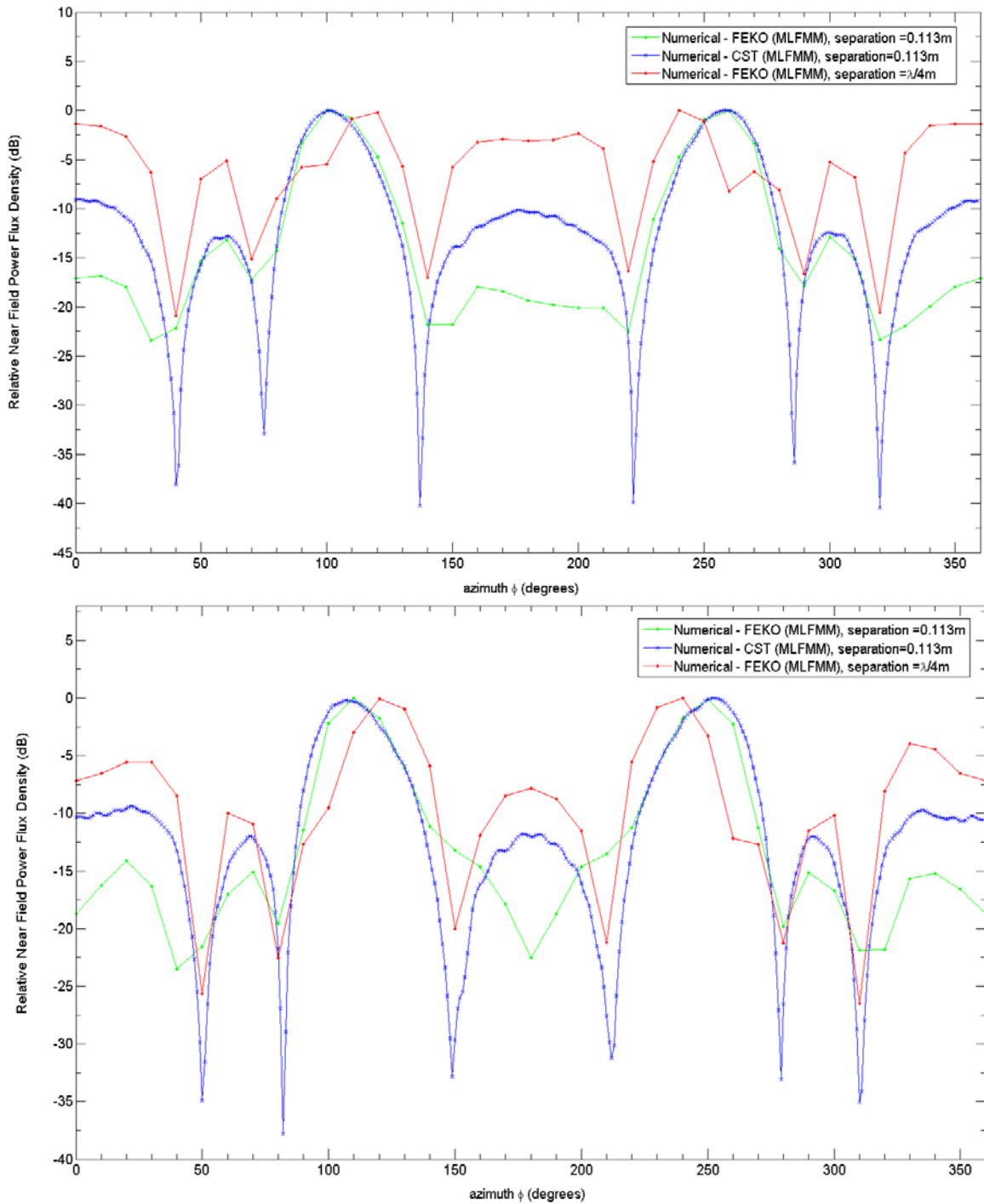
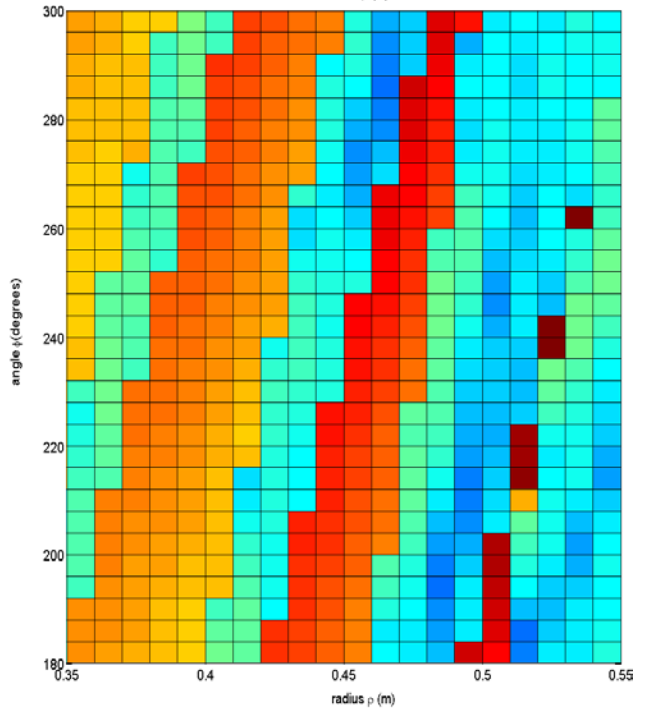
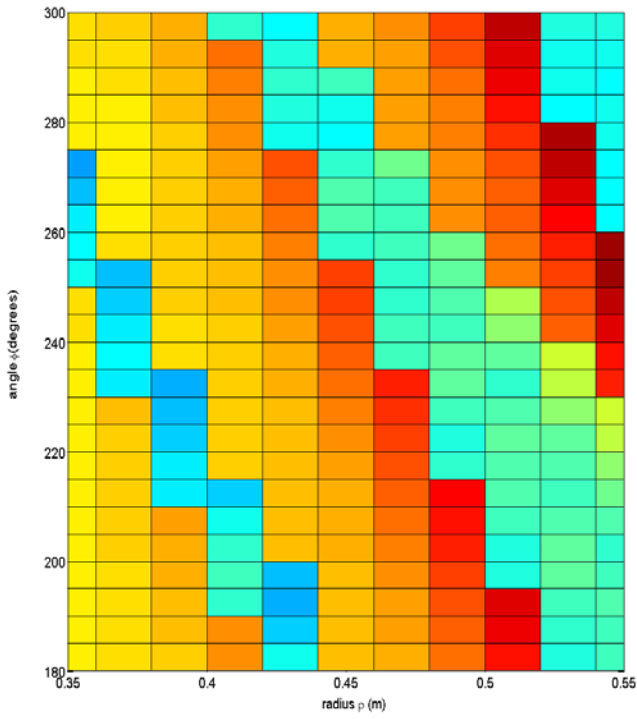
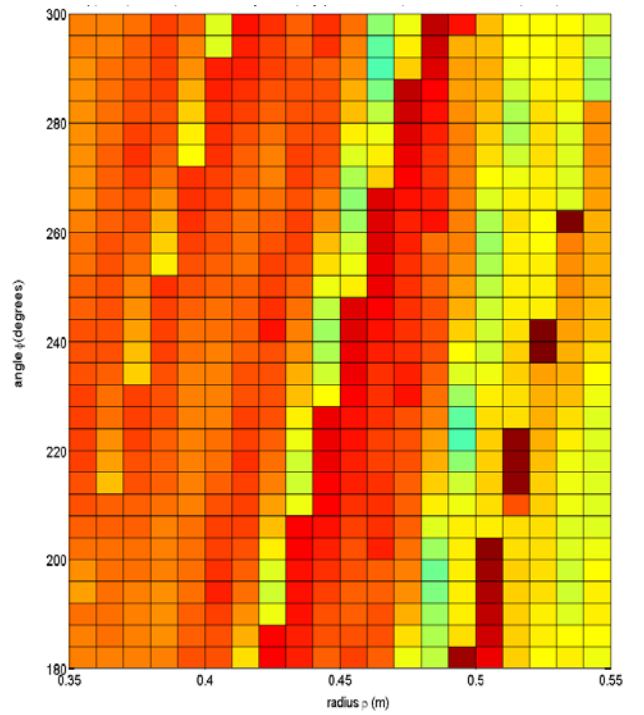
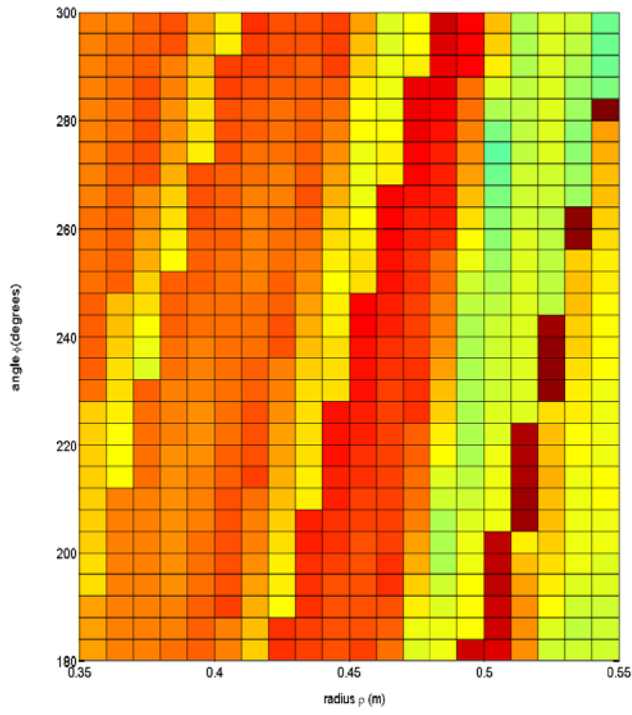


Figure 44. Comparison of fitted relative near field power flux density as a function azimuth ϕ , cut at elevation $\theta=90^\circ$ at a radial distance $R=0.75$ m, from center of the 4×1 linear array antenna, for different antenna-to-mast separation (i.e., $\lambda/4$ m and 0.113m) and different antenna scan angles θ (From *Top to Bottom*) $\theta=0^\circ$, $\theta \sim 5^\circ$, $\theta \sim 11^\circ$, and $\theta \sim 18^\circ$. Here the transmit antenna is located at a vertical height $h \sim 0.74$ m from the base of the mast structure frontpanel.

As illustrated in **Figure 44** for an antenna-to-mast separation of 0.113m there is good agreement between the fitted relative near field power flux density results from FEKO and MWS (or CST). However, there are some differences in the antenna near field radiation pattern in the sidelobe and back lobes of the radiation pattern. This is due to the difference in the assumptions and methodology used for each simulation. For example, in FEKO a 4x1 linear array antenna model was used, whereas in MWS (or CST) a 3-D antenna radiation pattern of the 4x1 linear array was used, which was calculated using CST's internal array wizard, which was then placed at the distance from the MAST structure.

However, when the antenna is placed closer to the mast structure, i.e., from 0.113m to $\lambda/4$ m the near field power flux density differs quite significantly in that the near field power flux density has elevated sidelobes and also distortion in the main beam. This is mostly likely due to mutual coupling between antenna radiation pattern and mast structure, which would be as expected as an antenna gets closer to a large structure. The sharpness in the FEKO results compared to the CST results is due to the angle increments used in each of the simulations i.e., 5° in FEKO and 1° in CST. This sharpness can be smoothed by reducing the angle increment in any future FEKO simulations.

Figure 45 illustrates the simulated fitted relative near field power flux density in a cross sectional area of region 3. The cross sectional area of region 3 that is presented here is at a radial distance ρ between $0.35 \text{ m} \leq \rho \leq 0.55 \text{ m}$ and angle φ between $180^\circ \leq \varphi \leq 300^\circ$ cut at a height $y \sim 0.8\text{m}$. Other cross-sectional areas of region 3, could have been chosen and presented here. However, the present cross-sectional area of region 3, was chosen as it represented, the near field at the mid-height of the mast structure sidepanel (i.e., $y \sim 0.8\text{m}$). At different distances from the mast structure, sidepanel surface (i.e., $0.35 \text{ m} \leq \rho \leq 0.55 \text{ m}$, here $\rho = 0.35\text{m}$ refers to distances very close or on sidepanel surface, and $\rho = 0.55\text{m}$ refers to vertical (or radial) distances away from the sidepanel surface). At positions along the mast structure sidepanel, relative from the mast structure edge joining the front panel and side panel (i.e., $180^\circ \leq \varphi \leq 300^\circ$, here $\varphi = 180^\circ$ refers to positions further away from the mast structure edge joining front and side panels, and $\varphi = 300^\circ$ refers to positions closer to the mast structure edge joining front and side panels). The transmitter antenna was positioned at different distances (i.e., $\lambda/4\text{m}$ and 0.113m) from the mast structure front panel and different transmitter antenna scan angles (i.e., $\theta = 0^\circ$, $\sim 5^\circ$, $\sim 11^\circ$ and $\sim 18^\circ$) were considered.



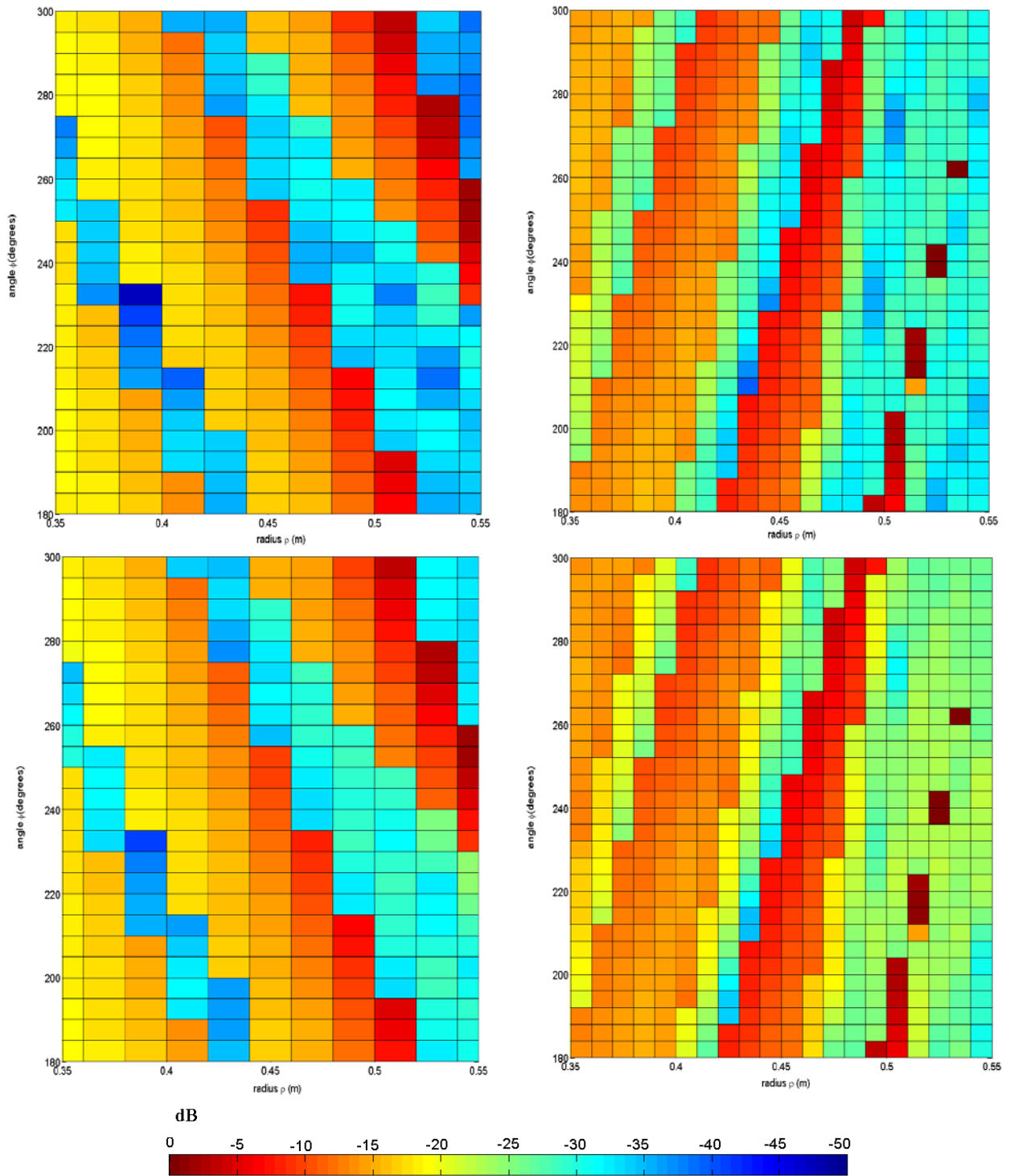


Figure 45. Fitted relative near field power flux density (dB) in a cross sectional area of region 3, in particular radial ρ , $0.35 \text{ m} \leq \rho \leq 0.55 \text{ m}$ as a function of angle ϕ , $180^\circ \leq \phi \leq 300^\circ$, cut at height $y \sim 0.8\text{m}$, at different antenna-to-mast separation (L to R) $\lambda/4\text{m}$ and 0.113m and different antenna scan angles (from top to bottom) $\theta=0^\circ$, $\sim 5^\circ$, $\sim 11^\circ$ and $\sim 18^\circ$. All near field computed using FEKO.

As illustrated in **Figure 45**, for a transmit antenna scan angle $\theta=0^\circ$ and at different antenna-to-mast separations (i.e., $\lambda/4\text{m}$ and 0.113m), there does not appear to be much difference in the fitted relative near field power flux density along the sidepanel, at least at a height $y \sim 0.8\text{m}$. At positions further away from the transmit antenna, i.e., φ value decreasing towards 180° and at radial distances from the side panel surface, i.e., ρ increasing towards 0.55m , the fitted relative near field power density is low, i.e., low as -25dB . Whereas, as we get closer to the transmit antenna, at least to the mast structure edge which joins the front and side panels, i.e., φ increasing towards 300° and ρ decreasing towards 0.35m (close to the sidepanel surface) the fitted relative near field power density is $\sim -15\text{dB}$. However, there are small pockets of regions around the sidepanel where the fitted near field power flux density are significantly high, reaching as high as 0dB (i.e., $0.5 < \rho \leq 0.55\text{m}$ and $285^\circ < \varphi \leq 180^\circ$). In addition, there are also a defined region around the sidepanel where the fitted relative near field power density is $\sim -10\text{dB}$ (i.e., $300^\circ \leq \varphi \leq 180^\circ$ and $0.42 < \rho < 0.47\text{m}$). Overall, over the cross-sectional of region 3 presented here the dominant fitted near field power flux density varies between $\sim -10\text{dB}$ to -15dB .

Similarly, for an antenna scan angle $\theta \sim 5^\circ$, and at different antenna-to-mast separations (i.e., $\lambda/4\text{m}$ and 0.113m), there does not appear to be much difference in the fitted relative near field power flux density along the sidepanel, at least at a height $y \sim 0.8\text{m}$. However, compared to antenna scan angle $\theta=0^\circ$, the overall fitted relative power flux density has reduced to vary between $\sim -10\text{dB}$ to $\sim -35\text{dB}$. This reduction in near field power flux density is as expected, since the antenna scan angles in the present analysis directed the antenna mainbeam away from the side panel, for which region 3 near fields were calculated. The reduction trend in the fitted relative near field power flux density along the side panel is also similar for antenna scan angles $\theta \sim 11^\circ$ and $\sim 18^\circ$, where, overall, the fitted near field power flux density varies between $\sim -10\text{dB}$ to $\sim -35\text{dB}$. However, there are very small regions along the sidepanel, at both of these antenna scan angles, where there is a significantly high fitted near field power flux density (reaches 0dB), but these regions seem to occur at positions very close to the mast structure edge that joins the front and side panels. However, this reduction in the fitted near field power flux density along the sidepanel at these larger antenna scan angles may not be the same occurrence for the other sidepanel on the other side of the front panel. In this circumstance, the fitted relative near field power flux density may instead increase, since the antenna main beam is directed towards it. Further analysis would need to be done to confirm this in future work.

4.2.3.3 Fitted Near Field Power Flux Density - Antenna fitted Side panel of Mast Structure

Figure 46 illustrates the regions around the transmitting antenna and mast structure where the near fields were calculated. Here the antenna was positioned at different distances (i.e., 0.113m and $\lambda/4$ m) away from the mast structure side panel and at different antenna scan angles, i.e., $\theta=0^\circ$, $\theta\sim 5^\circ$, $\theta\sim 11^\circ$, $\theta\sim 18^\circ$.

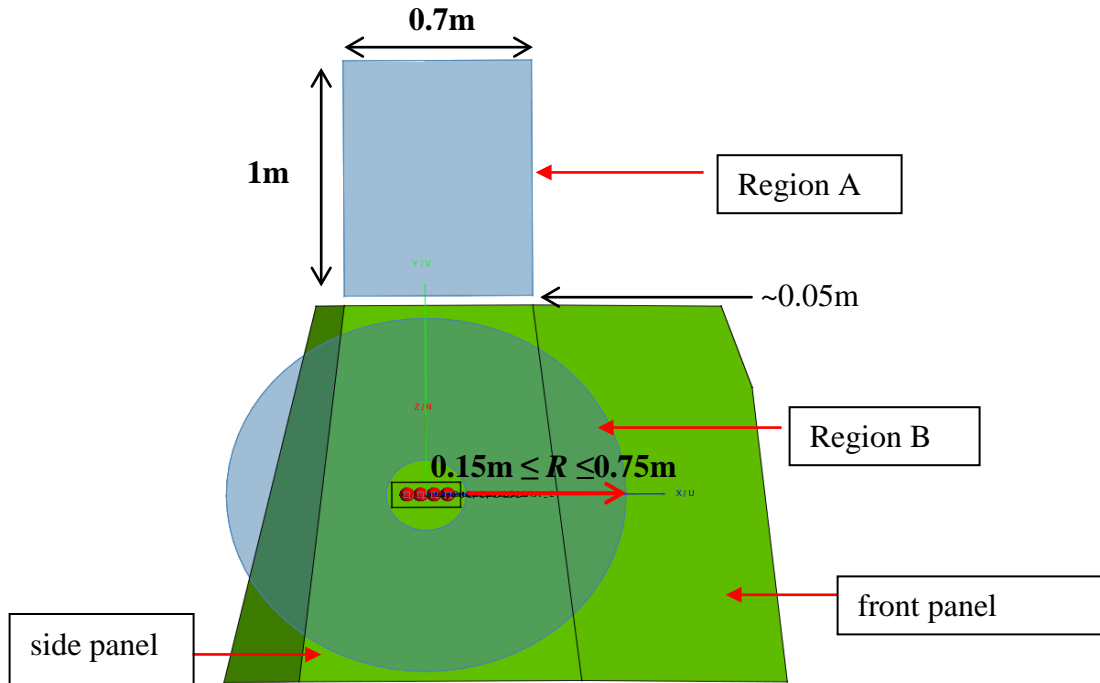
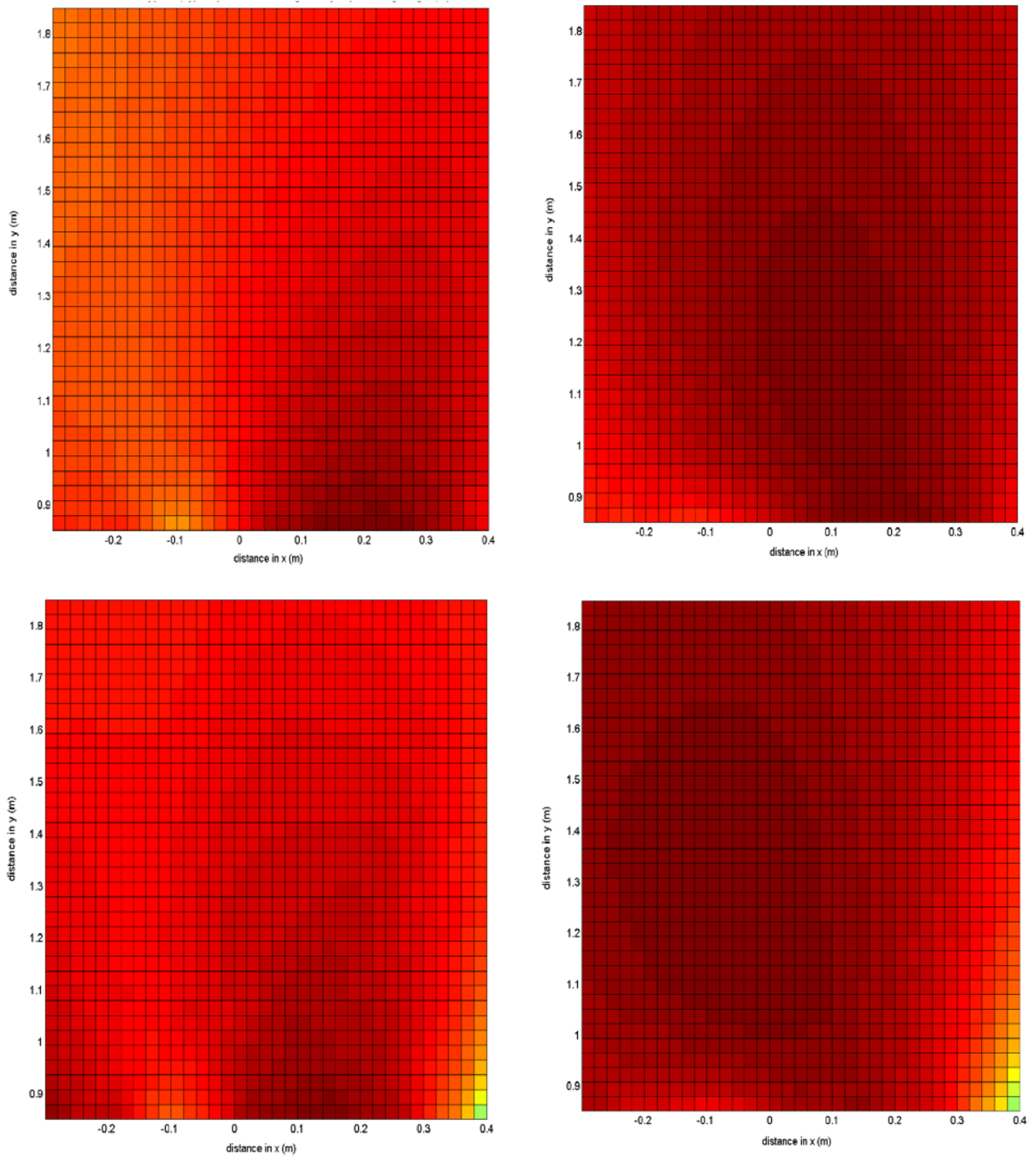


Figure 46. Schematic of the near field regions nearby the transmitting antenna when antenna mounted side panel at different separation distances from mast structure for FEKO simulations. Here only near fields were calculated for regions A (i.e., above antenna) and B (i.e., around antenna). Near field regions were calculated in FEKO.

As illustrated in **Figure 46** the near field was calculated in two regions around the antenna and mast structure. In particular,

- **Region A** was a 2-D plane region of dimensions 1m \times 0.7m (i.e., a 0.7m² area) above the transmitting antenna, at a position \sim 0.05m from the top edge of the mast structure side panel, and
- **Region B** was a circular region around the antenna of radial distances $0.15\text{m} \leq R \leq 0.75\text{m}$, from the center of the antenna, and azimuth angles $0^\circ \leq \varphi \leq 360^\circ$, cut at an elevation angle $\theta \sim 90$ degrees.

Figure 47 illustrates the simulated fitted relative power flux density (including near field power flux density) range for region A, at different transmit antenna scan angles (i.e., $\theta=0^\circ$, $\sim 5^\circ$, $\sim 11^\circ$ and $\sim 18^\circ$), and different antenna separations (i.e., $\lambda/4$ m and 0.113m) from the mast structure sidepanel.



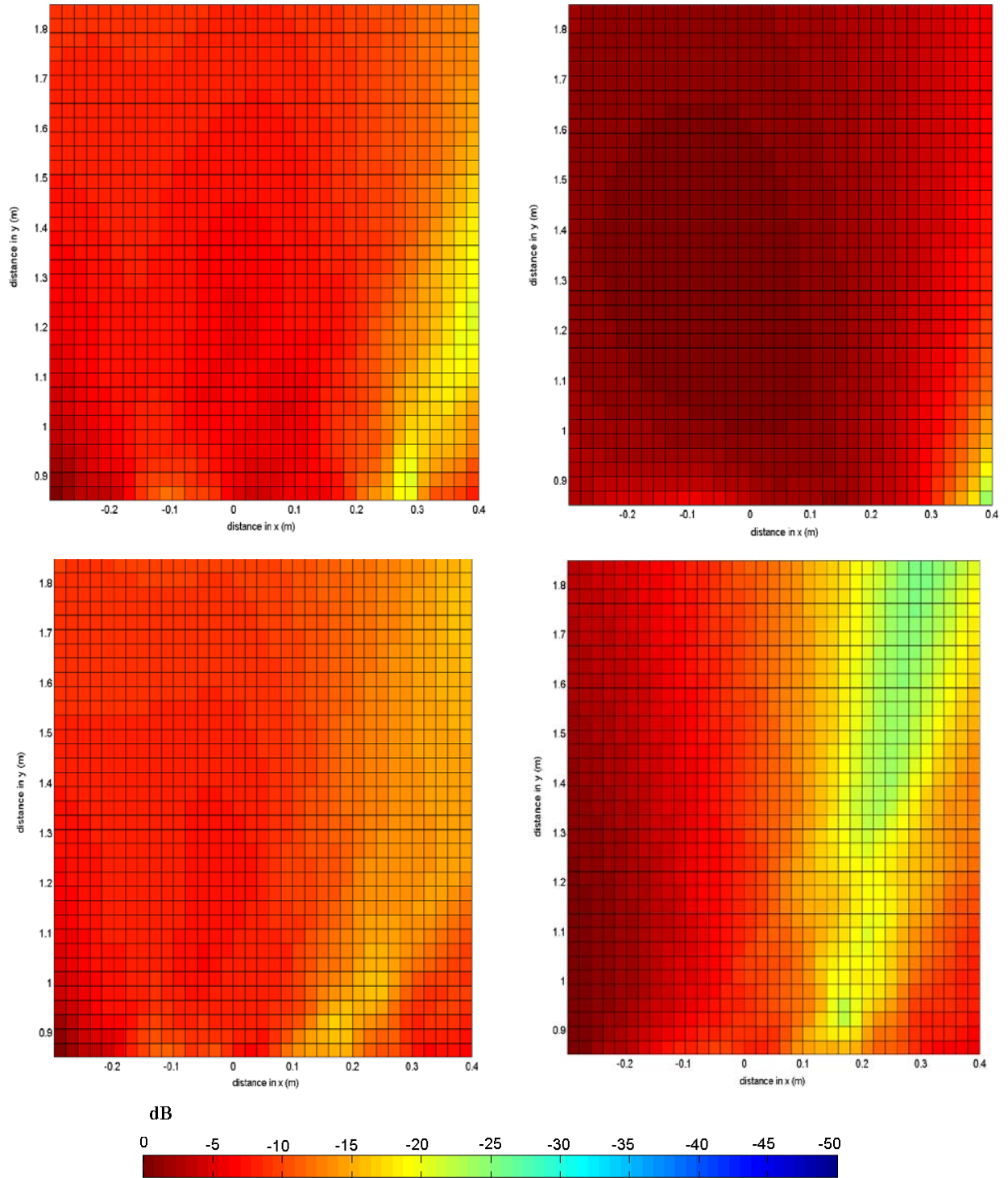
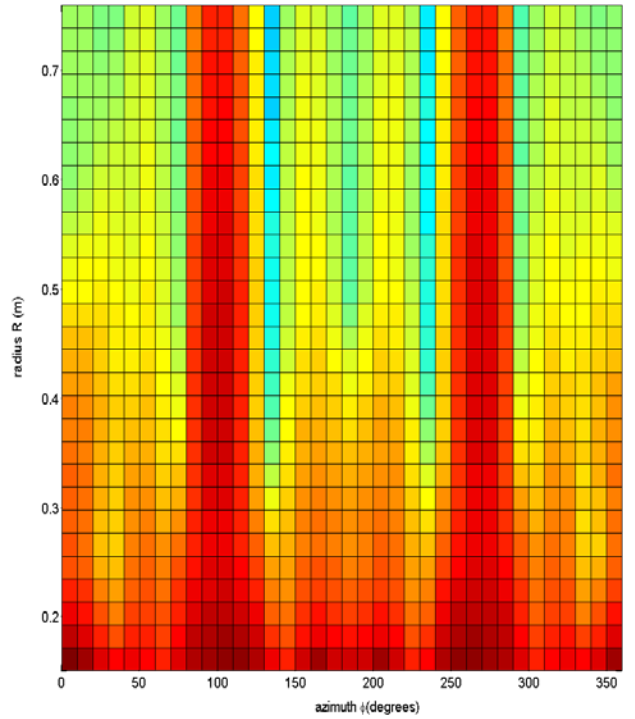
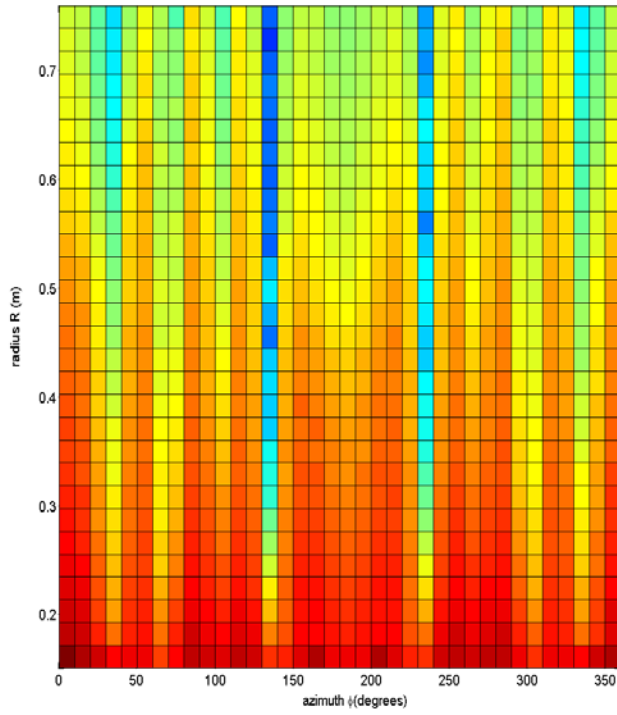
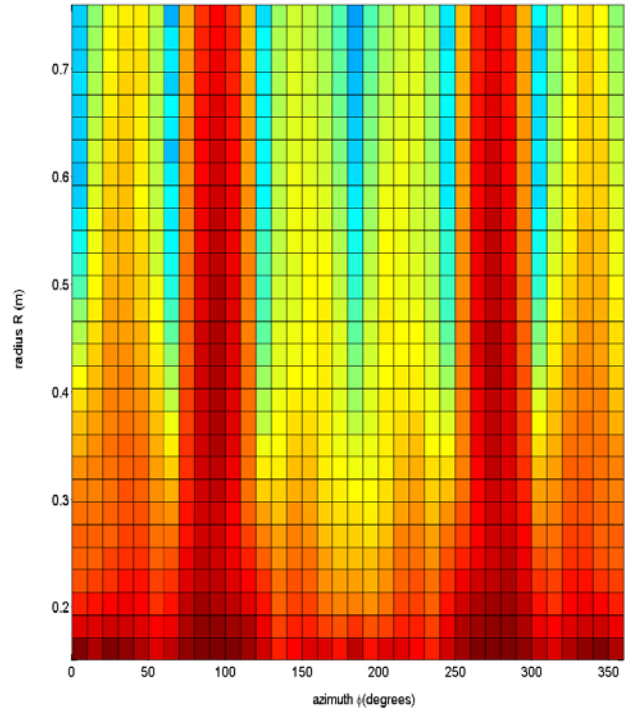
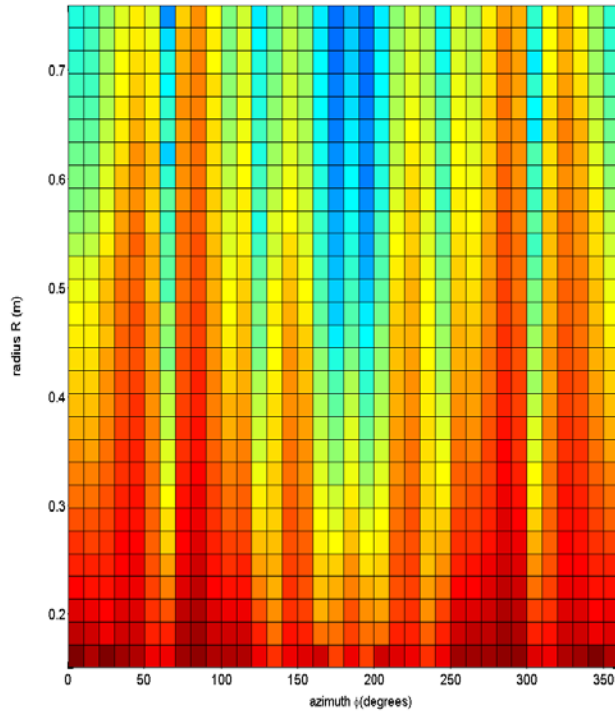


Figure 47. Fitted relative near field power flux density in region A, i.e., above transmit antenna. Here it is assumed different distances from the mast structure sidepanel (*From L to R*) $\lambda/4$ m and 0.113m, and different antenna scan angles (*From Top to Bottom*) $\theta=0^\circ, \theta\sim 5^\circ, \theta\sim 11^\circ$ and $\theta\sim 18^\circ$. All near fields calculated using FEKO.

As illustrated by **Figure 47**, at a region in the same plane as the mast structure sidepanel and above the transmitting antenna, for each of the different antenna scan angles (i.e., $\theta=0^\circ$, $\sim 5^\circ$, $\sim 11^\circ$, $\sim 18^\circ$) and antenna-to mast separations (i.e., $\lambda/4\text{m}$ and 0.113m) overall the fitted relative near field power flux density is significantly high (i.e., between -5dB and 0dB). However, overall for the antenna-to mast separation of $\lambda/4\text{m}$ the fitted near field power flux density in region A is slightly lower ($\sim -5\text{dB}$) with small regions reaching a relative near field power flux density of 0dB for each of the antenna scan angles. Whereas, for an antenna-to-mast separation of 0.113m , overall the fitted near field power flux density is as high as 0dB for each of the antenna scan angles. However, for an antenna-to-mast separation of 0.113m and antenna scan angle $\sim 18^\circ$ there does tend to be a narrow diagonal section (i.e., from the bottom to top right corner of region A) within region A, at antenna scan angle $\theta\sim 18^\circ$, where the fitted relative near field power flux density is low, i.e., $-15\text{dB} \leq S \leq -25\text{dB}$. A similar effect is also evident, however, to a less extent, for the antenna-to-mast separation of $\lambda/4\text{m}$, where the fitted relative near field power flux density reaches down to $\sim -15\text{dB}$. The occurrence in the reduction in the fitted relative near field power flux density, is most likely attributed to the projection of the antenna radiation, pattern sidelobe, as the antenna mainbeam is directed away from region A. The significantly high fitted relative near field power flux density in region A is most likely attributed to the antenna main beam, which for all antenna scan angles, namely $\theta=0$, ~ 5 and $\sim 11^\circ$

Figure 48 illustrates the relative fitted near field power flux density for region B (i.e., in the vicinity of the antenna) plotted in a 2-D plane (i.e., the circular region extended out, as a rectangular plane, with azimuth φ as a function of radial distance R) at different transmit antenna scan angles (i.e., $\theta= 0^\circ$, $\sim 5^\circ$, $\sim 11^\circ$ and $\sim 18^\circ$), and different antenna distances (i.e., $\lambda/4\text{ m}$ and 0.113m) from the mast structure side panel.



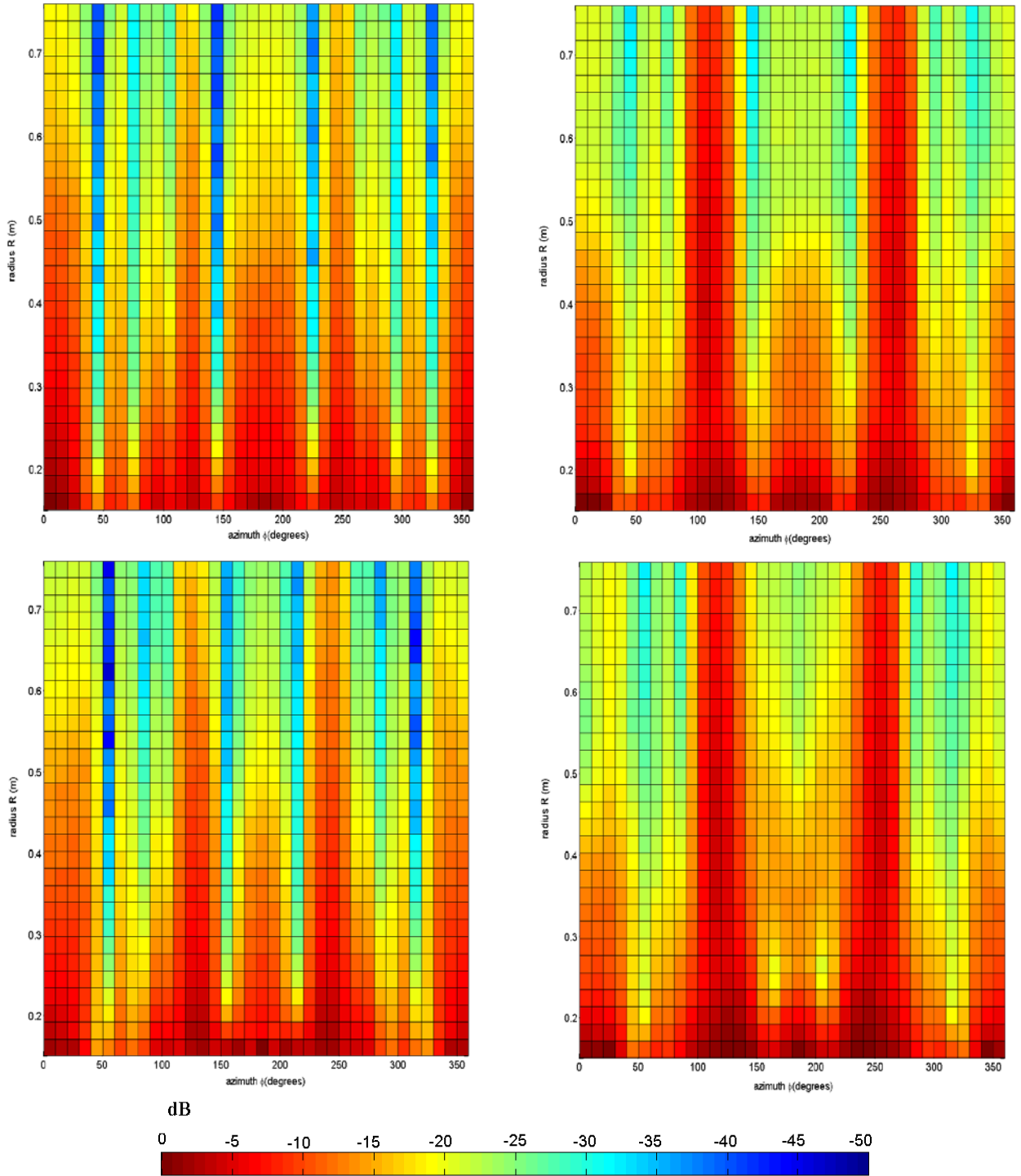
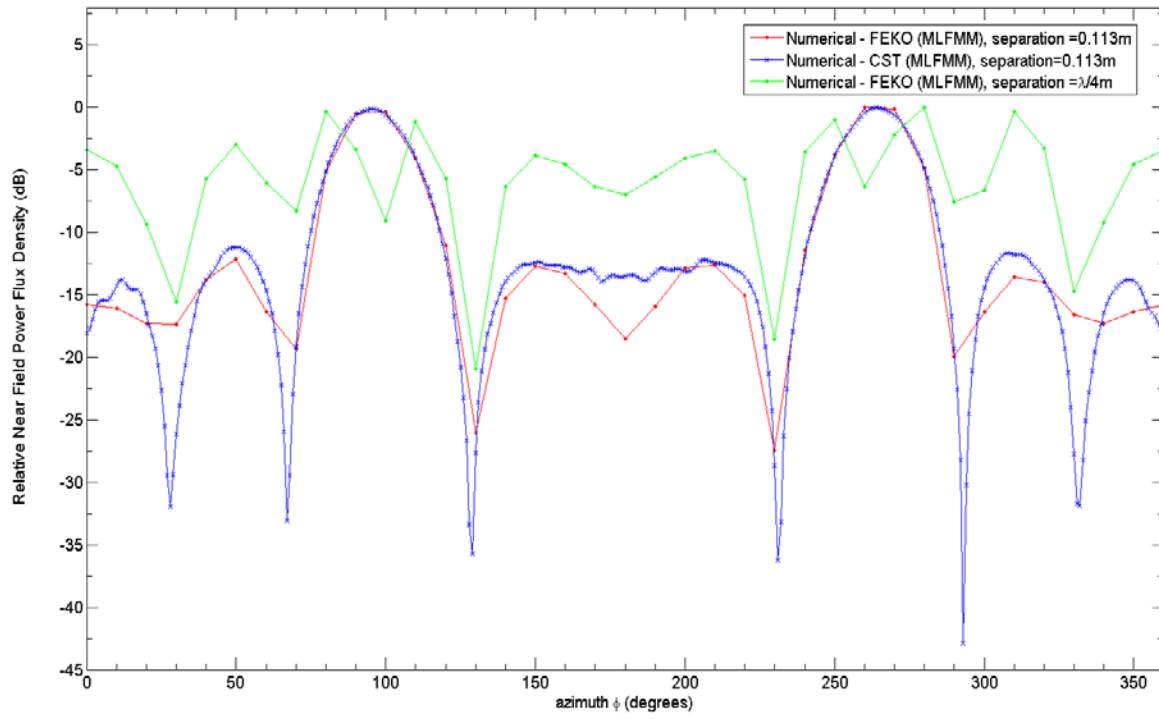
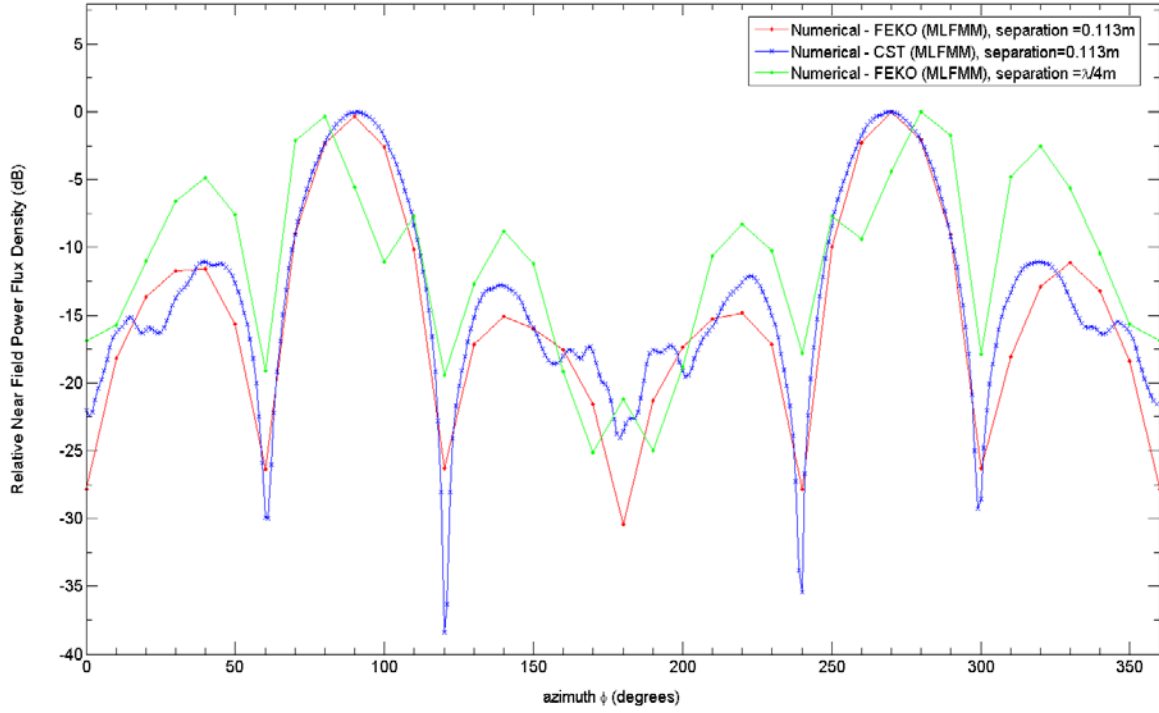


Figure 48. Relative fitted near field power flux density in region B i.e., around antenna and mast structure side panel. Here it is assumed different antenna distances from mast structure side panel (*From L to R*) $\lambda/4$ m and 0.113m, for different antenna scan transmit antenna angles (*From Top to Bottom*) $\theta=0^\circ$, $\theta\sim 5^\circ$, $\theta\sim 11^\circ$, and $\theta\sim 18^\circ$. All near fields computed using FEKO.

As **Figure 48** shows, there are regions around the mast structure panel where the transmitting antenna and nearby the transmitting antenna the fitted relative near field power flux density is significantly high, reaching up to 0dB for each antenna scan angle, i.e., $\theta=0^\circ$, $\sim 5^\circ$ and $\sim 11^\circ$ and $\sim 18^\circ$ and for each antenna to mast separations (i.e., $\lambda/4\text{m}$ and 0.113m). In addition, there are also some areas within region B where the fitted relative near field power flux density is reduced i.e., $< -30\text{dB}$. As mentioned previously, the areas in region B where the fitted relative near field power flux density is most likely attributed to the antenna main beam, and as the antenna is scanned at different angles the areas of significantly high relative near field power flux density will also change. Whereas, for the areas where there is reduced fitted relative near field power flux density is most likely attributed to the antenna sidelobes. Similarly, with the antenna mainbeam, as the antenna is scanned to different angles the areas in region B where there is low fitted relative near field power flux density will also vary.

These fitted relative near field power flux density results provide some indication of the power signal level within **regions A and B**, and if in case another sensor system, for example a receiver system is located in either **region A** or **region B**. Then with significantly high power signal levels could cause either damage to the front end of the receiver system or non-linear effects, such as desensitization (or gain compression), to the receiver system, impacting its operational performance.

Figure 49 illustrates the comparison between the fitted relative near field power flux density as a function of azimuth ϕ , cut at elevation $\theta=90^\circ$ at a radial distance $R=0.75\text{m}$ for FEKO and MWS (or CST) within **region B**. The transmit antenna is positioned at different distances (i.e., $\lambda/4\text{m}$ and 0.113m) from the mast structure side panel at different antenna scan angles (i.e., $\theta=0^\circ$, $\theta\sim 5^\circ$, $\theta\sim 11^\circ$ and $\theta\sim 18^\circ$).



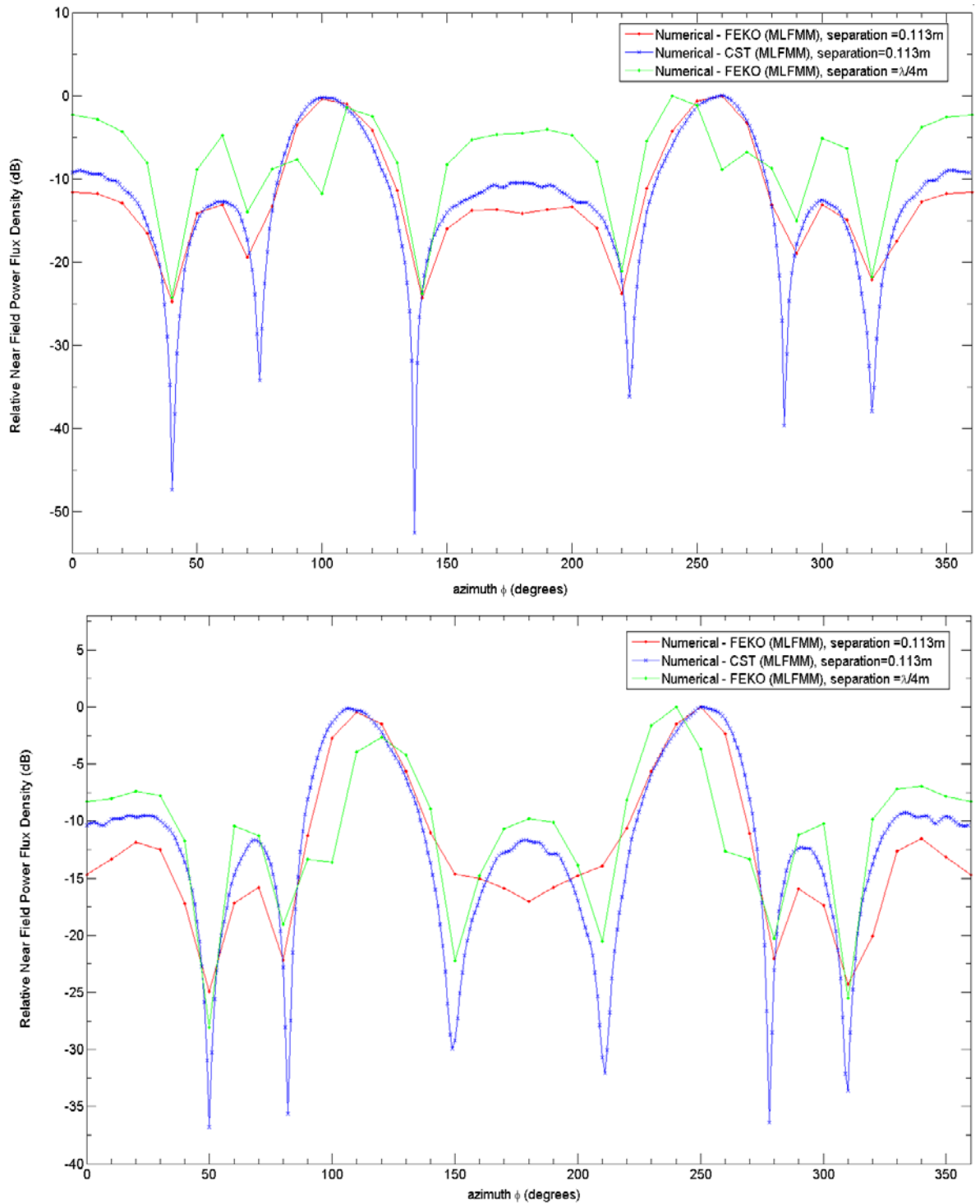


Figure 49. Fitted relative near field power flux density (dB) as a function of azimuth ϕ , cut at elevation $\theta=90^\circ$ at a radial distance $R\approx 0.75$ m, for 4x1 linear array antenna located at different distances (i.e., $\lambda/4$ m and 0.113m) from the mast structure side panel for different antenna scan angles (From *Top* to *bottom*) $\theta=0^\circ$, $\theta\sim 5^\circ$, $\theta\sim 11^\circ$, and $\theta\sim 18^\circ$.

As illustrated in **Figure 49** there is reasonably good agreement between the fitted relative near field power flux density results from FEKO and MWS simulations, for an antenna distance of 0.113m from the mast structure side panel, for each antenna scan angle $\theta=0^\circ$, $\sim 5^\circ$, $\sim 11^\circ$ and $\sim 18^\circ$. However, when the antenna is placed closer to the mast structure (i.e., $\lambda/4$ m) there is an overall elevation in the fitted relative near field power flux density. This elevation in the relative near field power flux density is most likely attributed to an increase in the mutual coupling between the antenna and mast structure, which would be as expected. No comparison between the FEKO and MWS fitted relative near field power flux density results for an antenna-to-mast separation of $\lambda/4$ m could be done, because MWS gave an error and simulation crashed, stating that antenna was too close to mast structure. The minimum antenna-to-mast separation permissible in MWS for the fitted simulations was 0.113m (i.e., $\sim \lambda$ m).

The MWS (or CST) relative fitted near field power flux density plot in **Figure 49** tends to be smoother compared to the FEKO plots. This is mainly attributed to the difference in the angle increment that was used for the simulations in each of the different CEM simulation tool (i.e., $\Delta\varphi=1^\circ$ in MWS (or CST) and $\Delta\varphi=5^\circ$ in FEKO). The FEKO results could be improved further by reducing the angle increment.

4.3 MUTUAL ANTENNA-TO-ANTENNA COUPLING

4.3.1 Antenna 2 located Above Antenna 1

4.3.1.1. Free space (Without Mast Structure)

Figure 50 illustrates the schematic of the locations of antenna 1 and antenna 2 for the free space mutual antenna-to-antenna coupling. Here antenna 2 (i.e., denoted as the receive antenna) is assumed to be orientated at an angle $\Phi\sim 92.2^\circ$ and at distance $d=0.9039$ m relative from the center of antenna 1 (i.e., denoted as the transmit antenna). Antenna 1 was a 4x1 linear array and antenna 2 was a 1x1 linear array antenna.

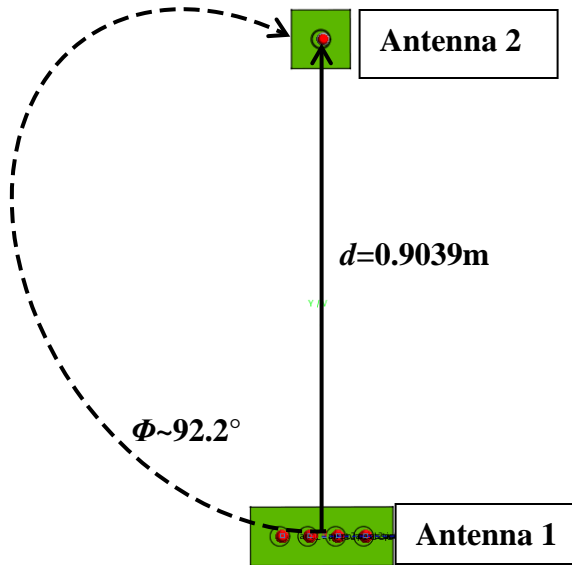


Figure 50. Schematic of the locations of antenna 1 and antenna 2. Here the z -axis, or boresight of antenna 1 is directed out of page, and the angle of orientation Φ of antenna 2 is measured relative from the boresight of antenna 1. Therefore, the antenna 2 angle of orientation curve is highlighted here as a dotted line to indicate that the direction is going from out of page into the page.

Figure 51 illustrates the free space mutual antenna-to-antenna coupling between antenna 1 and antenna 2 for the case where antenna 2 is at orientated at an angle= 92.2° and distance $d=0.9039\text{m}$ away from the center of antenna 1. Antenna 1 is assumed to have a scan angle $\theta=0^\circ$. In **Figure 51** the analytical results, which were determined using Friis transmission equation and Scattering Matrix and Reciprocity Theorem [39], were compared to numerical simulated results using two different techniques namely Method of Moments (i.e., FEKO) and a Shooting and Bouncing Rays asymptotic technique (i.e., Savant).

The S parameter results from FEKO simulations shows four different coupling plots (i.e., S_{12} , S_{13} , S_{14} and S_{15}) in **Figure 51** this is because the 4×1 linear array antenna assumed that each linear array antenna element had their own antenna feed port. Therefore the transmission coupling was determined between each of the $4 \times$ linear array antenna element feed ports and the 1×1 receive antenna element feed port. Linear array port description will not be given here, but is illustrated in detail in **Appendix A.2**. In most linear array antenna and subsequently phased array radars designs there is typically only one electromotive generator and from there the radiation is adjusted by phase shifting at each of the array elements. Future work can modify the present model of the linear array antenna to include a single antenna electromotive generator in order to determine a single transmission S -parameter (i.e., S_{12}) between the linear array and receive antennas.

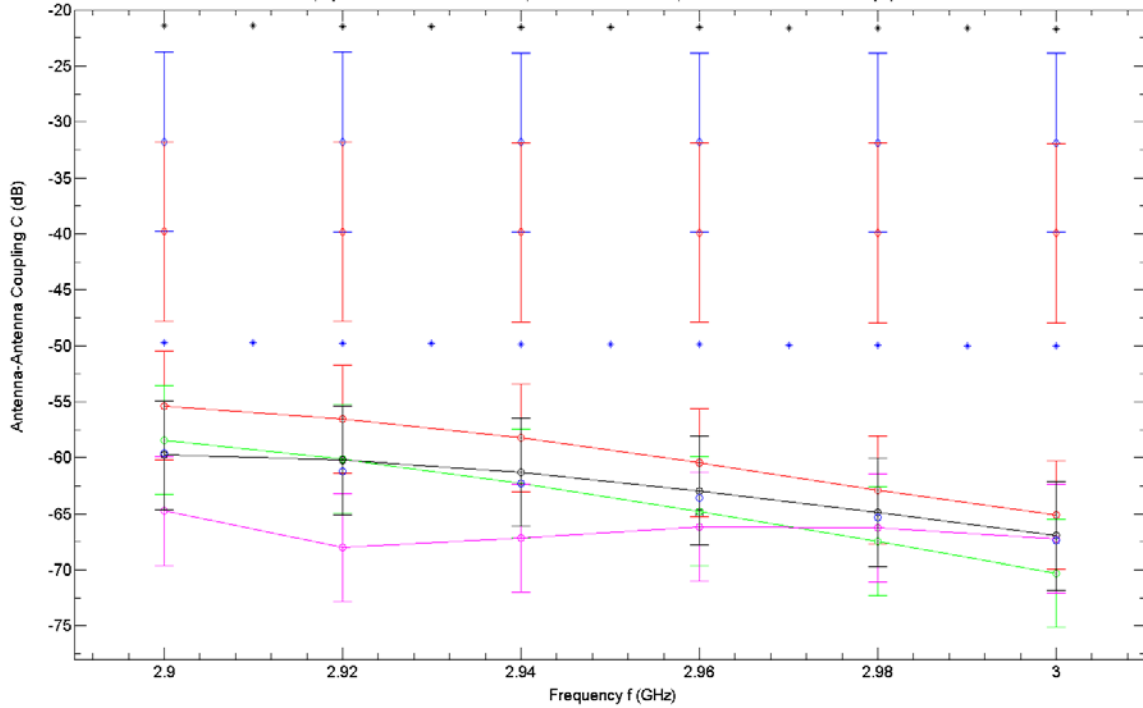


Figure 51. Free space mutual antenna-to-antenna coupling between a 4x1 linear array transmitter and a 1x1 linear array receiver, for transmit antenna scan angle $\theta=0^\circ$. Receiver antenna is located at a distance $d=0.9039\text{m}$ and orientated at an angle $\Phi=92.2^\circ$, relative from the center of the 4x1 linear array transmitter antenna to feed port of receive antenna. Antenna aperture efficiency η for both transmitter and receiver antenna in the Friis transmission calculation is assumed to be unity (i.e., 100% efficiency). * Friis transmission with mismatch polarization and free space path losses * Friis transmission with free space path loss without mismatch polarization loss, \square Scattering Matrix & Reciprocity Theorem (Roubine and Bolomey (1987) [39]), \diamond S_{12} parameter –Savant (SBR) Tx and Rx current sources, \diamond S_{12} parameter –Savant (SBR) Tx current source and Rx radiation pattern, \circ S_{15} parameter –FEKO (MoM), \circ S_{14} parameter –FEKO (MoM), \circ S_{13} parameter –FEKO (MoM), \circ S_{12} parameter –FEKO (MoM), and \circ S parameters average –FEKO.

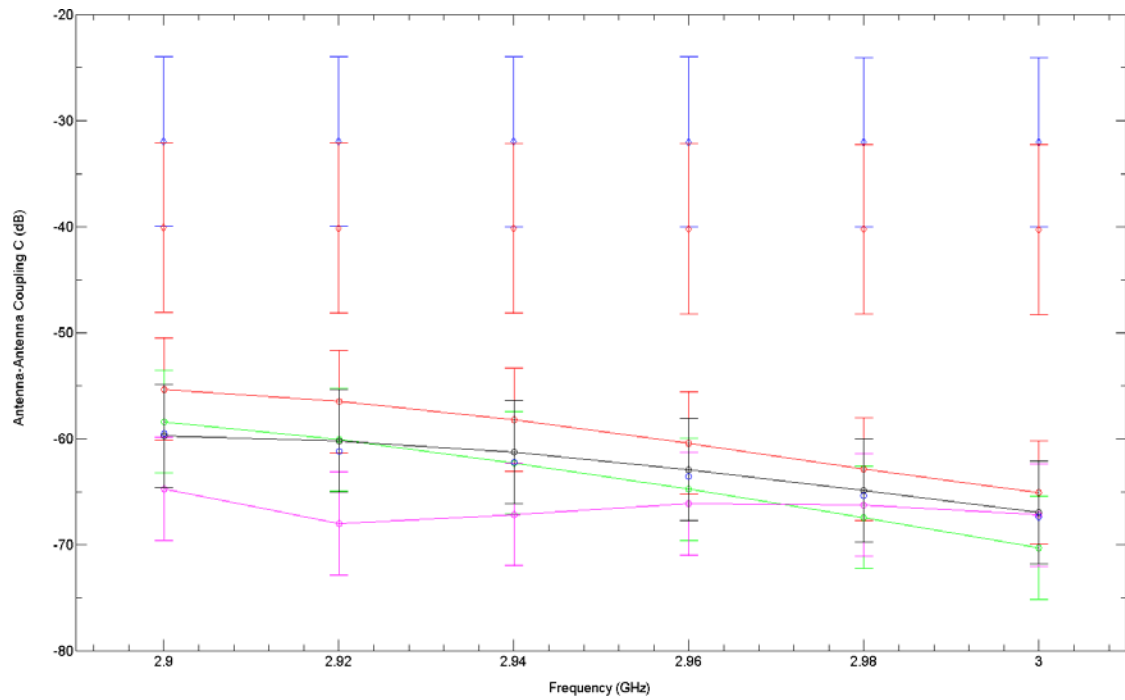
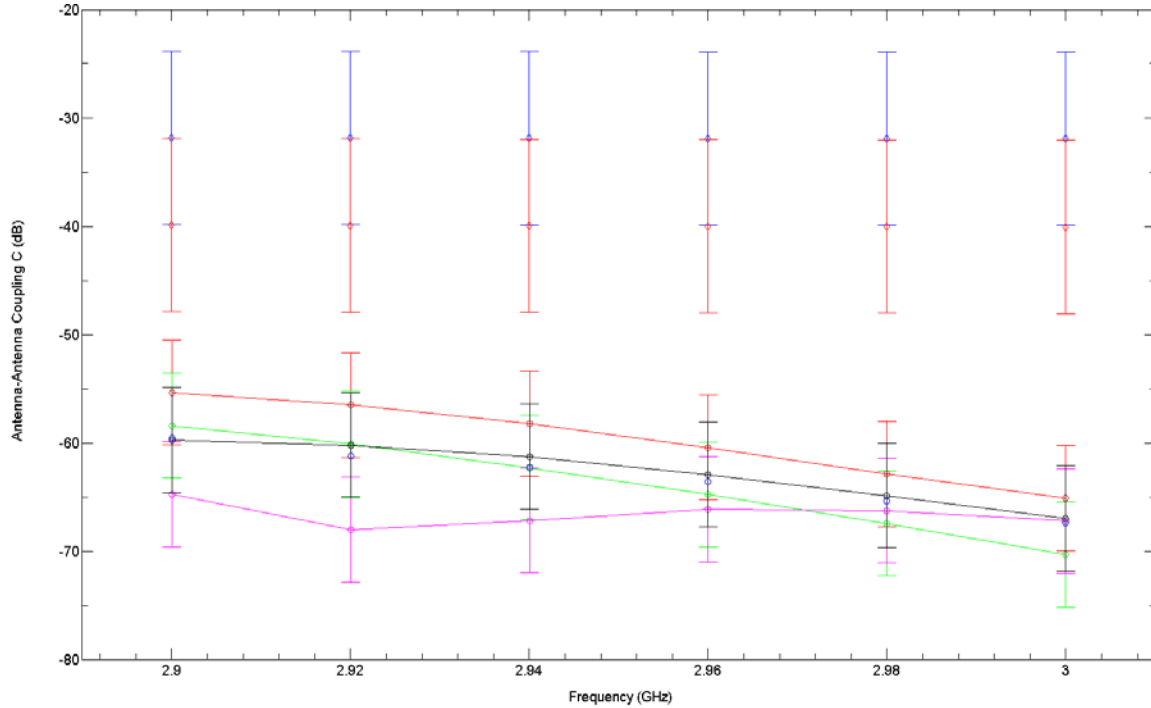
As illustrated in **Figure 51** there is good agreement between the simulated results (i.e., FEKO and Savant) and the analytical results (i.e., Friis transmission and Scattering Matrix and Reciprocity Theorem [39]). The Friis transmission mutual antenna-to-antenna coupling analytical results tend to lie in between the simulated mutual antenna-to-antenna coupling results from FEKO and Savant, across all the frequencies (i.e., 2.9GHz to 3GHz). In particular, the Friis transmission mutual antenna-to-antenna coupling results are higher in value, despite considering power loss due to mismatch polarization, than the simulated FEKO mutual antenna-to-antenna coupling results. The high Friis transmission analytical coupling results are most likely attributed to the assumption that both antenna 1 and antenna 2 had unity antenna aperture efficiency. Antennas aperture efficiency η is

always < 1 , which is due to losses within the antenna, including illumination efficiency (i.e., ratio of the directivity of the antenna to the directivity of a uniformly illuminated antenna of the same aperture size); phase error loss due to the fact that the aperture is not a uniform phase surface, mismatch (VSWR) loss; and RF losses between the antenna and the antenna feed port or measurement point. Therefore, this assumption of unity aperture efficiency was not valid. Therefore, if the antenna aperture efficiency was correctly assumed in the Friis Equation calculations, this would in turn reduce the gain for the transmit and receive antennas, and hence lower the Friis transmission analytical mutual antenna-to-antenna coupling results in **Figure 51**, to fit within the simulated FEKO mutual antenna-to-antenna coupling results.

The simulated mutual antenna-to-antenna coupling from Savant results (i.e., assuming current source files for both antenna 1 and antenna 2, and current source for antenna 1 and 3-D radiation pattern for antenna 2) lie below the analytical Friis transmission mutual antenna-antenna coupling results, assuming no mismatch polarization, but higher than the analytical Friis transmission mutual antenna-to-antenna coupling results, assuming mismatch polarization. It is interesting to note that when current source files were used for both antenna 1 and antenna 2 in Savant the mutual antenna-to-antenna coupling results are higher in value compared to when a current source is used for antenna 1 and the 3-D radiation pattern for antenna 2. Furthermore, it is interesting to highlight that when current sources are considered for antenna 1 and antenna 2, the simulated mutual antenna-to-antenna coupling results lay closer to the Friis transmission mutual coupling, assuming no mismatch polarization loss. Whereas, when a current file for antenna 1 and a 3-D radiation pattern for antenna 2 is used the Savant simulated mutual antenna coupling results tends to be lower and comparable more with the Friis transmission coupling results, assuming losses due to mismatch polarization.

It is interesting to note further from **Figure 51**, that the mutual antenna-to-antenna coupling decreases with increasing frequency. This result was evident for all analytical (Friis transmission equation) and simulation results (i.e., FEKO and Savant). However, from **Figure 51**, this conclusion is quite evident from the FEKO results, but not so from the analytical Friis transmission equation and the Savant simulated results. This is attributed to the large antenna-to antenna coupling (i.e., y-scale) scale that is used in **Figure 51** in order to fit all analytical and simulated results on the one graph. By plotting the analytical Friis transmission and simulated Savant results on their own separate figures (refer to **Appendix A.5, Section A.5.3**) this decrease in the mutual antenna-to-antenna-coupling with increasing frequency becomes distinct. This decrease in the mutual antenna-to-antenna coupling with increasing frequency is as expected, since as frequency increases the transmitted power increases as a function of f^2 , and since the mutual coupling constant, from the Friis transmission theory, $C = \frac{P_r}{P_t} \propto \frac{1}{f^2}$, means that that as frequency increases the mutual coupling constant C decreases as a function of $\frac{1}{f^2}$.

Figure 52 illustrates the free space mutual antenna-to-antenna coupling for different transmitter antenna (i.e., antenna 1) scan angles (i.e., $\theta \sim 5^\circ, 11^\circ,$ and 18°) using the different numerical techniques (i.e., MoM and SBR). The receiver antenna (i.e., antenna 2) is assumed to be orientated at an angle $\Phi=92.2^\circ$ and distance $d=0.9039\text{m}$ away from the center of antenna 1 to the antenna 2 feed port.



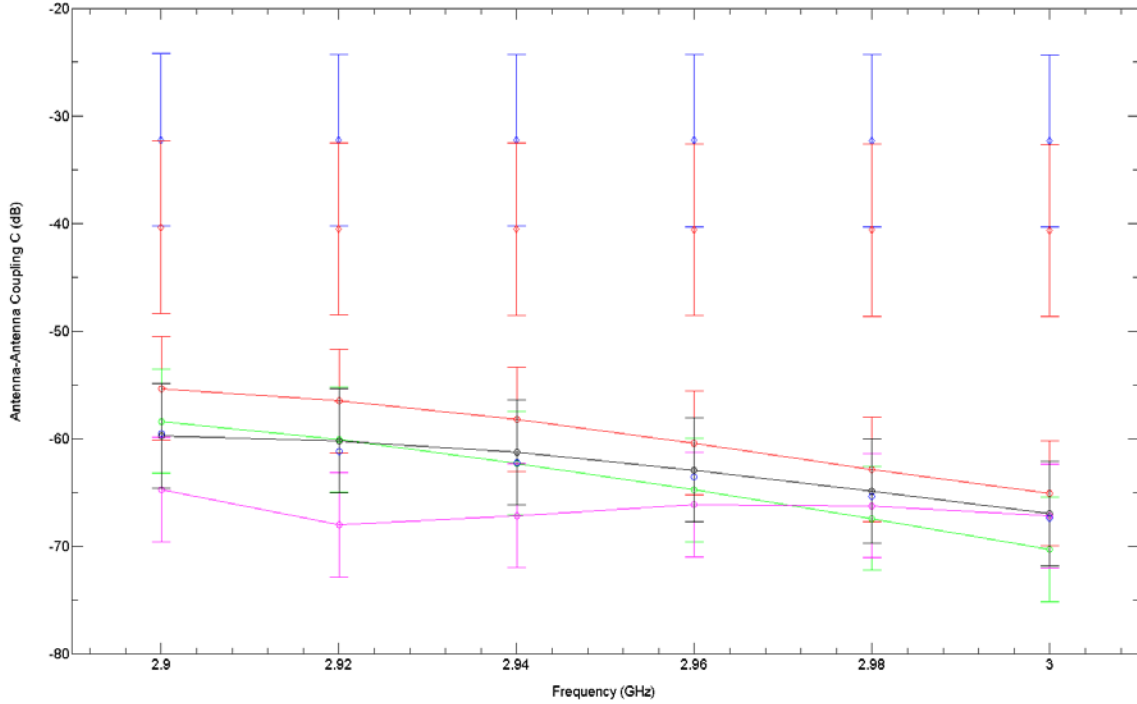


Figure 52. Freespace mutual antenna-to-antenna coupling between a 4x1 linear array transmitter and a 1x1 linear array receiver, for different transmitter antenna scan angles (from *Top to Bottom*) $\theta \sim 5^\circ$, $\theta \sim 11^\circ$ and $\theta \sim 18^\circ$. Receiver is assumed to be at an angle $\Phi=92.2^\circ$ and distance $d=0.9039\text{m}$ relative from the center of the 4x1 linear array transmitter antenna to feed port of receive antenna. \diamond S_{12} parameter – Savant (SBR) Tx and Rx current sources, \diamond S_{12} parameter–Savant (SBR) Tx current source and Rx radiation pattern, \circ S_{15} parameter–FEKO (MoM), \circ S_{14} parameter–FEKO (MoM), \circ S_{13} parameter–FEKO (MoM), \circ S_{12} parameter –FEKO (MoM), and \circ S parameters average–FEKO.

As illustrated in **Figure 52** the free space mutual antenna-to-antenna coupling Savant results are higher in value compared to the coupling results from FEKO. This could be due to the fact that Savant calculations did not consider mismatch polarization between transmit and receive antennas, as was noted in the freespace mutual coupling results for a transmit antenna scan angle of zero degrees. If mismatch polarization is considered in the Savant calculations, then this in turn may reduce the coupling factor to be comparable with the FEKO results.

It is also interesting to note, that the Savant freespace mutual antenna-to-antenna coupling results, assuming current sources for both the transmit and receive antenna, are in better agreement with the FEKO freespace antenna-to-antenna coupling results. Compared to the Savant freespace mutual antenna-to-antenna coupling when a current source is used for the transmitter and a 3-D radiation pattern is used for the receive antenna.

The FEKO antenna-to-antenna coupling results decrease with increasing frequency, which is as expected, as more power is lost at high frequencies than at low frequencies. However, this decrease is not so evident in the Savant coupling results.

Overall, the free space mutual antenna-to-antenna coupling between the transmit antenna and receive antenna, assuming the receive antenna is located at a distance $d = 0.9039\text{m}$ and orientated at an angle $\Phi \approx 92.2^\circ$, is $\sim -55\text{dB}$.

4.3.1.1 Fitted (With Mast Structure)

Figure 53 illustrates a schematic of the locations of antenna 1 and antenna 2 for the fitted mutual antenna-to-antenna coupling FEKO simulations. Antenna 1 is located at a vertical height $h_1 \approx 0.740\text{m}$ from the base of the mast structure, and not explicitly shown in **Figure 53**, is positioned at a distance $\sim \lambda/4\text{m}$ away from the mast structure front panel. Antenna 2 is located at a vertical height $h_2 \approx 1.643\text{m}$ from the base of the mast structure, and slightly displaced from the top edge of the mast structure, front panel by a distance $d' \approx 0.03\text{m}$. Relative to antenna 1, antenna 2 is orientated at an angle $\Phi \approx 92.2^\circ$, from the boresight of antenna 1, and a distance $d=0.9039\text{m}$ away from the center of antenna 1 to the feedport of antenna 2. Similar positions for antenna 1 and antenna 2 were used for the Savant fitted mutual antenna-to-antenna coupling simulations.

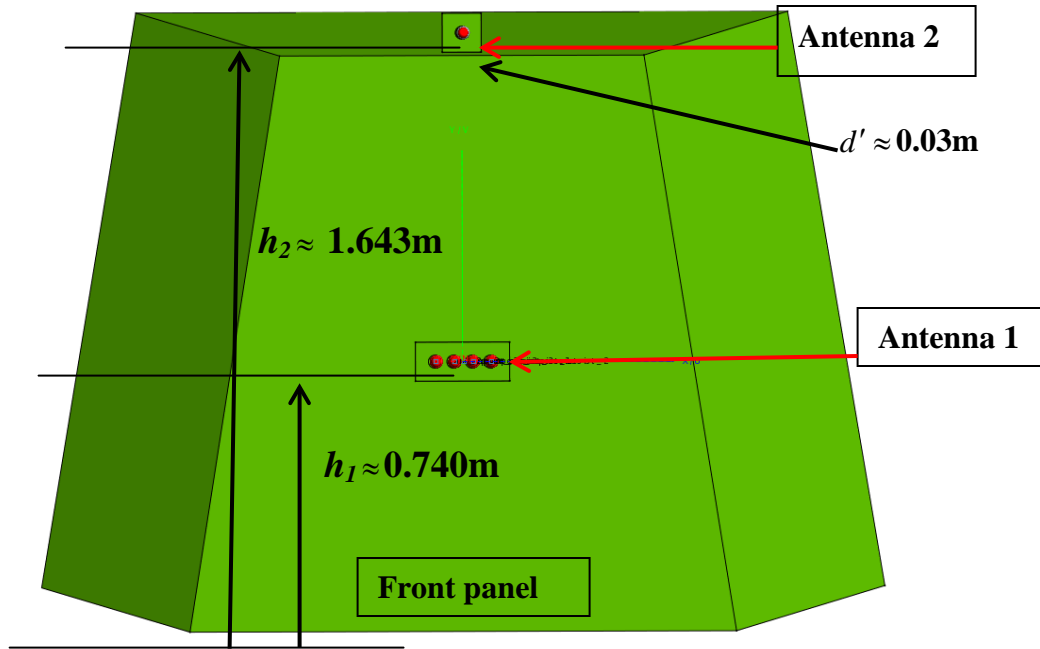
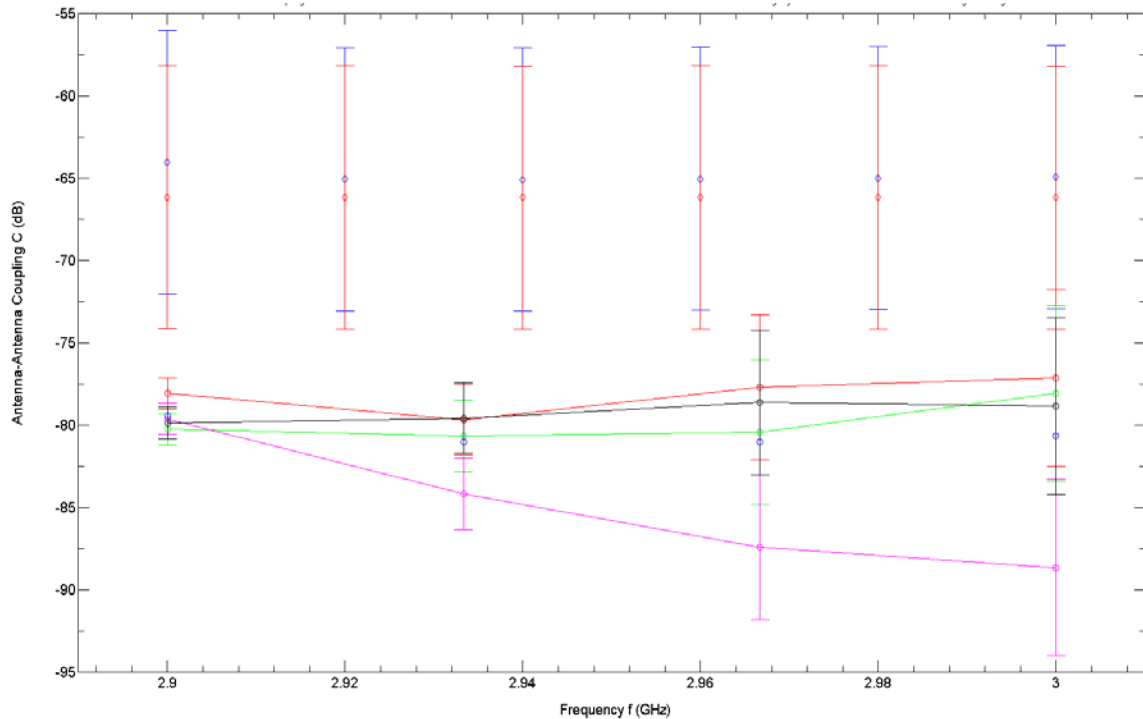
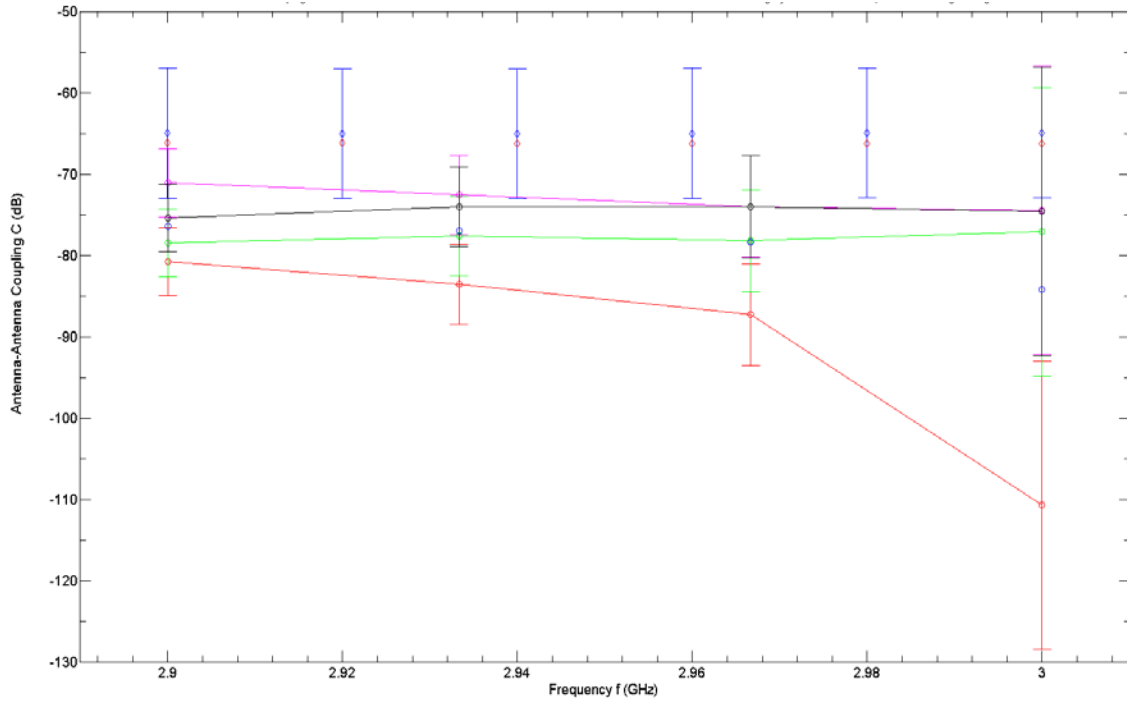


Figure 53. Schematic of the locations of antenna 1 and antenna 2 for the fitted mutual antenna-to-antenna coupling FEKO simulations. Antenna 1, not shown here, is located at distance $\sim \lambda/4$ m away from the mast structure, front panel. Antenna 2 is located at a vertical height $h_2 \approx 1.643$ m from the base of the mast structure, and slightly displaced from the top edge of the mast structure, front panel by a distance $d' \approx 0.03$ m. Relative to antenna 1, antenna 2 is orientated at an angle $\Phi \approx 92.2^\circ$, from the boresight of antenna 1, and a distance $d=0.9039$ m away from the center of antenna 1 to the feedport of antenna 2. Similar, antenna locations and positions were used for the Savant simulations.

Figure 54 illustrates the comparison of the fitted (i.e., with mast structure) mutual antenna-to-antenna coupling between a 4x1 linear array transmitter (i.e., antenna 1) and a 1x1 linear array antenna passive receiver (i.e., antenna 2) for different linear array antenna scan angles, i.e., $\theta=0^\circ, \sim 5^\circ, \sim 11^\circ \sim 18^\circ$ from FEKO and Savant simulations.



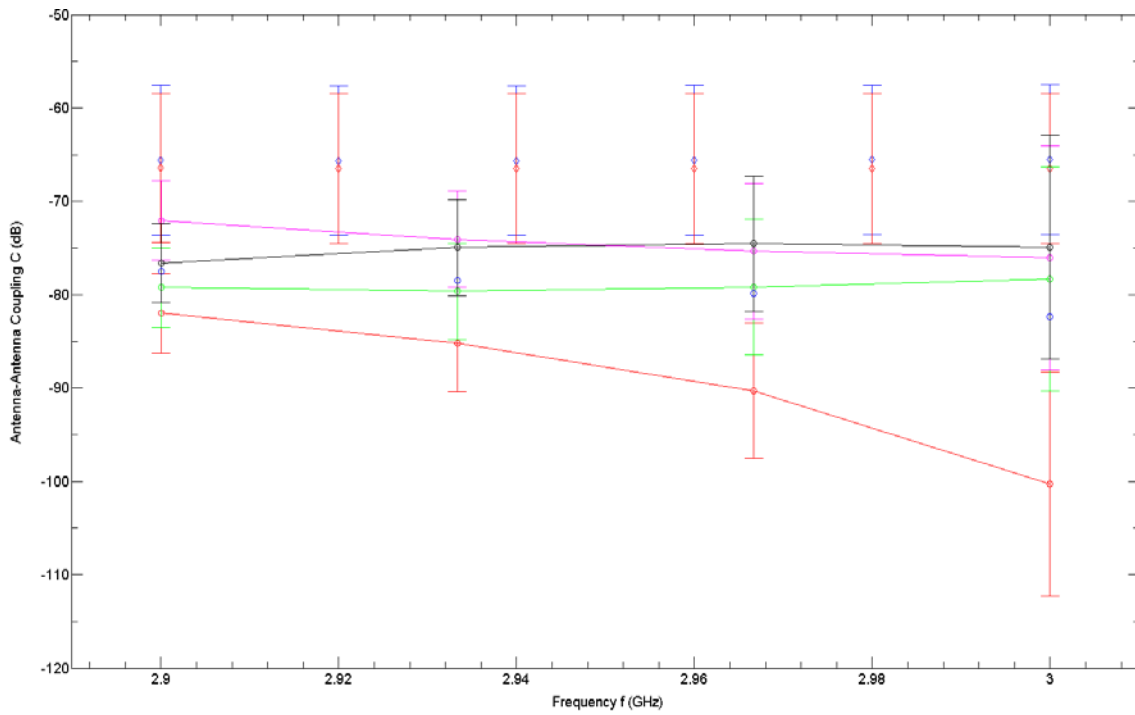
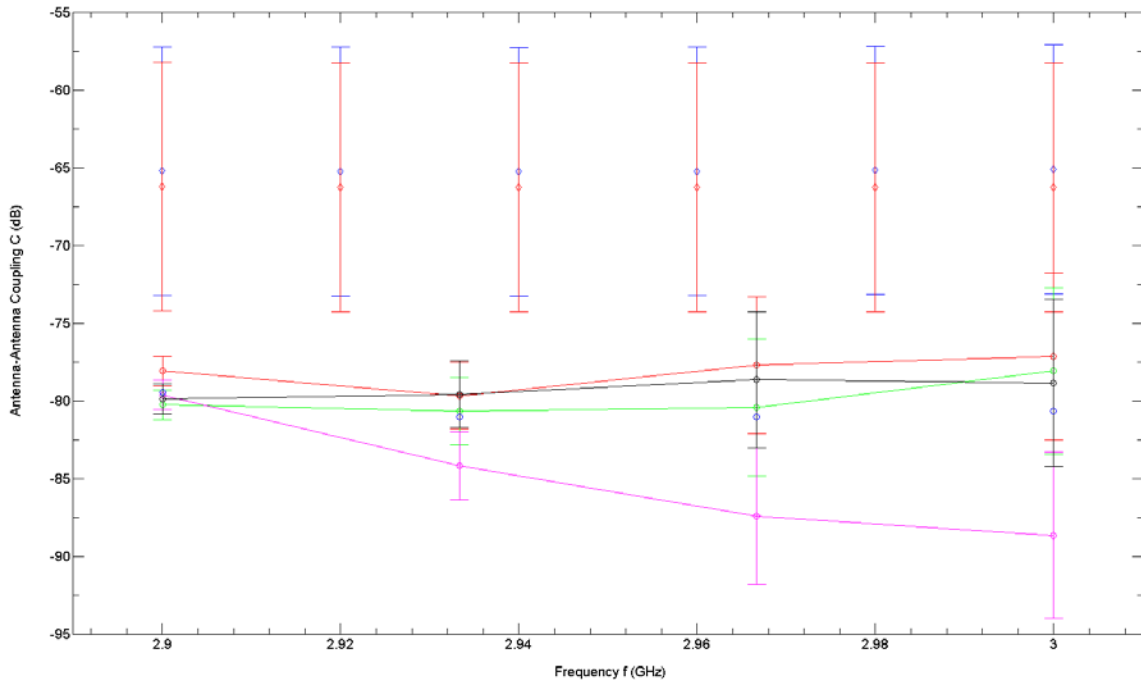


Figure 54. Fitted mutual antenna-to-antenna coupling between a 4x1 linear array transmitter and a 1x1 linear array receiver, for different transmitter antenna scan angles (from *Top to Bottom*) $\theta=0^\circ$, $\sim 5^\circ$, $\sim 11^\circ$ and $\sim 18^\circ$. Receiver is assumed to be at an angle $\Phi=92.2395^\circ$ and distance $d=0.9039\text{m}$ relative from the center of the 4x1 linear array transmitter antenna to feed port of the receive antenna. $\diamond S_{12}$

parameter–Savant (SBR) Tx and Rx current sources, \diamond S_{12} parameter–Savant (SBR) Tx current source and Rx radiation pattern, \circ S_{15} parameter–FEKO (MLFMM), \circ S_{14} parameter–FEKO (MLFMM), \circ S_{13} parameter–FEKO (MLFMM), \circ S_{12} parameter –FEKO (MLFMM), and \circ S parameters average–FEKO. Savant results included internally defined diffraction model.

As illustrated in **Figure 54** overall there is good combined error agreement between the simulated fitted mutual antenna-to-antenna coupling between FEKO and Savant. The Savant fitted mutual antenna-to-antenna coupling tends to agree (with combined error) better across all frequencies with the FEKO fitted S-parameters, S_{13} and S_{12} , for transmit antenna scan angles $\theta=0^\circ$ and $\sim 18^\circ$. Whereas, for transmit antenna scan angles, $\theta\sim 5^\circ$ and $\sim 11^\circ$ the Savant fitted mutual antenna-to-antenna coupling agrees better with the FEKO S-parameters, S_{15} , S_{12} and S_{14} , at the high frequency (i.e., $f=3\text{GHz}$) than at the lower frequencies (i.e., $2\text{GHz} \leq f < 3\text{GHz}$).

Overall, the magnitude of the Savant fitted mutual antenna-to-antenna coupling results tend to be larger (i.e., $\sim 10\text{dB}$) compared to the FEKO fitted mutual antenna-to-antenna coupling results over all the frequencies (2.9GHz to 3GHz). There could be a number of reasons that attribute to this; for example, Savant does not consider losses due to mismatch polarization between transmit and receive antennas, as was indicated in the free space mutual antenna-to-antenna coupling results. In addition, the transmit antenna model using current source file, assumed that the current moments at each of the frequencies were unity and all the same. Furthermore, errors could also have slipped in with regards to the methodology in each CEM software tool to determine the mutual antenna-to-antenna coupling, and the location and orientation of the antennas in each simulation tool. In Savant the mutual antenna-to-antenna coupling was based on using the antenna radiation patterns, whereas in FEKO the coupling was based on the coupling between each of the linear array antenna element feed ports and the receive antenna feed port. In addition, antenna 2 was assumed to be at a distance $d \approx 0.9039\text{m}$ relative from the antenna 1 in Savant. For FEKO, the feed ports of the linear array antenna elements, which refer to the S-parameters S_{15} and S_{14} both are at a distance $d \approx 0.9120\text{m}$ away from the receiver antenna feed port. Whereas, the feed ports of the linear array antenna elements, which refer to S-parameters S_{13} and S_{12} are both at a distance $d \approx 0.9067\text{m}$ away from the receive antenna feed port. Therefore, the distance between the feed ports of the linear array antenna elements, which refer to the FEKO S-parameters S_{12} and S_{13} , are both closer to the calculated distance (i.e., 0.9039m , relative from the center of the transmit antenna to receive antenna feedport) between transmit and receive antennas used in Savant calculations. Then it would be expected that there would be some differences in the coupling results and why the Savant coupling results are more comparable with the FEKO S-parameters S_{12} and S_{13} , compared to S_{15} and S_{14} .

Overall, for the case in which the receive antenna is fitted on a mast structure (perfect electrical conductor) and placed above a transmit antenna, at a distance $d \approx 0.9039\text{m}$ and orientated at an angle, relative from the transmit antenna, $\Phi \approx 92.2^\circ$, the fitted antenna-to-antenna coupling is between $\sim -70\text{dB}$ to $\sim -80\text{dB}$.

Comparing the fitted (i.e., with mast structure) mutual antenna-to-antenna coupling factor (i.e., ~ -70 to ~ -80 dB) to the free space (i.e., without mast structure) mutual antenna-to-antenna coupling (i.e., ~ -60 dB). Assuming the receive antenna is located at a distance $d \approx 0.9039$ m and $\Phi \approx 92.2^\circ$, relative to the center of the transmit antenna, it appears that there is a reduction, (i.e., ~ 10 dB), in the coupling. This would tend to indicate that there is some further power loss when the antennas are fitted on the mast structure than in free space. This in turn would suggest that there is most likely interference or scattering occurring between the transmit antenna and the mast structure, where the mast structure (due to its shape and structural design), is re-directing any scattered electromagnetic (EM) power from the transmit antenna away from the receive antenna. In addition, there could also be some blockages between transmit and receive antennas by the mast structure, where the mast structure is blocking some of the transmit antenna EM power from reaching the receive antenna.

4.3.2 Antenna 2 located on Side Panel

4.3.2.1 Free space (Without mast structure)

Figure 55 illustrates the schematic of the locations of antenna 1 and antenna 2 for the free space mutual antenna-to-antenna coupling simulations in FEKO. Where antenna 2 is orientated at an angle $\Phi \approx 89.5^\circ$ (i.e., $97.5^\circ - 8.8^\circ$ (due to a slight tilt in antenna)) and at a distance $d = 0.9101$ m, relative from the center of antenna 1 to the feed port of antenna 2. Similar locations for antenna 1 and antenna 2 were used in the free space mutual antenna-to-antenna coupling for the Savant simulations.

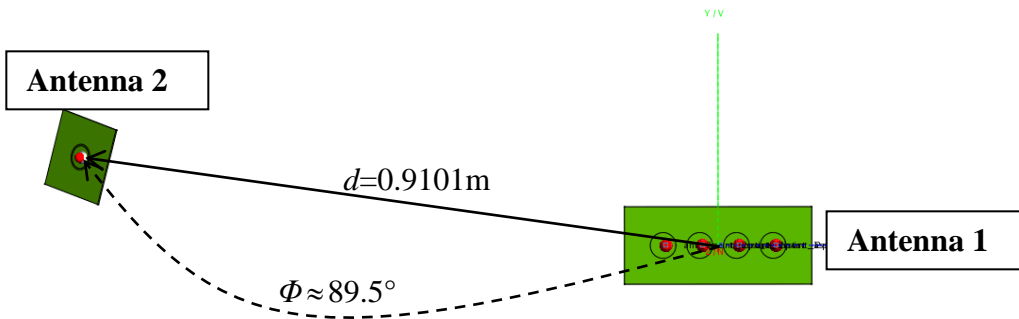


Figure 55. Schematic of the locations of antenna 1 and antenna 2 for the mutual antenna-to-antenna coupling, where antenna 2 is orientated at an angle $\Phi \approx 89.5^\circ$ and at a distance $d = 0.9101$ m, relative from the center of antenna 1 to the feed port of antenna 2. The angle of orientation Φ for antenna 2 is depicted as a dashed curve to represent that the angle is measured relative from the boresight (i.e., z -axis) of antenna 1, which is directed out of page here.

Figure 56 illustrates the free space mutual antenna-to-antenna coupling between a 4×1 linear array antenna (i.e., antenna 1) and a 1×1 linear array receive antenna (i.e., antenna 2), for an antenna 1 scan angle $\theta = 0^\circ$. The receiver antenna is orientated at an angle $\Phi \approx 89.5^\circ$ and at a distance $d = 0.9101$ m, relative from the center of the antenna 1 to the feed port of antenna 2.

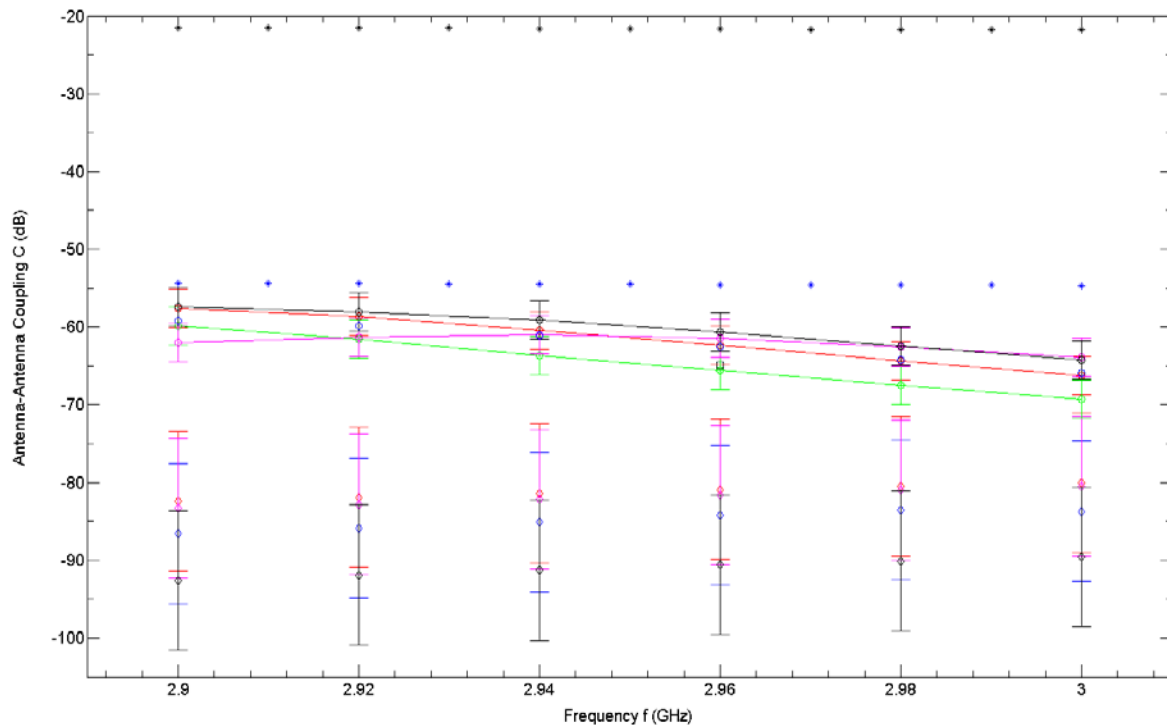


Figure 56. Free space mutual antenna-to-antenna coupling between a 4x1 linear array transmitter and a 1x1 linear array receiver for transmit antenna scan angle $\theta=0^\circ$. Receiver is assumed to be at an angle $\Phi \approx 89.5^\circ$ and distance $d=0.9101\text{m}$ relative from the center of the 4x1 linear array transmitter antenna to the receiver antenna port. Antenna aperture efficiency η for transmit and receive antennas in Friis equation is assumed to be unity (i.e., 100% efficiency). *Friis transmission with mismatch polarization and free space path losses * Friis transmission without mismatch polarization loss with free space path loss, \square Scattering Matrix & Reciprocity Theorem (Roubine and Bolomey 1987) [(39)], \diamond S_{12} parameter –Savant (SBR) Tx and Rx current sources w/o line of sight (LOS), \diamond S_{12} parameter–Savant (SBR) Tx and Rx current sources with LOS, \diamond S_{12} parameter –Savant (SBR) Tx current sources and Rx radiation pattern w/o LOS, \diamond S_{12} parameter –Savant (SBR) Tx current sources and Rx radiation pattern with LOS, \circ S_{15} parameter–FEKO (MoM), \circ S_{14} parameter –FEKO (MoM), \circ S_{13} parameter–FEKO (MoM), \circ S_{12} parameter –FEKO (MoM), and \circ S parameters average–FEKO.

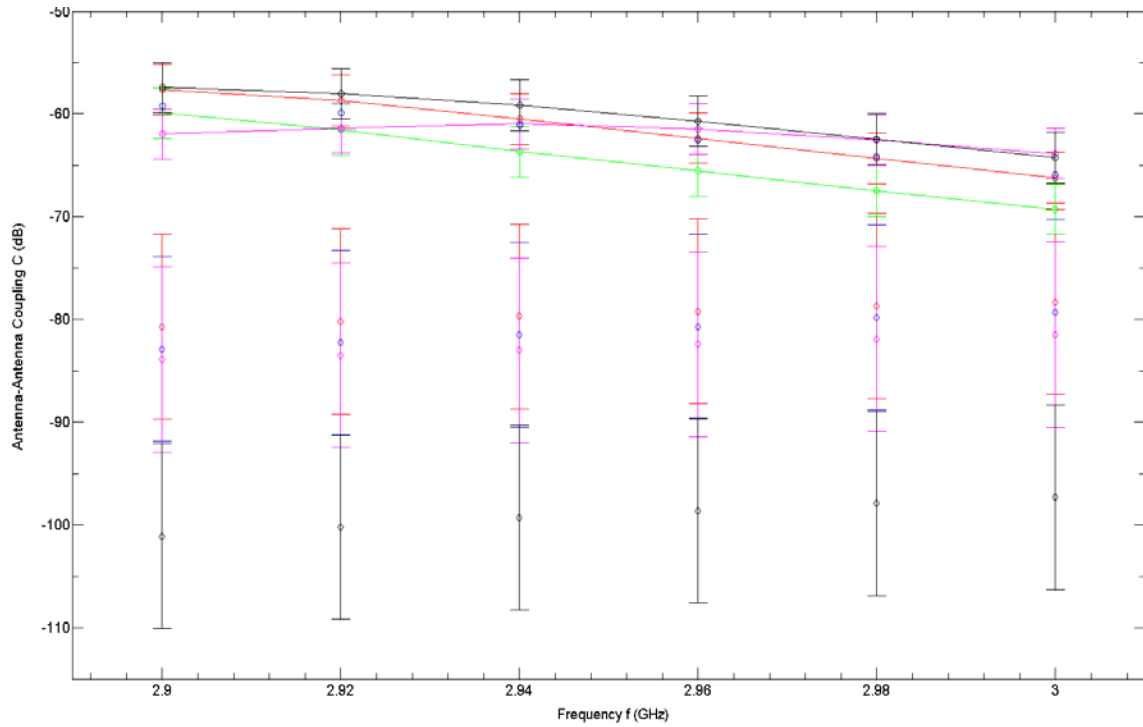
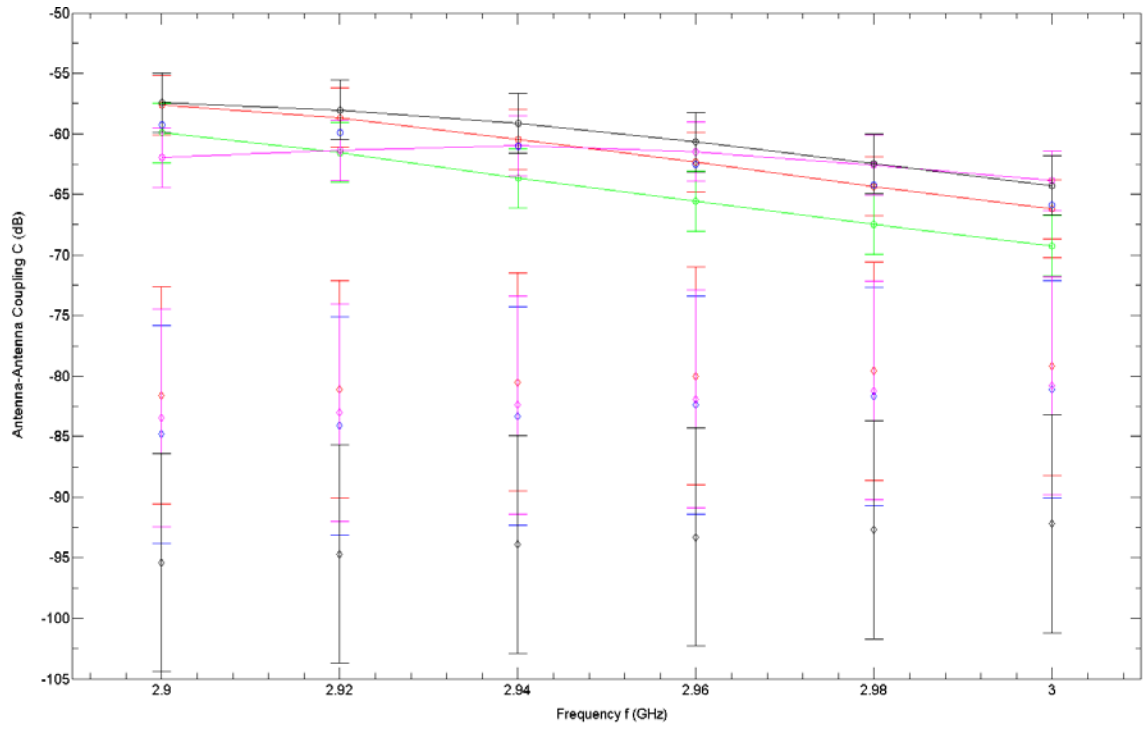
As illustrated in **Figure 56** overall the Savant free space mutual antenna-to-antenna coupling results (i.e., $\sim 85\text{dB}$) are significantly lower (i.e., $\sim 20\text{dB}$) compared to the simulated FEKO free space mutual antenna-to-antenna coupling (S-parameters) results and the analytical Friis transmission equation results. However, tend to be good combined error between the Savant coupling results with simulated FEKO and analytical results at the high frequencies (i.e., $2.98\text{GHz} \leq f \leq 3\text{GHz}$) than at the lower frequencies, i.e., $2.9\text{ GHz} \leq f < 2.98\text{GHz}$.

This difference of ~20dB in the coupling between Savant and FEKO and Friis transmission results at the lower frequencies, maybe due to mismatch polarization not being considered in the Savant calculation. However, from the free space mutual coupling results at a transmit scan angle $\theta=0^\circ$ for a receive and transmit antenna separation of ~ 0.9039m and angle orientation $\Phi \sim 92.2^\circ$ the power loss due to mismatch polarization would only reduce the coupling by a few dB, whereas, in this particular case, the reduction is much greater. Therefore, there must be other additional reasons attributing to this difference. Some of the reasons could include that the receive antenna and thus its antenna radiation pattern, had a look direction, due to the angle of the mast structure side panel, away from the look direction of the transmit antenna and its main beam. Consequently, the method in which Savant calculates the coupling by adding coherently adding the antenna radiation patterns, could be that the corresponding points of the two antenna patterns to determine the coupling was not a maximum or not a minimum when it needed to be. In addition, the transmit antenna using current source file in the Savant simulations assumed unity current moments at each of the frequencies, which may not be a valid assumption. Alternatively, there may be further power losses occurring between transmit and receive antennas in this case that need to be considered and were not considered in the FEKO simulations and the Friis transmission results. However, this latter reason seems less likely as there tends to be good agreement between the simulated (i.e., Savant and FEKO) and analytical (i.e., Friis transmission) coupling results at the higher frequencies.

As mentioned previously, using current sources for the transmit and receive antenna in Savant calculations provide results closer to the FEKO coupling results, compared to the Savant coupling results when an antenna current source and 3-D antenna radiation pattern are used in the simulations.

The FEKO freespace mutual antenna-to-antenna coupling parameters tend to decrease with increasing frequency. However, the S_{14} parameter tends to decrease much faster over the frequencies, compared to the other FEKO parameters, S_{12} , S_{13} and S_{15} .

Figure 57 illustrates the free space mutual antenna-to-antenna coupling between a 4x1 linear array transmitter antenna and a 1x1 linear array receiver antenna for different transmit antenna scan angles, $\theta \sim 5^\circ$, $\sim 11^\circ$ and $\sim 18^\circ$.



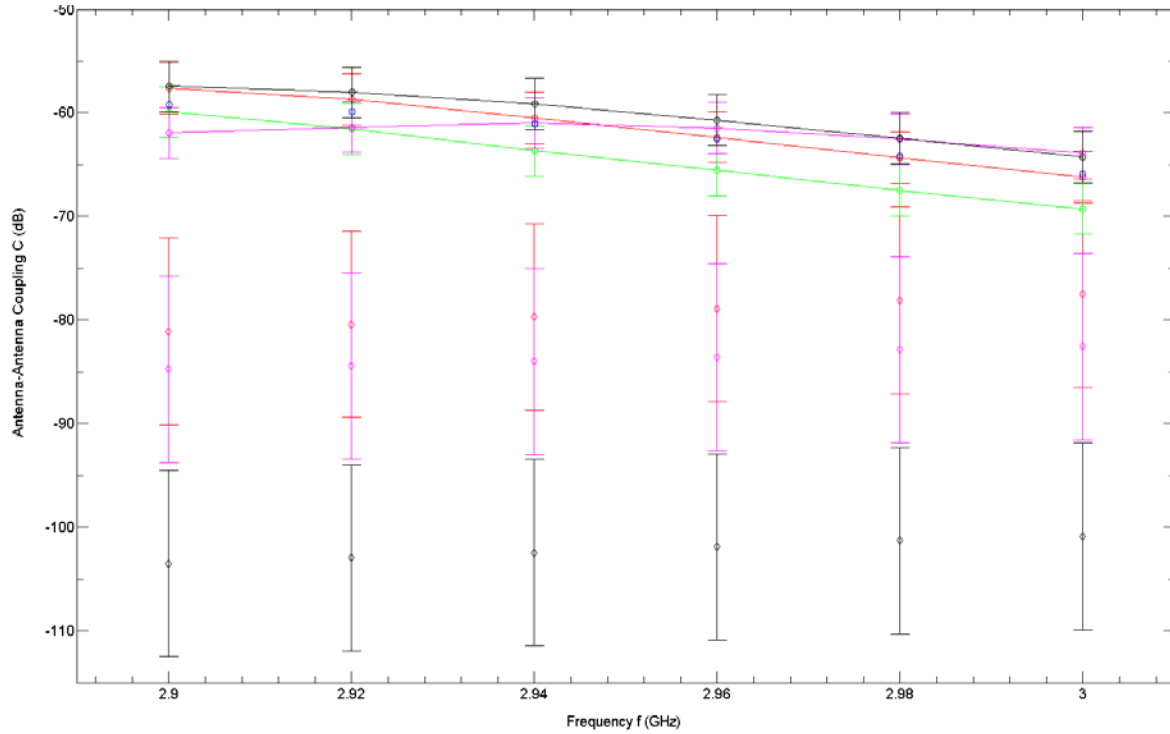


Figure 57. Free space mutual antenna-to-antenna coupling between a 4x1 linear array transmitter and a 1x1 linear array receiver antenna, for difference scan angles (from *Top to Bottom*) $\theta \sim 5^\circ$, $\theta \sim 11^\circ$ and $\theta \sim 18^\circ$. Receiver is assumed to be located at an angle $\Phi \approx 89.5^\circ$ and distance $d=0.9101\text{m}$ relative from the center of the 4x1 linear array transmitter antenna to the receiver antenna feed port. \diamond S_{12} parameter – Savant (SBR) Tx and Rx current sources w/o line of sight (LOS), \diamond S_{12} parameter–Savant (SBR) Tx and Rx current sources with LOS, \diamond S_{12} parameter –Savant (SBR) Tx current sources and Rx radiation pattern w/o LOS, \diamond S_{12} parameter –Savant (SBR) Tx current sources and Rx radiation pattern with LOS, \circ S_{15} parameter–FEKO (MoM), \circ S_{14} parameter –FEKO (MoM), \circ S_{13} parameter–FEKO (MoM), \circ S_{12} parameter –FEKO (MoM), and \circ S parameters average–FEKO.

As illustrated in **Figure 57**, similar results occur, as per **Figure 56**, for different transmit antenna scan angles. Overall, there tends to be good combined error agreement between the calculated free space mutual antenna-to-antenna coupling using FEKO and Savant for each of the different antenna scan angles. However, the agreement tends to be better at the high frequencies (i.e., $2.98\text{GHz} \leq f \leq 3\text{GHz}$), than at the lower frequencies (i.e., $2.9\text{GHz} \leq f < 2.98\text{GHz}$). There is $\sim 20\text{dB}$ difference between the Savant freespace coupling with the simulated FEKO coupling at the lower frequencies. Some reasons that could be attributed to this difference, have already been described previously above, for the case of a transmit scan angle $\theta=0^\circ$, and therefore will not be repeated here. However, suffice to say the difference could be a combination of errors that occur relating to the assumptions made with antenna locations (or distances), coupling calculation methodology and antenna models.

It is also interesting to note that the FEKO coupling decreases with increasing frequency, which is as expected, since $C \propto \frac{1}{f^2}$. Whereas, the Savant coupling tends to increase with increasing frequency. Further work will need to be done to determine the reason for this difference, in what we expect from theory.

In addition, the antenna-to antenna coupling results in **Figure 57** also show that using current sources, rather than a current source file and 3-D radiation pattern, for the transmit and receive antennas in Savant simulations provide results that are in better agreement with the FEKO coupling results.

Overall, the freespace mutual antenna-to-antenna coupling between a transmit antenna and receive antenna, assuming the receive antenna is located at a distance $d \sim 0.9101\text{m}$ and orientated at an angle $\Phi \sim 89.5^\circ$, relative to the center of the transmit antenna, is $\sim -65\text{dB}$.

4.3.2.1 Fitted (With Mast Structure)

Figure 58 illustrates a schematic of the locations of antenna 1 and antenna 2 for the fitted mutual antenna-to-antenna coupling simulations in FEKO. Antenna 1 is located at a vertical height $h_1 \approx 0.740\text{m}$ along the mast structure, front panel, and positioned at a distance $\sim \lambda/4\text{m}$ away from the mast structure, front panel surface. Antenna 2 is placed also positioned at a distance $\sim \lambda/4\text{m}$ away from the mast structure side panel surface, however, at a vertical height $h_2 \approx 0.840\text{m}$ along the mast structure side panel. Similar locations for antenna 1 and antenna 2 were also used for the mutual antenna-to-antenna coupling simulations in Savant.

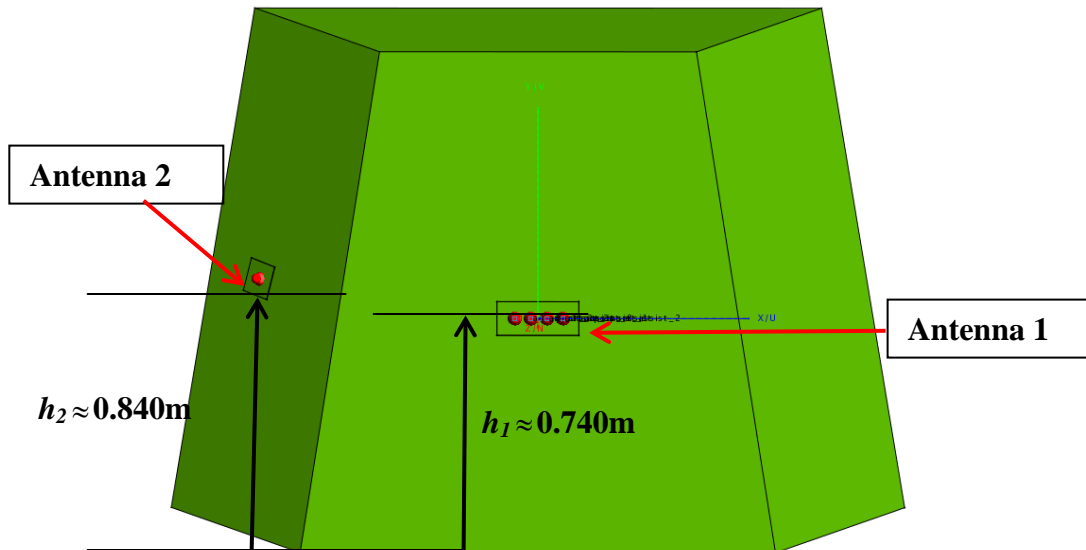
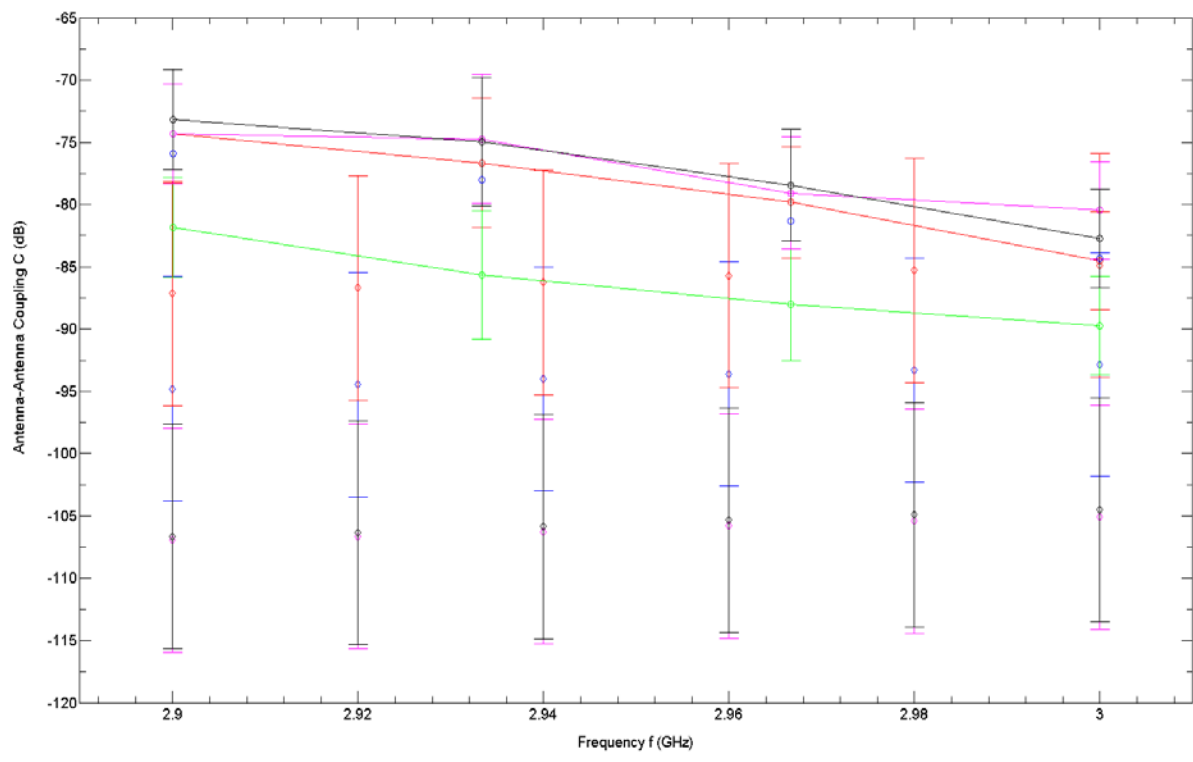
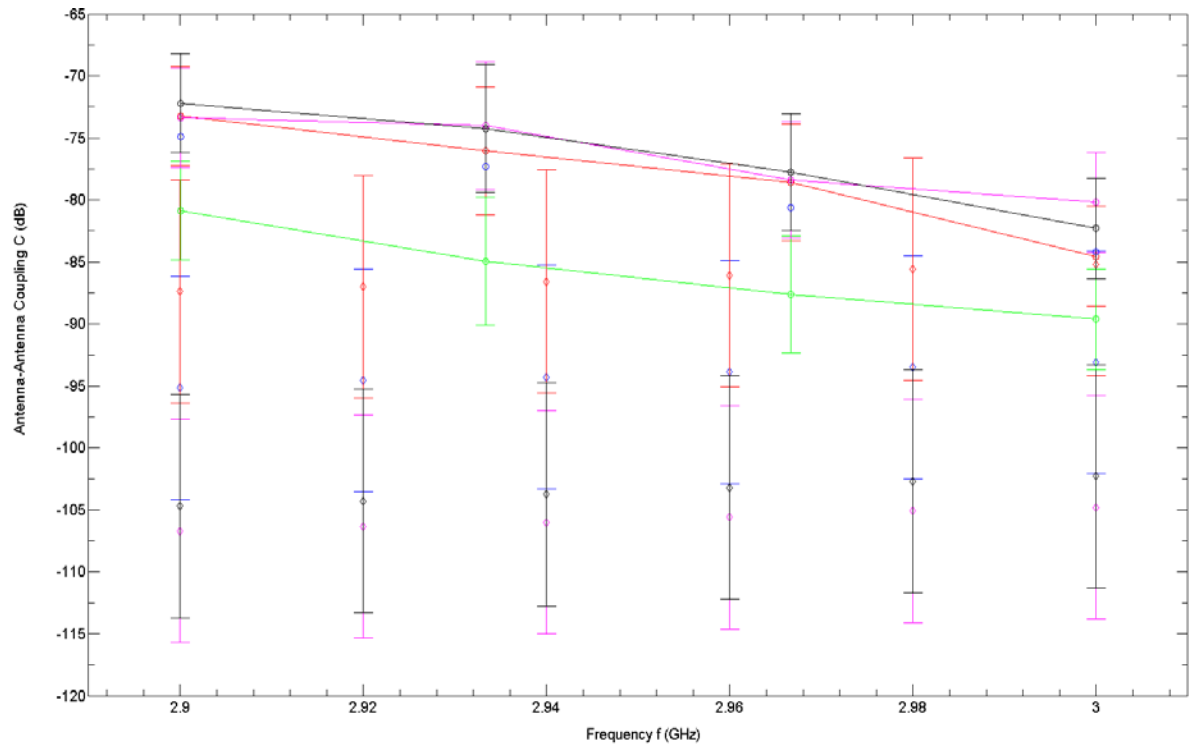


Figure 58. Schematic of locations of antenna 1 and antenna 2 for fitted mutual antenna-to-antenna coupling simulations in FEKO. Antenna 1 is located at a vertical height $h_1 \approx 0.740\text{m}$ along the mast structure front panel, and positioned at a distance $\sim \lambda/4\text{m}$ away from the mast structure front panel surface. Antenna 2 is also positioned at a distance $\sim \lambda/4\text{m}$ away from the mast structure side panel surface, however, located at a vertical height $h_2 \approx 0.840\text{m}$ from the base of the mast structure. Similar locations for antenna 1 and antenna 2 were used also for the mutual antenna-to-antenna coupling simulations in Savant.

Figure 59 illustrates the comparison in the fitted mutual antenna-to-antenna coupling between a 4x1 linear array transmitter antenna and a 1x1 receiver antenna, for different transmitter antenna scan angles, $\theta=0$, $\sim 5^\circ$, $\sim 11^\circ$, and $\sim 18^\circ$ from the FEKO and Savant simulations. Relative to antenna 1, antenna 2 is orientated at an angle $\Phi \approx 89.5^\circ$ and located at a distance $d=0.9101\text{m}$, from the center of the 4x1 linear array transmitter to the receiver antenna feed port.



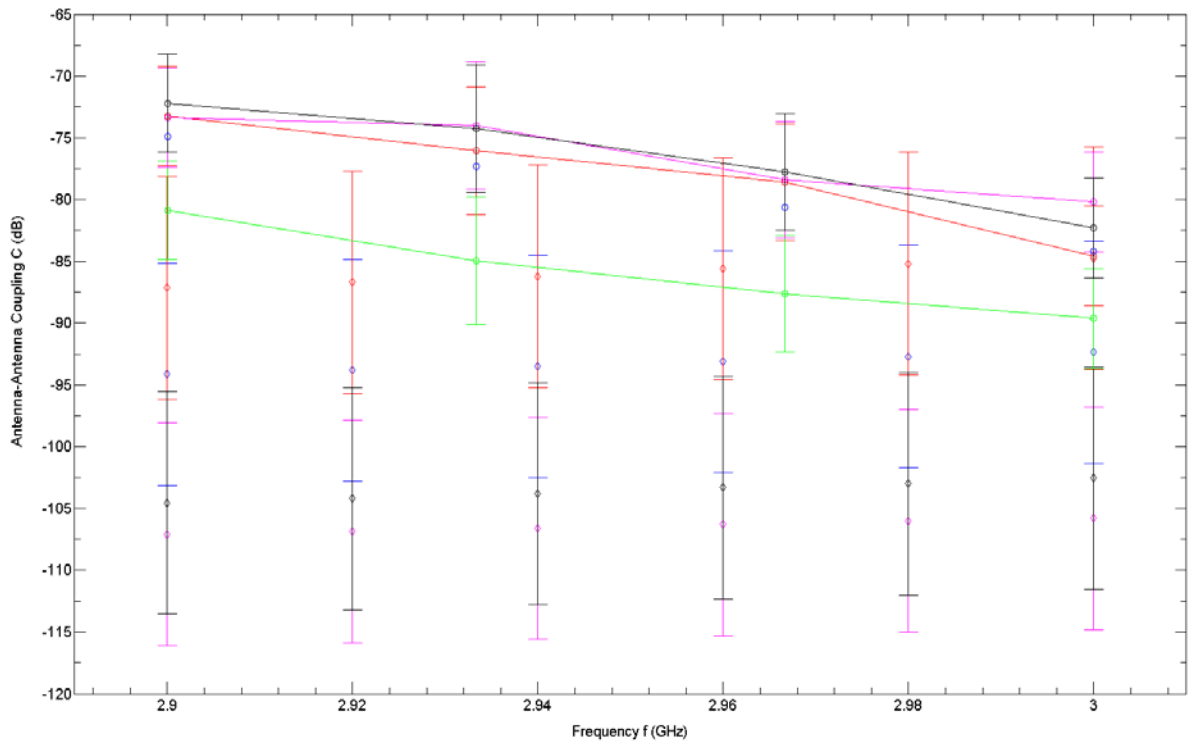
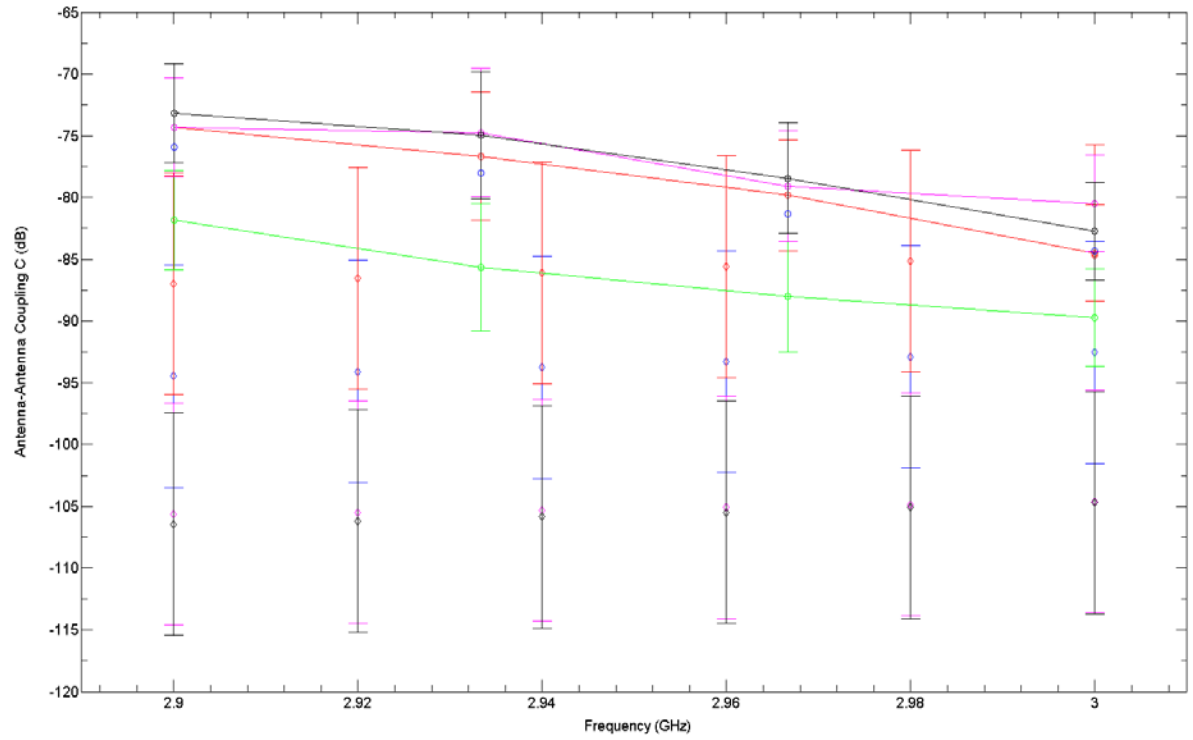


Figure 59. Fitted mutual antenna-to-antenna coupling between a 4x1 linear array transmitter antenna and a 1x1 linear array receiver, for different transmit antenna

scan angles (from *Top to Bottom*) $\theta=0^\circ$, $\theta \sim 5^\circ$, $\theta \sim 11^\circ$ and $\theta \sim 18^\circ$. Receiver antenna is assumed to be located at an angle $\Phi \approx 89.5^\circ$ and distance $d=0.9101\text{m}$ relative from the center of the 4x1 linear array transmitter antenna to the receiver antenna feed port. \diamond S_{12} parameter –Savant (SBR) Tx and Rx current sources w/o line of sight (LOS), \diamond S_{12} parameter–Savant (SBR) Tx and Rx current sources with LOS, \diamond S_{12} parameter –Savant (SBR) Tx current sources and Rx radiation pattern w/o LOS, \diamond S_{12} parameter –Savant (SBR) Tx current sources and Rx radiation pattern with LOS, \circ S_{15} parameter–FEKO (MoM), \circ S_{14} parameter –FEKO (MoM), \circ S_{13} parameter–FEKO (MoM), \circ S_{12} parameter –FEKO (MoM), and \circ S parameters average–FEKO. Savant results included internally defined diffraction model.

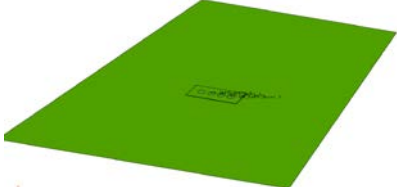

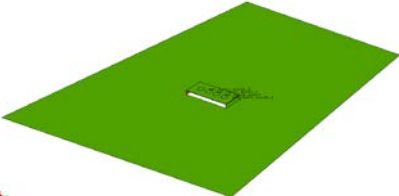
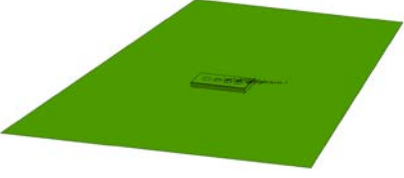
As illustrated in **Figure 59** overall there is good combined error agreement between the fitted mutual antenna-to-antenna coupling between FEKO and Savant across all the different transmit antenna scan angles, i.e., $\theta=0^\circ$, $\sim 5^\circ$, $\sim 11^\circ$, $\sim 18^\circ$, and all frequencies, i.e., $2.9 \text{ GHz} \leq f \leq 3 \text{ GHz}$. There does tend to be better agreement between the Savant and FEKO fitted antenna-to-antenna coupling results. When in the Savant simulations the receive antenna was positioned on the mast structure sidepanel where the receive antenna had some line-of-sight with the transmit antenna radiation pattern compared to when the receive antenna had no line-of-sight (i.e., blocked by the mast structure) with the transmit antenna. Overall, in Savant using current sources files to model transmit and receive antennas, including the internal Savant diffraction model, did indeed give better fitted mutual antenna-to-antenna coupling results with the FEKO coupling, compared to using a current source file and a 3-D antenna radiation pattern.

Overall, the fitted mutual antenna-to-antenna coupling between transmit and receive antennas when both are fitted on a mast structure, and assuming that the receive antenna is located at distance $d \approx 0.9101\text{m}$ and at an angle $\Phi \approx 89.5^\circ$, relative from the center of the transmit antenna, is $\sim -85\text{dB}$. By comparing the freespace mutual antenna-to-antenna coupling (i.e., $\sim -65\text{dB}$), assuming the same receive antenna orientation and distance from antenna 1 (i.e., distance $d \approx 0.9101\text{m}$ and at an angle $\Phi \approx 89.5^\circ$), to the fitted mutual antenna-to-antenna coupling (i.e., $\sim 85\text{dB}$), the coupling is reduced by $\sim 20\text{dB}$. This in turn suggests that the mast structure either blocks, scatters, or a combination of both, electromagnetic energy of the transmit antenna away from the receive antenna.

4.4 DIFFERENT ANTENNA MOUNTING OPTIONS

It was of interest to investigate some extra different mounting options for the linear array on the mast further to the $\lambda/4\text{m}$ or 0.113m separations of the antenna and the large electrical mast structure, which have been modeled in mid-air without any form of attachment/mounting to the mast structure, which is not realistic. Therefore, to simulate some reality to the model four different mounting options of the antenna on the mast structure were considered. The mounting options considered are listed and described in **Table 10**. The different antenna mounting options in **Table 10** are not meant to be an exhaustive list.

Table 10 Summary of Different antenna Mounting Options and description

Antenna Mounting Options	Brief Model Description
<p>A) Fully Integrated (or flush mounted)</p> 	<p>Antenna mounted on front panel of rectangle panel mast where the antenna PEC ground plane is attached to the PEC mast panel structure</p>
<p>B) Integrated partial boxed – front ends</p> 	<p>Antenna located $\lambda/4$ m from mast front panel , mast panel cut with the same dimensions as of the antenna , and antenna attached to mast by perfect electrical conductor panels (length of antenna) at both front and back</p>
<p>C) Integrated partial boxed-side ends</p> 	<p>Antenna located $\lambda/4$ m from mast front panel, mast panel cut with the same dimensions of the antenna, and antenna attached to mast by perfect electrical conductor panels (width of antenna) at both side ends</p>
<p>D) Integrated fully boxed</p> 	<p>Antenna located $\lambda/4$ m from mast front panel, mast panel cut with the same dimensions as of the antenna, and antenna attached to mast by perfect electrical conductor panels (width of antenna) at front, back and side ends</p>

4.4.1 Antenna Radiation Pattern

Figure 60 illustrates the comparison of the normalized free space and fitted antenna radiation patterns as a function of elevation θ , cut at $\varphi=0^\circ$, for each of the different antenna mounting options of the 4x1 linear array antenna on the mast structure. Here the transmit antenna scan angle $\theta=0^\circ$.

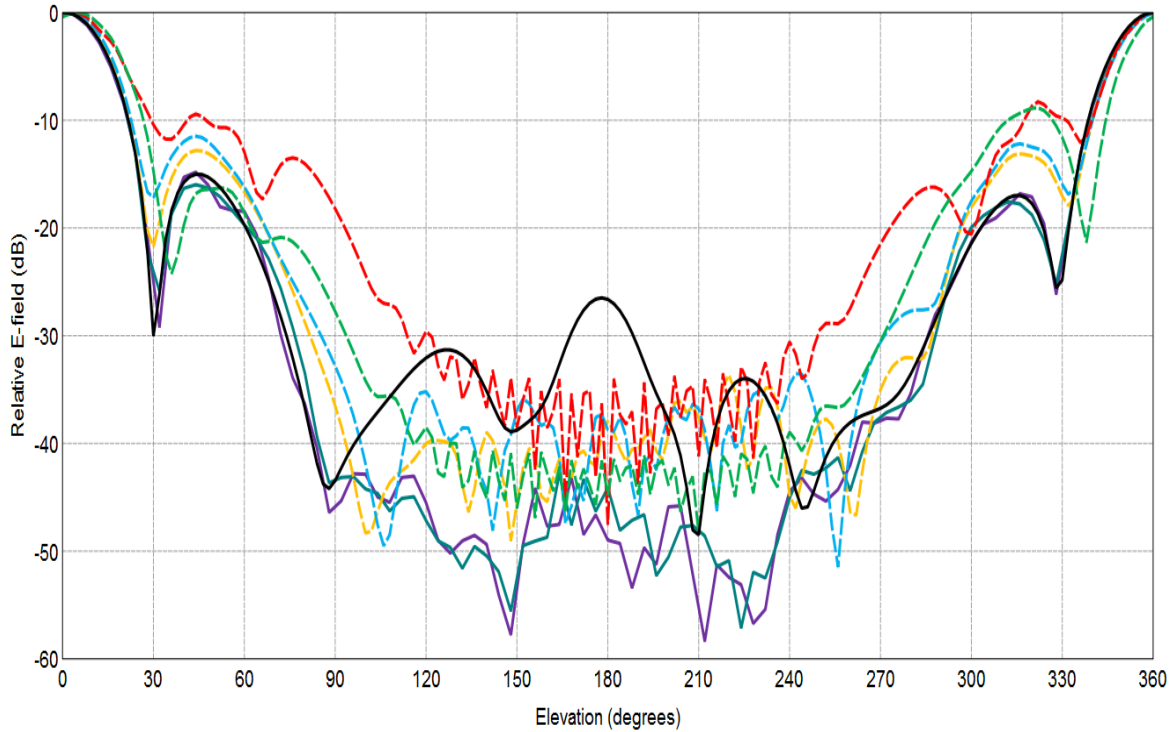


Figure 60. Free space and fitted radiation patterns as a function elevation θ , cut at $\varphi=0^\circ$, for different antenna mounting options of the 4x1 linear array antenna on mast structure front panel. All results from FEKO simulations. — 4x1 linear array antenna free space, — 4x1 linear array antenna separated 0.113m from complete mast structure, — 4x1 linear array antenna separated $\lambda/4$ m from complete mast structure, - - 4x1 linear array antenna fully integrated with mast (mounting option A), - - 4x1 linear array antenna partial boxed-front ends (mounting option B), - - 4x1 linear array antenna partial boxed-side ends (mounting option C) and - - 4x1 linear array antenna fully boxed (mounting option D).

As illustrated in **Figure 60** there are overall good agreement in the antenna radiation patterns in elevation θ , cut at an azimuth angle $\varphi=0^\circ$, for each of the different antenna mounting options on the mast structure. However, there are significant differences in the radiation pattern in the levels of the sidelobes and backlobes. In most of the different mounting options these sidelobes and backlobes levels, in general, did not impact too much on the antenna main beam. Except for the case when the antenna is fully integrated with the mast structure that there is decrease in the level of the mainbeam and a slight difference in the look direction, i.e., not 1 at elevation $\theta=0^\circ$. It needs to be noted that for the case of the fully integrated antenna mounting option, it was assumed that the mast was part of the antenna ground plane, i.e., the distance between the antenna and mast structure was equivalent to the substrate height (i.e., 0.002m). It may be of interest in any

future work to adjust this substrate height to determine the impact of this to the antenna radiation pattern, taking into consideration that the adjustment in substrate height may affect the antenna design and its performance.

It is interesting to note that there appears to be oscillations occurring in the backlobe region of the antenna radiation pattern in elevation θ , cut at azimuth $\varphi=0^\circ$, for antenna mounting options B, C and D (i.e., antenna is fully boxed or partially boxed). Initially, these oscillations were thought to be attributed to possibly some cavity resonance effects. However, given that the oscillations occur in the backlobe of the antenna radiation pattern and therefore most likely occurring at large distances, suggesting that maybe the oscillations are due to diffraction off some large structure at large distances. Possibly the diffraction could be off the edges of the mast structure model that was used in the simulation. Further analysis would need to be done to confirm the exact cause of these oscillations in the antenna radiation pattern.

The fitted antenna radiation pattern for antenna mounting option D is comparable with the freespace antenna radiation pattern, however sidelobes are significantly elevated (i.e., ~8dB). For antenna mounting options B and C, the fitted antenna radiation patterns are also comparable with the free space antenna, radiation pattern. However, compared to the free space antenna, radiation pattern the sidelobes are also elevated by ~5dB. Similarly, the fitted antenna radiation pattern for antenna mounting option A (or flushed mounting), is comparable with the free space antenna radiation pattern. However, the fitted antenna radiation pattern for mounting option A has a larger beamwidth and elevated antenna radiation pattern first sidelobes, i.e., ~15dB compared to the free space antenna radiation pattern.

Furthermore, all the different mounting options tend to have reduced fitted antenna radiation pattern backlobe level (i.e., down ~10-20dB at $\theta=180^\circ$) compared to the freespace antenna radiation pattern.

Figure 61 illustrates the comparison of the free space and fitted antenna radiation patterns as a function of azimuth φ , cut at elevation $\theta \approx 90^\circ$, for each of the different mounting options of the 4x1 linear array antenna on the mast structure front panel.

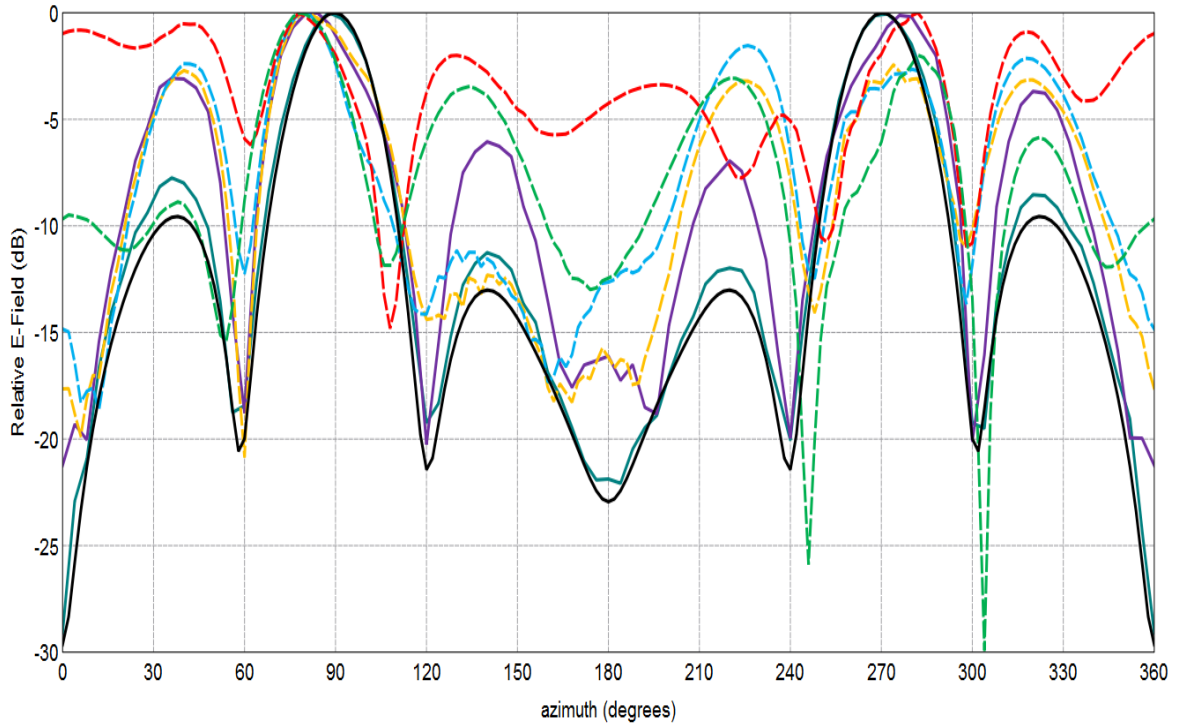


Figure 61. Free space and fitted antenna radiation patterns as a function of azimuth ϕ , cut at elevation $\theta \approx 90^\circ$, for each of the different mounting options of the 4x1 linear array antenna on mast structure front panel, at an antenna scan angle $\theta = 0^\circ$. All results from FEKO simulations. — 4x1 linear array antenna free space, — 4x1 linear array antenna separated 0.113m from complete mast structure, — 4x1 linear array antenna separated $\lambda/4$ m from complete mast structure, --- 4x1 linear array antenna fully integrated with mast structure (mounting option A), --- 4x1 linear array antenna partial boxed-front ends (mounting option B), --- 4x1 linear array antenna partial boxed-side ends (mounting option C) and --- 4x1 linear array antenna fully boxed (mounting option D).

As illustrated in **Figure 61** there is significant difference in the fitted antenna radiation patterns for the different options in azimuth cut an elevation angle ~ 90 degrees. The difference is so significant that the main beam of the fitted antenna radiation pattern has changed looked directions, at azimuth angles $\phi = 90^\circ$ and $\phi = 270^\circ$ in free space, compared to $\phi \sim 80^\circ$ and $\phi \sim 280^\circ$ for the fitted antenna mounting options of linear antenna fully boxed (i.e., mounting option D) and partially boxed-side ends (i.e., mounting option C).

The oscillations in the backlobe of the antenna radiation in the azimuth ϕ , cut at elevation $\theta \sim 90^\circ$ does not occur, as per the fitted antenna radiation pattern in elevation θ , cut at

$\varphi=0^\circ$. The fitted antenna radiation pattern for antenna mounting option D, i.e., the fully boxed, there tends to be significant elevation in antenna sidelobes.

It is interesting to note that for the antenna mounting option A, i.e., fully integrated (or flush mounted) there are distortions in the fitted antenna radiation pattern compared to the free space antenna, radiation pattern. However, the fitted antenna radiation pattern has sidelobes levels lower compared to the free space antenna radiation pattern (i.e., $\varphi=245^\circ$ and 305° , down $\sim 5\text{dB}$ and $\sim 10\text{dB}$, respectively) compared to the free space antenna radiation pattern. For the other entire antenna mounting options (i.e., options B and C) the fitted antenna radiation pattern is similar to the free space antenna pattern. However, sidelobes of the fitted antenna radiation pattern are elevated, i.e., $\sim 5\text{dB}$ compared to the free space antenna radiation pattern.

4.4.2 Fitted Near Field Power Flux Density in Vicinity of Antenna and Around Mast Structure

Figure 62 illustrates the three regions around the antenna and mast structure where the antenna near field was calculated for each of the different antenna mounting options.

As illustrated in **Figure 62** near fields were calculated in three regions around the antenna and mast structure.

- Region 1 is a 2-D plane region with dimensions $1\text{m} \times 0.95\text{m}$, positioned at a distance 0.01m from the top edge of the mast structure front panel, and above the transmit antenna,
- Region 2 is a 2-D circular region with radial distances $0.15\text{m} \leq R \leq 0.75\text{m}$ and azimuth $0^\circ \leq \varphi \leq 360^\circ$, cut at elevation angle $\theta=90^\circ$, and
- Region 3 is a 3-D cylindrical region, using cylindrical co-ordinates (ρ, ϕ, y) , with radius $0.2\text{m} \leq \rho \leq 0.55\text{m}$, and angular $180^\circ \leq \phi \leq 300^\circ$ and height $0\text{m} \leq y \leq 1.7\text{m}$.

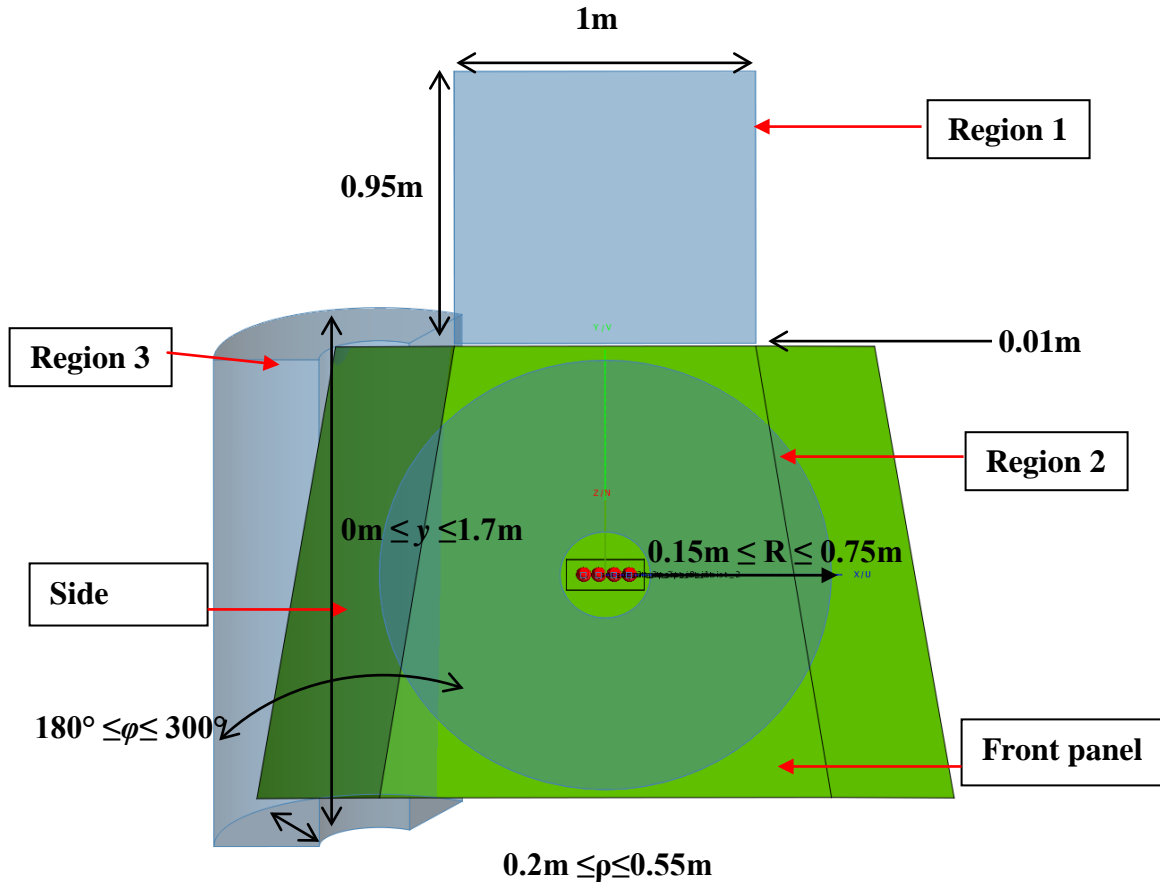
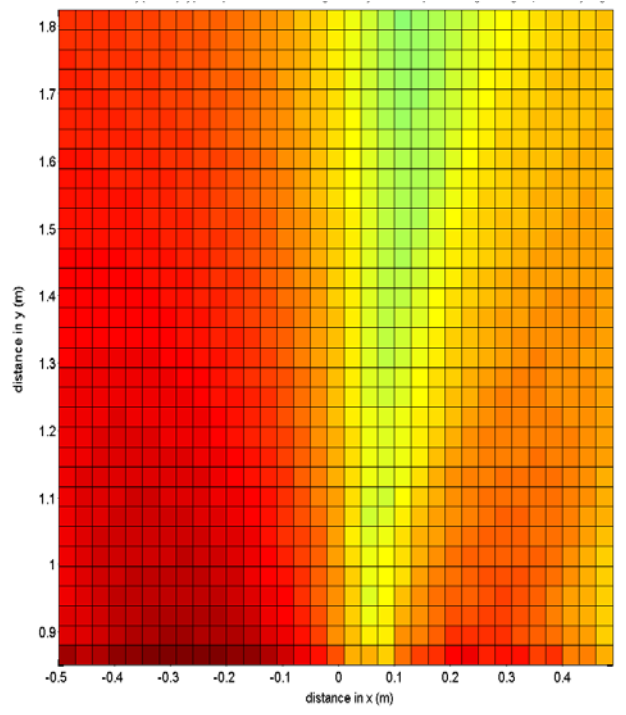
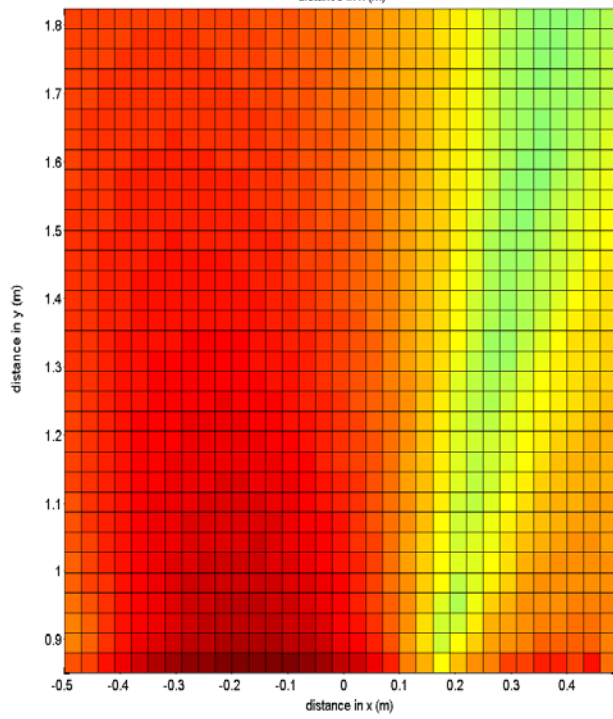
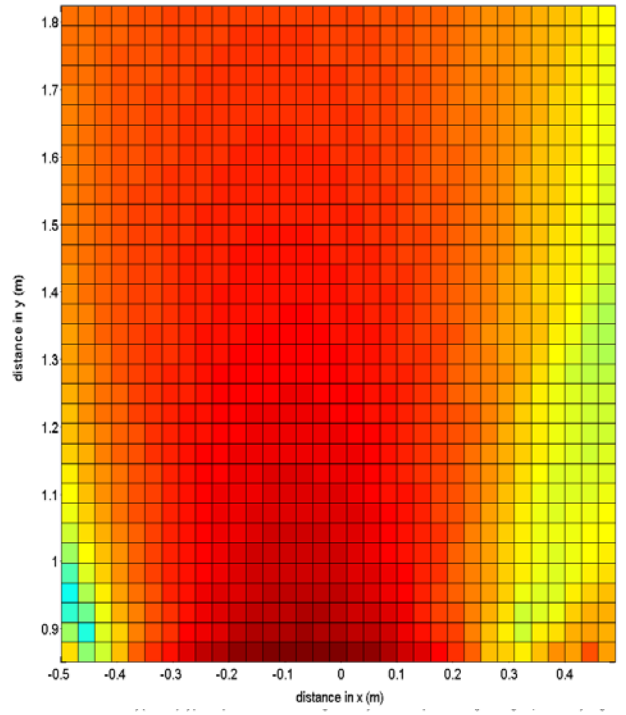
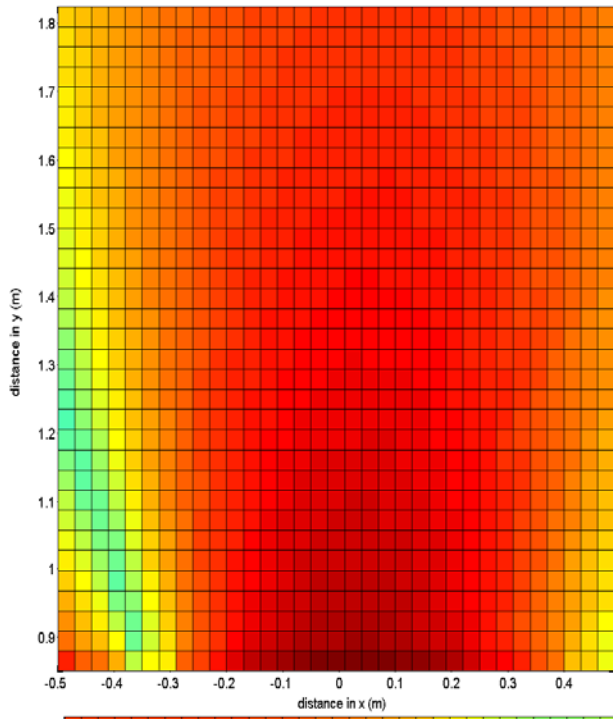


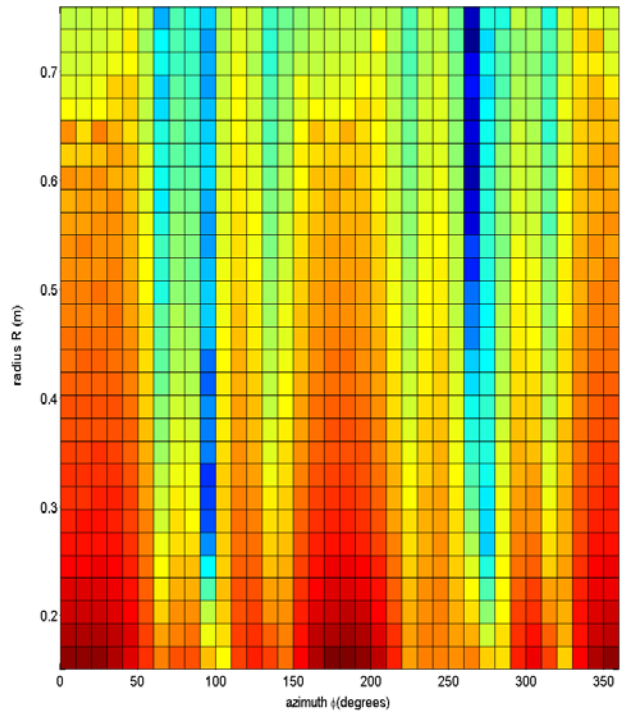
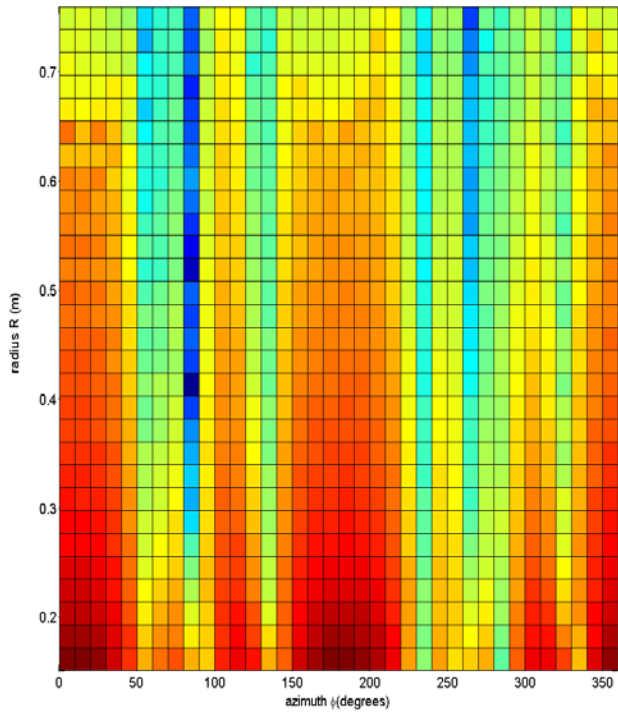
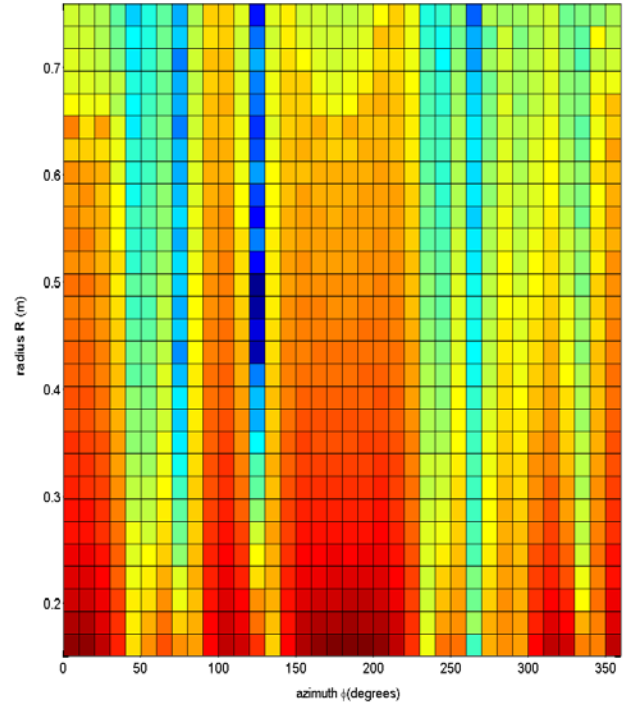
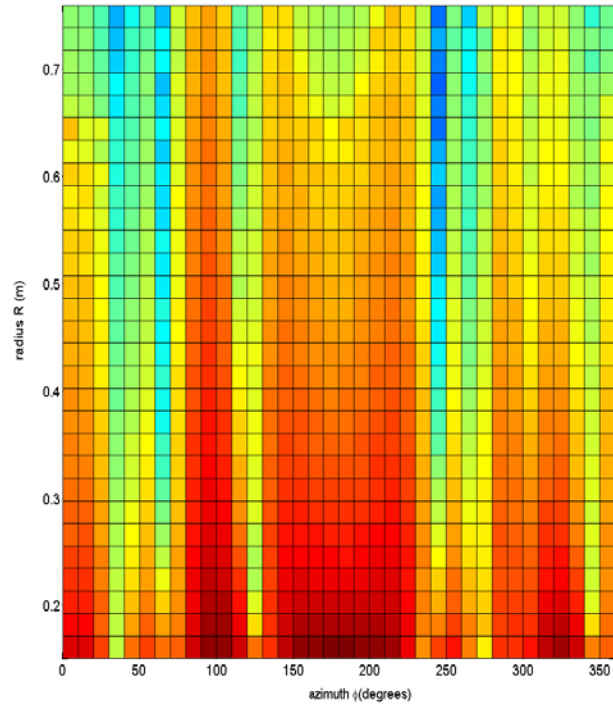
Figure 62. Near field regions in the vicinity of the integrated 4x1 linear array antenna and around mast structure.

4.4.2.1 Antenna Fully Integrated (Flush Mounted) – Option A

Figure 63 illustrates the fitted relative near field power flux density the different regions around the transmit antenna and mast structure for a transmit antenna that is fully integrated with the mast structure (i.e., antenna mounting option A) for different antenna scan angles, i.e., $\theta=0^\circ$, $\theta\sim 5^\circ$, $\theta\sim 11^\circ$, and $\theta\sim 18^\circ$. **Figure 63 (a)** illustrates the fitted relative near field power flux density in region 1 at each antenna scan angle. **Figure 63 (b)** illustrates the fitted relative near field power flux density in region 2 (plotted as a 2-D plane) at each antenna scan angle. **Figure 63 (c)** illustrates the fitted relative near field power flux density in region 3, in a 2-D plane with radii $0.35\text{ m} \leq \rho \leq 0.55\text{ m}$ as a function of angle $180^\circ \leq \phi \leq 300^\circ$, cut at height $y\sim 0.8\text{ m}$, at each antenna scan angle.



(a)



(b)

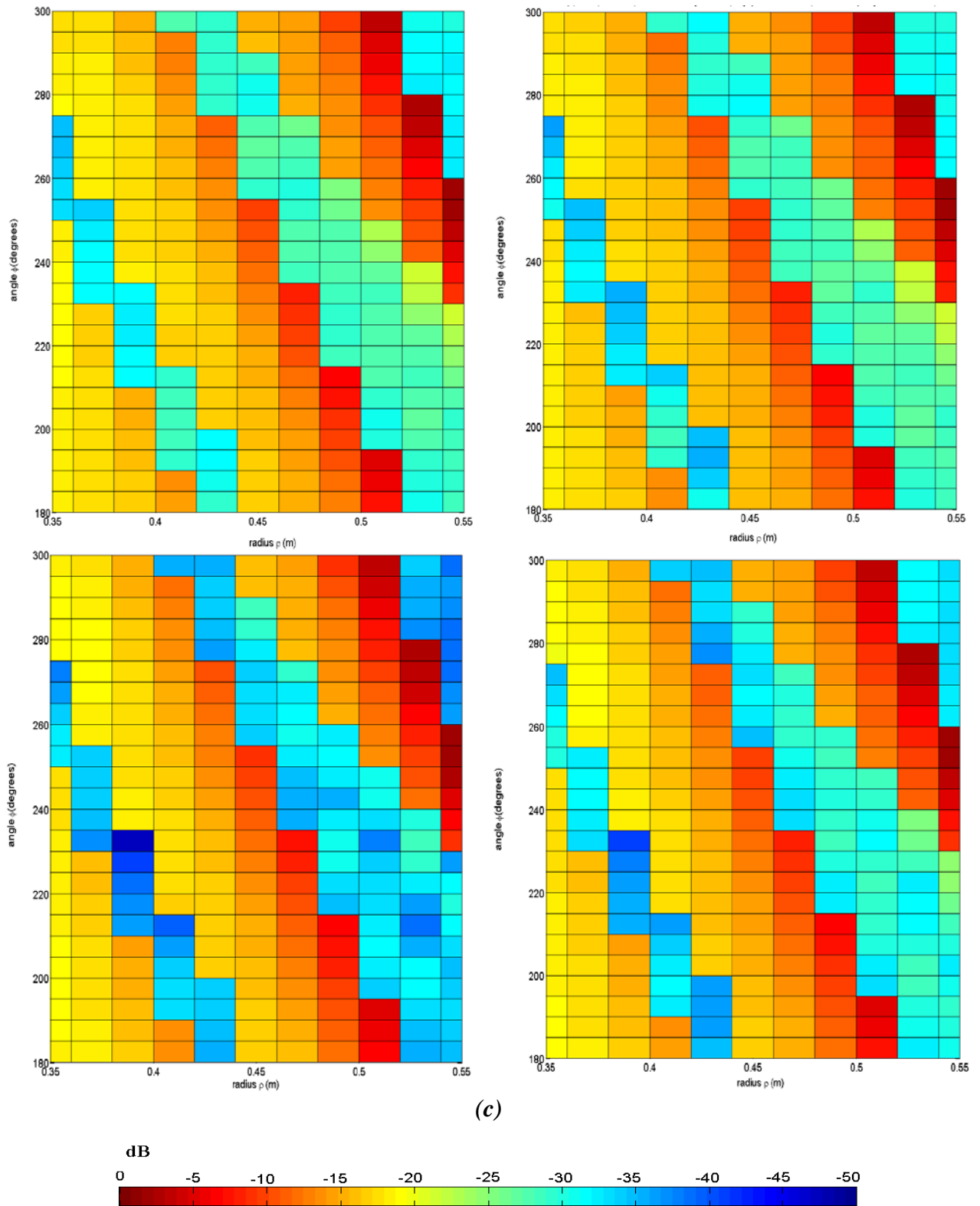
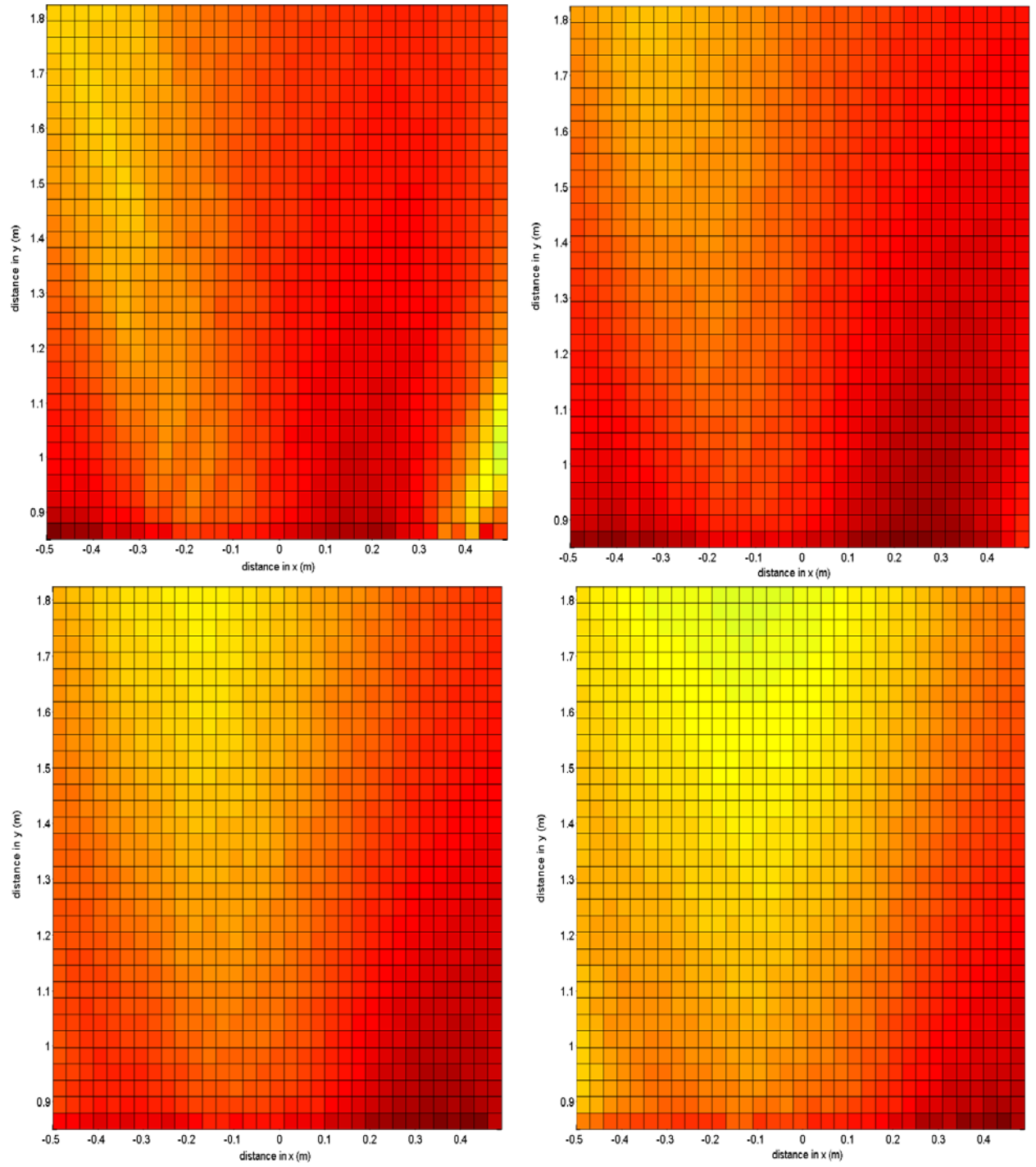


Figure 63. Fitted relative near field power flux density (dB) at different regions around the antenna and mast structure for a 4x1 linear array antenna fully

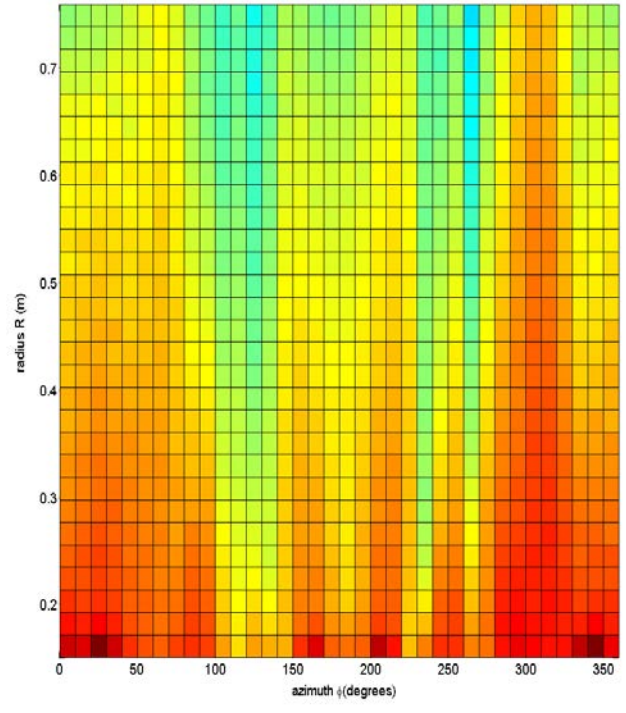
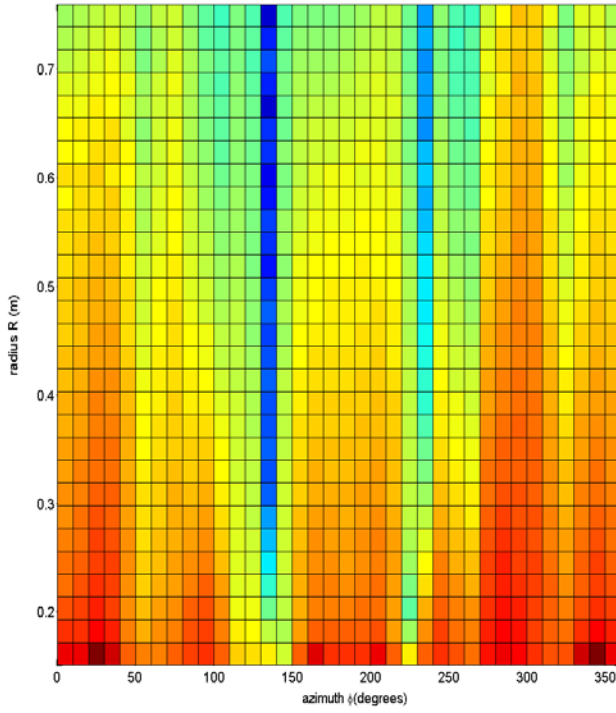
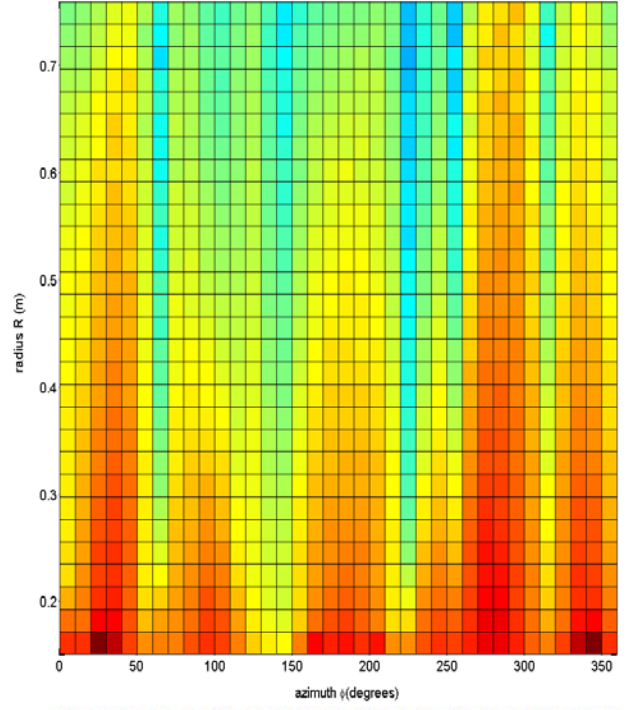
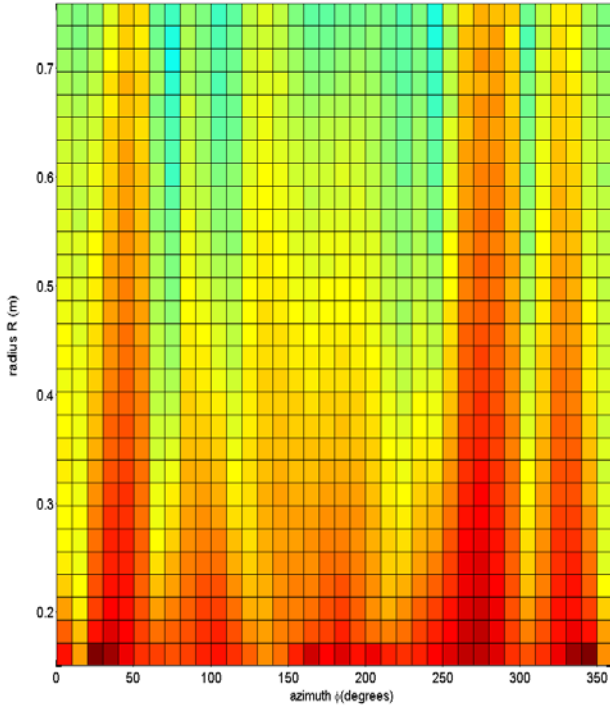
integrated (or flush mounted) with mast structure, i.e., antenna mounting option A for different antenna scan angles. (a) Fitted relative near field power flux density in region 1 for each antenna scan angle (L to R) $\theta=0^\circ$, $\sim 5^\circ$, $\sim 11^\circ$ and $\sim 18^\circ$, (b) Fitted relative near field power flux density in region 2 for each antenna scan angle (L to R) $\theta=0^\circ$, $\theta \sim 5^\circ$, $\theta \sim 11^\circ$ and $\theta \sim 18^\circ$, and (c) Fitted relative near field power flux density in region 3, at radii $0.35 \text{ m} \leq \rho \leq 0.55 \text{ m}$ as a function of angle $180^\circ \leq \phi \leq 300^\circ$, cut at height $y \sim 0.8\text{m}$, for each antenna scan angle (L to R) $\theta=0^\circ$, $\theta \sim 5^\circ$, $\theta \sim 11^\circ$ and $\theta \sim 18^\circ$.

4.4.2.2 Integrated Antenna Partially boxed-front ends – Option B

Figure 64 illustrates the fitted relative near field power flux density at different locations around the antenna and mast structure for a 4x1 linear array antenna mounted partially boxed-front ends on a mast structure (i.e., mounting option B) at different antenna scan angles, i.e., $\theta=0^\circ$, $\sim 5^\circ$, $\sim 11^\circ$ and $\sim 18^\circ$. **Figure 64 (a)** illustrates the fitted relative near field power flux density in region 1 at each antenna scan angle. **Figure 64 (b)** illustrates the fitted relative near field power flux density in region 2 (plotted as a 2-D plane), at each antenna scan angle, and **Figure 64 (c)** illustrates the fitted relative near field power flux density in region 3, in a 2-D plane with radii $0.35 \text{ m} \leq \rho \leq 0.55 \text{ m}$ and angles $180^\circ \leq \phi \leq 300^\circ$, cut at height $y \sim 0.8\text{m}$ at each antenna scan angle.



(a)



(b)

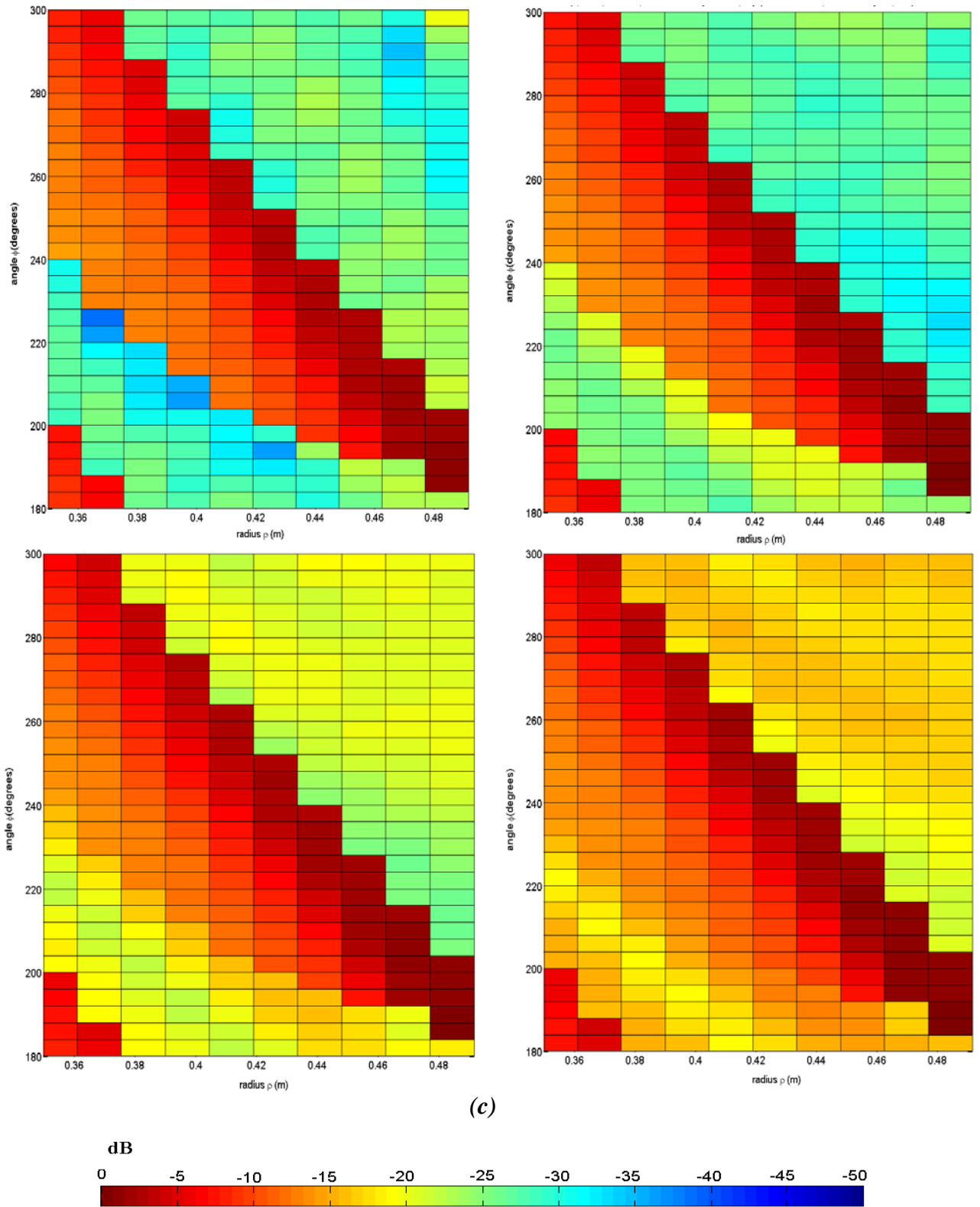
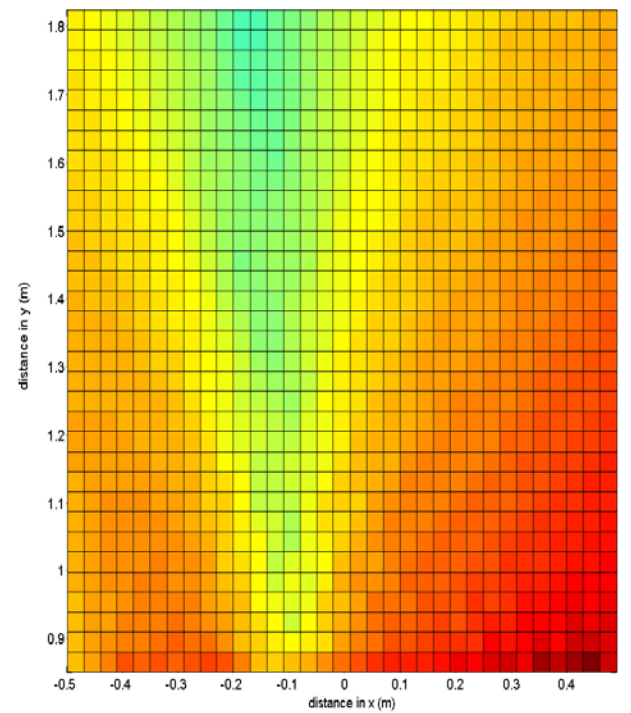
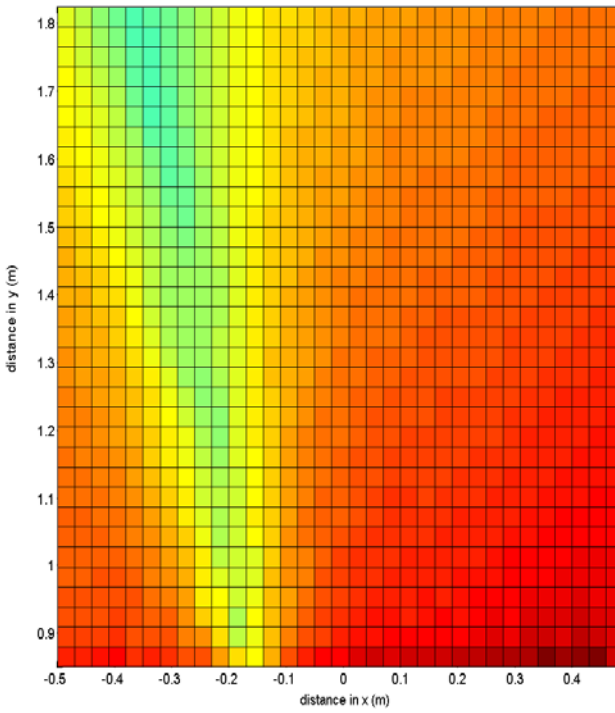
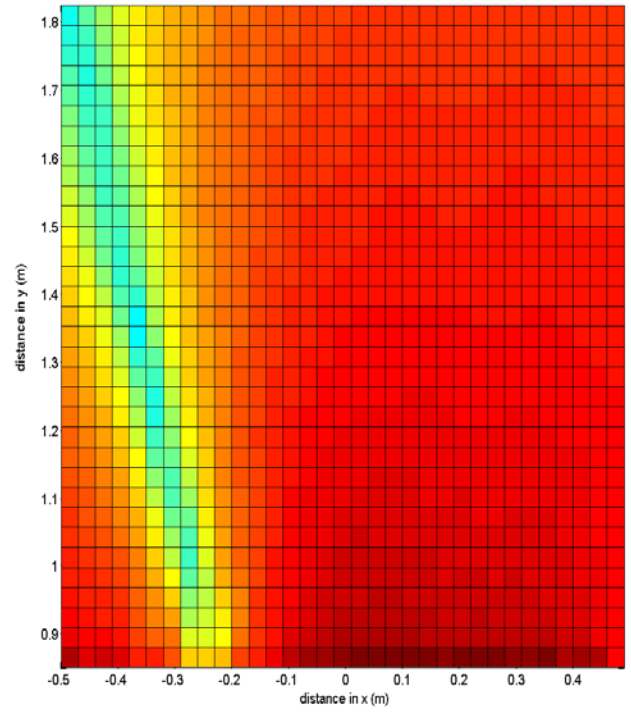
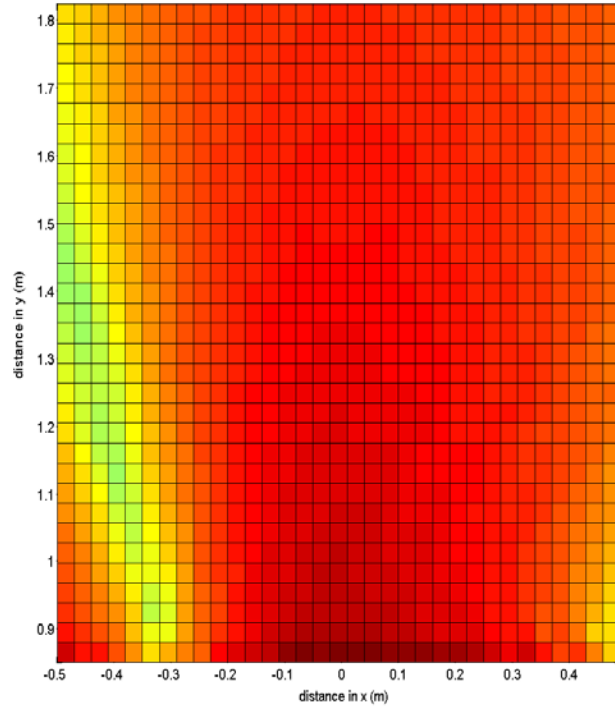


Figure 64. Fitted relative near field power flux density (dB) at different locations around antenna and mast structure for a 4x1 linear array antenna partially boxed-

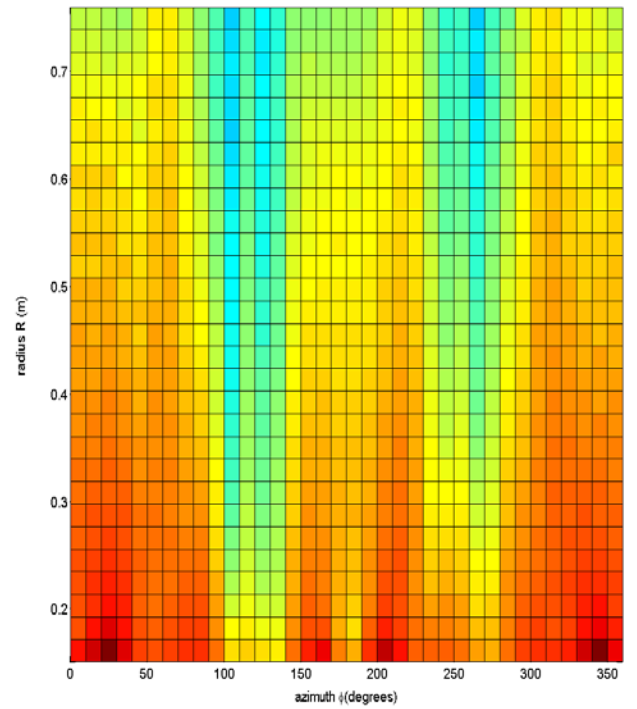
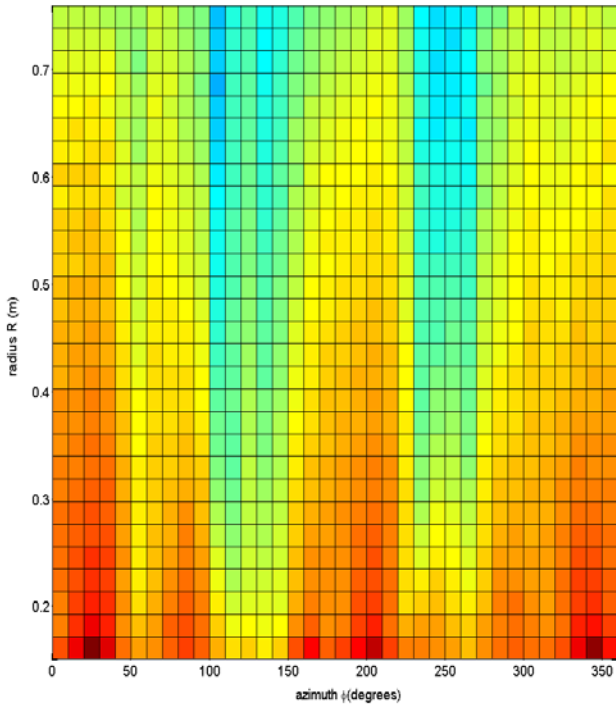
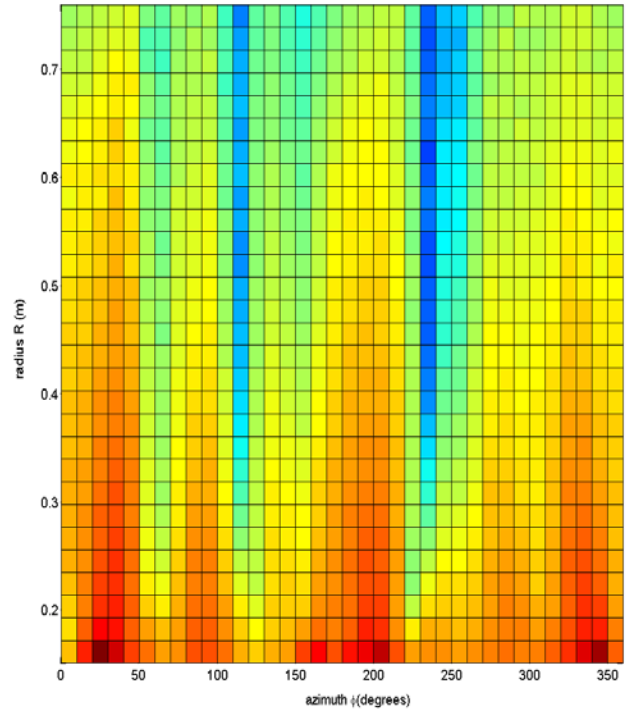
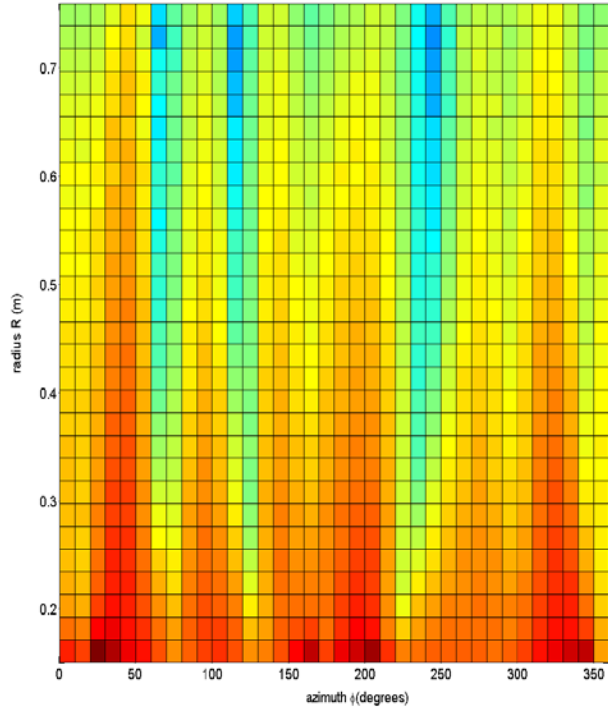
front ends, i.e., mounting option B at different antenna scan angles. (a) Fitted relative near field power flux density in region 1, for different antenna scan angles (L to R) $\theta=0^\circ$, $\theta \sim 5^\circ$, $\theta \sim 11^\circ$ and $\theta \sim 18^\circ$, (b) Fitted relative near field power flux density in region 2, for different antenna scan angles (L to R) $\theta=0^\circ$, $\theta \sim 5^\circ$, $\theta \sim 11^\circ$ and $\theta \sim 18^\circ$, and (c) Fitted relative near field power flux density in region 3, at radii $0.35 \text{ m} \leq \rho \leq 0.55 \text{ m}$ as a function of angle $180^\circ \leq \phi \leq 300^\circ$, cut at a height $y \sim 0.8 \text{ m}$ for different antenna scan angles (L to R) $\theta=0^\circ$, $\theta \sim 5^\circ$, $\theta \sim 11^\circ$ and $\theta \sim 18^\circ$.

4.4.2.3 Integrated Antenna partially boxed –side ends – Option C

Figure 65 illustrates the fitted relative near field power flux density at different locations around the antenna and mast structure for a 4x1 linear array antenna mounted partially boxed–side ends on the mast structure, for different antenna scan angles (i.e., $\theta=0^\circ$, $\sim 5^\circ$, $\sim 11^\circ$ and $\sim 18^\circ$). **Figure 65 (a)** illustrates the fitted relative near field power flux density in region 1 at each antenna scan angle. **Figure 65 (b)** illustrates the fitted relative near field power flux density in region 2 at each antenna scan angle, and **Figure 65 (c)** illustrates the fitted relative near field power flux density in region 3 (in a 2-D plane) with radii $0.35 \text{ m} \leq \rho \leq 0.55 \text{ m}$, and angles $180^\circ \leq \phi \leq 300^\circ$, cut at height $y \sim 0.8 \text{ m}$ at each antenna scan angle.



(a)



(b)

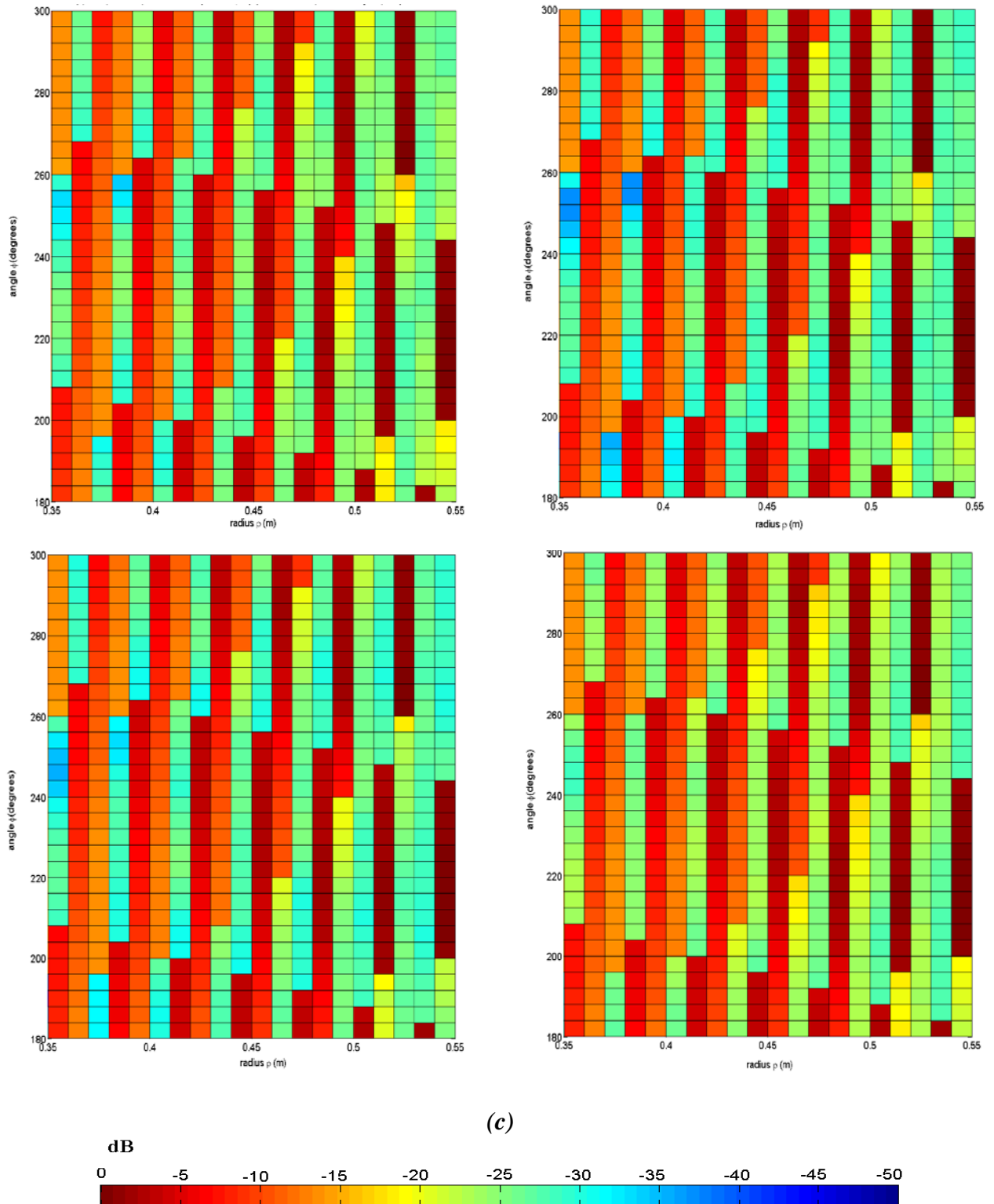
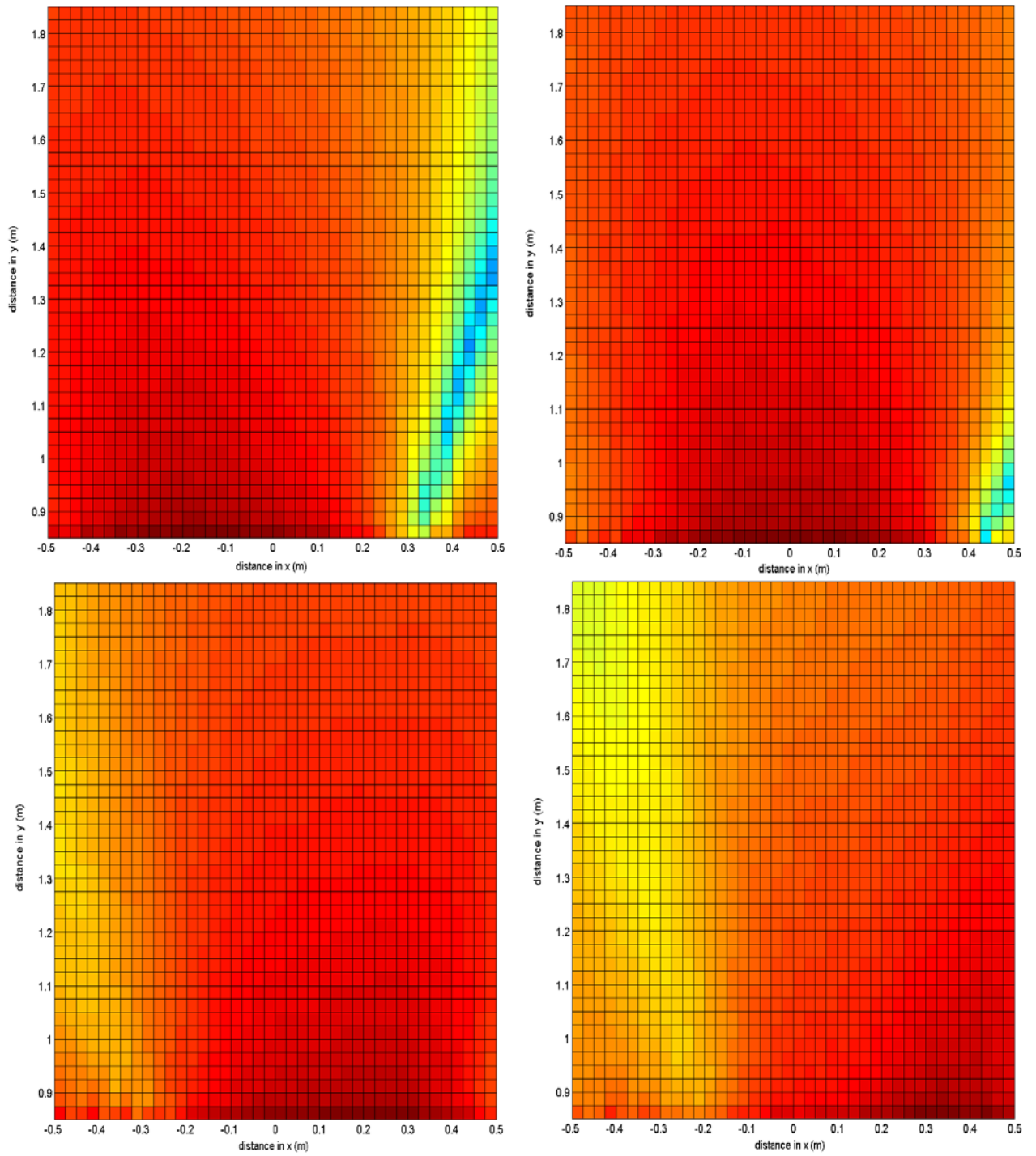


Figure 65. Fitted relative near field power flux density (dB) at different locations around the antenna and mast structure for a 4x1 linear array antenna mounted partially boxed-side ends on mast structure, i.e., mounting option C for different

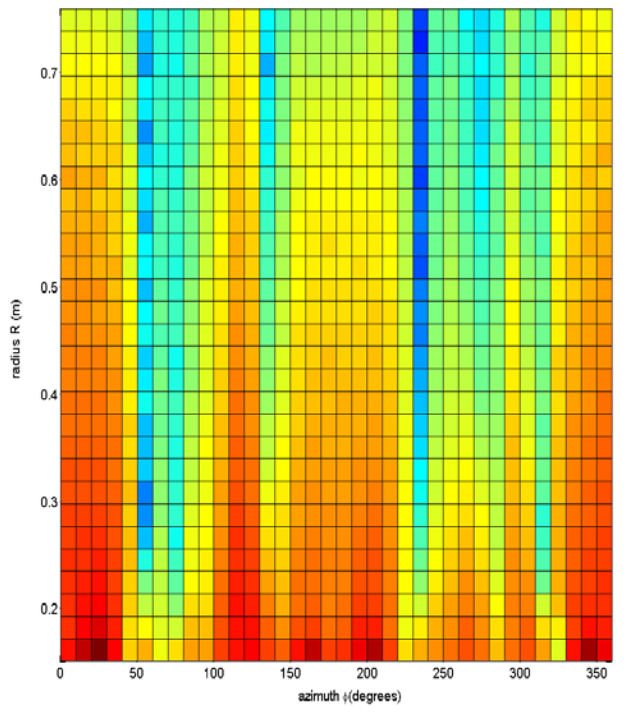
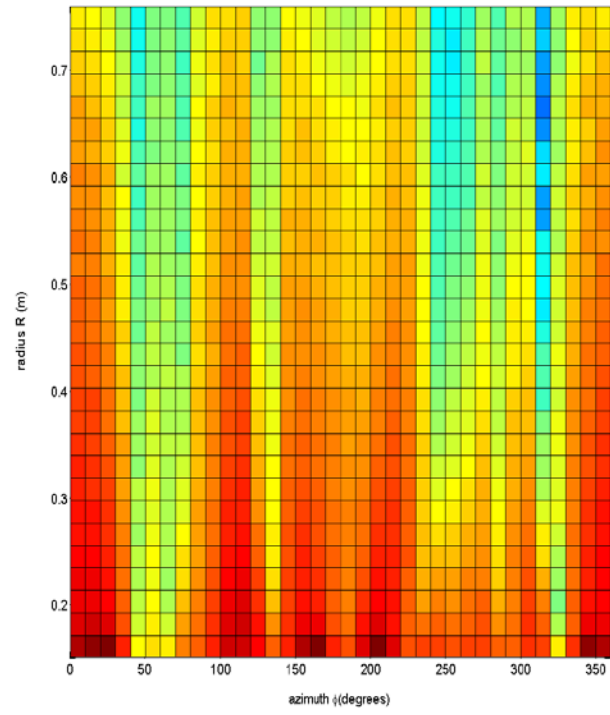
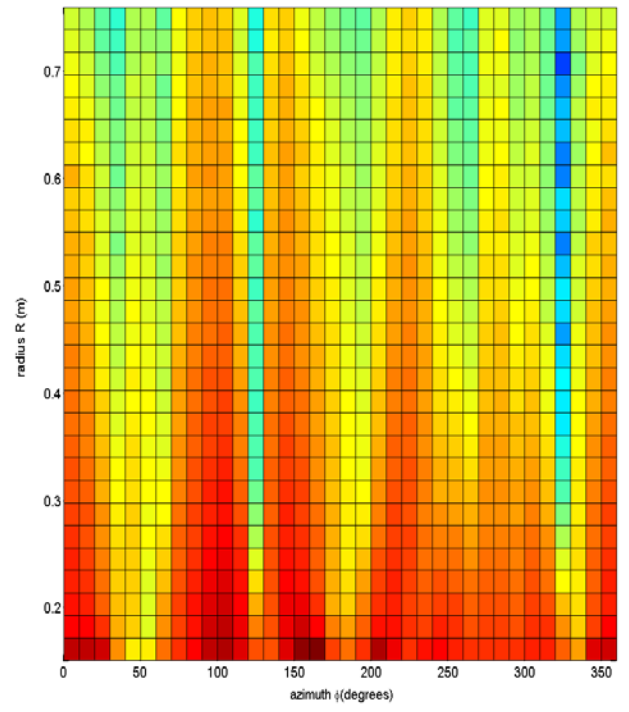
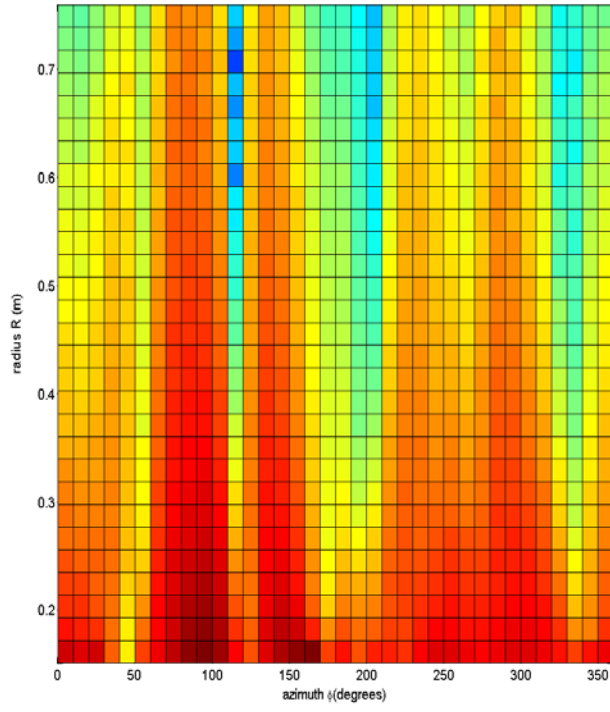
antenna scan angles, $\theta=0^\circ$, $\theta \sim 5^\circ$, $\theta \sim 11^\circ$ and $\theta \sim 18^\circ$. **Figure 65 (a)** Fitted relative near field power flux density in region 1 at each antenna scan angle, **Figure 65 (b)** Fitted relative near field power flux density (dB) in region 2 at each antenna scan angle, and **Figure 65 (c)** Fitted relative near field power flux density (dB) in region 3, for radii $0.35 \text{ m} \leq \rho \leq 0.55 \text{ m}$ as a function of angles $180^\circ \leq \phi \leq 300^\circ$, cut at a height $y \sim 0.8 \text{ m}$ at each antenna scan angle.

4.4.2.4 Integrated Antenna – Fully boxed – Option D

Figure 66 illustrates the fitted relative near field power flux density at different locations around the antenna and mast structure for a 4x1 linear array antenna mounted fully boxed on the mast structure, for different antenna scan angles, i.e., $\theta=0^\circ$, $\sim 5^\circ$, $\sim 11^\circ$ and $\sim 18^\circ$. **Figure 66 (a)** illustrates the fitted relative near field power flux density in region 1 at each antenna scan angle. **Figure 66 (b)** illustrates the fitted relative near field power flux density in region 2 at each antenna scan angle, and **Figure 66 (c)** illustrates the fitted relative near field power flux density in region 3 (in a 2-D plane), at radii $0.35 \text{ m} \leq \rho \leq 0.55 \text{ m}$ and angles $180^\circ \leq \phi \leq 300^\circ$, cut at height $y \sim 0.8 \text{ m}$ at each antenna scan angle.



(a)



(b)

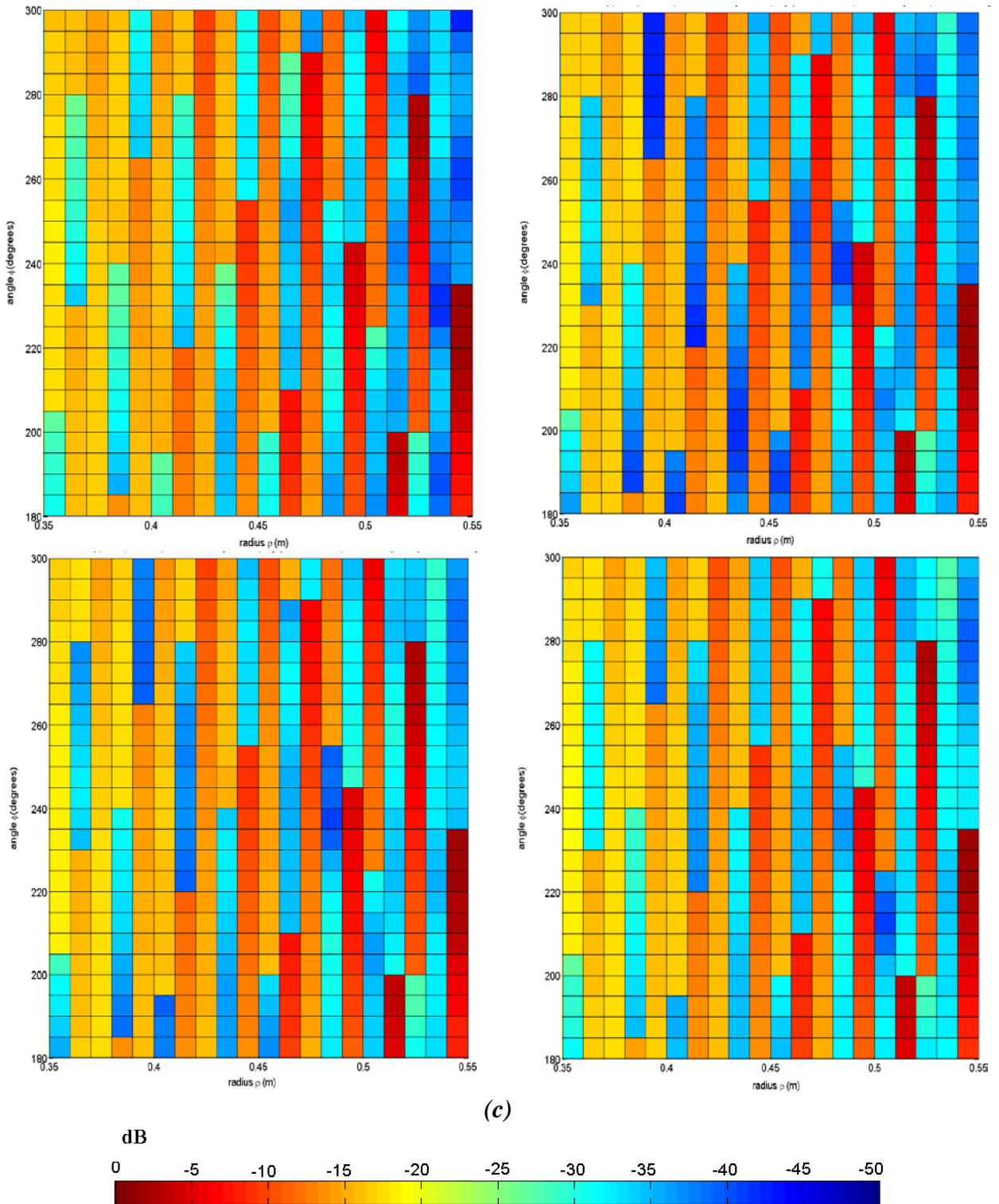


Figure 66. Fitted relative near field power flux density (dB) at different locations on around antenna and mast structure for a 4x1 linear array antenna mounted fully boxed on mast structure, i.e., mounting option D, for different antenna scan angles
(a) Fitted relative near field power flux density in region 1 for each antenna scan

angle (L to R) $\theta=0^\circ$, $\theta \sim 5^\circ$, $\theta \sim 11^\circ$ and $\theta \sim 18^\circ$, (b) Fitted relative near field power flux density in region 2 for each antenna scan angle (L to R) $\theta=0^\circ$, $\theta \sim 5^\circ$, $\theta \sim 11^\circ$ and $\theta \sim 18^\circ$, and (c) Fitted relative near field power flux density in region 3, for radii $0.35 \text{ m} \leq \rho \leq 0.55 \text{ m}$ as a function of angle $180^\circ \leq \phi \leq 300^\circ$, cut at height $y \sim 0.8 \text{ m}$ for each antenna scan angle (L to R) $\theta=0^\circ$, $\theta \sim 5^\circ$, $\theta \sim 11^\circ$ and $\theta \sim 18^\circ$.

As illustrated in **Figure 63 (a)**, **Figure 64 (a)**, **Figure 65 (a)** and **Figure 66 (a)** the fitted relative near field power flux density in region 1, (i.e., above transmit antenna), overall is significantly high (i.e., up to 0dB) for each of the different antenna mounting options (i.e., A, B, C and D) and different antenna scan angles, i.e., $\theta=0^\circ$, $\sim 5^\circ$, $\sim 11^\circ$ and $\sim 18^\circ$. However, as the antenna scan angle increases the fitted relative near field power flux density in region 1 decreases from 0dB at the lower scan angles $\theta=0^\circ$ and 5° to $\sim -20\text{dB}$ to -30dB at antenna scan angle $\theta \sim 18^\circ$. This decrease in the fitted relative near field power flux density with increase in antenna scan angle is attributed to the variation in the look direction of the antenna's main beam. Therefore, the significantly high fitted relative near field power flux density in region 1 is attributed to the large power and energy in the antenna's radiation mainbeam. For an antenna mounting option where the antenna is fully boxed (i.e., option D) the fitted relative near field power flux density in region 1 ranges from 0dB at smaller antenna scan angles $\theta=0^\circ$ to -20dB (small area) at the larger scan angles (i.e., 18°). Similarly, for the antenna mounting option where the antenna is mounted partially boxed-side ends (i.e., option C) the fitted relative near field power flux density in region 1 ranges from 0dB at the small antenna scan angles, i.e., $\theta=0^\circ$ and $\sim 5^\circ$ to -30dB , over a large area at the large antenna scan angles, i.e., $\theta \sim 11^\circ$ and $\sim 18^\circ$. Similarly, For the mounting option where the antenna is mounted partially boxed-front ends (i.e., option B) the fitted relative near field power flux density ranges for 0dB at smaller scan angles $\theta=0^\circ$ to -20dB (large area, most of region 1) at the larger scan angles, i.e., $\theta \sim 18^\circ$. Whereas, for the mounting option, where the antenna is fully integrated (flush mounted) with the mast structure (i.e., option A) the fitted relative near field power flux density ranges from 0dB at small antenna scan angle, (i.e., $\theta=0^\circ$ to $\sim -20\text{dB}$) at the larger scan angles, (i.e., $\theta \sim 18^\circ$), with a very small narrow area in region 1 where the fitted relative near field power flux density reaches down to -30dB .

As illustrated in **Figure 63 (b)**, **Figure 64 (b)**, **Figure 65 (b)** and **Figure 66 (b)** the fitted relative near field power flux density in the vicinity of the antenna, i.e., in region 2, is overall significantly high (i.e., reaching up to 0dB (maximum)) for the different mounting options at all radial distances close to the transmit antenna, (i.e., $0.15 \text{ m} \leq R \leq 0.75 \text{ m}$) Over all the azimuth angles $0^\circ \leq \phi \leq 360^\circ$ for all different antenna scan angles. However, there are slight differences for each antenna mounting option as to where the fitted relative near field power flux density reduces at different radial distances from the antenna. For example, antenna mounting option D, (i.e., antenna mounted fully boxed), the fitted relative near field power flux density tends to be significantly high (reaching up to 0dB) for most of the radial distances and azimuth angles, compared to the other antenna mounting options A then option B and option C. For antenna mounting option C, i.e., antenna mounted partially boxed-side ends the fitted relative near field power flux density is overall relatively low (i.e., $\sim -25\text{dB}$, reaching low as -30dB to -35dB

(minimum) in small areas) , compared to the other antenna mounting options (B, A and D), for most of the radial distances (i.e., $R > 0.2$ m) and azimuth angles. There are, however, radial distances and azimuth angles where the fitted relative near field power flux density is high i.e., 0dB, but this tends to be at the smaller radial distances $0.15 \text{ m} \leq R < 0.2 \text{ m}$. The fluctuations between high and low fitted relative near field power flux density may be attributed to the antenna radiation pattern and how it interferes with the mast structure. For significantly high (0dB) fitted relative near field power flux density at azimuth angles where the antenna main beam look direction should be, then this is mainly attributed to the to the antenna main beam. However, for other azimuth angles where the near field power flux density may be high could be attributed to coupling between the antenna and mast structure. For the low (i.e., ~ -5 to -25 dB) to significantly low near field power flux density (i.e., ~ -25 dB to -30 dB) at the radial distances and azimuth angles, this may be attributed to the antenna radiation pattern sidelobes and nulls, and also mast structure blockages.

The regions of high and low near field power flux density around the antenna will change with different antenna scan angle. This means that for an antenna scan angle there will be regions around the antenna where the near field power flux density will be low. However, as the antenna scan angle changes, the same region that initially have low near field power flux density may now have a high near field power flux density.

As illustrated in **Figure 63 (c)**, **Figure 64 (c)**, **Figure 65 (c)** and **Figure 66 (c)** the fitted near field power flux density in general is lower in region 3 (i.e., $0.35 \text{ m} \leq \rho \leq 0.55 \text{ m}$, angle $180^\circ \leq \phi \leq 300^\circ$, cut $y \sim 0.8$ m, which refers to a cross-section of region 3 along the mid-section of the sidepanel). Compared to regions 1 and 2, for all different antenna mounting options and for different antenna scan angles.

It is interesting to note, that for antenna mounting options A (i.e., fully integrated) and B (i.e., mounted partially boxed-front ends) there tends to be a distinct repetitive pattern of low and high near field power flux density in region 3. Going from the top right corner of region 3 (i.e., nearby the edge between front panel and side panel of the mast structure) towards the bottom left corner of region 3 (i.e., further along the sidepanel moving away from the edge adjacent the front panel and sidepanel) for each of the antenna scan angles $\theta = 0^\circ, \sim 5^\circ, \sim 11^\circ$ and $\sim 18^\circ$.

For antenna mounting option A, and at each antenna scan angles the repetitive pattern in the near field power flux density, going from the top right corner ($\rho = 0.55 \text{ m}$ and $\phi = 300^\circ$) to bottom left corner (i.e., $\rho = 0.35 \text{ m}$ and $\phi = 180^\circ$) of region 3, is low, i.e., ~ -30 dB, then increases to between -10 dB to 0 dB, then decreases again to ~ -25 dB to -30 dB, and then increases to ~ -10 dB to -15 dB, then another decrease to ~ -30 dB and then another increases again to ~ -15 dB to ~ -20 dB. The first low near field power flux density region in the pattern occurs at distances from the sidepanel surfaces $\rho \sim 0.2$ m, assuming the surface of the sidepanel is at $\rho = 0.35$ m at an angle $\phi \sim 300^\circ$. This means that in regions at vertical distances of ~ 0.2 m from the surface of the sidepanel, and

relatively close to the edge adjacent to the sidepanel and front panel and at height $y \sim 0.8\text{m}$ there is a small region where the near field power flux density is low. This may be attributed to a blocking effect that the front panel has on the sidepanel due to the difference in angle that the sidepanel surface has relative to the front panel surface. The other low near field power flux density occurs at vertical distances from the sidepanel between 0.15m at angles $\sim 300^\circ$ and 0.2m for angles $\sim 180^\circ$. At the small vertical distances and large angles again would refer to a region very close to the edge adjacent the front and side panels. So the low near field power flux density maybe attributed, as mentioned above, to the blocking effect that the front panel on the sidepanel due to the difference in angle that the sidepanel has relative to the front panel. The low near field power flux density at the larger vertical distances from the sidepanel surface $\rho \sim 0.2\text{m}$ and at smaller angles $\phi \sim 180^\circ$ is as expected, since this refers to a region further down along the sidepanel, moving away from the edge adjacent to the sidepanel and front panel. Similar reasoning can be asserted for the third low near field power flux density area in region 3. Conversely, for the sectors in region 3 where there is an increase in the near field power flux density mainly between $-20\text{ dB} \leq S \leq -5\text{dB}$, occurs at vertical distances from the surface of the sidepanel. In positions along the sidepanel where the front panel is not able to provide enough blockage to the sidepanel, so it is exposed to the antenna's radiation either from antenna mainlobe, sidelobes and backlobes.

For antenna mounting option B (i.e., antenna mounted partially boxed–front ends) the repetitive pattern for the near field power flux density in region 3, has large distinct areas of low and high near field power flux density. In addition, the two sectors in region 3, where there is low near field power flux densities, i.e., $\sim -25\text{dB}$, for the small antenna scan angles (i.e., $\theta = 0$ and $\theta \sim 5^\circ$) for the same sectors the near field power flux density increases to $\sim -20\text{dB}$ at the larger scan angles, $\theta \sim 11^\circ$ and $\theta \sim 18^\circ$. There is no difference in near field power flux density in the sector of region 3 where the near field power flux density increases the near field power flux density is $-10\text{ dB} \leq S \leq 0\text{ dB}$ for the difference antenna scan angles.

It is interesting to note that for antenna mounting option A the area in region 3 where the near field power flux density increases the near field power flux density ranges between $-20\text{ dB} \leq S \leq -5\text{dB}$. Whereas, for antenna mounting option B the near field power flux density of increase near field power density is between $-10\text{ dB} \leq S \leq 0\text{ dB}$. This in turn suggests that there is an increase in power reaching the sidepanel when the antenna is mounted as a partial-box with opened box side ends, compared to when the antenna is integrated with the mast structure. This increase in power may be attributed to resonance cavity effects occurring in the boxed antenna mounting, causing an increase in the EM energy and dissipated energy from the antenna and the open side panels of the boxed antenna mount.

For the antenna mounting options C (i.e., antenna mounted partially boxed-side ends) and D (i.e., antenna mounted fully boxed) the near field power flux density in region 3 does not follow a distinct repetitive pattern as per antenna mounting options B and A. Instead, the near field power flux density for mounting options C and D is dispersed across region

3 (i.e., $0.35 \text{ m} \leq \rho \leq 0.55 \text{ m}$, angles $180^\circ \leq \phi \leq 300^\circ$ at height $y \sim 0.8 \text{ m}$) ranging from 0dB to $\sim -35 \text{ dB}$ for antenna scan angles. However, for the antenna mounting option C the near field power flux density within region 3 overall tends to be significantly high ranging from $-25 \text{ dB} \leq S \leq 0 \text{ dB}$, however, with many areas scattered within region 3 reaching near field power flux density 0dB compared to antenna mounting option D (i.e., fully boxed) where the near field power flux density mainly between $-5 \text{ dB} \sim S < -35 \text{ dB}$.

This in turn suggests that for an antenna mounted fully boxed produces less near field power flux density at the side panel compared to an antenna that is mounted partially boxed-side ends. This increase in near field power flux density for an antenna partially boxed, as mentioned previously could be attributed to resonance cavity effect, where a buildup of energy occurs and is dissipated through the openings of the box mount.

The fitted relative near field power flux density, overall, tends to decrease along the mid-section of the mast structure sidepanel (i.e., cross-section of region 3) with increasing antenna scan angle. This would be as expected, since as the antenna scan angle increases the antenna mainbeam is directed away from the sidepanel where near fields are calculated for region 3. However, this decrease in near field power flux density with increasing antenna scan angle may not be the same paradigm for the other side panel, since the antenna mainlobe is directed towards it with increasing antenna scan angle. It would be of interest in any future work to calculate the near fields at this other sidepanel with increasing antenna scan angles.

The fitted relative near field power flux density presented here for region 3 is only a cross-section along the mid-section (i.e., height $y \sim 0.8 \text{ m}$) of the mast structure sidepanel. Therefore, it necessitates to be stated that the fitted relative near field power flux density may vary at different places along the sidepanel mast structure. It would be of interest in any further work to determine the fitted relative near field power flux density at different positions around the mast structure sidepanel, e.g. top and bottom portions of the side panel.

4.5 NON-LINEAR EFFECTS OF A RF RECEIVER SYSTEM

4.5.1 Receiver System

Figure 67 illustrates a simple schematic of a radio frequency receiver system with an **automatic gain control (AGC)** loop. The RF receiver system schematic template was based on the simple RF receiver system schematic from ADS Systems [54], with several modifications in the electronic component parameters. Antenna and demodulator components, which are typically associated with RF receiver system, were omitted from the RF receiver system schematic in **Figure 67** because such components were not permitted in a budget analysis simulation in ADS Systems. A budget analysis was performed for the RF system depicted in **Figure 67**. Electronic component parameters and specifications for the RF receiver system depicted in **Figure 67** are provided in **Appendix A, Section A.6, Table 13**.

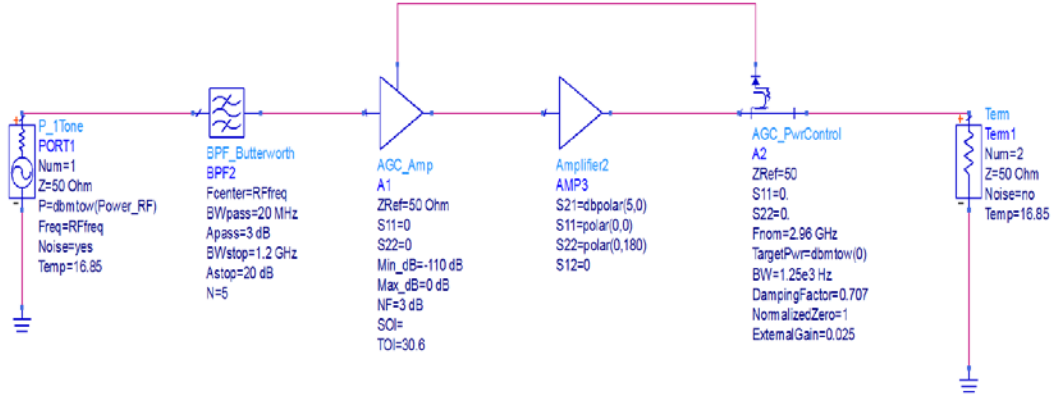


Figure 67. Schematic of RF receiver system with an AGC loop. RF system circuit template extracted from ADS Systems *Budget Analysis_AGC* examples [54], with several modifications in the electronic component parameters.

The input signal power level P_{in} (in dBm) to be used as input power in the budget analysis simulations was determined by calculating the transmitted power (in dBm) received at the receiver antenna assuming a receiver antenna effective area A_e .

The transmitted power in this present study relates to the simulated fitted near field power flux density results for the 4x1 linear transmitting antenna presented in the previous chapter, Chapter 3, which ranged from -50dB to 0dB. To convert this fitted relative near field power flux density, which was normalized relative to $1W/m^2$, into dBm, a factor of 30 dB is subtracted, which gives a range for the fitted near field power flux density (in dBm) between -80dBm to -30dBm. Then assuming that all of this fitted relative near field power flux density (in dBm) reaches the receiver antenna, then the actual input power signal level, P_{in} entering the RF receiver system is the fitted near field power flux density (in dBm) plus the effective antenna area of the receiver (in dB). The receiver antenna effective area $A_e \approx 4 \times 10^{-3} m^2 (\approx \frac{\lambda^2 G_r}{4\pi})$, assuming wavelength $\lambda = 0.10135m$ and antenna power gain $G_r \sim 5$ for the 1x1 single circular patch antenna) which is equivalent to -24dB. Therefore, the input signal power level P_{in} from the transmitted linear array antenna entering the receiver system is assumed to be $-104 dBm \leq P_{in} \leq -54 dBm$. It is this input signal power level P_{in} range (i.e., $-104 dBm \leq P_{in} \leq -54 dBm$) that is used as the varying input power signal level for the budget analysis simulations. In addition, the input frequency, f for all the budget analysis simulations was 2.96GHz.

Figure 68 illustrates the calculated noise figure NF (denoted by parameter NF_RefIn_dB as defined by ADS Systems budget analysis) from system input to component output (assuming a 50 Ω source and load resistance) as a function of each component index for the RF receiver system circuit depicted in **Figure 67**.

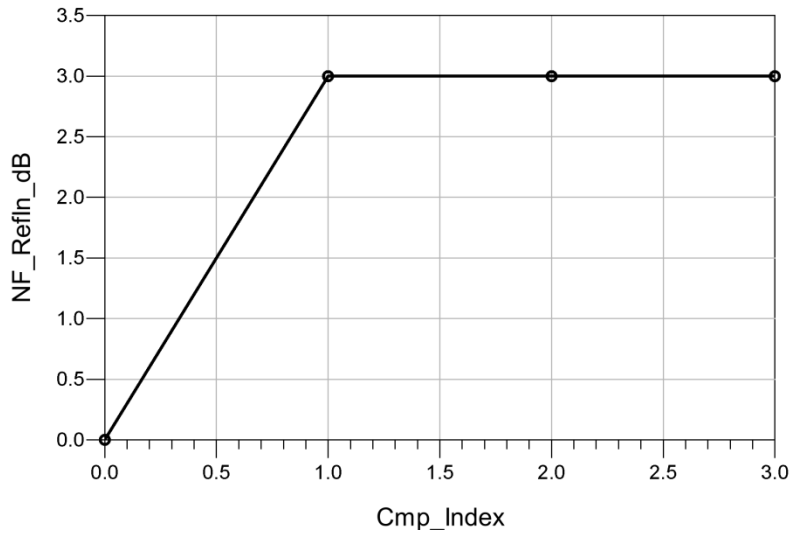


Figure 68. Noise figure/factor for each component in RF system depicted in RF system depicted in Figure 67. Here, $Cmp_index=0$ denotes bandpass filter (BPF2), $Cmp_index=1$ denotes the automatic control gain amplifier (AGC_Amp), $Cmp_index=2$ denotes the RF amplifier (AMP2), and $Cmp_index=3$ denotes the automatic gain control power control (AGC_Pwr_control).

As illustrated in **Figure 68** the noise factor increases from 0dB, at the bandpass filter (denoted by $Cmp_index=0$) to 3dB at the AGC amplifier (denoted by $Cmp_index=1$) and remains at this level at each of the other circuit components (RF amplifier and AGC power control). From the budget analysis this means that the RF receiver system, depicted in **Figure 67**, has a noise factor NF of 3dB.

Figure 69 (a) illustrates the computed output power, $OutPwr_dBm$ from each system component (i.e., $Cmp_Index=0, 1, 2$ and 3) for varying input signal power P_{in} (i.e., $-104\text{ dBm} \leq P_{in} \leq -54\text{ dBm}$) for the RF receiver system depicted in **Figure 67**. **Figure 69 (b)** illustrates the computed total output signal-to-noise ratio, $OutSNR_Total_dB$ from each system component (i.e., $Cmp_Index 0, 1, 2$ and 3) for varying input signal power P_{in} (i.e. $-104\text{ dBm} \leq P_{in} \leq -54\text{ dBm}$) for the RF receiver system depicted in **Figure 67**.

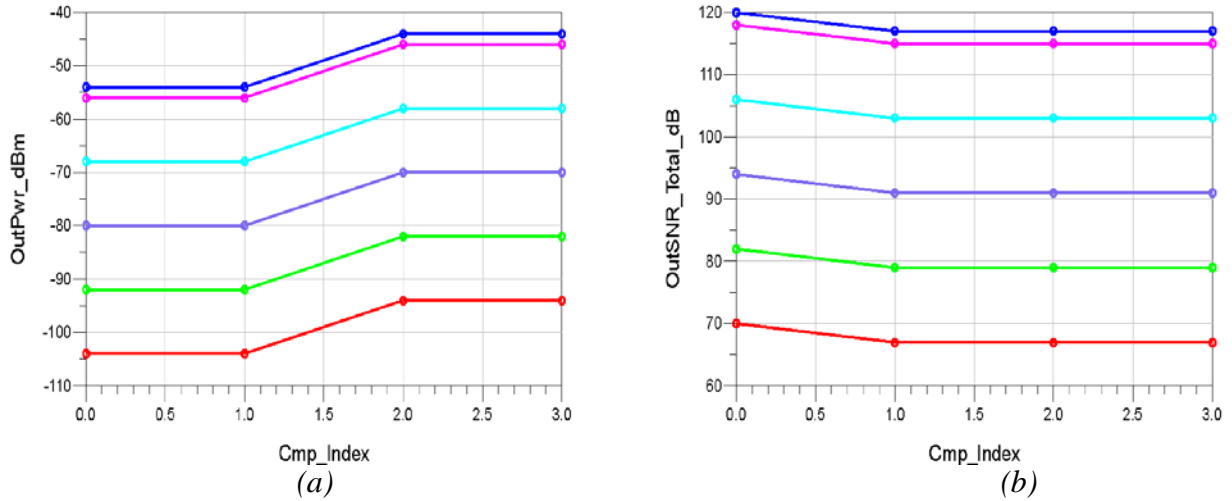


Figure 69 Power delivered into system at component output (left image, (a)) and signal-to-noise (S/N) for power delivered into system load at component output (right image, (b)) for each component of RF system depicted in Figure 67. Here $P_{in} = -104$ dBm, $P_{in} = -92$ dBm, $P_{in} = -80$ dBm, $P_{in} = -68$ dBm, $P_{in} = -56$ dBm, and $P_{in} = -54$ dBm. Here $Cmp_Index=0$ refers to the electronic component denoted as *BPF_Butterworth*, $Cmp_Index=1$ refers the electronic component denoted as *AGC_Amp*, $Cmp_Index=2$ refers to electronic component denoted as *Amplifier2* and $Cmp_Index=3$ refers to the electronic component denoted as *AGC_PwrControl*, as depicted in the RF receiver system in Figure 67.

As illustrated in **Figure 69**, as the input signal power P_{in} into the RF system increases, the output power of the system also increases, as would be expected. In particular, for each input power signal level there is a ~ 10 dB increase in the output power after the nonlinear AGC amplifier (i.e., $Cmp_Index=1$). Similarly, as the input power P_{in} increases so too does the signal-to-noise ratio, i.e., $OutSNR_Total_dB$, which is as expected, assuming the noise level is constant. However, for each input power signal P_{in} , the output signal-to-noise ratio, $OutSNR_Total_dB$ decreases, i.e., ~ 3 dB, from its maximum value at the output of the bandpass filter (i.e., $Cmp_index=0$) to the output of the nonlinear AGC amplifier component (i.e., $Cmp_index=1$). Where it remains at this level for each of the other RF circuit components (i.e., $Cmp_index=2$ (amplifier 2) and $Cmp_index=3$ (AGC power control)).

4.6.3 Receiver Desensitization (or Gain Compression)

Desensitization (or gain compression) occurs when a strong signal applied to a RF receiver system can reduce the receiver gain and overall sensitivity, reducing its ability to detect RF signals. If it is assumed, for discussion purposes, that the sensitivity (or

minimum input signal required to produce a specified signal-to-noise ratio $\left(\frac{S}{N}\right)$ at the output port of the receiver) $(S)_{\min}$ for the RF receiver system, depicted in **Figure 67**, has a threshold at $\sim -65\text{dBm}$. This threshold level corresponds to a minimum signal-to-noise ratio $\left(\frac{S}{N}\right)_{\min}$ of $\sim 105\text{dB}$, assuming a receiver system noise factor/figure, NF of 3dB , operating temperature $T=290^\circ\text{K}$ and bandwidth $(\text{BW})=1.25\text{ kHz}$.

From the above Figure, **Figure 69 (b)**, illustrates that for input power signal levels $P_{\text{in}} \geq -68\text{dBm}$, the simulated output $\left(\frac{S}{N}\right)$ has minimum values $> 105\text{dBm}$. Therefore, this indicates that for a receiver system with similar circuitry schematics, as depicted in **Figure 67**, with a minimum input signal required to produce a specified signal-to-noise ratio $\left(\frac{S}{N}\right)$ threshold of -65dBm , a bandwidth of 1.25kHz , $NF=3\text{dB}$ and operating at temperature 290K . The output power signal level from the transmitting 4×1 linear array antenna transmitter may indeed be high enough to cause desensitization (or gain compression) to the RF receiver system.

Figure 70 illustrates the minimum signal to noise ratio level as a function of input power, signal level. Assuming the RF receiver system has a minimum signal power, level threshold of -65dBm , for it to be able to detect RF signals; this in turn corresponds to a minimum S/N ratio for the RF receiver system of -105dB . However, as the input signal power levels increases the minimum S/N ratio will also increase. However, as RF receiver systems are designed to operate with different specifications and with limitations, as per the minimum input signal power threshold, then if input power signal levels exceed this threshold (related also to antenna gain) this in turn will cause a gain compression (or desensitization) of the receiver system affecting its operations.

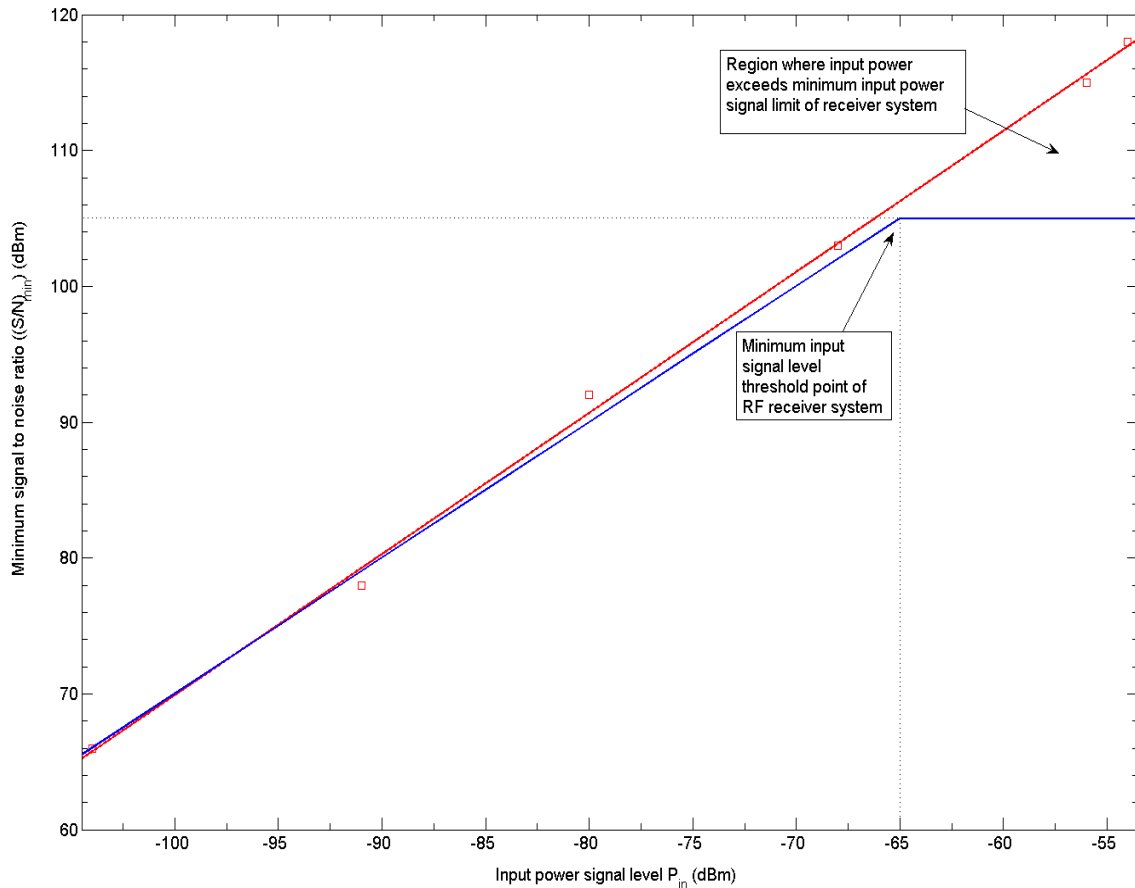


Figure 70. Minimum signal to noise ratio $(S/N)_{\min}$ as a function of input signal power level P_{in} for a RF receiver system with a noise factor $NF=3\text{dB}$, operating temperature $T=290\text{K}$ and $BW=1.25\text{kHz}$, and a minimum signal level threshold $\sim -65\text{dBm}$. Here — Theory, and — Budget analysis simulation (i.e., from above figure, Figure 69 (b)) with a least square fit curve denoted by red line.

Desensitization of an RF receiver system due to large input signal powers can also be described by gain compression of a non-linear electronic component.

Figure 71 illustrates a simple RF system with only a nonlinear electronic component, i.e., an amplifier. The amplifier, depicted in **Figure 71**, is assumed to have the same specifications as the amplifier (i.e., Amp2) in the RF receiver system depicted in **Figure 67**. It was further assumed that the amplifier had a gain $G=5$, operating frequency of 2.96GHz , third order intercept of (or third order harmonic) of 30.6 , and a power saturation/threshold level of -65dBm . The input power signal levels P_{in} were varied from -100dBm to 0dBm . Output power level, P_{out} as a function of input power signal level, P_{in} was computed and plotted doing a gain compression simulation in ADS Systems.

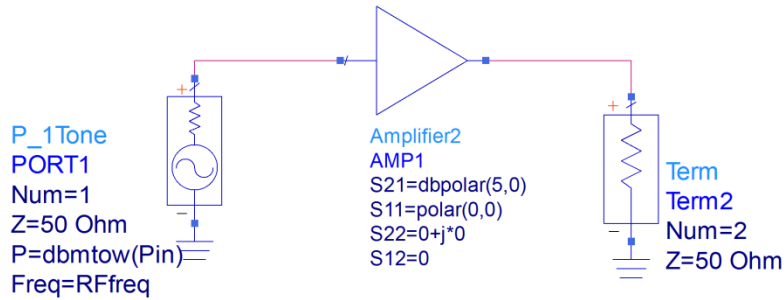


Figure 71. Schematic of RF system to evaluate gain compression of a non-linear component due to large input signal power levels. Schematic template adopted from ADS Systems examples [54].

Figure 72 illustrates the comparison of simulated output signal power level, P_{out} as a function of input signal power level, P_{in} for a linear and non-linear component response.

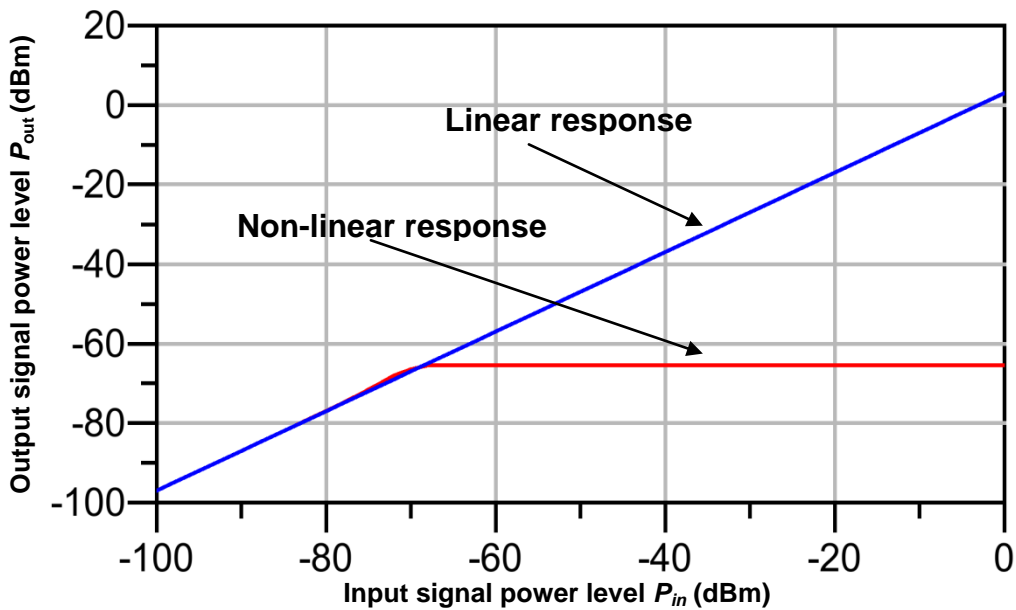


Figure 72. Simulated output signal power level P_{out} as a function of input signal power level P_{in} .

As illustrated in **Figure 72**, and as expected, for a linear component the output power response increases linearly with increasing input signal power levels. However, for the cases of nonlinear components, there is a saturation level where as the input power signal level increases there is no further increase in the output signal power.

Figure 73 illustrates the simulated gain G of the nonlinear component (i.e., amplifier denoted as *Amplifier2* depicted in **Figure 71**) as a function of input signal power level P_{in} .

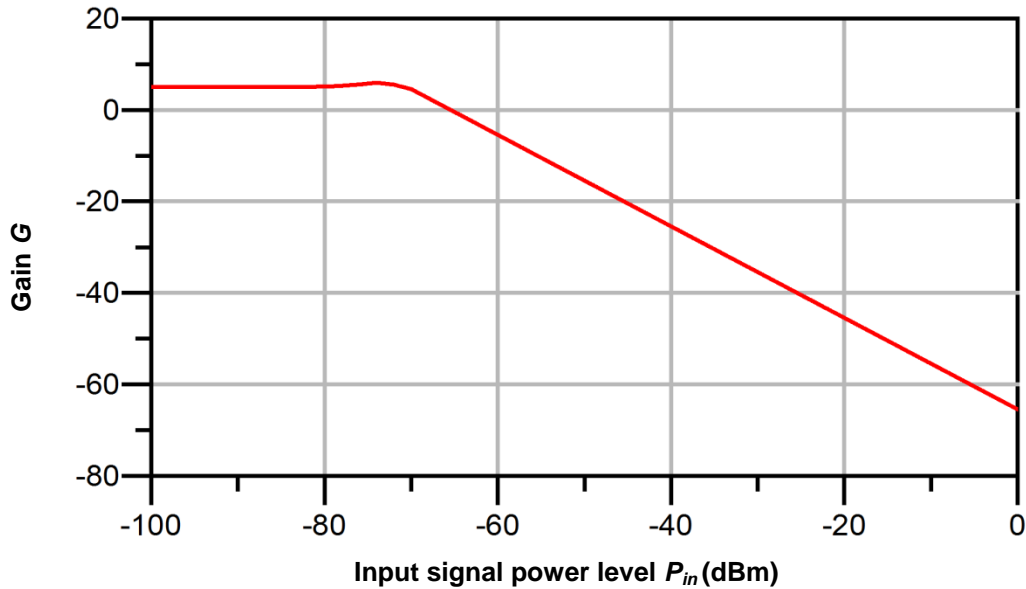


Figure 73. Simulated gain compression of the nonlinear component (i.e., amplifier) as a function of input signal, power level. In this simulation an interpolation was used to give better resolution.

As illustrated in **Figure 73** the gain G of the amplifier remains constant (i.e., 5) as input power, signal level P_{in} increases. However, when the input power signal level P_{in} reaches the pre-defined amplifier's power threshold (i.e., ~ -65 dBm) the amplifier gain G commences to decrease (or compresses) and continues to decrease as the input power P_{in} increases. This compression in the amplifier's gain G , if an amplifier is included in a RF receiver system, can impact the ability of the receiver system to detect weak RF signals. **Figure 74** illustrates a schematic of another type of a RF receiver system, which includes a mixer and local oscillator. The RF system circuit template was adopted from ADS Systems Budget Analysis examples [54]. Parameters and specifications for each electronic component of the RF receiver system, depicted in **Figure 74**, are presented in **Appendix A.6** in Table 14.

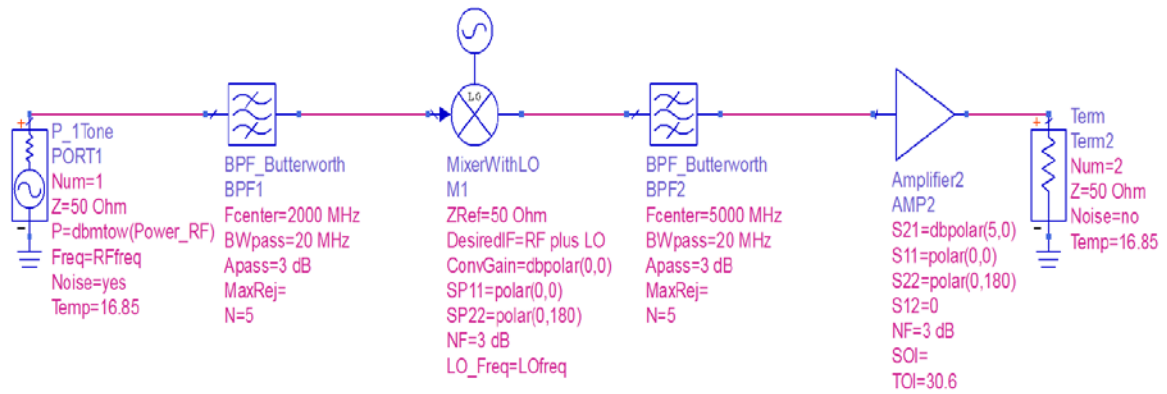


Figure 74. RF receiver system schematic with mixer and local oscillator. RF system circuit template adopted from ADS Systems' Budget Analysis Examples [54].

Figure 75 illustrates the RF system budget, analysis parameters for the RF receiver system depicted in **Figure 74**, assuming no nonlinear effects. Input power signal levels P_{in} were varied from -104dBm to -50dBm and component and system performance parameters were computed doing a budget analysis simulation in ADS Systems.

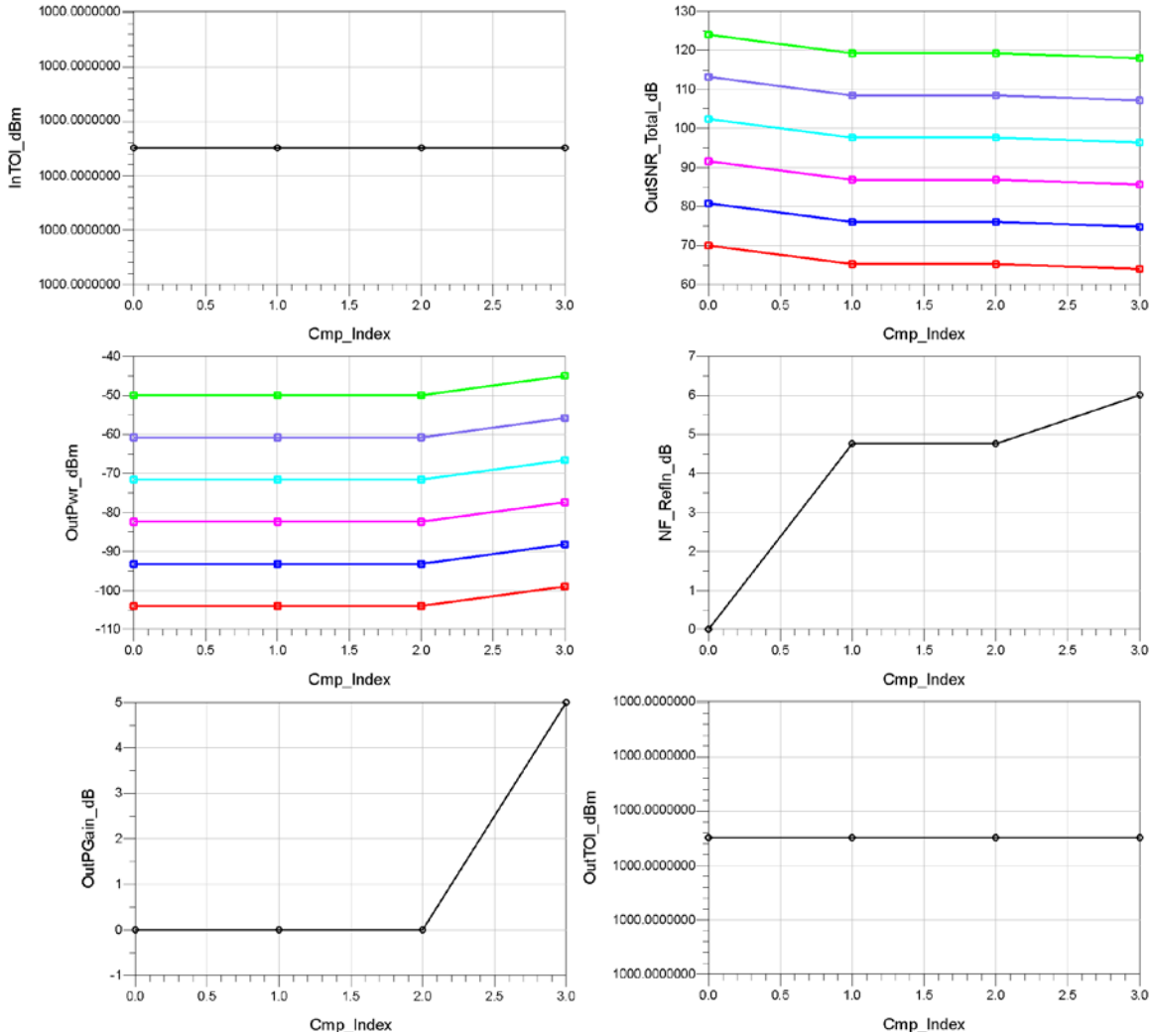


Figure 75. RF system parameters for RF receiver system depicted in Figure 74. Here nonlinear effects are not enabled in the simulation. For graphs *OutSNR_Total_dB* vs. *Cmp_Index* and *OutPwr_dBm* vs. *Cmp_Index* — $P_{in} = -104\text{dBm}$, — $P_{in} = -93.2\text{dBm}$, — $P_{in} = -82\text{dBm}$, — $P_{in} = -71.6\text{dBm}$, — $P_{in} = -60.8\text{dBm}$, and — $P_{in} = -50\text{dBm}$.

As illustrated in **Figure 75** the **third order intercept (TOI)** parameters (i.e., *OutTOI* and *InTOI*) shows a result of 1000 for each of the circuit component, which is as expected, since 1000 is the default value given to these parameters by ADS Systems’ budget analysis when nonlinear effects are excluded from the budget analysis simulations. All other output parameters (e.g. output power, output gain and noise factor NF and S/N ratio) show the typical linear responses to a varying input signal, power level.

Figure 76 illustrates the RF system parameters for the RF receiver system depicted in **Figure 74** when nonlinear effects (3rd order in this case) are enabled in the simulation. It was assumed that the amplifier (i.e., *Amplifier2*) had a maximum power level of -65dBm.

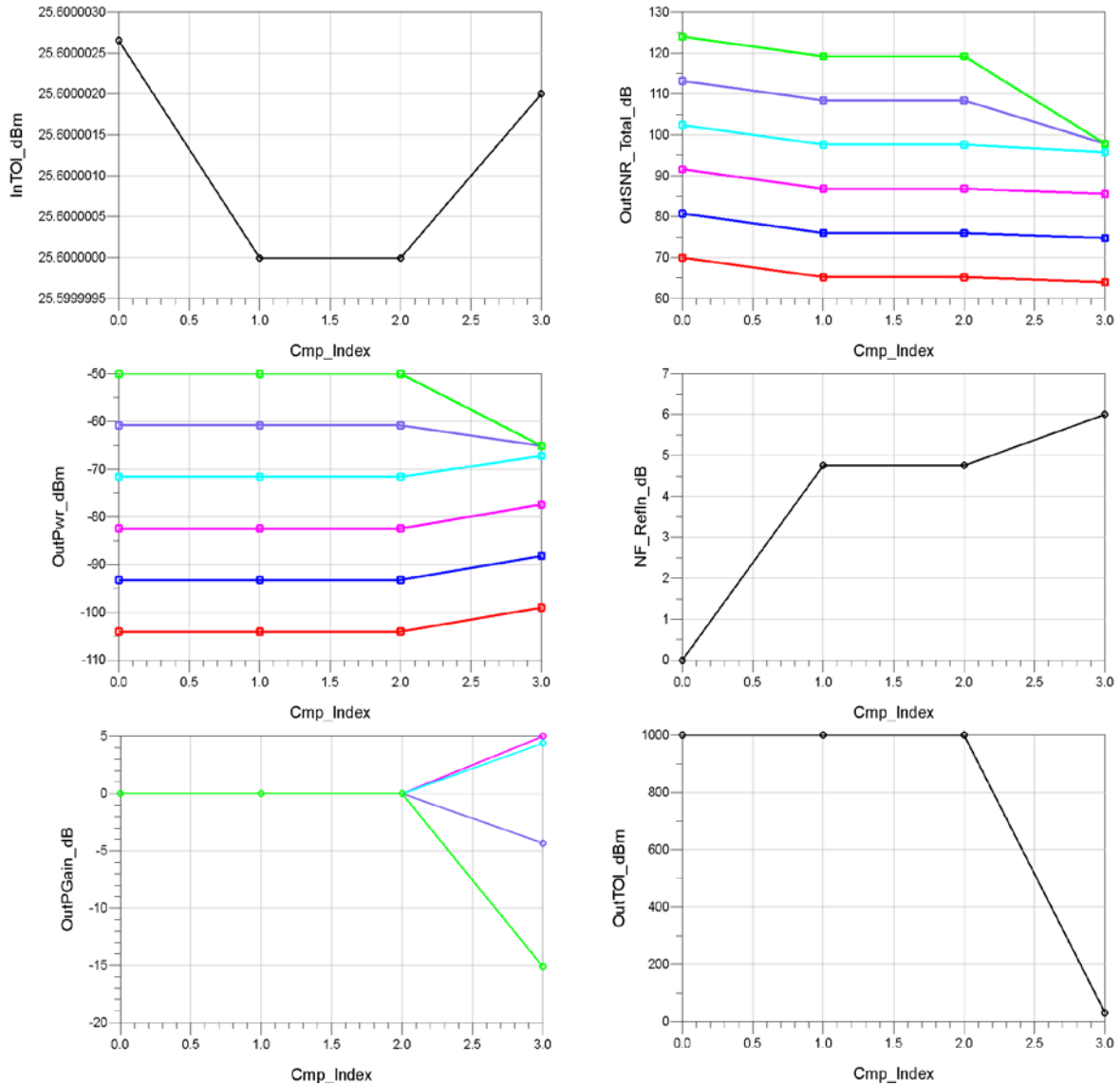


Figure 76. RF system parameters for RF receiver system depicted in **Figure 74**. Here nonlinear analysis (3rd order) is enabled. For graphs *OutSNR_Total_dB* vs. *Cmp_Index*, *OutPwr_dBm* vs. *Cmp_Index*, and *OutPGain_dB* vs. *Cmp_Index* — $P_{in} = -104\text{dBm}$, — $P_{in} = -93.2\text{dBm}$, — $P_{in} = -82\text{dBm}$, — $P_{in} = -71.6\text{dBm}$, — $P_{in} = -60.8\text{dBm}$, and — $P_{in} = -50\text{dBm}$.

As illustrated in **Figure 76** the **third order intercept (TOI)** parameters (i.e., *OutTOI* and *InTOI*) vary in magnitude compared to when nonlinear effects are excluded from the simulation. For example, the input TOI (i.e., *InTOI_dBm* parameter) is ~ 25 dB, and the **output TOI (*OutTOI_dBm*)** has varied from 1000 for the linear components to ~ 25 dB at the non-linear electronic components. Furthermore, there are also some significant compression occurring in the output power *OutPwr_dBm* and output signal-to-noise ratio *OutSNR_Total_dB* for input signal power levels, $P_{in} = -60.8$ dBm and $P_{in} = -50$ dBm, which is most likely attributed to the nonlinear effects. For example, there is a ~ 10 dB reduction in the output signal-to-noise ratio, *OutSNR_Total_dB* for the input power signal level $P_{in} = -50$ dBm and -60.8 dBm. Furthermore, for the output power *OutPwr_dBm* there is a reduction of -15 dB for the input signal power level $P_{in} = -50$ dBm and -5 dB reduction for the input power signal level $P_{in} = -60.8$ dBm. This reduction or compression is further illustrated by the reduction in the computed output gain, *OutPGain_dB* for similar input power signal levels, $P_{in} = -60.8$ dBm and -50 dBm. Furthermore, as illustrated in **Figure 76**, the computed output gain, *OutPGain_dB* from the non-linear components (i.e., *Amplifer2*, denoted by *Cmp_Index=2*) reduces significantly, i.e., ~ 5 dB for input power signal level $P_{in} = -60.8$ dBm and ~ 15 dB for input signal power level $P_{in} = -50$ dBm.

4.6.2 Sub-Harmonic Distortion

Sub-harmonic distortion is due to interference between a transmitter and receiver systems is when the transmitter causes a harmonic distortion effect in the receiver system. If we consider a RF receiver system, as depicted in **Figure 67**, where it is assumed that the RF receiver system has an input third harmonic (or order) intercept (TOI) of 30.6 dBm and a maximum 3rd harmonic level *HL* of -100 dBm, then the maximum allowable input power P_{in} at the fundamental is -12.93 dBm (i.e., $= (n-1)TOI + HL / n$). Therefore, this means that input powers P_{in} at the fundamental less than < -12.93 dBm is allowed before any third order harmonic distortions occur in the receiver system, assuming a TOI of 30.6 and harmonic limit of -100 dBm.

Since the input signal power levels of the 4×1 linear array antenna P_{in} (i.e., -104 dBm to -54 dBm) in the present case is significantly less than the maximum allowable signal power level (i.e., -12.9 dBm) of the receiver system before any 3rd order sub-harmonic distortions should occur, this suggests that these input power signal levels there should be no or very minimal 3rd order sub-harmonic distortion to the receiver system.

4.6.3 Other Non-linear Effects

Damage to front-end of the receivers, intermodulation distortions and cross modulation non-linear effects has not been considered here. Damage to front end receivers has not been considered, as this will depend on the damage level thresholds of the receiver system itself and will differ for different systems. Damage level threshold of a receiver antenna is typically provided by the systems manufacturer's specifications as a power density, and by calculating the transmitted power density and comparing to the front end receiver damage thresholds provided by the system's manufacture can an assessment be made to determine for damage will occur to the front end of the receiver system.

Intermodulation distortions and cross modulation non-linear effects are typically due to interference between multiple transmitters and a receiver. Therefore, since in the present study only one transmitter and one receiver system was considered non-linear effects due to intermodulation and cross modulation was not assessed. However, for any future work where more transmitters are considered on a mast structure, such non-linear effects will need to be considered.

THIS PAGE INTENTIONALLY LEFT BLANK

5 CONCLUSIONS AND FUTURE WORK

The present work provides a preliminary electromagnetic characterization of integrated masts as a possible mitigation strategy for ship radio frequency electromagnetic interference. Radio frequency systems (e.g. electronic warfare, radar and communication) systems integrated on a central mast structure is not a new concept for modern navy ships, and is becoming practically standard for modern navy ships. However, the concept of integrating radio frequency system on a central mast structure has in most cases been attributed to the housing of phased array radar systems, as part of a ship's upgrade programs. It is only in recent years, i.e., <~5 years, that there has been papers published claiming that integrated masts can eliminate co-site electromagnetic interference between radio frequency systems. However, there is a dearth of information in the open literature supporting such claims, especially when one considers that having RF systems collocated on a central mast structure and in close proximity to each other, and in many cases possibly within the near field of transmitting systems, that large near field power signals can cause major interference between such systems. In addition, having antennas in close vicinity of a large structure can interfere with the antenna radiation pattern and also cause structural blockages, thus affecting the operational performance of the radio frequency system.

Therefore, this study provides an electromagnetic assessment of co-located antennas on a central mast structure. In particular, it assumed a worst case scenario, whereby the mast structure is a perfect electrical conductor to maximize the interference between mast structures and the antennas. Small scale models for antennas and mast structure was considered in the present study for a number of reasons. One reason was due to the limitations of the computation electromagnetic tools available for the present study but also to understand the physics and science in assessing the electromagnetics.

The electromagnetic characterization assessment for the present study was done using different numerical techniques including full wave solvers and asymptotic solvers. The full wave solver numerical techniques used include Finite Element Method, Method of Moments (includes Multi-Level Fast Method of Moments), Finite Difference Time Domain. The asymptotic technique used was a shooting and bouncing ray technique. All simulation results for the present study was primarily done using full wave solver techniques, mainly to maintain accuracy. All simulated numerical results, where possible, were compared to analytical results. For cases where comparisons between simulated numerical results with analytical results were not possible, the simulated numerical results were compared with each other, however, using different numerical solver techniques (e.g. MoM vs SBR).

From this study for a 4x1 linear array transmit antenna on a generic octagon shape rectangular faceted sloped panel mast structure the following conclusions can be asserted:

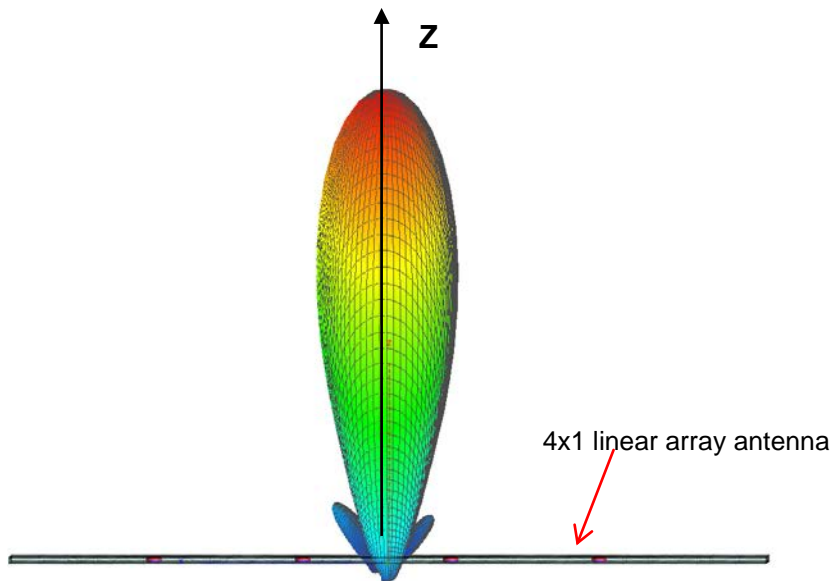
- Overall, the mast structure did reduce the mutual antenna-to-antenna coupling. The mutual antenna-to-antenna coupling was reduced greater (i.e., by ~20dB) when the receiver antenna was located on the mast structure side panel, relative to the mast structure panel where the transmit antenna was located. Compared to when the receiver antenna was placed above and on the same mast structure panel as the transmit antenna, where the mutual antenna-to-antenna coupling was reduced by ~10dB. However, further work will need to be done to fully conclude that integrated masts do indeed eliminate RF EMI. However, the present analysis does provide some positive indication that a central mast structure may aid in reducing mutual coupling between antennas collocated on a central mast.
- The mast structure can affect the antenna radiation pattern, depending on how the antenna is mounted on the mast structure. For the 4x1 linear array antenna used in the present study the mast structure had some significant effect on the antenna radiation pattern in azimuth φ , cut an elevation $\theta=90^\circ$.
- The fitted relative near field power flux density when the 4x1 linear array transmit antenna was fitted onto the mast structure was significantly high, reaching up to 0dB, mainly in regions around and above the transmit antenna. However, there were regions around the mast structure, mainly on the mast structure side panel, relative to the transmit antenna location, where the fitted relative near field power flux density was low i.e., ~ -20dB to -30dB.
- Transmit antenna scan angles are important to consider, since there may be regions around the transmit antenna and mast structure where for certain antenna scan angles there is a low near field power flux density and thus a relatively benign place to locate another antenna. However, such benign locations tend to depend on the scan angle of the transmit antenna.
- Non-linear effects of RF receiver systems are a critical concern for integrated masts. From the present analysis, despite only a simple RF receiver systems being considered, there were significantly high input power signal levels, due to the calculated near field power flux density from the transmit antenna, that caused desensitization (or gain compression) to the RF receiver system.

In any future work it would be interesting to consider different type of material for the present analysis mast structure model, rather than perfect electrical conductor material, and to add more features and complexity to the mast structure model to replicate a more realistic ship mast structure. In addition, future work should consider different mast structure shapes (e.g. cylindrical or conformal shape masts). In any future work, this initial study could be built upon, that is to increase the size of the mast structure, antennas and include ship structure, to reflect more closely a real ship with its onboard systems and its central mast structure. As the number of sensor systems accommodated on a central mast structure increases other non-linear effects (e.g. cross modulation and intermodulation), other than desensitization (or gain compression) and sub-harmonic effects can occur and need to be considered, in particular when sensor systems are located in very close vicinity to each other, and the effect of high intensity near electric fields.

APPENDIX A

A.1 FREE SPACE 4X1 LINEAR ARRAY RADIATION PATTERN AND BEAMWIDTHS

Figure 77 illustrates the simulated 3-D antenna radiation patterns for the 4x1 linear array antenna from each of the different computational electromagnetic software tools, namely FEKO and CST and Savant at frequency $f=2.96\text{GHz}$. Each antenna radiation pattern for the 4x1 linear array antenna was calculated using different models of the 4x1 linear array. For example, in FEKO the antenna radiation pattern was based on manually designing the linear array using the circular patch single element antenna. In Microwave Studio (or CST), the antenna radiation pattern was calculated by using the MWS internal array wizard functionality, whereby the radiation pattern of a multiple array antenna can be calculated by just determining the radiation pattern of the single element of the array. In Savant, the radiation pattern was calculating by designing a 4x1 linear array antenna with current sources, assuming Hertzian electric and magnetic pair dipoles.



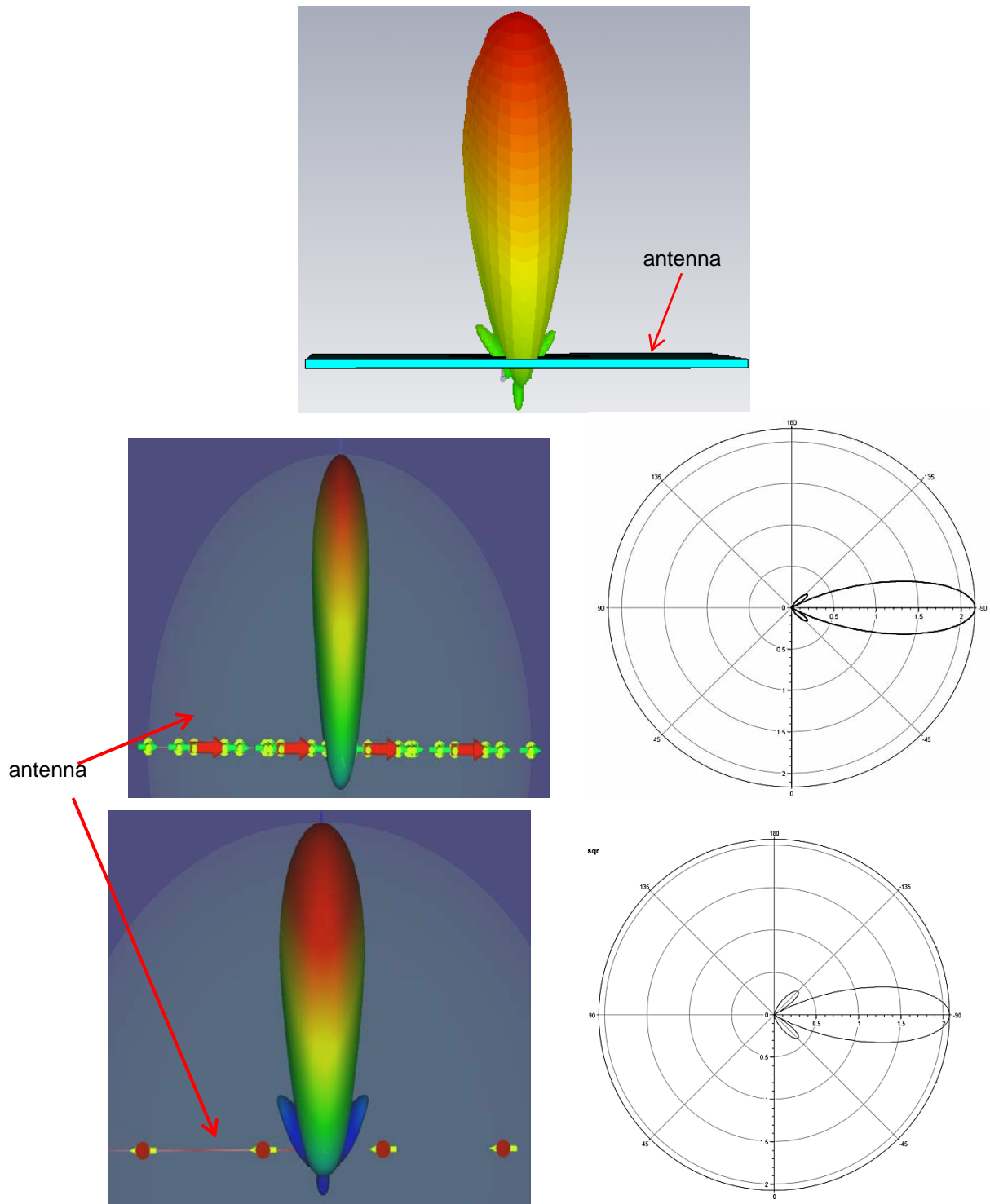


Figure 77. 3-D radiation pattern along boresight for the 4x1 linear array antenna in the computation electromagnetic software tools (From *top to bottom*) FEKO (MoM), Microwave Studio (or CST) (FDTD) and Savant (SBR-current source, 2x models).

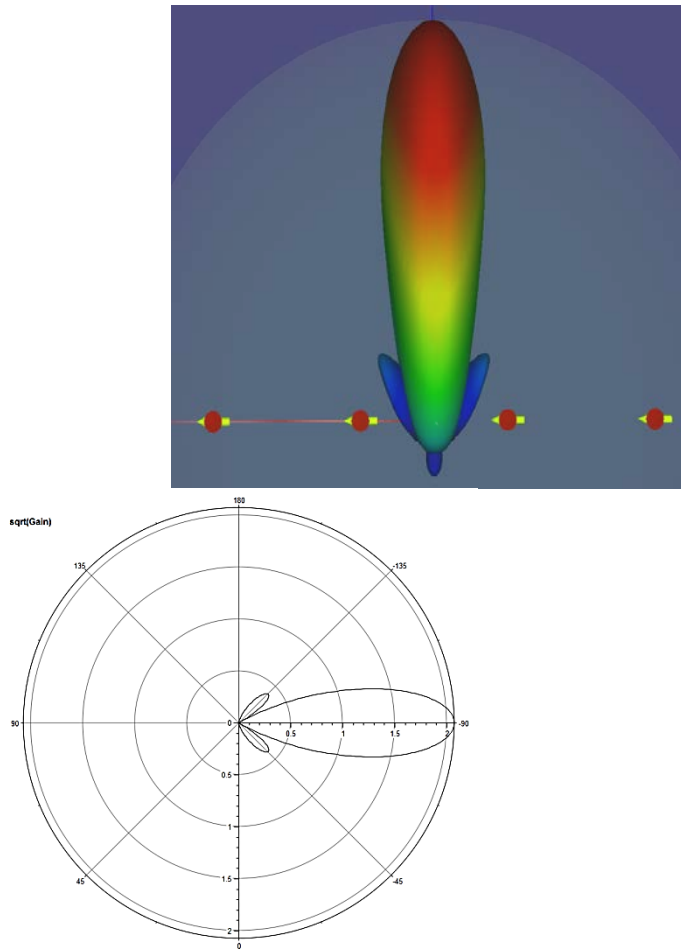


Figure 77 the 3D radiation pattern for 4x1 linear array antenna are similar in shape. However, there is some difference in the radiation pattern from Savant compared to FEKO and Microwave Studio. The significant difference is that the side lobes do not appear, from the perspective in which the image is shown. However, the sidelobes are present but are just not large enough to be seen in the image. To illustrate that the side lobes are present a polar plot of the radiation pattern is also shown in Figure 77.

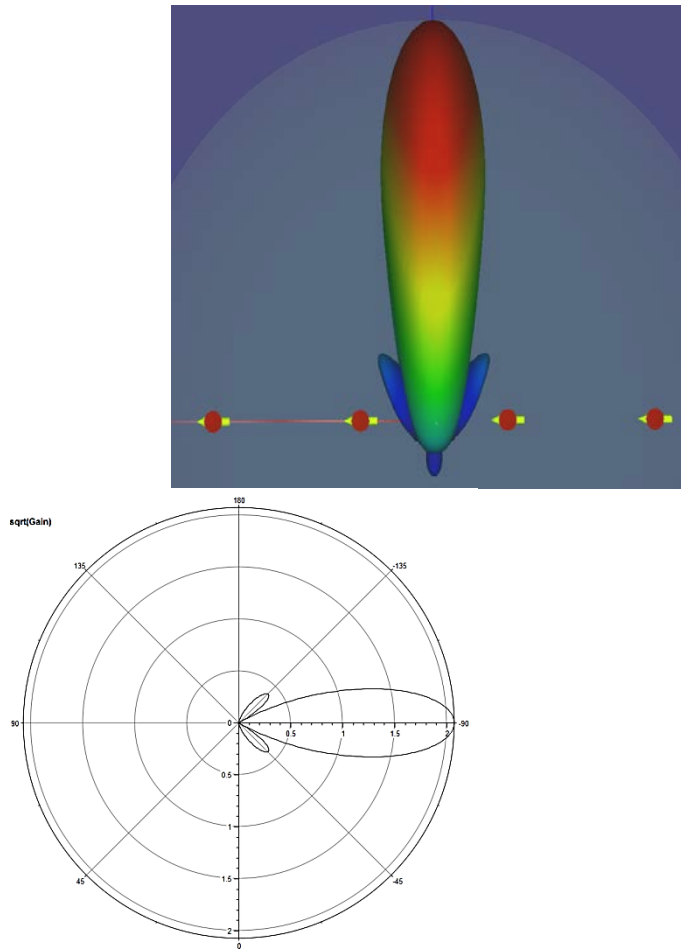


Figure 77. Alongside the Savant 3D radiation pattern. Another difference between all three antenna radiation patterns are the color radiation pattern intensity this difference is due to the different default color bar used by in each software not the same.

Figure 78 illustrates the normalized free space radiation pattern $f(\theta)$ as a function of elevation θ (in radians) along boresight for 4x1 linear array antenna with uniform illumination.

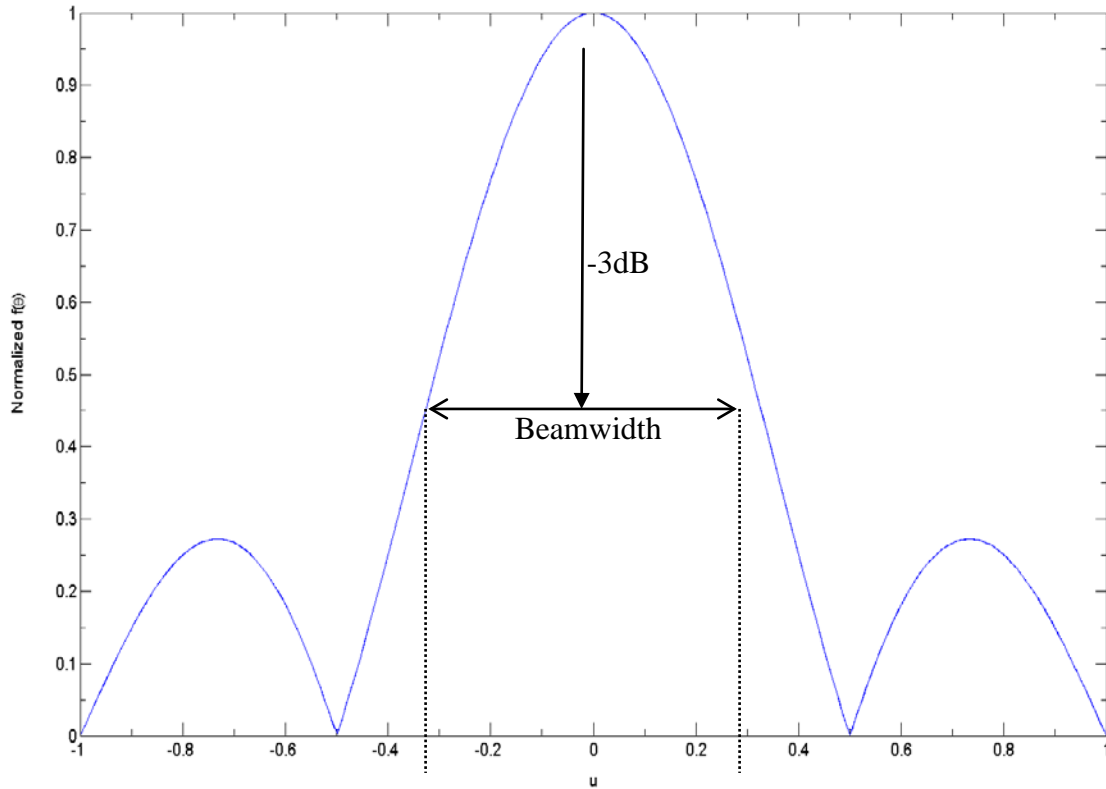


Figure 78. Normalized free space radiation pattern $f(\theta)$ as a function of u ($=\sin(\theta)\cos(\phi=0)$), (Mailloux 2005 [32]) along boresight for a 4x1 linear array antenna with uniform illumination. Beamwidth ($=-3\text{dB}$ from maximum or FWHM) $\approx 36.87^\circ$ ($=0.644$ radians).

Figure 79 illustrates the normalized free space radiation pattern as a function of azimuth (along boresight for a 4x1 linear array antenna using current sources in Savant.

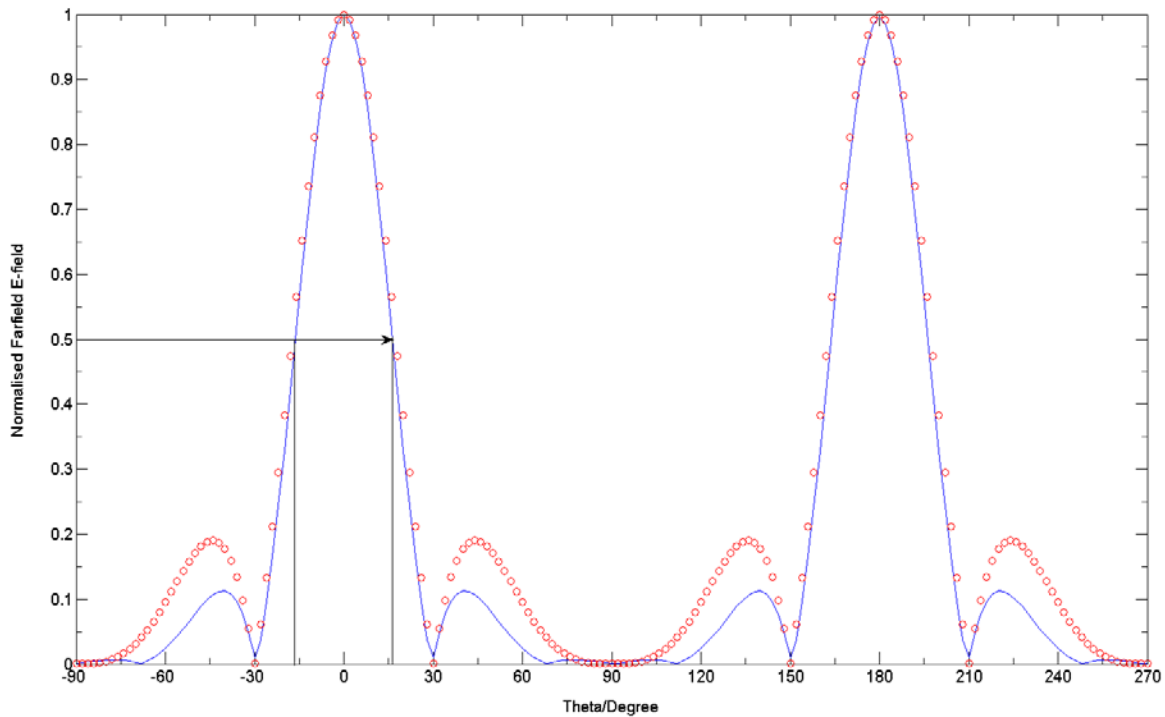


Figure 79. Normalized free space radiation pattern as a function of elevation (along boresight for a 4x1 linear array antenna using current sources in Savant. Beamwidth (= -3dB (or 0.5) from maximum or FWHM) $\approx 32^\circ$. — 4x1 linear array antenna current source model, assuming 4x electric dipoles to replicate each of the PEC single element antenna and 42x electric & magnetic dipole pairs to replicate an infinite substrate and ground plane, and \circ 4x1 linear array antenna current source model assuming 4x electric and magnetic dipole pairs replicating each PEC single element antenna, as depicted below in Figure 80.

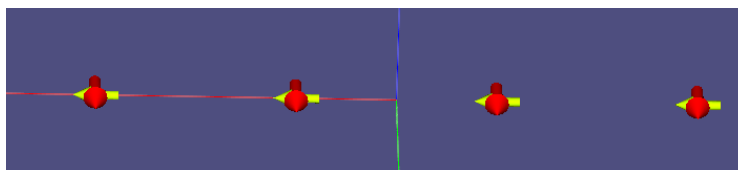


Figure 80. Image of antenna current source model in Savant assuming 4x electric and magnetic dipole pairs to replicate the PEC single element antenna.

Figure 81 illustrates the normalized free space radiation pattern as a function of azimuth (along boresight) for a 4x1 linear array antenna in FEKO.

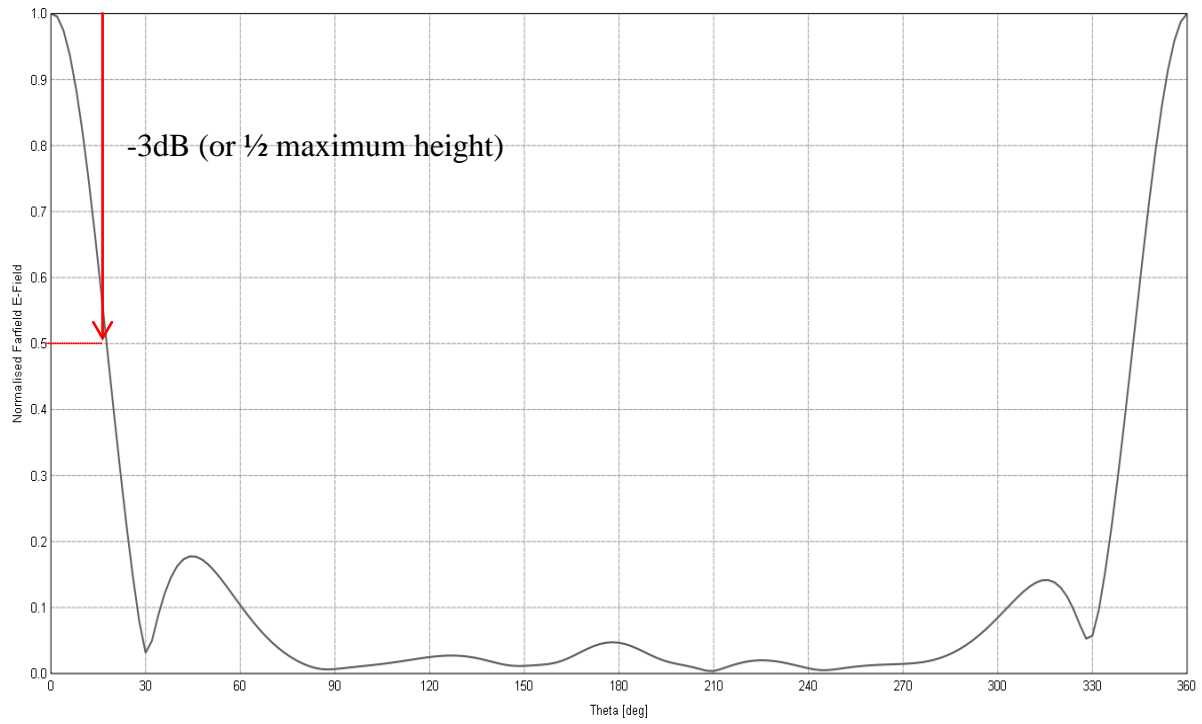


Figure 81. Free space radiation pattern as a function of elevation θ , cut at azimuth $\phi=0^\circ$ for 4x1 linear array antenna model in FEKO. Beamwidth ($=-3\text{dB}$ (or 0.5) from maximum or FWHM) $\approx 35^\circ$ ($=2x \approx 17.5^\circ$).

Figure 82 illustrates the normalized free space radiation pattern as a function of azimuth (along boresight) for a 4x1 linear array antenna in Microwave Studio (or CST).

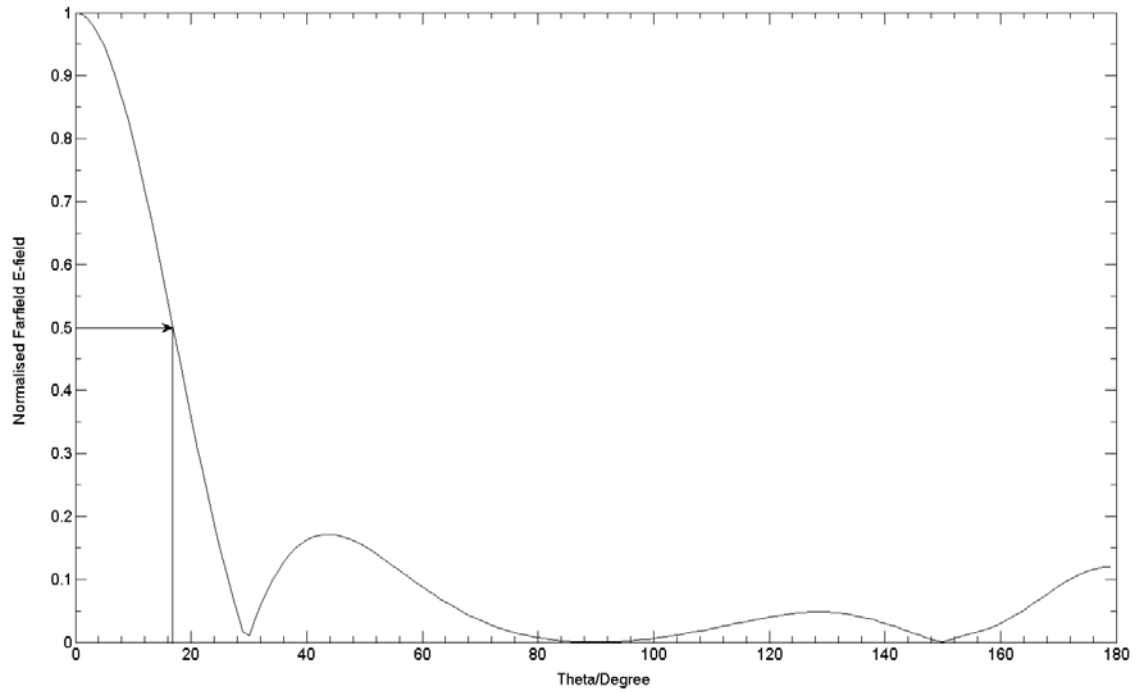


Figure 82. Free space radiation pattern as a function of elevation θ , cut at azimuth $\phi=0^\circ$ for 4x1 linear array antenna model in Microwave Studio (or CST). Beamwidth ($= -3\text{dB}$ (or 0.5) from maximum or FWHM) $\approx 34^\circ$ ($=2\times \approx 17^\circ$).

A.2 FREE SPACE AVERAGE NEAR FIELD POWER DENSITY CALCULATIONS FIGURES

Figure 83 illustrates the extrapolated normalized correction factor of the normalized correction factor electric field from the APD Program [36]. The extrapolation curve was done using MATLAB curve fitting tools. The extrapolated curve fit had a function of $y = -4.728x^{0.259} + 5.902$ with a root mean square error (RMSE) = 0.1038 and 95% confidence bound.

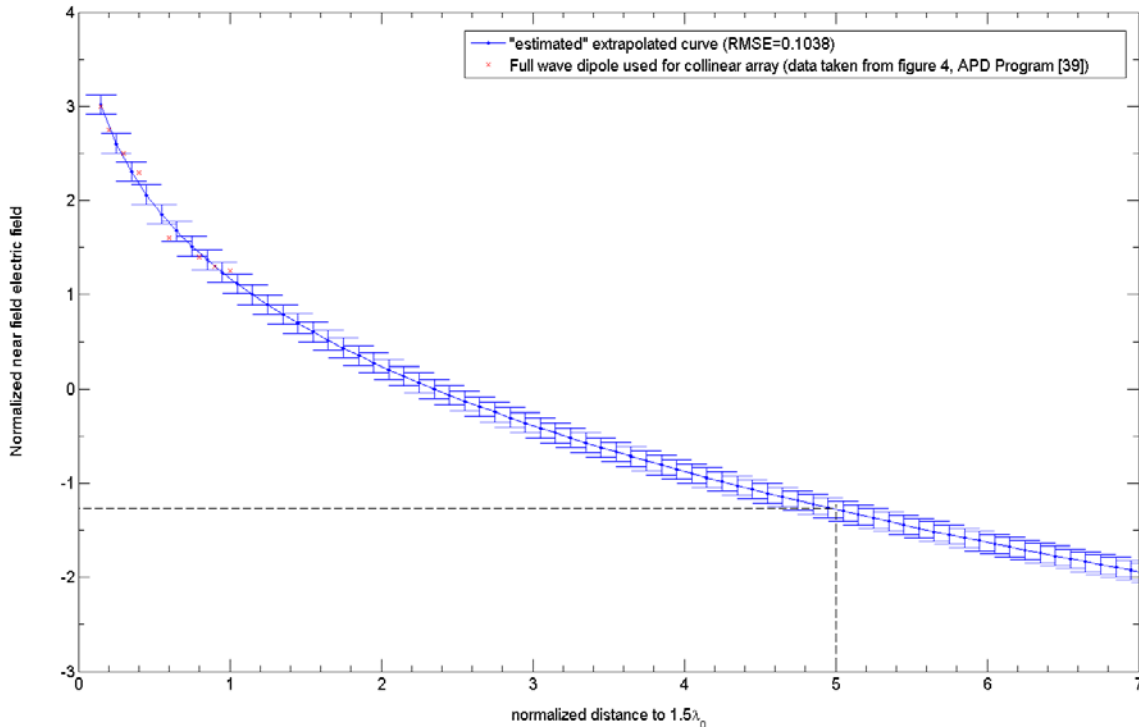
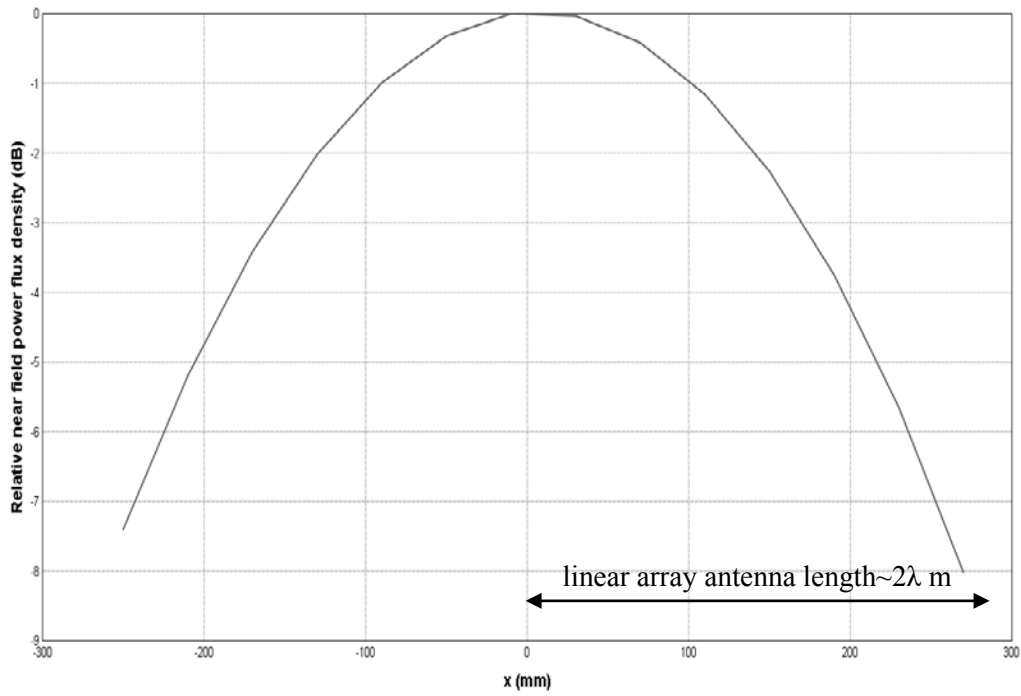
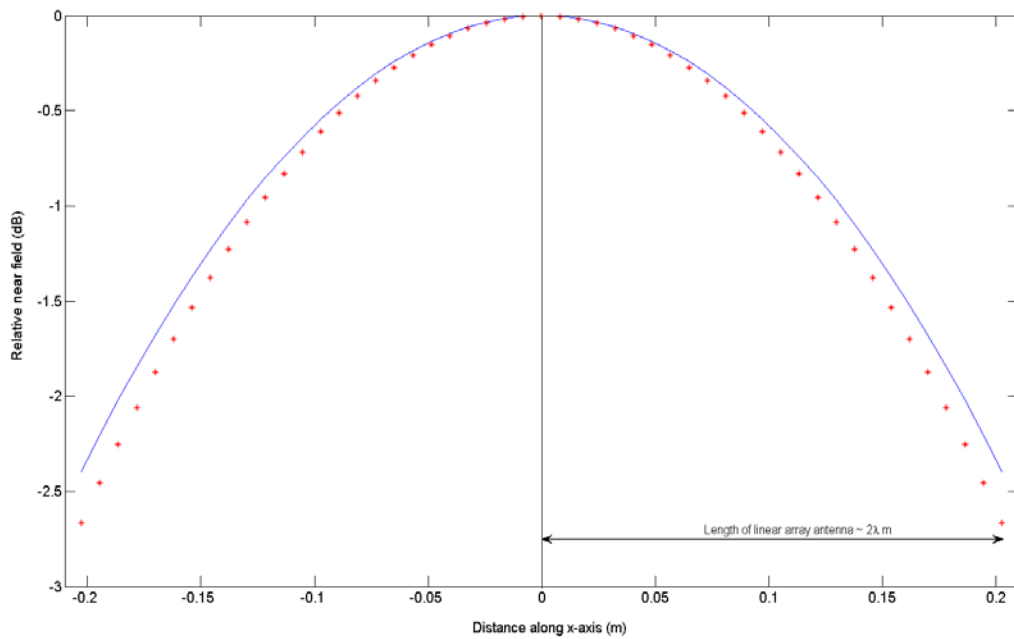


Figure 83. Calculated extrapolated normalized correction factor and normalized correction factor electric field from the APD_Program [36] distance all normalized to 1.5λ . Extrapolated curve fit function is $y = -4.728x^{0.259} + 5.902$, using MATLAB curve fitting tools.

Figure 84 illustrates the calculated relative near field power, density (dB) along the x-axis for the 4x1 linear array antenna model in FEKO. The near field was calculated at a distance 0.75m away from the center of the linear array antenna. Only the near field in the main beam was considered to calculate the free space average near field power density.



(a)



(b)

Figure 84. Relative near field power density (dB) along the linear array (assumed along x -axis), excluding sidelobes, at a distance $R= 0.75$ m away from and in front of antenna. (a) FEKO results; and (b) Savant Results, $-4\times$ electric and magnetic dipole

pair linear array antenna model; and * 4x electric dipole and 46x electric and magnetic dipole pair linear array antenna model.

Figure 85 illustrates the schematic of the near field calculations in the vicinity of the 4x1 linear array antenna using FEKO. In particular, near field power density was calculated for four different regions in the vicinity of the antenna, they include (i) above, (ii) below and (iii) right side and (iv) left side of the antenna. The analysis was done using FEKO and assumed a linear array antenna scan angle $\theta=0^\circ$.

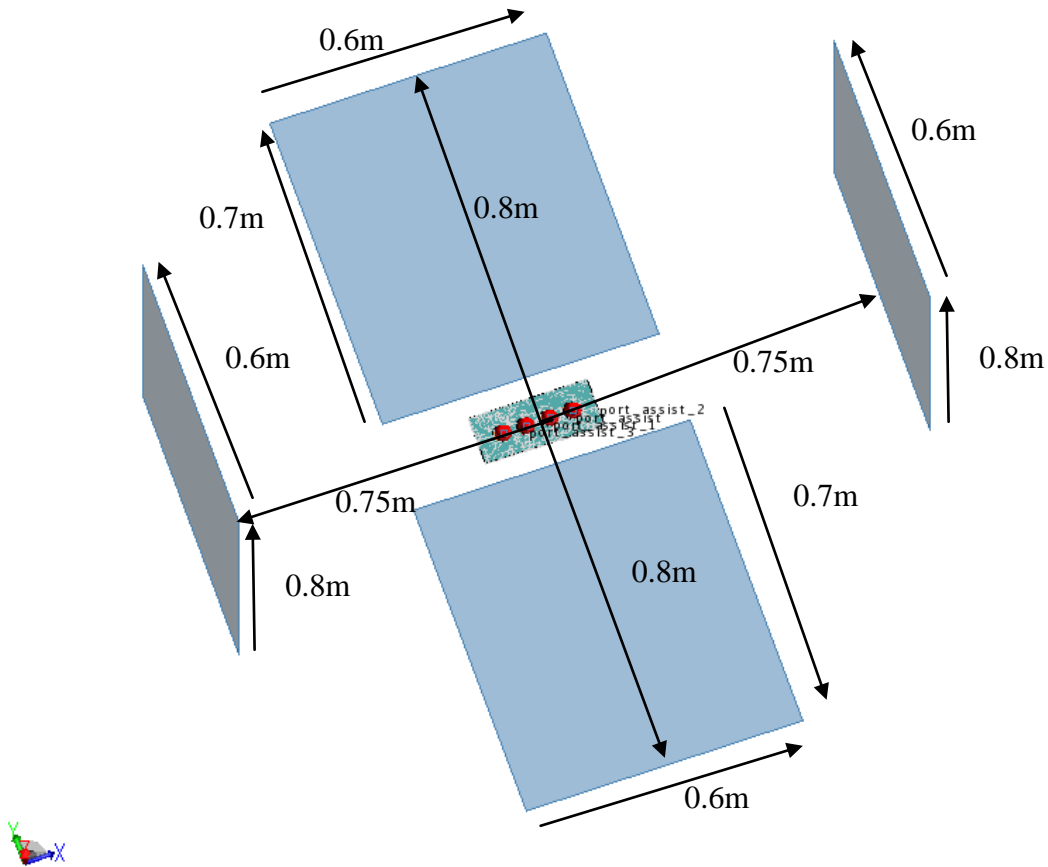


Figure 85. 3D schematic in FEKO of locations where near field power density was calculated at different locations in the vicinity of the 4x1 linear array antenna.

As illustrated in **Figure 85** the near field regions on either side of the antenna were calculated at a distance 0.75m from the center of the linear array over an area of 0.48m^2 ($0.6\text{m} \times 0.8\text{m}$). For the near field regions above and below the antenna, the near field was calculated in regions 0.1m above and below the antenna, from the center of the antenna, over an area of 0.42m^2 ($0.6\text{m} \times 0.7\text{m}$). The calculated average near field power density results are presented in Table 11.

Table 11 Calculated average near field power density in locations in the vicinity of the 4x1 linear array in free space. For completeness previously calculated boresight average near field power density has been included.

Location in vicinity of antenna	Calculated average Near field Power Density (dBW/m ²)
Above & Below (at a distance 0.75m from center of antenna)	-4.21
Right & Left Side (at a point along y-axis 0.05m from center of antenna) -perpendicular to array axis.	-6.64
Boresight	-2.90

As presented in Table 11 it is, as expected, the average near field power density above and below the antenna is high (i.e., -4.21 dBW/m²) compared to the near field power density along the axis of the array and perpendicular to the array (-6.64 dBW/m²), but lower than the near field power density along boresight (-2.90 dBW/m²). These results provide some overall indication as to the regions around the antenna of high and low near field power density when an antenna is to be fitted on a mast structure on a ship platform. Fitted near field power density analysis is provided in section, **Section 4.2.4.2**

A.3 ESTIMATED VERTICAL HEIGHT AS A FUNCTION OF AZIMUTH ANGLE WITH DIFFERENT RADIUS OF A CIRCLE

Figure 86 illustrates the estimated vertical height (in m) as a function of angle (in degrees) for different radial distances. **Figure 86** was used to relate the calculated power density flux in region 2 (i.e., radial distance as a function of azimuth angle) defined in FEKO, with the partial region of region 2 as defined in Savant, which was defined as a radial distance as a function of vertical distance.

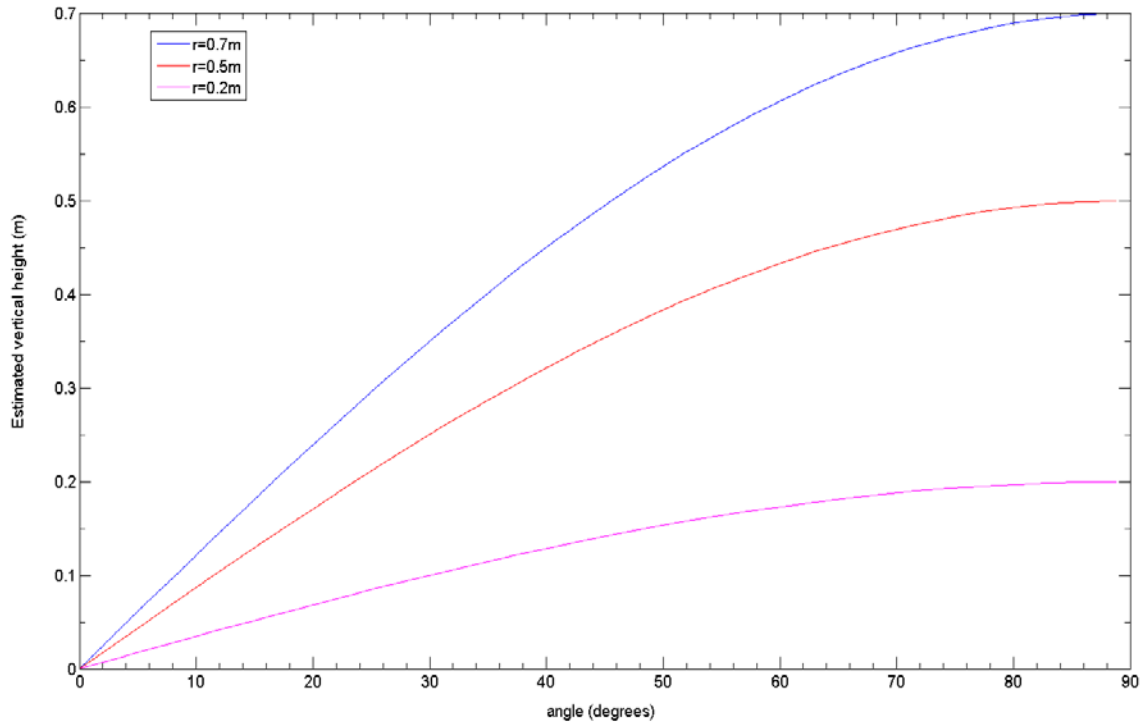
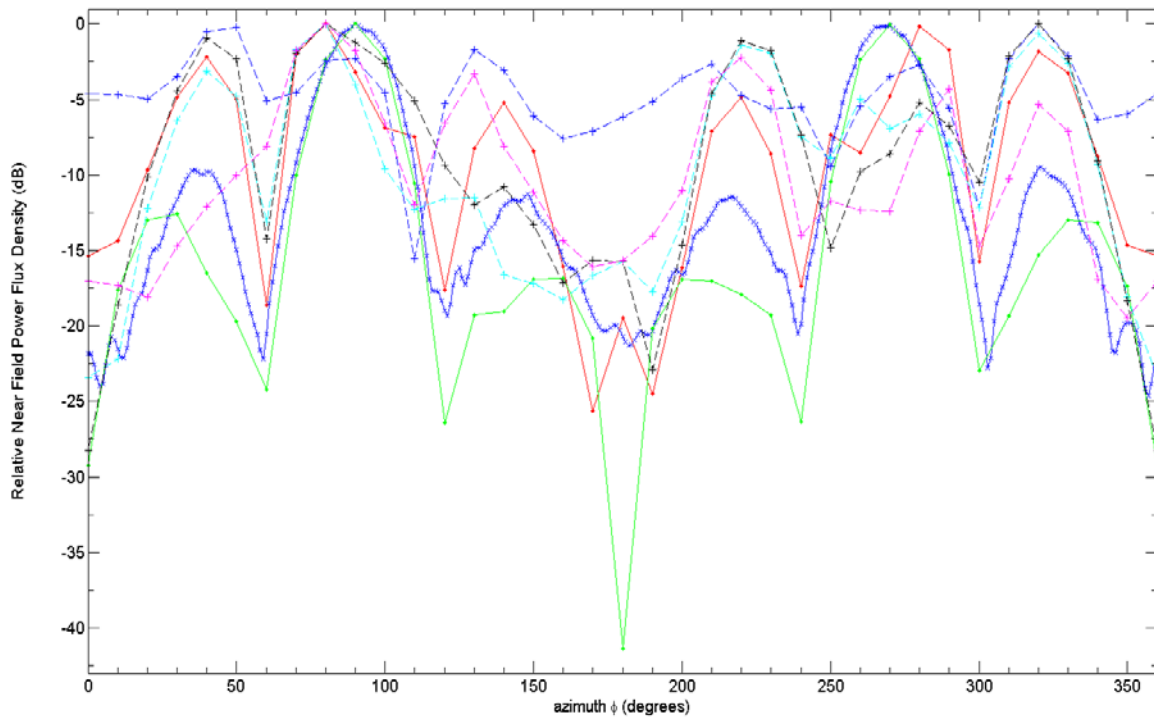
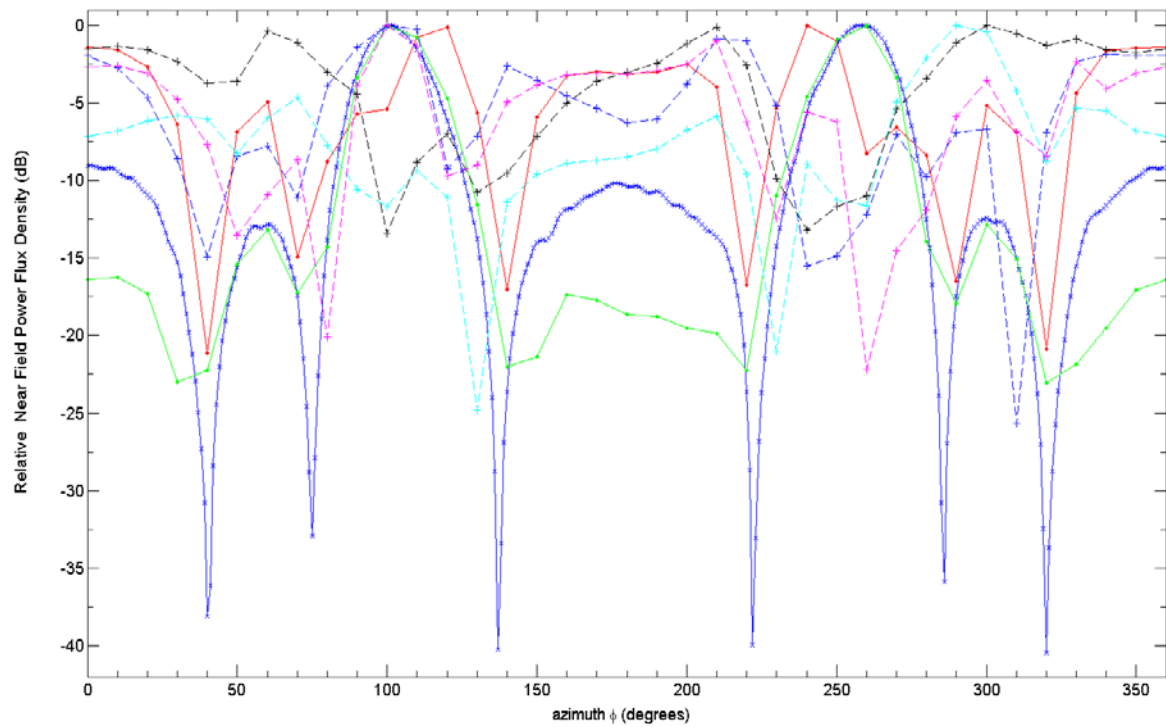
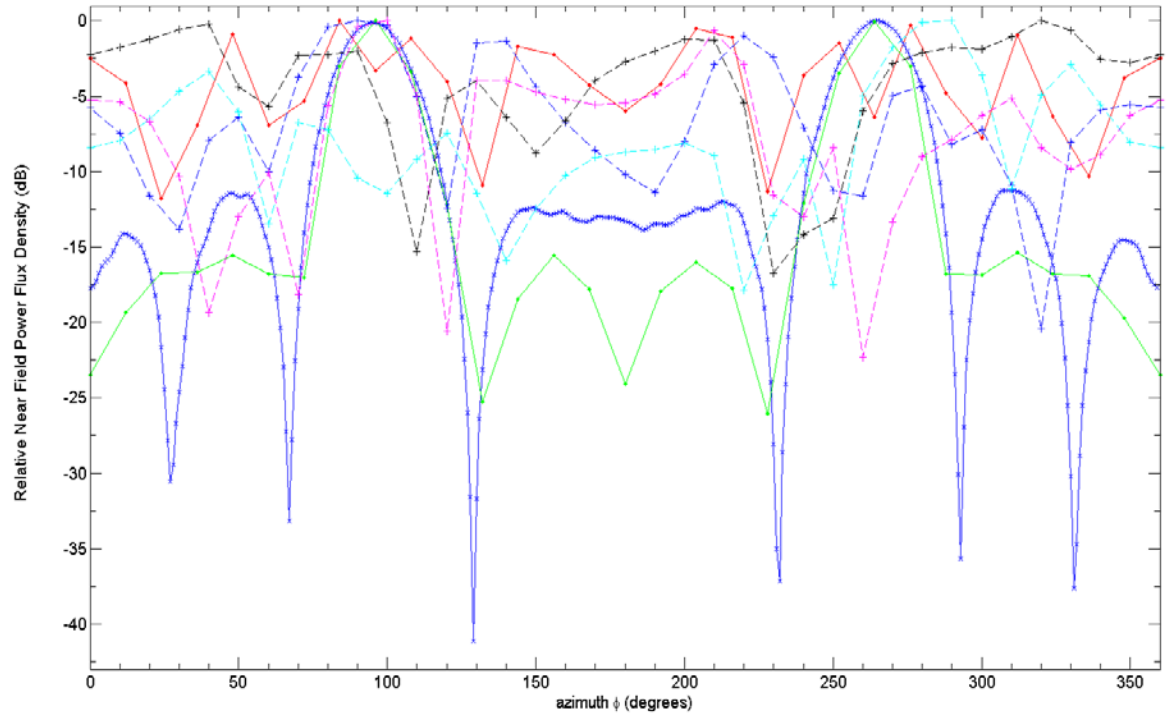


Figure 86. Estimated vertical height (in m) as a function of angle ($^{\circ}$) for different radial distances r (i.e., $r=0.2\text{m}$, 0.5m and 0.7m) from center of the transmit antenna.

A.4 FITTED RELATIVE NEAR FIELD POWER FLUX DENSITY IN REGION 2 AT RADIAL DISTANCE $R \approx 0.75M$ FOR DIFFERENT ANTENNA MOUNTING OPTIONS

Figure 87 illustrates a comparison of the fitted relative near field power flux density (in dB) in region 2 at a radial distance $R \approx 0.75m$, from the center of the array antenna for each of the different antenna mounting options on the mast structure and for different antenna scan angles (i.e., $\theta=0^\circ$, $\theta \sim 5^\circ$, $\theta \sim 11^\circ$ and $\theta \sim 18^\circ$). For completeness, the calculated relative near field power flux density (i.e., FEKO and CST) when the transmit antenna is positioned at distances $0.113m$ and $\lambda/4m$ from the complete mast structure are included also in **Figure 87**.





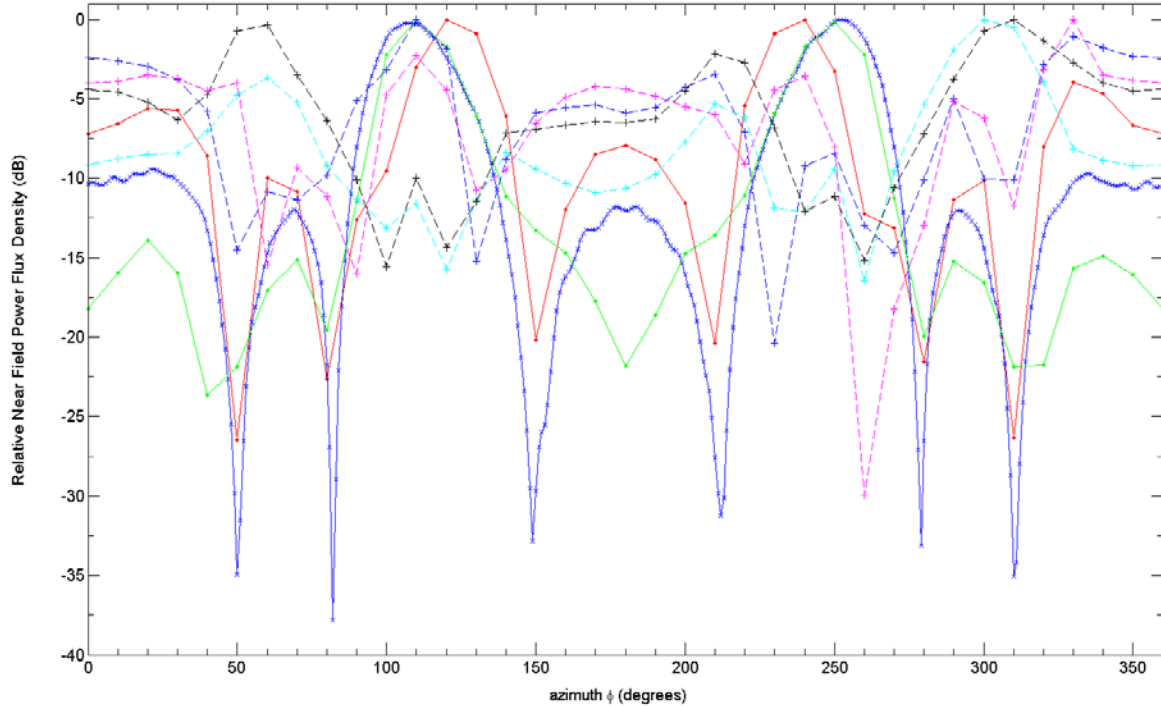


Figure 87. Fitted relative near field power flux density (dB) in region 2 at a radial distance $R \approx 0.75\text{m}$ from the center of the array antenna for different mounting positions and different antenna scan angles (from *Top to Bottom*) $\theta = 0^\circ$, $\sim 5^\circ$, $\sim 11^\circ$, and $\sim 18^\circ$. ● Numerical-FEKO 4x1 linear array antenna separated $\lambda/4\text{m}$ from complete mast structure, x Numerical-Microwave Studio (or CST) 4x1 linear array antenna separated 0.113m from complete mast structure, ● Numerical-FEKO 4x1 linear array antenna separated 0.113m from complete mast structure, + Numerical-FEKO 4x1 linear array antenna fully integrated with mast structure (mounting option A), + Numerical-FEKO 4x1 linear array antenna partial boxed-front ends (mounting option B), + Numerical-FEKO 4x1 linear array antenna partial boxed-side ends (mounting option C), and + Numerical-FEKO 4x1 linear array antenna fully boxed (mounting option D).

As illustrated by **Figure 87**, there is an overall elevation in the relative near field power density at a distance of $R = 0.75\text{m}$ from the center of the transmit antenna for each of the different mounting options at for each antenna scan angle. More so, at the larger scan angles (i.e., 11° and 18°) than the lower antenna scan angles (0° and $\sim 5^\circ$) compared to when the antenna is placed from the mast structure at distances of 0.113m and $\lambda/4\text{m}$.

Overall, antenna mounting option A (i.e., flush mounted or fully integrated) compared to the other antenna mounting options (B, C, and D) appears to have distinct regions of high and low relative near field power density regions, at all antenna scan angles, around the antenna and mast structure. The relative near field power densities for the different

mounting options B, C and D tend to have an overall high relative near field power flux densities around the antenna, at each different antenna scan angle.

The coarseness in the FEKO curves in **Figure 87** is attributed to the increment that was used in the FEKO simulations for the azimuth φ (i.e., $\Delta\varphi=5^\circ$) compared to an angle increment ($\Delta\varphi=1^\circ$) in Microwave Studio (or CST). This coarseness can be smoothed out by reducing the increments in future FEKO simulations.

A.5 MUTUAL ANTENNA-TO-ANTENNA COUPLING

A.5.1 Mutual antenna-to-antenna coupling S-parameters notation in computational electromagnetic software

Figure 88 illustrates the 4x1 linear array antenna numbering system used for the antenna-to-antenna mutual coupling S_{ij} parameters in FEKO for the present study. In FEKO the subscript i in S parameter S_{ij} refer to the receiver and the j subscript in the S parameter S_{ij} refers to the transmitter.

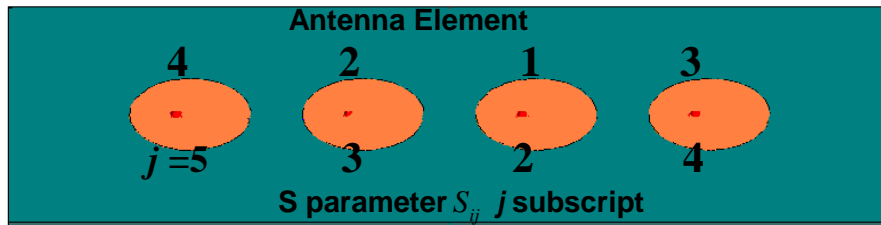


Figure 88. The antenna-to-antenna mutual coupling S-parameter notation for the 4x1 linear array antenna in FEKO.

As illustrated in **Figure 88** antenna element denoted by the number 4 refers to the j subscript =5, element number 2 refers to S parameter j subscript =3, element number 1 refers to the S parameter j subscript =2, and element number 3 refers to the S parameter j subscript=4. For example, the S parameter S_{ij} for the mutual coupling between the 4x1 linear array antenna element 2 and the 1x1 receiver antenna ($i=1$) would be denoted as S_{13} , given the present notation. Similarly, S_{14} would be the S parameter that refers to the coupling between 4x1 linear array antenna element number 3 and the receiver antenna ($i=1$). S_{15} would be the S parameter that refers to the coupling between 4x1 linear array antenna element number 4 and the receiver antenna ($i=1$), and S_{12} would be the S parameter that refers to the coupling between 4x1 linear array antenna element number 1

and the receiver antenna ($i=1$). A similar notation, as for FEKO, was adapted in displaying the Savant results for the present study.

A.5.2 Antenna locations in Savant for Mutual antenna-to-antenna coupling

Table 12 provides the actual co-ordinates for transmitter and receiver antenna for the mutual antenna-to-antenna coupling simulations in Savant. Co-ordinates were taken from FEKO relative from the center of the 4x1 linear array antenna model in FEKO located at co-ordinates (0, 0, 0). In Savant once the mast structure was included in model, the structure was fixed, there was no way of adjusting the position of the mast relative to the antennas. Therefore, in Savant the antennas had to be repositioned relative to the mast structure, whereas, in FEKO the mast structure was repositioned relative to the antennas.

Table 12 Co-ordinates for transmitter and receiver antenna for mutual antenna-antenna coupling simulations in Savant. Antenna scan angles were done mechanically.

Antenna & Location on mast	Co-ordinates Relative to (0,0,0) (m)	Orientation (°)
Transmitter (Tx) located front panel RFM	X=0.000	Roll= -110
	Y= -0.295 (~ $\lambda/4$ m from mast structure)	Yaw= 0
	Z=0.8405	Pitch= 0
Receiver (Rx) located above transmit antenna	X=0.004	Roll = -110
	Y=0.035	Yaw=0
	Z= -0.063	Pitch=0
Receiver (Rx) located on side panel	X= -0.878	Roll = -110
	Y=0.115	Yaw= -44
	Z= -0.0753 (No LOS with Tx) = -0.400 (LOS with Tx)	Roll=7.5

A.5.3 Analytical and Savant simulated Mutual antenna-to-antenna coupling

Figure 89 and **Figure 90** illustrate the typical free space mutual antenna-to-antenna coupling as a function of frequency f simulated Savant and analytical Friis transmission equation results respectively. As illustrated in both figures, i.e., **Figure 89** and **Figure 90** as frequency increases the mutual antenna-to-antenna coupling decreases.

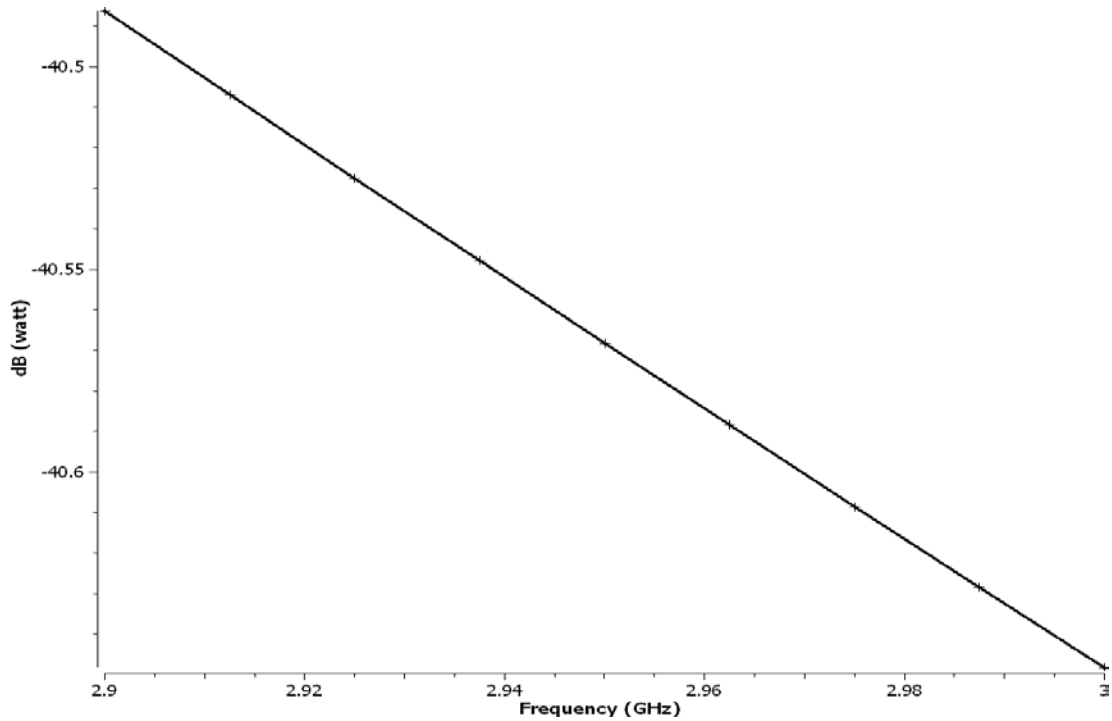


Figure 89. Typical Savant free space mutual antenna-to-antenna coupling as a function of frequency f .

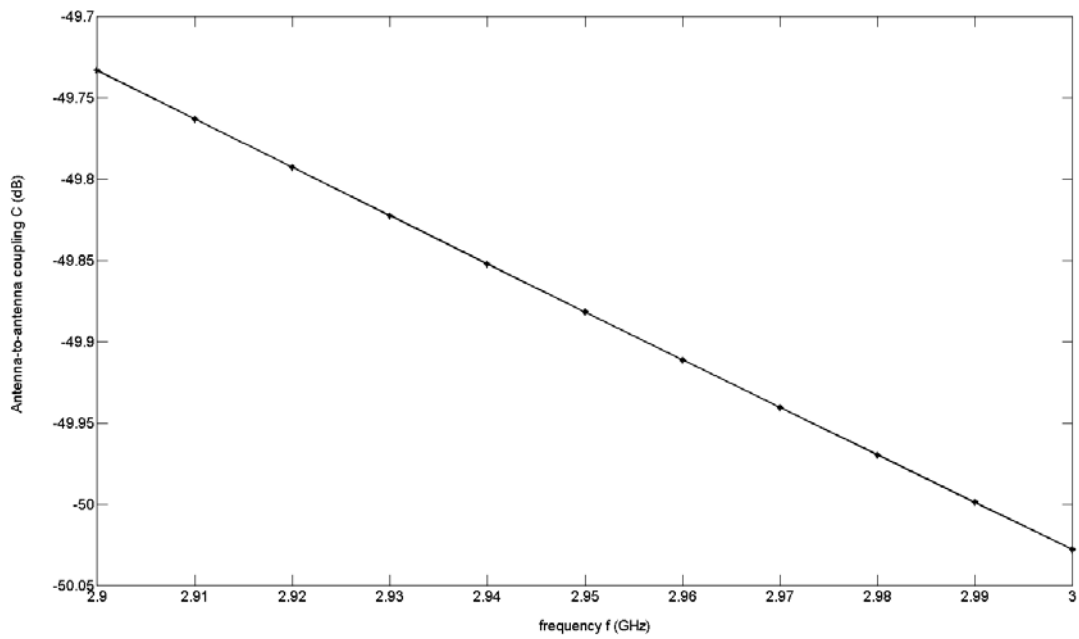


Figure 90. Typical Friis transmission equation mutual antenna-to-antenna coupling as a function f .

A.6 NON-LINEAR EFFECTS OF A RF RECEIVER SYSTEM

Table 13 presents the parameters and specifications for each of the electronic components in the RF receiver system, as depicted in **Figure 67**.

Table 13 Electronic component parameters and specifications for RF receiver system, as depicted in Figure 67.

Electronic Component	Component Index	Parameters & Values	
Power Source -Port 1	N/A	Impedance (Z)	50 Ω
		Power (P)	dBmtow ($Power_{RF}$) where $Power_{RF} = -104\text{dBm}$ to 0dBm steps 12
		Frequency ($Freq$)	RF_Freq=2960MHz
		Temperature (T)	290°K (=16.85°C)
		Noise	Yes
Bandpass Filter (BPF) Butterworth	Cmp_Index=0	F_{center}	RF_Freq=2960MHz
		BW_{pass}	20MHz
		A_{pass}	20MHz
		BW_{stop}	1.2GHz
		A_{stop}	20dB
		N	5
AGC_Amp	Cmp_Index=1	Z_{ref}	50 Ω
		S_{11}	0
		S_{22}	0
		Min_{dB} (dBm)	-110
		Max_{dB} (dBm)	0
		NF (dB)	3
		TOI (Third order intercept)	30.6
Amplifier 2	Cmp_Index=2	S_{21}	dpolar(5,0)
		S_{11}	polar(0,0)
		S_{22}	polar(0,180)
		S_{12}	0
AGC Power Control	Cmp_Index=3	Z_{ref}	50 Ω
		S_{11}	0
		S_{22}	0
		F_{norm}	2.96GHz
		$TargetPwr$	dBmtow(0)
		BW	1.25kHz
		$Damping\ Factor$	0.707
		$Normalized\ Zero$	1
		$External\ Gain$	0.025
Termination Port –Port2	N/A	Impedance Z	50 Ω
		Noise	no
		Temperature	16.85° (=290°K)

Figure 91 illustrates some of the output parameters from the budget analysis simulation in ADS Systems, for a RF receiver system circuit, as depicted in **Figure 67**, i.e., with an automatic gain control loop. The budget analysis included third order non-linearity in the receiver system. Similar results were obtained when the non-linearity was excluded from the simulation. This is most likely due to the automatic gain control loop in the circuit.

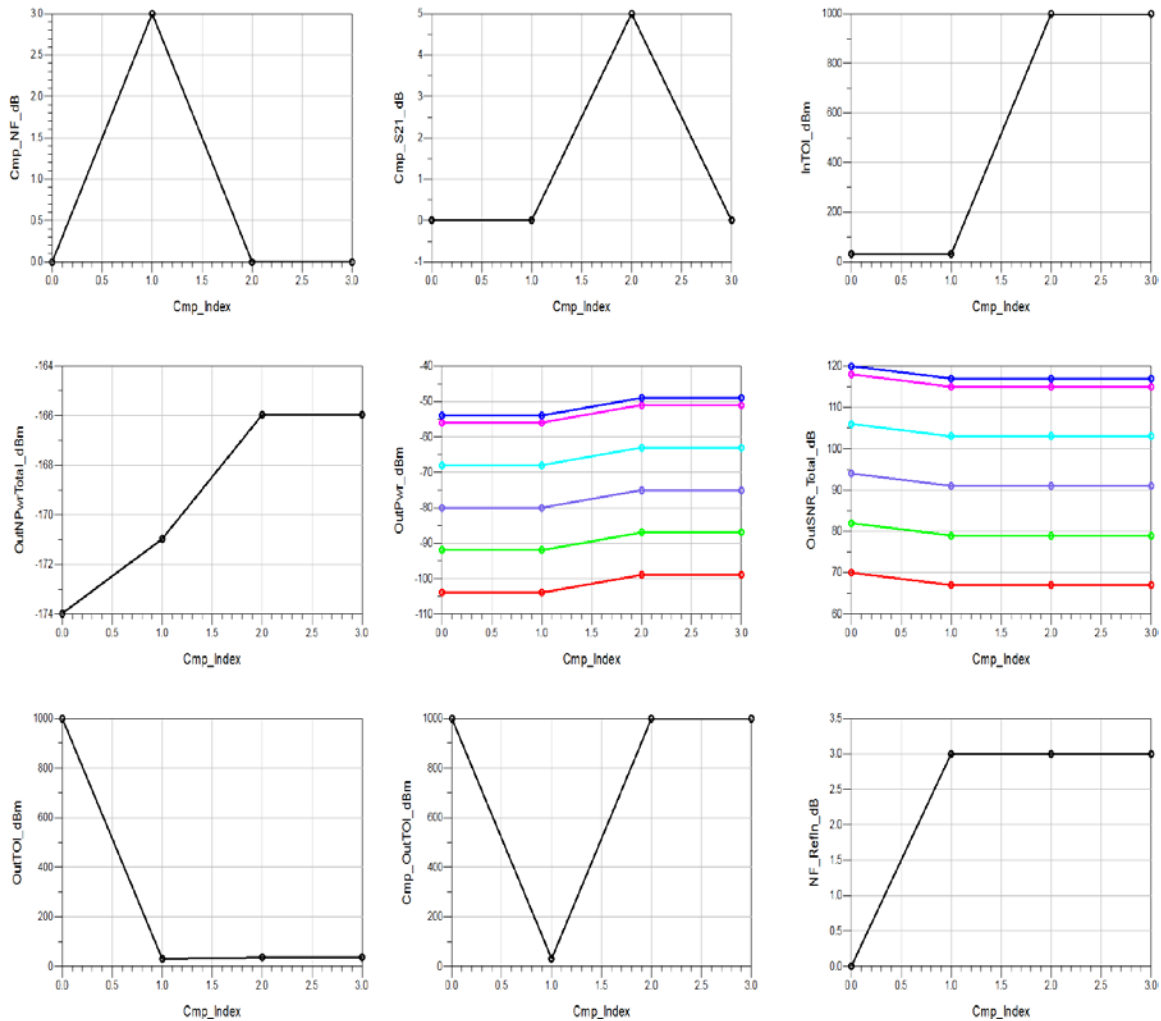


Figure 91. Budget Analysis RF circuit performance parameters as a function of component index for RF receiver system depicted in Figure 67. Here 3rd order nonlinearities included in analysis. Similar results are obtained when nonlinearities are not considered in simulation. For completion NF (NF_RefIn_dB) and output power (OutPwr_dBm), and S/N (OutSNR_Total_dB) figures, as depicted in Figure 68 and Figure 69, respectively, have been included here. Here $P_{in} = -104\text{dBm}$, $P_{in} = -92\text{dBm}$, $P_{in} = -80\text{dBm}$, $P_{in} = -68\text{dBm}$, $P_{in} = -56\text{dBm}$, and $P_{in} = -54\text{dBm}$.

Table 14 presents the electronic component parameters and specifications for the RF receiver system, as depicted in **Figure 74**.

Table 14 Electronic component parameters and specifications for RF receiver system depicted in Figure 74 .

Electronic Component	Component Index	Parameters & Values	
Power Source-Port 1	N/A	<i>Temperature (T)</i>	16.85°C (=290°K)
		<i>Input Power P</i>	dBmtow(<i>Power_RF</i>) <i>Power_RF</i> = -104dBm to -50dBm with 10.8 step size
		<i>Freq</i>	<i>RFreq</i> =2960MHz
		<i>Noise</i>	yes
		<i>Impedance Z</i>	50Ω
Band pass Filter (BPF) Butterworth (BPF1)	Cmp_Index=0	<i>Fcenter</i>	2000MHz
		<i>BWpass</i>	20MHz
		<i>Apass</i>	3dB
		<i>N</i>	5
Mixer With Local Oscillator (MixerWithLO)	Cmp_Index=1	<i>Zref</i>	50Ω
		<i>DesiredIF</i>	RFplusLO (=2000MHz+3000MHz)
		<i>ConvGain</i>	dpolar(0,0)
		<i>SP11</i>	polar(0,0)
		<i>SP22</i>	polar (0,180)
		<i>NF</i>	0dB
		<i>LO_Freq</i>	3000MHz
Band pass Filter (BPF) Butterworth (BPF2)	Cmp_Index=2	<i>Fcenter</i>	5000MHz
		<i>BWpass</i>	20MHz
		<i>Apass</i>	3dB
		<i>N</i>	5
Amplifier2 (AMP2)	Cmp_Index=3	<i>S21</i>	dpolar(5,0)
		<i>S11</i>	polar(0,0)
		<i>S22</i>	polar(0,180)
		<i>S12</i>	0
		<i>NF</i>	3dB
		<i>P_{sat}</i>	-65 dBm
		<i>TOI</i>	30.6
Termination Port - Port2	N/A	<i>Impedance Z</i>	50Ω
		<i>Noise</i>	no
		<i>Temperature (T)</i>	16.85°C (=290°K)

Table 15 provides the description for each of the measurements (i.e., *Cmp_NF_dB*, *Cmp_21_dB*, *InTOI_dBm*, *OutNPwrTotal_dBm*, *OutPwr_dBm*, *OutSNR_Total_dB*, *OutTOI_dBm*, *Cmp_OutTOI_dBm* and *NF_Refln_dB*) as defined from the budget analysis. Budget analysis measurements can be done at both the component and system levels.

Table 15 Description each output parameter defined in ADS Systems' Budget Analysis. Each description provided here was taken directly from ADS Systems RF System Budget Analysis documentation [52].

Budget Analysis Output Parameter	Description
<i>Cmp_NF_dB</i>	Component noise figure with source and load impedance of 50Ω
<i>Cmp_21_dB</i>	Component 50 Ω S ₂₁ (S parameter) in dB
<i>InTOI_dBm</i>	3 rd order intercept power delivered into system load at component input
<i>OutNPwrTotal_dBm</i>	Noise power per noise simulation frequency span centered at the RF fundamental frequency of noise power delivered into system load at component output
<i>OutTOI_dBm</i>	3 rd order intercept power delivered into system load at component output
<i>Cmp_OutTOI_dBm</i>	Component output 3 rd -order intercept with source reflection coefficient equal to the real part of the component small signal S ₁₁ and the load reflection coefficient equal to the real part of the component small signal S ₂₂
<i>OutPwr_dBm</i>	Power delivered into system load at component output
<i>OutSNR_Total_dB</i>	Ratio of signal power to total noise power for power delivered into system load at component output
<i>NF_Refln_dB</i>	Noise figure from system input to component output with 50Ω source and load resistance

6. BIBLIOGRAPHY

- [1] Rockway J.W., Russell L.C., Manry C.W., M^cGee J.B., and Meloling J.H., "EM Design Technology for Topside Antenna System Integration", 2001, *Naval Engineers Journal*, pp. 33-43.
- [2] Kildal Per-Simon, Kishk Ahmed A., and Tengs Audun, "Reduction of Forward Scattering from Cylindrical Objects using Hard Surfaces", 1996, *IEEE Transactions on Antenna and Propagation*, Vol. 44, pp. 1509-1520.
- [3] <http://www.thalesgroup.com/integratedmast/>
- [4] DeLong Betsy, "Integrated Topside, an Office of Naval Research Innovative Naval Prototype Program", Presentation at DSTO-Edinburgh, South Australia, 11th, August 2009.
- [5] <http://www.onr.navy.mil/~media/Files/Fact%20Sheets/Integrated%20Topside%20Innovative%20Naval%20Prototype%20Program.ashx>
- [6] Jenn David, Loke Yong, Matthew Tong Chen Hong, Choon Yeo Eng, Siang Ong Chin, and Yam Yeo Siew, "Distributed Phased Arrays and Wireless Beamforming Networks", 2009, *International Journal of Distributed Sensor Networks*, Vol. 5, pp. 283-302.
- [7] Private correspondence with Dr Warren Marwood, DSTO Research leader. Adelaide, September 2009.
- [8] Burkholder R. J., Pathak P. H., Sertel K., Marhefka R. J., Volakis J. L., and Kindt R. W., "A Hybrid Framework for Antenna/Platform Analysis". 2006, *ACES Journal*, Vol. 21, pp. 177-195.
- [9] van Werkhoven G.H.C., and van Aken R. H., "Evolutions in Naval Phased Array Radar at Thales Nederland B.V.", 2010, *Proc. 4th European Conference on Antennas and Propagation (EuCAP)*, pp. 1-4.
- [10] Barsoum Roshdy George S., "The Best of Both Worlds: Hybrid Ship Hulls Use Composites and Steel", 2003, *Advanced Materials, Manufacturing and Testing (AMTIAC) Quarterly*, Vol. 7.
- [11] <http://www.fas.org/man/dod-101/sys/ship/docs/aems.html>
- [12] <http://www.fas.org/programs/ssp/man/uswpns/navy/amphibious/lpd17.html>
- [13] http://en.wikipedia.org/wiki/Zumwalt_class_destroyer

- [14] <http://www.naval-technology.com/projects/dezeven/dezeven3.html>
- [15] http://www.cisco.com/en/US/prod/collateral/wireless/ps7183/ps469/prod_whitepaper_0900aecd806a1a3.html
- [16] <http://www.rfglobalnet.com/product.mvc/Antenna-Software-0001>
- [17] <http://www.ewca-home.org/about.html>
- [18] Josefsson Lars and Persson Patrik. "Conformal Array Antenna Theory and Design", *IEEE Press Series on Electromagnetic Wave Theory*, 2006, Wiley Interscience.
- [19] Ioannides Panayiotis and Balanis Constantine A., "Uniform Circular Arrays for Smart Antennas", 2005, *IEEE Antennas and Propagation Magazine*, Vol. 47, pp. 192-208.
- [20] http://www.baesystems.com/ProductServices/ss_tes_atc_electromags.html
- [21] <http://sgforums.com/forums/1164/topics/327354>
- [22] <http://www.websters-online-dictionary.org>
- [23] <http://sitelife.aviationweek.com/ver1.0/Content/images/store/2/12/0291ddd1-9d8d-4790-acb1-3d3d02e96fb9.Full.bmp>
- [24] Bird William R., Haradder Wayne R., Metzler Dr Thomas A., and M^cMillan Dr Stan B., "Shipboard Low Observable Antenna Concepts". 1995, *Naval Engineers Journal*.
- [25] Karavassilis N., Davies D.E.N., and Guy C.G., "Experimental HF Circular Array with Direction Finding and Null Steering Capabilities", 1986, *IEE Proceedings*, Vol. 133, pp. 147-154.
- [26] <http://www.globalsecurity.org/military/systems/ships/ssn-774-spiral.htm>
- [27] <http://www.gizmowatch.com/entry/phalcon-is-called-weirdest-airplane-in-the-world/>
- [28] <http://www.urel.feec.vutbr.cz>
- [29] <http://www.urel.feec.vutbr.cz/~raida/multimedia/images/4-7A-1.jpg>
- [30] Bahl I.J. and Bhartia P., "Microstrip Antennas", 1980, Artech House.
- [31] Garg Ramesh, Bhartia Prakash, Bahl Inder, and Ittipiboon Apisak, "Microstrip Antenna Design Handbook", 2001, Artech House.

- [32] Mailloux Robert J., "Phased Array Antenna Handbook - 2nd Edition". 2005, Artech House.
- [33] Grant I.S. and Phillips W.R., "Electromagnetism", 1975, John Wiley & Sons Ltd.
- [34] Kizer George., "Microwave Antenna Near Field Power Estimation", 2010, *Fourth European Conference on Antennas and Propagation (EuCAP)*.
- [35] Faraone Antonio, Yew-Siow Tay Roger, Joyner Ken H., Balzano Quirino, "Estimation of the Average Power Density in the Vicinity of Cellular Base-Station Collinear Array Antennas", 2000, *IEEE Transactions on Vehicular Technology*, Vol. 49.
- [36] http://www.ntiacsd.ntia.doc.gov/msam/APD/APD_PROGRAM.doc
- [37] Chen Yen-Sheng, Chen Shih-Yuan and Li Hsueh-Jyh, "Analysis of Antenna Coupling in Near-Field Communication Systems", 2010, *IEEE Transactions on Antennas and Propagation*, Vol. 58.
- [38] Whites Keith W., "Lecture 34:Antenna Effective Aperture.Friis Equation". 2011, <http://whites.sdsmt.edu/classes/ee382/notes/382Lecture34.pdf>.
- [39] Roubine E. and Bolomey J.C. , "Antennas: General Principles-Vol 1", 1987, Hemisphere Publishing Corporation.
- [40] <http://wireless.ictp.it/handbook/C4.pdf>
- [41] http://Aeronix.aeronix.com/products/defense_products/electronic_support_measures/finderpluds
- [42] <http://en.wikipedia.org/wiki/File:Superhet2.png>
- [43] http://www.ve7zsa.net/technical/advsgtxt/c8rcvrs_r00.htm
- [44] http://www.qsl.net/va3iul/LNA%20Design/LNA_design.htm
- [45] Jerse Tom, "Predicting Cosite Interference Nonlinear Effects", 2011, *IEEE International Electromagnetic Compatibility Symposium Workshop*.
- [46] http://www.tscm.com/rcvr_sen.pdf
- [47] Private correspondence with Dr Robert Kipp, Delcross Technologies, Savant Software, August 2011.
- [48] Fumeaux Christophe, "An Introduction to Computational Electromagnetics", 2010, *Lecture Notes*.

[49] Knott Eugene F., "Chapter 11-Radar Cross-Section", 1990, from "Radar Handbook 2nd Edition", author: Merrill Skolnik, McGraw Hill.

[50] Antenna-to-Antenna Coupling Notes, 2011, *Delcross Technologies Savant Software help contents*.

[51] Agilent Technologies, ADS Systems Software, "About ADS Systems", 2011.

[52] Agilent Technologies ADS Systems, "RF Systems Budget Analysis", May 2011, *Notes from ADS Systems software help section*.

[53] Rhinoceros v4.0, "Notes about Rhinoceros 4.0 software", 2011

[54] Agilent Technologies, ADS Systems, "RF Systems Budget Analysis Examples", 2011.

INITIAL DISTRIBUTION LIST

1. Jackie Craig
Defence Science and Technology Organization
2. Dr. Andrew Shaw
Defence Science and Technology Organization
3. Dr. Bevan Bates
Defence Science and Technology Organization
4. DSTO Research Library
Defence Science and Technology Organization
5. Dr. David Jenn
Naval Postgraduate School
6. Dr. Phillip Pace
Naval Postgraduate School